On The Development And Application Of A Modified Boundary Element Method For The Analysis Of Three-Dimensional Elastostatic Problems In Thick Plates

Thesis by
Lingyun Lu

In Partial Fulfillment of the Requirements
for the Degree of
Doctor of Philosophy

California Institute of Technology
Pasadena, California
1992
(Submitted November 21, 1991)

to my wife, Jennifer,

and to my daughter, Stephany

ACKNOWLEDGMENTS

It is very difficult to express my thanks to all the people who have helped me to accomplish this project. Perhaps, the first person I ought to thank is my advisor and friend Prof. Ares J. Rosakis, who has given me constant support and guidance through the various stages of my research. I am also indebted to Prof. Francisco G. Benitez. His insight knowledge of the fundamental solution and experience in numerical calculation have given me inspiration and guidance. I will never forget the work we did together in Sevilla, Spain. I am grateful to Prof. Thomas A. Cruse for his help in the analytical calculation of Kelvin's solution, and for his generosity for providing me with his precious notes. Prof. John F. Hall helped me a great deal on numerical integration and some other numerical problems that occurred in my research. His physical insight has extended my understanding of the problems.

I owe much too much to my wife, Jennifer, for her unending patience, love and friendship. I can not imagine being able to accomplish so much without her constant encouragement.

I would like to thank all the people in SM group for their support and all the fun time we had together. Especially, I would like to express my gratitude to my officemate Dr. Carl Schultheisz for all the help he gave me throughout the years.

I also would like to thank my Chinese friends, Dr. Dawei Dong, Zhao Bin, Dr. Yong Gao, Dr. Minsheng Han, Yixin Liu, and Xinlei Hua for being there whenever I needed a hand.

Finally, I would like to thank my family, especially my parents, for the support they gave me over all these years. Their support and encouragement will never be forgotten.

ABSTRACT

A modified three-dimensional Boundary Element Method (BEM) is developed. This method is specially tailored towards applications in three-dimensional elasticity, involving regions containing two parallel planar surfaces. Typical structures are the three-dimensional plate structures. The formulation makes use of the three-dimensional fundamental solution of a concentrated load applied in an infinite three-dimensional plate of uniform finite thickness (obtained by Benitez and Rosakis in 1985). The most attractive feature of this modified BEM is that, for the class of problems involving structures described above subjected to traction-free boundary conditions on the planar surfaces, discretization is only required on the lateral surfaces of the plate and the surfaces of the cavities, holes, and cracks in the plate. No discretization is needed on the planar surfaces of the plate. In this initial study, three problems involving a pressurized hole in an infinite three-dimensional plate are analyzed. The shapes of the holes include a circular hole and two elliptical holes with the aspect ratios of 4 and 10, respectively. In all the cases, the accuracy of the modified BEM is established by direct comparison of its results with those of finite element calculations. The results of the modified BEM are also compared with the plane-stress and plane-strain approximations of the problems under consideration. This comparison make it possible to access the important three-dimensional effects near the surface of the elliptical hole.

Table Of Contents

CHAPTER 1

INTRODUCTION

Boundary Element Methods (BEMs)[1][2][3] have grown in the shadow of finite element methods since their birth. The finite element methods [4][5] have been widely used in the analysis of problems in various fields of engineering practice because of the simplicity and flexibility in their formulations. On the contrary, boundary element methods have not received the attention they deserve. Among other things, the complexity of the mathematics involved in formulating these methods perhaps is the single most important obstacle that has prevented many from seeing the attractive sides of these methods.

Perhaps one way to understand the boundary element methods is to explore their physical aspects [3]. Many science and engineering problems can be reduced to mathematical models that belong to a class of problems known as *boundary value problems.* These problems are characterized by a region of interest $\mathcal{R}$ whose boundary is $\partial\mathcal{R}$. A set of partial differential equations model the physics of the problem in $\mathcal{R}$, and these equations have to be solved subject to certain constraints or conditions described on the boundary $\partial\mathcal{R}$. The basic principles of boundary element methods can be illustrated with the reference to Figures 1.1. Figure 1.1a represents a region $\mathcal{R}$. A boundary value problem is considered in the region $\mathcal{R}$ in Figure 1.1a. Figure 1.1b represents an infinite region and $\partial\mathcal{R}'$ is a tracing of the boundary $\partial\mathcal{R}$ onto the infinite region E_3. It is easier to find analytical solutions to the relevant partial differential equations in the infinite region of Figure 1.1b than in the actual region $\mathcal{R}$ of Figure 1.1a.

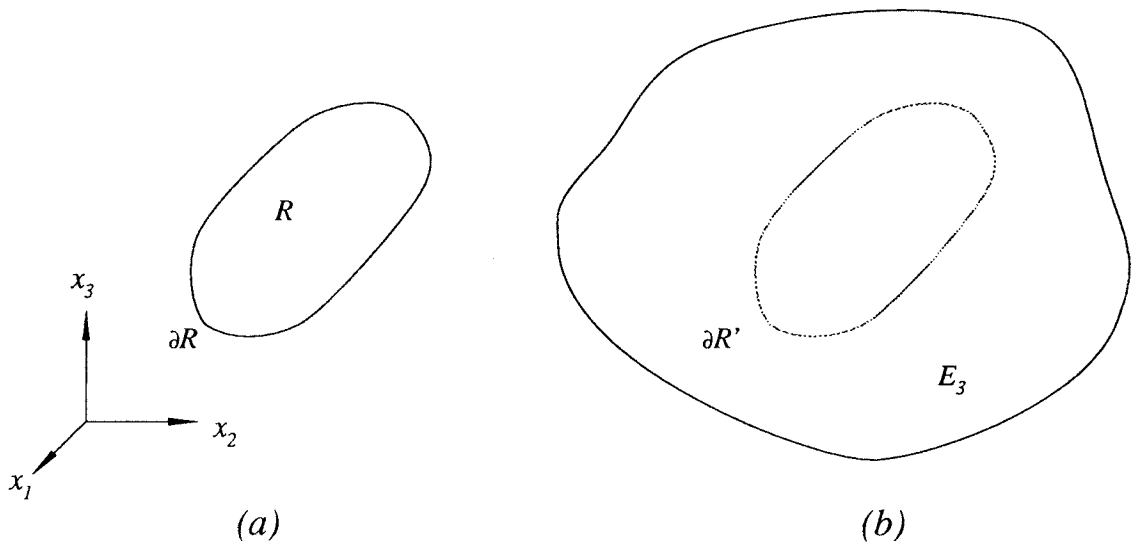

FIGURE 1.1 Finite Region $\mathcal{R}$ and Infinite Region E_3

In particular, the pioneering work by Kelvin has resulted in the analytical solution for such a problem. The Kelvin problem consists of a concentrated load acting in the interior of an infinite body composed of homogeneous, isotropic, linear elastic material. The Kelvin solution gives the displacement and stress at any point different from the loading point in the interior of the body. This solution is derived in Kelvin & Tait's treatise [6] through a limiting process. The Kelvin solution belongs to a class of solutions that have the property that when the point of observation approaches the loading point, the solution becomes singular.

Consider now how a boundary value problem may be solved through the use of Kelvin's solution. Suppose for the moment that it so happened that the Kelvin solution produced precisely the same conditions on the virtual boundary $\partial\mathcal{R}'$ in the infinite region as those prescribed on the boundary $\partial\mathcal{R}$ in Figure 1.1a. If this were the case then, because the solutions to well posed problems are unique in elastostatics, the problem in Figure 1.1a is solved by addressing the problem in

Figure 1.1b.

For most problems, the above case is unlikely to happen. However, a numerical procedure can be developed to find a number of Kelvin solutions which, when superimposed, produce approximately the correct conditions on $\partial\mathcal{R}'$. This is the basic concept of the boundary element method. This numerical procedure is developed as follows with the understanding that an approximate solution is considered to be acceptable when it can match the prescribed conditions on $\partial\mathcal{R}$ at some *designated* points on $\partial\mathcal{R}'$. In the numerical procedure, the virtual boundary $\partial\mathcal{R}'$ is discretized into a number of elements, for instance, the total number is N. For simplicity, the designated points are chosen to be at the midpoints of the elements. The task is then to find the amplitudes of N Kelvin solutions applied at the midpoints of the elements. When these Kelvin solutions are superimposed, they will give the required conditions at the midpoints of the elements. The combination effect can then be expressed in terms of the amplitudes of the Kelvin solutions, and the final effect at N midpoints should be the same as that prescribed on the boundary $\partial\mathcal{R}$. Thus, the N unknown amplitudes can be obtained by solving a system of linear algebraic equations.

In the early developments, boundary element methods were considered as the summation of a series of the singular solutions with proper amplitudes as presented above, and the boundary element method was normally referred to as the *indirect method*. However, boundary element methods can be constructed through the so called *direct method* as well. The direct method was given the name of boundary integral-equation (BIE) method by Swedlow and Cruse [7]. Somewhat after that time, other authors, notably Banerjee and Brebbia, saw the need to relate the numerical capability of the method to the finite element method, and the name

boundary element method was coined. In some literature, e.g., [8], the formulation is referred to as the Boundary Integral Equations (BIEs), while the method of numerical implementation is referred to as the Boundary Element Method (BEM). The essential elements for building up any boundary integral equations in the direct method are: a) the use of the ellipticity property of the governing differential equations, b) the use of the reciprocal work theorem, c) the existence of an analytical (fundamental) solution to the governing differential equations. Nonlinear and dynamic BEM analyses follow the same formulation strategy. This *direct method* for BEM formulations is a mathematical approach, and it makes use of the full Somigliana integral identities. These identities are written directly in terms of the physical boundary conditions, regardless of the nature of the mixed boundary conditions being considered. The physics involved in the *direct method* can not be seen as clearly as the *indirect method.*

One significant difference between the boundary element and the finite element methods becomes clear from the above illustration. The finite element methods require the discretization of the whole region into elements. The solutions are evaluated at the element nodes, and the solutions between the nodes are expressed in a simple, approximate form in terms of the values at the nodes. A system of linear algebraic equations is formed with regards to the unknown values at the nodes. This system of linear equations is large but sparse. However, in boundary element methods, only the boundary $\partial\mathcal{R}$ needs to be discretized. The numerical solution is built on the basis of analytical solutions, such as the Kelvin solution, that have already been obtained for simple problems involving infinite regions. The numerical solution satisfies approximately the specified boundary conditions at each element on $\partial\mathcal{R}$. Because Kelvin's solution satisfies the governing partial differential equations in E_3, there is no need to discretize the interior of $\mathcal{R}$. Hence, the BEM

reduces the dimension of the problem by one and results in a smaller problem size. To solve the same boundary value problem, the system of equations generated by the boundary element methods is much smaller than that for the finite element methods although the matrix associated with the equations is full and unsymmetric. With the use of the boundary element methods, it is possible to solve relatively large engineering problems using relatively small scale computers.

Boundary element methods have emerged as a powerful alternative to finite element methods. A great advantage of the BEM can be seen from the fact that the analytical solution, such as the Kelvin solution, satisfies the partial differential equations in the region $\mathcal{R}$. Once the solution for the problem of interest is numerically obtained on the boundary, the values in the interior of the region can be easily related to those on the boundary through the Boundary Integral Equations. No further approximation is introduced. This feature of the boundary element methods is particularly advantageous for modeling regions of high stress gradients. The boundary element methods can deal with this type of problems with great accuracy and efficiency [9]. The BEM is also seen as a significant aid to engineering for fracture mechanics [10], [11], [12], as well as elasto-dynamic problems [13]. Another great advantage of boundary element methods is its inherent ability to deal with infinite domain problems [1] [14]. While the boundary element methods have advantages in many areas, the finite element methods still hold merits in dealing with stress distributions and natural frequency problems [15]. The BEM has also many limitations, for example, if the region $\mathcal{R}$ of the problem is nonhomogeneous then it would no advantage to use the BEM since the whole region has to be approximated. The BEM loses almost all the advantages in this case.

The *direct method* shines light on how to construct different boundary ele-

ment methods. A number of publications have shown that, for particular classes of boundary value problems, different boundary integral formulations may be developed to take advantage of the properties of the problems under consideration. The main difference between these methods is the use of diverse fundamental solutions that are more appropriate to deal with the particular geometries and loading conditions of the problems. The boundary element method using the Kelvin solution as the fundamental solution has been applied to two-dimensional problems by Rizzo [16] and subsequently extended to three-dimensional problems by Cruse [17][18][19]. Kermanidis [20] developed a fundamental solution specially for axially symmetrical elasticity problems, and this fundamental solution is used to construct the boundary element scheme appropriate to the above type of problems. Mindlin [21] developed a fundamental solution for the half-space problem, Telles and Brebbia [22] used the Mindlin solution in their boundary element method. For problems involving a traction-free flat surface, it is not necessary to model that surface with elements since the Mindlin solution already satisfies the traction-free boundary conditions on the same surface. Snyder and Cruse [23] developed a fundamental solution for anisotropic materials. Their solution modified the two-dimensional Kelvin solution in an infinite body by including a straight, traction-free crack of length $2a$ at an arbitrary location and orientation in the infinite region. A boundary element method is built on the basis of this fundamental solution. In this approach, the fundamental solution completely accounts for the presence of a crack, thus two-dimensional crack problems can be solved with no discretization on the crack required. The above are just a few examples of different BEMs. In all the above examples, the modeling effort for the particular problem is greatly reduced, and so are the problem sizes. More importantly, these different boundary element methods have shown great accuracy and efficiency compared with the conventional boundary element methods

which employs the Kelvin solution.

Current research on this subject is inspired by these innovative developments. A modified boundary element method using a special fundamental solution is developed through the following chapters. This modified boundary element method is tailored to deal with problems in three-dimensional regions involving parallel planar surfaces. Three-dimensional plate structures are the most common structures involving this kind of regions. The fundamental solution used here was developed by Benitez and Rosakis [24], and it corresponds to the analytical solution of a concentrated load acting in an infinite plate of uniform finite thickness. The surfaces of the plate are traction-free. By making use of this special fundamental solution for the analysis of problems involving parallel planar surfaces, it will be shown that there is no need to discretize such surfaces as long as they are traction-free. Compared to the conventional boundary element method, the problem size may be further reduced by invoking this modified boundary element method. This method is particularly attractive in dealing with problems involving multi-crack-interactions. The savings in not to discretize these planar surfaces of the plate could be tremendous.

In this initial study, three test problems are investigated. One problem involves a pressurized circular hole embedded in an infinite plate of uniform finite thickness. The other two problems consist of a pressurized elliptical hole in an infinite plate of uniform finite thickness. The elliptical holes have aspect ratios of 4 and 10, respectively. These problems are analyzed by means of the modified boundary element method. This analysis will be compared with the results of the two-dimensional approximations of plane-stress and plane-strain and the results of the finite element analysis.

The plane-stress and plane-strain analyses are the two extreme cases of the

three-dimensional problems, since the two-dimensional cases of plane-stress and plane-strain represent the limiting cases of infinitesimally thin and infinitely thick three-dimensional bodies. However, in the pressurized circular hole case, it happens that the three-dimensional solution coincides with both the plane-stress and plane-strain solutions. The two-dimensional solutions are the exact solutions in both the displacement and stress for the three-dimensional pressurized circular hole problem. In this case, the two-dimensional solutions are used as the bench marks for the comparisons of the numerical results obtained from both the modified boundary element and finite element analyses. In the cases of the pressurized elliptical hole problems, the three-dimensional solutions are expected to differ from the two-dimensional plane-stress and plane-strain solutions. The three-dimensional effect is observed by comparing the numerical solutions of boundary element and finite element analyses with the two-dimensional solutions. The results of the boundary element analysis is further compared with those of finite element analysis in order to explore the differences in the methods.

CHAPTER 2

FUNDAMENTAL SOLUTION

2.1 Overview

The equilibrium problem of a single plate composed of a homogeneous, isotropic, linear elastic material was first considered by Dougall [25]. Dougall conducted an extensive study of the thick plate subjected to an arbitrary (surface and internal) loading using the method of potential functions. He obtained solutions in terms of infinite series. Teodone [26] studied the same problem using mapping techniques. Later, Orlando [27] obtained the solution of a plate under surface traction. Lur'e [28][29] constructed the solution for a plate subjected to surfaces loadings. Shapiro [30] and Sneddon [31] analyzed the distribution of stress in an infinite plate for the case of uniformly distributed normal loading over a circular area on the surface. Sneddon also obtained the close form solution of the stress field under an approximation assumption. His close form solution was expressed in the form of semi-infinite integrals.

The fundamental solution presented here was developed by F. G. Benitez and A. J. Rosakis; the work has been documented in [24]. Some important features of the fundamental solution are discussed in this chapter for the sake of completeness.

The fundamental solution is the three-dimensional analytical solution of the problem consisting an infinite plate with uniform finite thickness h; the plate is subjected to a concentrated load acting in its interior, and the upper and the lower surfaces of the plate are traction-free. Moreover, the plate is composed of a homogeneous, isotropic, linear elastic material. The concentrated load described here is defined in the sense discussed by Turteltaub and Sternberg [32]. The problem is shown schematically in Figure 2.1. No additional assumptions are made.

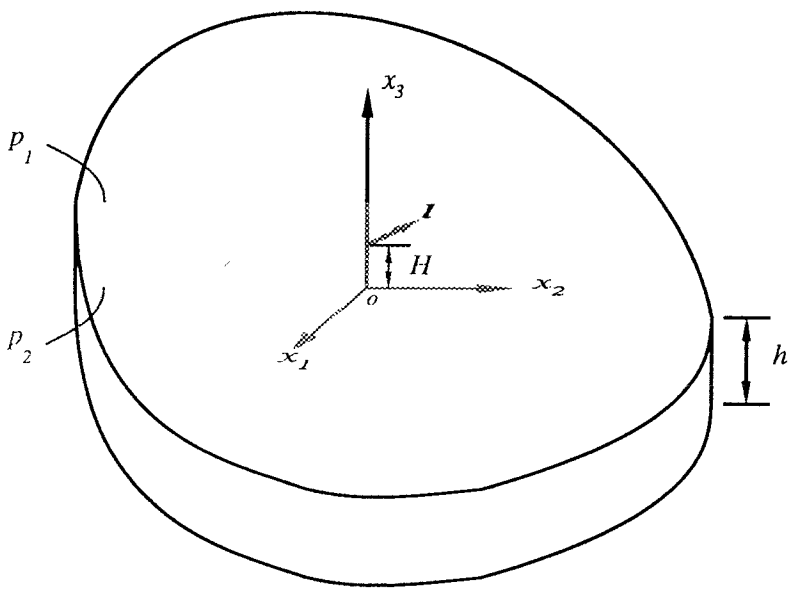

FIGURE 2.1 Definition Of The Problem

The method of solution is based on the transfer matrix formulation used by Vlasov and Leont'ev [33]. This method was further generalized by Bufler [34] to the problem of a three-dimensional plate containing a unit concentrated load acting arbitrarily in its interior. Although Bufler formulated the problem using this method, he never obtained a solution.

2.1.1 Nomenclature

$\boldsymbol{a}, \boldsymbol{b}, \boldsymbol{c}, \ldots$: the lower–case, boldface ***italic*** letters are reserved for vectors

$\boldsymbol{A}, \boldsymbol{B}, \boldsymbol{I}, \ldots$: the upper–case, boldface ***ITALIC*** letters are reserved for tensors of second order

$\boldsymbol{\sigma}, \boldsymbol{\tau}, \boldsymbol{\epsilon}, \ldots$: the boldface Greek letters are reserved for tensors of second order

E_3 : three-dimensional Euclidean space

$\boldsymbol{X} = \{0; \boldsymbol{e}_1, \boldsymbol{e}_2, \boldsymbol{e}_3\}$: the proper orthogonal Cartesian co- ordinate system

$\boldsymbol{x} = (x_1, x_2, x_3)$: the position vector of the observing point described in the Cartesian co-ordinate system

$\boldsymbol{H} = (0, 0, H)$: the position vector of the point of application of the concentrated load described in the Cartesian co-ordinate system

$\boldsymbol{\ell} = (\ell_1, \ell_2, \ell_3)$: the concentrated load–vector describ- ed in the Cartesian co-ordinate system

$\mathcal{R}$: an arbitrary regular region in E_3

$\partial\mathcal{R}$, $\bar{\mathcal{R}}$ & $\overset{\circ}{\mathcal{R}}$: the boundary, the closure and the interior of $\mathcal{R}$

$\mathcal{R} - \{\boldsymbol{x}\}$, $\boldsymbol{x} \in \mathcal{R}$: the set obtained by the deletion of a point $\{\boldsymbol{x}\}$ from $\mathcal{R}$

σ_{ij}^k, ϵ_{ij}^k, & u_i^k : the Cartesian components of stress, strain and displacement with the concentrated load acting in the kth axis-direction, respectively

(R, θ, x_3) : the cylindrical co-ordinates of the observing point where

$$R = \sqrt{(x_1^2 + x_2^2)}\ ,\ \theta = tan^{-1}(x_2/x_1)$$

h : the thickness of the plate

E, G, & ν : the modulus of elasticity, the shear modulus, and the Poisson's ratio, respectively

$b = R/h$, $\chi = x_3/h$, $\psi = H/h$: the dimensionless geometric parameters

$\partial\mathcal{B}_\eta(\boldsymbol{\xi})$: the spherical ball centered at the point $\boldsymbol{\xi}$ with an radius of η

Standard indicial notation will be used in connection with the Cartesian components of tensors of any order. Subscripts preceded by a comma indicate partial differentiation with respect to the corresponding Cartesian co-ordinate. For functions having more than one vector variables, the differentiation mentioned before will be understood to be performed with respect to the co-ordinates of the component of the first vector variable, thus

$$f_{,i}(\boldsymbol{x}, \boldsymbol{y}) = \frac{\partial f(\boldsymbol{x}, \boldsymbol{y})}{\partial x_i}. \tag{2.1.1}$$

As to the smoothness of a function, we write $g(\boldsymbol{x}) \in \mathcal{C}(\mathcal{R})$ if function g is defined and is continuous on a region $\mathcal{R} \subset E_3$. Moreover, if m is a positive integer, we write $g(\boldsymbol{x}) \in \mathcal{C}^m(\mathcal{R})$ when $g \in \mathcal{C}(\mathcal{R})$ and its partial derivatives of the order up to and including m are defined as well as continuous on $\mathcal{R}$ and they coincide with functions continuous on $\mathcal{R}$.

Definition 2.1.1 (an elastostatic state on $\mathcal{R}$).

Write

$$\mathcal{S} = [\boldsymbol{u}, \boldsymbol{\sigma}] \in \mathcal{E}_s(E, \nu, \boldsymbol{f}; \mathcal{R}), \tag{2.1.2}$$

and say that the ordered array $\mathcal{S} = [\boldsymbol{u}, \boldsymbol{\sigma}]$ *of displacement and stress field is an elastostatic state on* $\mathcal{R}$ *corresponding to the body force density* $\boldsymbol{f}$*, provided:*

a) $\boldsymbol{u} \in \mathcal{C}^2(\overset{\circ}{\mathcal{R}}) \cap \mathcal{C}^1(\mathcal{R})$, $\boldsymbol{f} \in \mathcal{C}(\mathcal{R})$, *with* $E > 0$, $-1 < \nu < 1/2$;

b) $\boldsymbol{u}$, $\boldsymbol{\sigma}$, $\boldsymbol{f}$, E *and* ν *satisfy the following equations on* $\overset{\circ}{\mathcal{R}}$,

$$\nabla \cdot \boldsymbol{\sigma} + \boldsymbol{f} = \boldsymbol{0},$$

$$\boldsymbol{\sigma} = \frac{\nu E}{(1+\nu)(1-2\nu)} \Big[\nabla \cdot \boldsymbol{u}\Big]\, \boldsymbol{I} + \frac{E}{2(1+\nu)} \Big[\nabla \boldsymbol{u} + \nabla^T \boldsymbol{u}\Big]. \tag{2.1.3}$$

Furthermore, if $\mathcal{S} = [\boldsymbol{u}, \boldsymbol{\sigma}]$ *is an elastostatic state on* $\mathcal{R}$*, and* Σ *is a regular surface with the unit normal* $\boldsymbol{n}$*, we call* $\boldsymbol{t}$ *the traction vector of* S *on* Σ *if*

$$t_i = \sigma_{ij} n_j, \quad \text{on } \overset{*}{\Sigma}, \tag{2.1.4}$$

where $\overset{*}{\Sigma}$ *is the subset of all points of* Σ *at which a normal is defined.*

2.2 Kelvin Solution

In the present section, the problem of a concentrated load applied at a point of an elastic solid occupying the entire space E_3 is dealt with according to the terms used by Turteltaub and Sternberg [32]. The solution of this problem was first given by Kelvin [35]; it is derived in Kelvin & Tait's treatise [6] through a limiting process, which is made fully explicit in [36].

Definition 2.2.1 (Sequence of body-force fields tending to a concentrated load).

Let $\boldsymbol{\xi} \in E_3$ *and let* $\boldsymbol{\ell}$ *be a vector. We say that* $\{\boldsymbol{f}^m\}$ *is a sequence of body-force fields on* E_3 *tending to a concentrated load* $\boldsymbol{\ell}$ *at (the point)* $\boldsymbol{\xi}$ *if:*

$$\begin{aligned} &a)\ \boldsymbol{f}^m \in \mathcal{C}(E_3) \qquad (m = 1, 2, 3, \ldots); \\ &b)\ \boldsymbol{f}^m = \boldsymbol{0} \text{ on } E_3 - \mathcal{B}_\rho^m(\boldsymbol{\xi}), \qquad (m = 1, 2, 3, \ldots); \\ &c)\ \lim_{m\to\infty} \int_{E_3} \boldsymbol{f}^m \, dV = \boldsymbol{\ell}; \\ &d)\ \text{the sequence } \left\{ \int_{E_3} \left| \boldsymbol{f}^m \right| dV \right\} \text{ is bounded.} \end{aligned} \tag{2.2.5}$$

where $\{\mathcal{B}_\rho^m(\boldsymbol{\xi})\}$ *is a sequence of spheres such that* $\rho \to 0$ *as* $m \to \infty$.

The theorem cited below supplies a representation of the solution to the problem under consideration.

Theorem 2.2.1 (Limit definition of the solution to Kelvin's problem). *Let* $\boldsymbol{\xi} \in E_3$ *and* $\boldsymbol{\ell}$ *be a vector. Further let* $\{\boldsymbol{f}^m\}$ *be a sequence of body-force fields on* E_3 *tending to a concentrated load* $\boldsymbol{\ell}$ *at* $\boldsymbol{\xi}$. *Then*

a) there exist a unique sequence of states $\{\mathcal{S}_K^m\}$ *such that*

$$\mathcal{S}_K^m = \left[\boldsymbol{u}_K^m, \boldsymbol{\sigma}_K^m \right] \in \mathcal{E}_s(E, \nu, \boldsymbol{f}^m; E_3), \qquad (m = 1, 2, 3, \ldots); \tag{2.2.6}$$

b) $\{\mathcal{S}_K^m\}$ *converges to a state* $\mathcal{S}_K = [\boldsymbol{u}_K, \boldsymbol{\sigma}_K]$ *on* $E_3 - \{\boldsymbol{\xi}\}$, *the convergence being uniform on any closed subset of* $E_3 - \{\boldsymbol{\xi}\}$;

c) the limit state $\mathcal{S}_K$ *is independent of the sequence* $\{\boldsymbol{f}^m\}$ *and admits the representation*

$$\mathcal{S}_K(\boldsymbol{x}, \xi) = \mathcal{S}_K^i(\boldsymbol{x}, \boldsymbol{\xi})\ell_i = \mathcal{S}_K(\boldsymbol{x}, \boldsymbol{\xi}, \boldsymbol{e}_i)\ell_i, \qquad \forall \boldsymbol{x} \in E_3 - \{\boldsymbol{\xi}\}, \tag{2.2.7}$$

where

$$\mathcal{S}_K^i(\boldsymbol{x}, \boldsymbol{\xi}) = \mathcal{S}_K^i(\boldsymbol{x} - \boldsymbol{\xi}, \boldsymbol{0}), \qquad \forall (\boldsymbol{x}, \boldsymbol{\xi}) \in E_3 \times E_3 - \mathcal{D}, \tag{2.2.8}$$

and

$$\begin{aligned} \mathcal{D} &= \{(\boldsymbol{x},\boldsymbol{\xi})|(\boldsymbol{x},\boldsymbol{\xi}) \in E_3 \times E_3,\ \boldsymbol{x} = \boldsymbol{\xi}\}, \\ E_3 \times E_3 - \mathcal{D} &= \{(\boldsymbol{x},\boldsymbol{\xi})|(\boldsymbol{x},\boldsymbol{\xi}) \in E_3 \times E_3,\ \boldsymbol{x} \neq \boldsymbol{\xi}\}. \end{aligned} \tag{2.2.9}$$

The displacements and stresses of $\mathcal{S}_K^i(\cdot, \boldsymbol{0})$ are, for all $\boldsymbol{x} \in E_3 - \{\boldsymbol{0}\}$, given by

$$\begin{aligned} u_j^i(\boldsymbol{x}, \boldsymbol{0}) &= \frac{1}{16\pi\mu(1-\nu)r}\left[\frac{x_i x_j}{r^2} + (3-4\nu)\delta_{ij}\right], \\ \sigma_{jk}^i(\boldsymbol{x}, \boldsymbol{0}) &= -\frac{1}{8\pi(1-\nu)r^3}\left[\frac{3x_i x_j x_k}{r^2} + (1-2\nu)(\delta_{ij}x_k + \delta_{ik}x_j - \delta_{jk}x_i)\right], \end{aligned} \tag{2.2.10}$$

where

$$\mu = \frac{E}{2(1+\nu)}, \tag{2.2.11}$$

and

$$r = |\boldsymbol{x}| = \sqrt{x_1^2 + x_2^2 + x_3^2}. \tag{2.2.12}$$

$\mathcal{S}_K$ is called the Kelvin state corresponding to a concentrated load $\boldsymbol{\ell}$ at $\boldsymbol{\xi}$ (and to the elastic constant μ and ν). In particular, we say that $\mathcal{S}_K^i(\cdot, \boldsymbol{\xi})$ is the Kelvin state corresponding to a unit concentrated load at $\boldsymbol{\xi}$ in the x_i–direction.

The theorem is proved by Sternberg and Eubanks [36]. The need for condition d) in definition 2.2.1 is also established in [36], where it is shown by means of a counter-example that conclusions b) and c) in Theorem 2.2.1 become invalid if this hypothesis is omitted. The foregoing requirement is no longer necessary if $\boldsymbol{f}^m$ is parallel and unidirectional, in which case condition d) is implied by c) of Definition 2.2.1.

Theorem 2.2.2 (Properties of the Kelvin state).

The Kelvin state $\mathcal{S}_K$ corresponding to a concentrated load $\boldsymbol{\ell}$ at point $\boldsymbol{\xi}$ has the properties:

$$
\begin{aligned}
&a)\ \mathcal{S}_K = [\boldsymbol{u}_K, \boldsymbol{\sigma}_K] \in \mathcal{E}_s(E, \nu, \boldsymbol{0}; E_3 - \{\boldsymbol{\xi}\});\\
&b)\ \boldsymbol{u}_K(\boldsymbol{x}, \boldsymbol{\xi}) = O(|\boldsymbol{x} - \boldsymbol{\xi}|^{-1}),\ \boldsymbol{\sigma}_K(\boldsymbol{x}, \boldsymbol{\xi}) = O(|\boldsymbol{x} - \boldsymbol{\xi}|^{-2}), \quad \text{as } \boldsymbol{x} \to \boldsymbol{\xi};\\
&c)\ \int_{\partial B_\rho(\boldsymbol{\xi})} \boldsymbol{t}_K(\boldsymbol{x}, \boldsymbol{\xi}; \boldsymbol{n})\, dA = \boldsymbol{\ell}\ ,\ \int_{\partial B_\rho(\boldsymbol{\xi})} (\boldsymbol{x} - \boldsymbol{\xi}) \wedge \boldsymbol{t}_K(\boldsymbol{x}, \boldsymbol{\xi}; \boldsymbol{n})\, dA = \boldsymbol{0}, \quad \forall \rho > 0,
\end{aligned}
\tag{2.2.13}
$$

where $\boldsymbol{t}_K(\boldsymbol{x}, \boldsymbol{\xi}; \boldsymbol{n})$ is the traction vector on the surface of $\partial\mathcal{B}_\rho(\boldsymbol{\xi})$ that faces $\boldsymbol{\xi}$. $\wedge$ indicates the cross-product of two vectors $\boldsymbol{a}$ and $\boldsymbol{b}$ that is defined as follows,

$$
\boldsymbol{a} \wedge \boldsymbol{b} = \epsilon_{ijk} a_i b_j \boldsymbol{e}_k, \qquad (i, j, k\ =\ 1, 2, 3), \tag{2.2.14}
$$

where

$$
\epsilon_{ijk} = \begin{cases} = \ \ 1, & \text{if the order of } i, j, k \text{ is } 1 \to 2 \to 3 \to 1;\\ = -1, & \text{if the order of } i, j, k \text{ is } 3 \to 2 \to 1 \to 3;\\ = \ \ 0, & \text{otherwise.} \end{cases} \tag{2.2.15}
$$

The formulation of Kelvin's problem in terms of a) and c) alone is incomplete in view of the existence of elastic states on $E_3 - \{\boldsymbol{\xi}\}$ that possess self-equilibrated singularities at $\boldsymbol{\xi}$. In contrast, properties a), b) and the first of c) suffice to characterize the Kelvin state uniquely.

2.3 Fundamental Solution For Infinite Plate Problem

In this section, we define the problem in mathematical terms. Consider now a proper orthogonal Cartesian co-ordinate system $\boldsymbol{X} = \{0; \boldsymbol{e}_1, \boldsymbol{e}_2, \boldsymbol{e}_3\}$. For the sake of convenience, we place the $x_1 - x_2$ plane of the co-ordinate system in the lower surface of the plate, and choose x_3-axis such that the loading point is located at a distance H from the origin on this axis. Define an infinite region $\mathcal{P} \subset E_3$ occupied by the body in question as follows:

$$\left.\begin{aligned} &\mathcal{P} = \{\boldsymbol{x} | \boldsymbol{x} \in E_3, \quad 0 \leq \boldsymbol{x} \cdot \boldsymbol{e}_3 \leq h\}, \\ &\partial\mathcal{P} = \partial\mathcal{P}_1 \cup \partial\mathcal{P}_2, \\ &\textit{where} \\ &\partial\mathcal{P}_1 = \{\boldsymbol{x} | \boldsymbol{x} \in E_3,\ \boldsymbol{x} \cdot \boldsymbol{e}_3 = 0\}, \quad \partial\mathcal{P}_2 = \{\boldsymbol{x} / \boldsymbol{x} \in E_3,\ \boldsymbol{x} \cdot \boldsymbol{e}_3 = h\}. \end{aligned}\right\} \tag{2.3.16}$$

Also, let $\boldsymbol{\xi}$ be the point of application of the concentrated load $\boldsymbol{\ell}$. Again, the concentrated load described here is in the sense discussed by Turteltaub and Sternberg [32].

Definition 2.3.1 (Sequence of body-force fields tending to a concentrated load).

Let $\boldsymbol{\xi} \in \mathcal{P}$ and let $\boldsymbol{\ell}$ be a vector. We say that $\{\boldsymbol{f}^m\}$ is a sequence of body-force fields on $\mathcal{P}$ tending to a concentrated load $\boldsymbol{\ell}$ at (the point) $\boldsymbol{\xi}$ if:

$$\begin{aligned} &a)\ \boldsymbol{f}^m \in \mathcal{C}(\mathcal{P}), \qquad (m = 1, 2, 3, \ldots); \\ &b)\ \boldsymbol{f}^m = \boldsymbol{0} \text{ on } \mathcal{P} - \mathcal{B}_\rho^m(\boldsymbol{\xi}) \cap \mathcal{P}, \qquad (m = 1, 2, 3, \ldots); \\ &c)\ \lim_{m \to \infty} \int_{\mathcal{B}_\rho^m(\boldsymbol{\xi}) \cap \mathcal{P}} \boldsymbol{f}^m \, dV = \boldsymbol{\ell}; \\ &d)\ \text{the sequence } \left\{ \int_{\mathcal{B}_\rho^m(\boldsymbol{\xi}) \cap \mathcal{P}} \left| \boldsymbol{f}^m \right| dV \right\} \text{ is bounded.} \end{aligned} \tag{2.3.17}$$

where $\left\{\mathcal{B}_\rho^m(\boldsymbol{\xi}) \cap \mathcal{P}\right\}$ *is a sequence of spheres such that* $\rho \to 0$ *as* $m \to \infty$.

Claim 2.3.1 (Limit definition of the solution to the plate problem). *Let* $\boldsymbol{\xi} \in \mathcal{P}$ *and* $\boldsymbol{\ell}$ *be a vector. Further let* $\{\boldsymbol{f}^m\}$ *be a sequence of body-force fields on* $\mathcal{P}$ *tending to a concentrated load* $\boldsymbol{\ell}$ *at* $\boldsymbol{\xi}$. *Then*

a) *there exists a unique sequence of states* $\{\mathcal{S}^m\}$ *such that*

$$\mathcal{S}^m = \left[\boldsymbol{u}^m, \boldsymbol{\sigma}^m\right] \in \mathcal{E}_s(E, \nu, \boldsymbol{f}^m; \mathcal{P}), \qquad (m = 1, 2, 3, \ldots); \tag{2.3.18}$$

b) $\{\mathcal{S}^m\}$ *converges to a state* $\mathcal{S} = [\boldsymbol{u}, \boldsymbol{\sigma}]$ *on* $\mathcal{P} - \{\boldsymbol{\xi}\}$, *the convergence being uniform on any closed subset of* $\mathcal{P} - \{\boldsymbol{\xi}\}$;

c) *the limit state S is independent of the sequence* $\{\boldsymbol{f}^m\}$ *and admits the representation*

$$\mathcal{S}(\boldsymbol{x}, \boldsymbol{\xi}) = \mathcal{S}^i(\boldsymbol{x}, \boldsymbol{\xi})\ell_i = \mathcal{S}(\boldsymbol{x}, \boldsymbol{\xi}, \boldsymbol{e}_i)\ell_i, \qquad \forall \boldsymbol{x} \in \mathcal{P} - \{\boldsymbol{\xi}\}, \tag{2.3.19}$$

where

$$\mathcal{S}^i(\boldsymbol{x}, \boldsymbol{\xi}) = \mathcal{S}^i(\boldsymbol{x} - \boldsymbol{\xi}, \boldsymbol{0}), \qquad \forall (\boldsymbol{x}, \boldsymbol{\xi}) \in \mathcal{P} \times \mathcal{P} - \mathcal{D}', \tag{2.3.20}$$

and

$$\begin{aligned} \mathcal{D}' &= \{(\boldsymbol{x}, \boldsymbol{\xi}) | (\boldsymbol{x}, \boldsymbol{\xi}) \in \mathcal{P} \times \mathcal{P},\ \boldsymbol{x} = \boldsymbol{\xi}\}, \\ \mathcal{P} \times \mathcal{P} - \mathcal{D}' &= \{(\boldsymbol{x}, \boldsymbol{\xi}) | (\boldsymbol{x}, \boldsymbol{\xi}) \in \mathcal{P} \times \mathcal{P},\ \boldsymbol{x} \neq \boldsymbol{\xi}\}. \end{aligned} \tag{2.3.21}$$

The displacement and stress fields of the fundamental solution can be written as

$$\begin{aligned} \boldsymbol{u}(\boldsymbol{x}, \boldsymbol{\xi}, \boldsymbol{\ell}) &= \left[u_j^i(\boldsymbol{x}, \boldsymbol{\xi})\ell_i\right] \boldsymbol{e}_j; \\ \boldsymbol{\sigma}(\boldsymbol{x}, \boldsymbol{\xi}, \boldsymbol{\ell}) &= \left[\sigma_{jk}^i(\boldsymbol{x}, \boldsymbol{\xi})\ell_i\right] \boldsymbol{e}_j \otimes \boldsymbol{e}_k. \end{aligned} \tag{2.3.22}$$

where $u^i_j(\boldsymbol{x},\boldsymbol{\xi})$ and $\sigma^i_{jk}(\boldsymbol{x},\boldsymbol{\xi})$ are the Cartesian components of the displacement and stress fields, respectively. $\boldsymbol{e}_j \otimes \boldsymbol{e}_k$ indicates the tensor of second order. The complete set of the expressions for $u^i_j(\boldsymbol{x},\boldsymbol{\xi})$ and $\sigma^i_{jk}(\boldsymbol{x},\boldsymbol{\xi})$, with $\boldsymbol{\xi} = H\boldsymbol{e}_3$ and $\boldsymbol{x} \in \mathcal{P}$, is given by Benitez and Rosakis [24].

It is not intended here to try to prove the uniqueness of the solution to the plate problem. Instead, the solution has been proved to satisfy all the equilibrium equations, the constitutive relations of the stress and the displacement, and the corresponding boundary conditions. Also, the solution satisfies the following theorem.

Theorem 2.3.1 (properties of the fundamental solution for infinite plate). *The fundamental solution corresponding to a concentrated load $\boldsymbol{\ell}$ at point $\boldsymbol{\xi}$ has the properties:*

$$
\begin{aligned}
&a)\quad \mathcal{S} = [\boldsymbol{u},\boldsymbol{\sigma}] \in \mathcal{E}_s(E,\ \nu,\ \boldsymbol{0};\ \mathcal{P} - \{\boldsymbol{\xi}\});\\
&b)\quad \boldsymbol{t}(\boldsymbol{x},\boldsymbol{\xi}) = \boldsymbol{\sigma}(\boldsymbol{x},\boldsymbol{\xi})\boldsymbol{n} = \boldsymbol{0};\quad
\begin{cases}
\forall \boldsymbol{x} \in \partial\mathcal{P} & for\ \boldsymbol{\xi} \in \overset{\circ}{\mathcal{P}},\\
\forall \boldsymbol{x} \in \partial\mathcal{P} - \{\boldsymbol{\xi}\} & for\ \boldsymbol{\xi} \in \partial\mathcal{P},
\end{cases}\\
&c)\quad
\left.
\begin{aligned}
&\lim_{\eta\to 0} \int_{\partial\mathcal{B}_\eta(\boldsymbol{\xi})\cap\mathcal{P}} \boldsymbol{t}(\boldsymbol{x},\boldsymbol{\xi}) dA_{\boldsymbol{x}} = \boldsymbol{\ell};\\
&\lim_{\eta\to 0} \int_{\partial\mathcal{B}_\eta(\boldsymbol{\xi})\cap\mathcal{P}} (\boldsymbol{x}-\boldsymbol{x}) \wedge \boldsymbol{t}(\boldsymbol{x},\boldsymbol{\xi})\ dA_{\boldsymbol{x}} = \boldsymbol{0};
\end{aligned}
\right\} \boldsymbol{\xi} \in \mathcal{P},\\
&d)\quad \boldsymbol{u}(\boldsymbol{x},\boldsymbol{\xi}) = O\Big(|\ \boldsymbol{x}-\boldsymbol{\xi}\ |^{-1}\Big),\ \boldsymbol{\sigma}(\boldsymbol{x},\boldsymbol{\xi}) = O\Big(|\ \boldsymbol{x}-\boldsymbol{\xi}\ |^{-2}\Big) \text{ as } \boldsymbol{x}\to\boldsymbol{\xi}.
\end{aligned}
\tag{2.3.23}
$$

where $\boldsymbol{t}(\boldsymbol{x},\boldsymbol{\xi};\boldsymbol{n})$ in b) and c) is the traction vector on the surface of $\partial\mathcal{B}_\eta(\boldsymbol{\xi}) \cap \mathcal{P}$ that faces $\boldsymbol{\xi}$.

If the fundamental solution for the infinite plate problem is compared with the Kelvin solution, it becomes obvious that the two solutions have common asymptotic

behavior. It has been proved in [24] that the fundamental solution tends to the Kelvin solution as the point of observation tends to the point of application of the load. Both analytical and numerical evidence will be given in the next section to show this important feature.

2.3.1 Numerical Treatment Of Fundamental Solution For Infinite Plate Problem

Close examination of the expressions for $u_i^k(\boldsymbol{x},\ \boldsymbol{\xi})$ and $\sigma_{ij}^k(\boldsymbol{x},\ \boldsymbol{\xi})$ in [24] reveals that all the expressions for the displacement and stress components can be cast in the general form shown below

$$v(x_1,x_2,x_3) = A\int_0^\infty \left\{ \frac{g'(\lambda,\ \chi,\ \psi)}{1+e^{-4\lambda}-(2+4\lambda^2)^{-2\lambda}} J_\nu\left(\frac{\lambda\sqrt{x_1^2+x_2^2}}{h}\right) - B\frac{e^{-\lambda}}{\lambda^\alpha} \right\} d\lambda, \tag{2.3.24}$$

where $v(x_1,x_2,x_3)$ is a displacement or stress component; $\psi = H/h$, and $\chi = x_3/h$; $A = A(E,\nu,h,x_1,x_2)$ and $B = B(\nu,x_1,x_2,\chi,\psi)$ are simple functions of the variables involved; α varies from 1 to 3 for different cases; $J_\nu(x)$ is the Bessel function of the order ν; and $g'(\lambda,\chi,\psi)$ is a function composed of the finite summation of the products of the following form,

$$g'(\lambda,\chi,\psi) = \sum_{i=1}^{K} C_i \lambda^{\rho_i}\chi^{\beta_i}\psi^{\gamma_i} e^{\lambda(a_i\chi+b_i\psi+c_i)}, \tag{2.3.25}$$

where C_i is a simple constant; ρ_i, β_i, γ_i, a_i, b_i, and c_i are integers; ρ_i may vary from 0 to 4; β_i and γ_i are either 0 or 1, and $a_i\chi + b_i\psi + c_i$ is always non-positive.

The second integrand in (2.3.24) eliminates the singularity in λ caused by the first one. In formula (2.3.24), $\alpha = 1$ if the order of singularity at $\lambda = 0$ in the first integrand is $O(1/\lambda)$, and $\alpha = 2$ and $\alpha = 3$ have the similar meaning. If the first integrand is non-singular, then $B = 0$. Hence the solution is well behaved for every λ.

The basic idea of evaluating the stress and the displacement components of the fundamental solution is to compute them partially analytically and partially numerically. To illustrate this idea, (2.3.24) is written in the following way,

$$v(x_1,x_2,x_3) = A\Bigg\{ \int_0^\infty g'(\lambda,\chi,\psi) J_\nu\left(\frac{\lambda\sqrt{x_1^2+x_2^2}}{h}\right) d\lambda$$

$$+ \int_0^\infty \Bigg[\left(\frac{g'(\lambda,\ \chi,\ \psi)}{1+e^{-4\lambda}-(2+4\lambda^2)e^{-2\lambda}} - g'(\lambda,\chi,\psi) \right) J_\nu\left(\frac{\lambda\sqrt{x_1^2+x_2^2}}{h}\right)$$

$$- B\frac{e^{-\lambda}}{\lambda^\alpha} \Bigg] d\lambda \Bigg\}. \tag{2.3.26}$$

Considering the first integral in (2.3.26), one has

$$\int_0^\infty g'(\lambda,\chi,\psi) J_\nu\left(\frac{\lambda\sqrt{x_1^2+x_2^2}}{h}\right) d\lambda = \tag{2.3.27}$$

$$\sum_{i=1}^{K} C_i \chi^{\beta_i} \psi^{\gamma_i} \int_0^\infty \lambda^{\rho_i} e^{\lambda(a_i\chi+b_i\psi+c_i)} J_\nu\left(\frac{\lambda\sqrt{x_1^2+x_2^2}}{h}\right) d\lambda.$$

Each individual integral in (2.3.27) can be computed analytically, and they can be expressed in the following form

$$\int_0^\infty \lambda^a e^{-c\lambda} J_\nu(b\lambda)\, d\lambda = G(\nu,a,c,b), \tag{2.3.28}$$

where a, b and c are not functions of λ, and they are non-negative. Appendix A gives the results of $G(\nu,a,c,b)$ for all the required integrals. Therefore, Eq. (2.3.26)

can then be written in a more efficient way as follows,

$$v(x_1,x_2,x_3)=A\Bigg\{\sum_{i=1}^{K}C_i\chi^{\beta_i}\psi^{\gamma_i}G\Big(\nu,\rho_i,\sqrt{x_1^2+x_2^2}\Big/h,-(a_i\chi+b_i\psi+c_i)\Big)$$

$$+\int_0^{\infty}\left[\frac{(2+4\lambda^2-e^{-2\lambda})e^{-2\lambda}}{1+e^{-4\lambda}-(2+4\lambda^2)e^{-2\lambda}}g'(\lambda,\chi,\psi)J_\nu\left(\frac{\lambda\sqrt{x_1^2+x_2^2}}{h}\right)-B\frac{e^{-\lambda}}{\lambda^\alpha}\right]d\lambda\Bigg\}. \tag{2.3.29}$$

Define now,

$$g(\lambda,\chi,\psi)=e^{-2\lambda}g'(\lambda,\chi,\psi). \tag{2.3.30}$$

Then

$$g(\lambda,\chi,\psi)=\sum_{i=1}^{K}C_i\lambda^{\rho_i}\chi^{\beta_i}\psi^{\gamma_i}e^{\lambda(a_i\chi+b_i\psi+c_i-2)}. \tag{2.3.31}$$

The most important feature in (2.3.31) is that $a_i\chi+b_i\psi+c_i-2$ is always negative, and it reaches its maximum at -2. This is the key feature that guarantees the convergence of the infinite integral in (2.3.29).

The integral in (2.3.29) can not be evaluated analytically. It has to be evaluated numerically. After checking its denominator, one finds that it's not necessary to evaluate the integral over the entire integration region. Instead, it can be computed *approximately* over a region from 0 to P with relatively good accuracy. P is a pre-set "big" number as compared to 1. The integration interval is extended from 0 to $2P$ for the second integrand in order to archive the same order of accuracy. The error caused by truncating the integral will be discussed in the next section. The

truncated version of (2.3.29) becomes

$$v(x_1,x_2,x_3) = A\Bigg\{\sum_{i=1}^{K} C_i\chi^{\beta_i}\psi^{\gamma_i}G\Big(\nu,\rho_i,\sqrt{x_1^2+x_2^2}\Big/h,-(a_i\chi+b_i\psi+c_i)\Big)$$

$$+\int_0^P\left[\frac{(2+4\lambda^2-e^{-2\lambda})g(\lambda,\chi,\psi)}{1+e^{-4\lambda}-(2+4\lambda^2)e^{-2\lambda}}J_\nu\left(\frac{\lambda\sqrt{x_1^2+x_2^2}}{h}\right)-B\frac{e^{-\lambda}}{\lambda^\alpha}\right]d\lambda$$

$$-B\int_P^{2P}\frac{e^{-\lambda}}{\lambda^\alpha}\,d\lambda\Bigg\}. \tag{2.3.32}$$

By substituting (2.3.31) into (2.3.29) and performing variable transformation, one obtains,

$$v(x_1,x_2,x_3) = A\Bigg\{\sum_{i=1}^{K} C_i\chi^{\beta_i}\psi^{\gamma_i}G\Big(\nu,\rho_i,\sqrt{x_1^2+x_2^2}\Big/h,-(a_i\chi+b_i\psi+c_i)\Big)$$

$$+\int_0^P\left[\frac{2+4\lambda^2-e^{-2\lambda}}{1+e^{-4\lambda}-(2+4\lambda^2)e^{-2\lambda}}\sum_{i=1}^{K}C_i\lambda^{\rho_i}\chi^{\beta_i}\psi^{\gamma_i}e^{\lambda(a_i\chi+b_i\psi+c_i-2)}\right.$$

$$\left.J_\nu\left(\frac{\lambda\sqrt{x_1^2+x_2^2}}{h}\right)-B\left(\frac{e^{-\lambda}}{\lambda^\alpha}+\frac{e^{-(\lambda+P)}}{(\lambda+P)^\alpha}\right)\right]d\lambda\Bigg\}. \tag{2.3.33}$$

The Gaussian Quadrature Scheme (GQS) is implemented to evaluate the integral. Since the integrand varies smoothly over the integral interval, the integration interval is then divided into equally sized integration subintervals. The size of the subinterval is crucial for the evaluation of an integral involving oscillatory Bessel functions. In order to determine the right size for the integration sub-intervals, the

following parameter transformation is performed on the integration variable λ. Let

$$\lambda_1 = \lambda b \qquad \text{and} \qquad b = \frac{\sqrt{x_1^2 + x_2^2}}{h}. \tag{2.3.34}$$

For the sake of simplicity, we write λ in the place of λ_1, then (2.3.33) becomes

$$v(x_1, x_2, x_3) = A\Bigg\{ \sum_{i=1}^{K} C_i \chi^{\beta_i} \psi^{\gamma_i} G(\nu, \rho_i, b, -(a_i\chi + b_i\psi + c_i))$$

$$+ \frac{1}{b}\int_0^{Pb} \left[\frac{2 + 4(\frac{\lambda}{b})^2 - e^{-2(\frac{\lambda}{b})}}{1 + e^{-4(\frac{\lambda}{b})} - (2 + 4\frac{\lambda}{b}^2)e^{-2\frac{\lambda}{b}}} \sum_{i=1}^{K} C_i \left(\frac{\lambda}{b}\right)^{\rho_i} \chi^{\beta_i}\psi^{\gamma_i} e^{(\frac{\lambda}{b})(a_i\chi + b_i\psi + c_i - 2)} \right.$$

$$\left. J_\nu(\lambda) - B\left(\frac{e^{-(\frac{\lambda}{b})}}{(\frac{\lambda}{b})^\alpha} + \frac{e^{-(\frac{\lambda}{b}+P)}}{(\frac{\lambda}{b}+P)^\alpha} \right) \right] d\lambda \Bigg\}. \tag{2.3.35}$$

The only oscillatory function in the integrand is the Bessel function $J_\nu(x)$. By examining the Bessel functions closely, one finds that although they are not periodic functions, they do have similar behaviors to Trigonometric functions with an approximate period of 2π as x $\rightarrow \infty$. Considering x to be greater than zero, the distance between the two adjacent zeros of the Bessel functions is greater than π. Therefore, it is decided to choose the size of the integration subinterval to be 3. Let N be the number of subintervals used. Then

$$N = [Pb/3], \tag{2.3.36}$$

where [.] stands for the closest integer to the variable enclosed. For instance, $[a] = 1$, if $a = 1.2$, and $[a] = 2$, if $a = 1.6$. The size of the integration subintervals is then Pb/N, and the subintervals are $[a_j, a_{j+1}]$ with $j = 1, \ldots, N$, where

$$a_i = \frac{Pb}{N}(i-1), \qquad (i = 1, ..., N+1). \tag{2.3.37}$$

Define now

$$f(\nu,x_1,x_2,\alpha,\chi,\psi,\lambda) =$$

$$\frac{2+4(\frac{\lambda}{b})^2-e^{-2(\frac{\lambda}{b})}}{1+e^{-4(\frac{\lambda}{b})}-(2+4\frac{\lambda}{b}^2)e^{-2\frac{\lambda}{b}}}\sum_{i=1}^{K}C_i\left(\frac{\lambda}{b}\right)^{\rho_i}\chi^{\beta_i}\psi^{\gamma_i}e^{(\frac{\lambda}{b})(a_i\chi+b_i\psi+c_i-2)}J_\nu(\lambda)$$

$$-B\left(\frac{e^{-(\frac{\lambda}{b})}}{(\frac{\lambda}{b})^\alpha}+\frac{e^{-(\frac{\lambda}{b}+P)}}{(\frac{\lambda}{b}+P)^\alpha}\right). \tag{2.3.38}$$

Then

$$v(x_1,x_2,x_3)=A\left\{\sum_{i=1}^{K}C_i\chi^{\beta_i}\psi^{\gamma_i}G(\nu,\rho_i,b,-(a_i\chi+b_i\psi+c_i))\right. \tag{2.3.39}$$

$$\left.+\frac{1}{b}\sum_{j=1}^{N}\int_{a_j}^{a_{j+1}}f(\nu,x_1,x_2,\alpha,\chi,\psi,\lambda)\,d\lambda\right\}.$$

By performing the following variable transformation

$$\lambda=\frac{a_{j+1}+a_j}{2}+\frac{a_{j+1}-a_j}{2}t, \tag{2.3.40}$$

$$(j=1,...,N),$$

$$d\lambda=\frac{a_{j+1}-a_j}{2}\,dt,$$

(2.3.39) becomes

$$v(x_1,x_2,x_3)=A\left\{\sum_{i=1}^{K}C_i\chi^{\beta_i}\psi^{\gamma_i}G\Big(\nu,\rho_i,b,-(a_i\chi+b_i\psi+c_i)\Big)\right.$$

$$\left.+\sum_{j=1}^{N}\frac{a_{j+1}-a_j}{2b}\int_{-1}^{1}f\left(\nu,x_1,x_2,\alpha,\chi,\psi,\frac{a_{j+1}-a_j}{2}t+\frac{a_{j+1}+a_j}{2}\right)dt\right\}. \tag{2.3.41}$$

Applying standard Gauss Quadrature Scheme yields,

$$v(x_1,x_2,x_3) = A\Bigg\{\sum_{i=1}^{K} C_i\chi^{\beta_i}\psi^{\gamma_i}G\Big(\nu,\rho_i,b,-(a_i\chi+b_i\psi+c_i)\Big)$$

$$+\sum_{j=1}^{N}\frac{a_{j+1}-a_j}{2b}\sum_{k=1}^{M} f\left(\nu,x_1,x_2,\alpha,\chi,\psi,\frac{a_{j+1}-a_j}{2}t+\frac{a_{j+1}+a_j}{2}\right)\omega_k\Bigg\}, \tag{2.3.42}$$

where M is the number of Gaussian Quadrature points used, t_k and ω_k with $k = 1,...,M$ are the positions and weights of the Gaussian Quadrature points, respectively. Eq. (2.3.42) involving different number of points has been tested. It is found that the six-point GQS produces both good accuracy and good efficiency. It needs to be emphasized that the numerical part of the integration is convergent due to the nature of the integrand, referred to Eq. (2.3.29), while the remaining part can be evaluated in a close form. In addition, the accuracy of the integral in (2.3.35) will depend on the choice of P. The bigger the P is, the more accurate the result will be, and the more time intensive it will become.

2.3.2 Error Analysis Of The Numerical Evaluation

The error introduced in the evaluation of the stress and displacement components of the fundamental solution is mainly due to the numerical integration. In order to perform an adequate error analysis, (2.3.29) is re-written in the following form,

$$
\begin{aligned}
v(x_1,x_2,x_3) = A\Bigg\{ & \sum_{i=1}^{K} C_i \chi^{\beta_i}\psi^{\gamma_i} G(\nu,\rho_i,b,-(a_i\chi+b_i\psi+c_i)) \\
& + \int_0^P \Bigg[\frac{(2+4\lambda^2-e^{-2\lambda})e^{-2\lambda}}{1+e^{-4\lambda}-(2+4\lambda^2)e^{-2\lambda}} g'(\lambda,\chi,\psi) J_\nu\left(\frac{\lambda\sqrt{x_1^2+x_2^2}}{h}\right) \\
& \qquad - B\left(\frac{e^{-\lambda}}{\lambda^\alpha}+\frac{e^{-(\lambda+P)}}{(\lambda+P)^\alpha}\right) \Bigg] d\lambda \\
& + \int_P^\infty \frac{(2+4\lambda^2-e^{-2\lambda})e^{-2\lambda}}{1+e^{-4\lambda}-(2+4\lambda^2)e^{-2\lambda}} g'(\lambda,\chi,\psi) J_\nu\left(\frac{\lambda\sqrt{x_1^2+x_2^2}}{h}\right) d\lambda \\
& - B\int_{2P}^\infty \frac{e^{-\lambda}}{\lambda^\alpha}\, d\lambda \Bigg\}.
\end{aligned}
\tag{2.3.43}
$$

Comparing the above formula with the proposed expression (2.3.33), it is found that the error in the numerical integration is mainly due to the truncation of the integration interval. Another source of the error is due to the use of the Gaussian Quadrature Scheme, and this part of the error is small compared with the truncation

error. Define the error caused by the truncation of the integration interval to be

$$\varepsilon = A\Bigg\{ \int_P^\infty \frac{(2+4\lambda^2-e^{-2\lambda})e^{-2\lambda}}{1+e^{-4\lambda}-(2+4\lambda^2)e^{-2\lambda}} g'(\lambda,\chi,\psi) J_\nu\left(\frac{\lambda\sqrt{x_1^2+x_2^2}}{h}\right) d\lambda$$

$$- B\int_{2P}^\infty \frac{e^{-\lambda}}{\lambda^\alpha}\, d\lambda \Bigg\}. \tag{2.3.44}$$

As indicated in (2.3.25), $g'(\lambda,\chi,\psi)$ is a summation of the terms of the form: $\lambda^{\rho_i} e^{\lambda(a_i\chi+b_i\psi+c_i)}$, with $i = 1,\ldots,K$. Examining the terms carefully, one finds that the dominant term is the one with zero exponent. The coefficient of this term is denoted as $C\lambda^\rho\chi^\beta\psi^\gamma$, in which $0 \le \rho \le 3$. The truncation error is then bounded by,

$$\varepsilon \le |A| \left\{ KC\chi^\beta\psi^\gamma \left| \int_P^\infty \frac{(2+4\lambda^2-e^{-2\lambda})e^{-2\lambda}}{1+e^{-4\lambda}-(2+4\lambda^2)e^{-2\lambda}} \lambda^3 J_\nu(\lambda b)\, d\lambda \right| \right.$$

$$\left. + |B| \left| \int_P^\infty e^{-\lambda} d\lambda \right| \right\}$$

$$\le |A| \left\{ KC\chi^\beta\psi^\gamma \int_P^\infty \left| \frac{(2+4\lambda^2-e^{-2\lambda})e^{-2\lambda}}{1+e^{-4\lambda}-(2+4\lambda^2)e^{-2\lambda}} \lambda^3 \right| \left| J_\nu(\lambda b) \right| d\lambda + |B|\, e^{-2P} \right\}. \tag{2.3.45}$$

For any Bessel function $J_\nu(x)$, with ν integer, the following holds,

$$|J_\nu(x)| \le 1, \qquad 0 \le x \le \infty. \tag{2.3.46}$$

Consequently,

$$\varepsilon \leq |A| \left\{ KC\chi^{\beta}\psi^{\gamma} \int_{P}^{\infty} \left| \frac{(2+4\lambda^2-e^{-2\lambda})e^{-2\lambda}}{1+e^{-4\lambda}-(2+4\lambda^2)e^{-2\lambda}} \lambda^3 \right| d\lambda + |B|\, e^{-2P} \right\}$$

$$= |A| \left\{ KC\chi^{\beta}\psi^{\gamma} \int_{P}^{\infty} \frac{(2+4\lambda^2-e^{-2\lambda})e^{-2\lambda}}{1+e^{-4\lambda}-(2+4\lambda^2)e^{-2\lambda}} \lambda^3 \, d\lambda + |B|\, e^{-2P} \right\}. \tag{2.3.47}$$

Since for any λ such that $P \leq \lambda < \infty$ and $P > 1$,

$$0 \leq 1+e^{-4P} - \left(2+4P^2\right)e^{-2P} \leq 1+e^{-4\lambda} - \left(2+4\lambda^2\right)e^{-2\lambda}. \tag{2.3.48}$$

The truncation error can then be expressed as follows,

$$\varepsilon \leq |A| \left\{ \frac{KC\chi^{\beta}\psi^{\gamma}}{1+e^{-4P}-(2+4P^2)} \int_{P}^{\infty} \left(2+4\lambda^2-e^{-2\lambda}\right)\lambda^3 d\lambda + |B|\, e^{-2P} \right\}. \tag{2.3.49}$$

As a result,

$$\varepsilon \leq |A| \left\{ \frac{KC\chi^{\beta}\psi^{\gamma}e^{-4P}}{128(1+e^{-4P}-(2+4P^2)e^{-2P})} \left[32e^{2P}\Big(8P^5+20P^4+44P^3 + 66P^2+66P+33\Big) - 32P^3-24P^2-12P-3 \right] + |B|\, e^{-2P} \right\}. \tag{2.3.50}$$

For $P = 10$, and $P = 20$, the error ε is of the order of 10^{-3}, and 10^{-10}, respectively. It can be seen from the above result that one may obtain fairly good numerical results of stress and displacement by taking $P = 10$, and the results may be improved very significantly by increase the integral limit to $P = 20$. Both $P = 10$ and $P = 20$ have been used in the numerical calculation to determine the stress and displacement. The results will be discussed in the later sections.

2.4 Comparison Of Fundamental Solution And Kelvin Solution

In this section, the properties of the fundamental solution of the infinite plate problem and the Kelvin solution are compared when the point of observation approaches the point of the application of the load. Only one stress component $\sigma^1_{33}(x_1, x_2, x_3)$ is chosen to demonstrate the process. $\sigma^1_{33}(x_1, x_2, x_3)$ is the stress component due to the concentrated load acting at point $\boldsymbol{\xi} = (0, 0, H)$ in the x_1- direction [24].

The proof that the fundamental solution tends to the Kelvin solution when the observing point approaches the loading point has been given originally in [24]. The following states only the basic ideas.

$$\sigma^1_{33}(x_1, x_2, x_3) = \frac{1}{4\pi(1-\nu)h^2} \frac{-x_1}{\sqrt{x_1^2 + x_2^2}} \int_0^\infty f^1_{33}(\lambda, \chi, \psi) J_1\left(\frac{\lambda\sqrt{x_1^2 + x_2^2}}{h}\right) d\lambda, \tag{2.4.51}$$

where

$$\begin{aligned} f^1_{33}(\lambda, \chi, \psi) = \frac{1}{\sinh(\lambda)^2 - \lambda^2} \Bigg\{ & \lambda^4 \chi (1-\psi) \cosh\lambda(\chi - \psi) \\ & - \frac{\lambda^3}{2} \Big[(1-\chi)(1-\psi) \sinh\lambda(\chi+\psi) + ((4\nu-3)\chi - \psi + 1) \sinh\lambda(\chi-\psi) \\ & \quad + \chi\psi \sinh\lambda(2-\chi-\psi) \Big] \\ & + \frac{\lambda^2}{4} \Big[((4\nu-3)\chi + 2(1-2\nu) + \psi) \cosh\lambda(\chi+\psi) \\ & \quad + (2(2\nu-1) + \chi - \psi) \cosh\lambda(\chi-\psi) \\ & \quad + ((3-4\nu)\chi - \psi) \cosh\lambda(2-\chi-\psi) + (\psi - \chi) \cosh\lambda(2+\chi-\psi) \Big] \\ & - (2\nu-1)\frac{\lambda}{4} \Big[\sinh\lambda(\chi+\psi) + \sinh\lambda(\chi-\psi) + \sinh\lambda(2-\chi-\psi) \\ & \quad - \sinh\lambda(2+\chi-\psi) \Big] \Bigg\} \\ & + \Big\{ \lambda^2(\chi-\psi)\cosh\lambda(\chi-\psi) - \lambda(2\nu-1)\sinh\lambda(\chi-\psi) \Big\} \mathcal{H}(\chi-\psi), \end{aligned} \tag{2.4.52}$$

and

$$\mathcal{H}(\chi-\psi)=\begin{cases}1, & \text{if } \chi\geq\psi;\\ 0, & \text{otherwise.}\end{cases} \tag{2.4.53}$$

Define

$$\cos\theta=\frac{x_1}{R},\qquad R=\sqrt{x_1^2+x_2^2}. \tag{2.4.54}$$

Therefore

$$\lim_{\boldsymbol{x}\to\boldsymbol{\xi}}\sigma_{33}^1(x_1,x_2,x_3)=-\frac{\cos\theta}{4\pi(1-\nu)h^2}\lim_{r\to 0}\int_0^\infty f_{33}^1(\lambda,\chi,\psi)J_1\left(\frac{\lambda R}{h}\right)d\lambda, \tag{2.4.55}$$

where

$$r=\sqrt{R^2+(x_3-H)^2}. \tag{2.4.56}$$

The expression for $f_{33}^1(\lambda,\chi,\psi)$ can be written in terms of exponential functions,

$$\begin{aligned}
f_{33}^1(\lambda,\chi,\psi)=&\frac{4}{1+e^{-4\lambda}-(2+4\lambda^2)e^{-2\lambda}}\Big\{\\
&\frac{\lambda^4}{2}\chi(1-\psi)\Big(e^{-\lambda(2-\chi+\psi)}+e^{-\lambda(2+\chi-\psi)}\Big)\\
&-\frac{\lambda^3}{4}\Big[(1-\chi)(1-\psi)\Big(e^{-\lambda(2-\chi-\psi)}-e^{-\lambda(2+\chi+\psi)}\Big)\\
&\qquad+((4\nu-3)\chi-\psi+1)\Big(e^{-\lambda(2-\chi+\psi)}-e^{-\lambda(2+\chi-\psi)}\Big)\\
&\qquad+\chi\psi\Big(e^{-\lambda(\chi+\psi)}-e^{-\lambda(4-\chi-\psi)}\Big)\Big]\\
&+\frac{\lambda^2}{8}\Big[((4\nu-3)\chi+2(1-2\nu)+\psi)\Big(e^{-\lambda(2-\chi-\psi)}+e^{-\lambda(2+\chi+\psi)}\Big)\\
&\qquad+(2(2\nu-1)-\psi+\chi)\Big(e^{-\lambda(2-\chi+\psi)}+e^{-\lambda(2+\chi-\psi)}\Big)\\
&\qquad+((3-4\nu)\chi-\psi)\Big(e^{-\lambda(\chi+\psi)}+e^{-\lambda(4-\chi-\psi)}\Big)\\
&\qquad+(\psi-\chi)\Big(e^{-\lambda(-\chi+\psi)}+e^{-\lambda(4+\chi-\psi)}\Big)\Big]\\
&-\frac{\lambda}{8}(2\nu-1)\Big[e^{-\lambda(2-\chi-\psi)}-e^{-\lambda(2+\chi+\psi)}+e^{-\lambda(2-\chi+\psi)}-e^{-\lambda(2+\chi-\psi)}\\
&\qquad+e^{-\lambda(\chi+\psi)}-e^{-\lambda(4-\chi-\psi)}-e^{-\lambda(-\chi+\psi)}+e^{-\lambda(4+\chi-\psi)}\Big]\Big\}\\
&+\Big\langle-\frac{\lambda^4}{2}(\chi-\psi)\Big[e^{-\lambda(2-\chi+\psi)}+e^{-\lambda(2+\chi+\psi)}\Big]\\
&\quad+\frac{\lambda^3}{2}(2\nu-1)\Big[e^{-\lambda(2-\chi+\psi)}-e^{-\lambda(2+\chi-\psi)}\Big]
\end{aligned}$$

$$+\frac{\lambda^2}{8}(\chi-\psi)\Big[e^{\lambda(\chi-\psi)}+e^{-\lambda(\chi-\psi)}+e^{-\lambda(4-\chi+\psi)}+e^{-\lambda(4+\chi-\psi)}$$
$$-2e^{-\lambda(2-\chi+\psi)}-2e^{-\lambda(2+\chi-\psi)}\Big]$$
$$-\frac{\lambda}{8}(2\nu-1)\Big[e^{\lambda(\chi-\psi)}-e^{-\lambda(\chi-\psi)}+e^{-\lambda(4-\chi+\psi)}-e^{-\lambda(4+\chi-\psi)}$$
$$-2e^{-\lambda(2-\chi+\psi)}+2e^{-\lambda(2+\chi-\psi)}\Big\rangle\mathcal{H}(\chi-\psi). \tag{2.4.57}$$

In both $\chi \geq \psi$ and $\chi < \psi$ cases, it is easily seen that the terms with positive exponents cancel themselves, only the ones with negative exponents left. Also $\left(1+e^{-4\lambda}-(2+4\lambda^2)e^{-2\lambda}\right)^{-1}$ can be expanded by using the Taylor series since

$$\left|e^{-4\lambda}-\left(2+4\lambda^2\right)e^{-2\lambda}\right|<1, \qquad \forall\lambda\in(0,\infty).$$

By expanding (2.4.57), and rearranging terms, (2.4.57) becomes

$$f_{33}^1(\lambda,\chi,\psi)=\frac{\lambda^2}{2}|\chi-\psi|e^{-\lambda|\chi-\psi|}+\frac{\lambda}{2}(2\nu-1)e^{-\lambda|\chi-\psi|}+\sum_{n=0}^{\infty}a_n(\chi,\psi)\lambda^n e^{-\lambda p_n(\chi,\psi)}, \tag{2.4.58}$$

where $a_n(\chi,\psi)$ and $p_n(\chi,\psi)$ $\forall n=1,2,3,\ldots$, are linear functions of χ and ψ, and

$$p_n(\chi,\psi)>0, \qquad \forall(\chi,\psi)\in[0,1] \quad (n=0,1,2,3,\ldots).$$

In particular

$$\lim_{\chi\to\psi}p_n(\chi,\psi)\neq 0, \qquad \forall(\chi,\psi)\in[0,1] \quad (n=0,1,2,3,\ldots).$$

From (A.6), (A.7), (A.8), (A.9), (A.10) ... in Appendix A, and for $\forall p_n(\chi,\psi)\neq 0$, it is easily seen that

$$\lim_{\substack{R\to 0\\ \chi\to\psi}}\int_0^\infty \lambda^n e^{-\lambda p_n(\chi,\psi)}J_1\left(\frac{\lambda R}{h}\right)d\lambda=0, \qquad \forall p_n(\chi,\psi)>0,\ n\geq 0. \tag{2.4.59}$$

The integration of the first and the second terms in (2.4.58) may not be computed using the same method as shown in (2.4.59) since $(\chi - \psi) \to 0$ as $\chi \to \psi$. Therefore, as the observing point tends to the loading point, they are the only two terms that dominate the component $\sigma^1_{33}(x_1, x_2, x_3)$, and the asymptotic form of $\sigma^1_{33}(x_1, x_2, x_3)$ as $\boldsymbol{x} \to \boldsymbol{\xi}$ can be written as,

$$\sigma^1_{33}(x_1, x_2, x_3)_{asymp} = \frac{-\cos\theta}{4\pi(1-\nu)h^2} \int_0^\infty \left\{ \frac{\lambda^2}{2}|\chi - \psi| e^{-\lambda|\chi-\psi|} J_1\left(\frac{\lambda R}{h}\right) + \frac{\lambda}{2}(2\nu - 1) e^{-\lambda|\chi-\psi|} J_1\left(\frac{\lambda R}{h}\right) \right\} d\lambda, \tag{2.4.60}$$

with $R << 1$, $\chi - \psi << 1$. Define

$$\varphi = \cos^{-1}\frac{R}{r} = \sin^{-1}(\frac{x_3 - H}{r});$$
$$\theta = \cos^{-1}\frac{x_1}{R} = \sin^{-1}\frac{x_2}{R}.$$

Since

$$\frac{1}{2}|\chi - \psi| \int_0^\infty \lambda^2 e^{-\lambda|\chi-\psi|} J_1\left(\frac{\lambda R}{h}\right) d\lambda = \frac{3h^2}{2r^2} \sin^2\varphi \cos\varphi, \tag{2.4.61}$$

and

$$\frac{2\nu - 1}{2} \int_0^\infty \lambda e^{-\lambda|\chi-\psi|} J_1\left(\frac{\lambda R}{h}\right) d\lambda = -\frac{(1-2\nu)h^2}{2r^2} \cos\varphi. \tag{2.4.62}$$

Therefore, as $r \to 0$, the asymptotic expression of $\sigma^1_{33}(x_1, x_2, x_3)$ is

$$\begin{aligned} \sigma^1_{33}(x_1, x_2, x_3)_{asymp} &= -\frac{\cos\theta}{4\pi(1-\nu)h^2}\left[\frac{3h^2}{2r^2}\sin^2\varphi\cos\varphi - \frac{(1-2\nu)h^2}{2r^2}\cos\varphi\right] \\ &= -\frac{1}{8\pi(1-\nu)r^2}\cos\varphi\cos\theta\left[3\sin^2\varphi - (1-2\nu)\right] \end{aligned} \tag{2.4.63}$$

$\sigma^1_{33}(x_1, x_2, x_3)_{asymp}$ of the fundamental solution expressed in (2.4.63) coincides with the same component in the Kelvin solution. By using the same method, it can be proved that the rest of the stress and displacement components of the fundamental solution tend to those of the Kelvin solution as the observing point tends to the loading point.

The following shows the numerical result of the asymptotic behaviors of both solutions.

Fundamental Solution Vs. Kelvin Solution			
Gauss Points	Distance $-\log_{10}(r)$	Fundamental Solution $\log_{10}(-\sigma^1_{33})$	Kelvin Solution $\log_{10}(-\sigma^1_{33})$
Two $P = 10$	0.10000000000E+01	0.26814712506E+00	0.29425272332E+00
	0.20000000000E+01	0.22942051483E+01	0.22942527233E+01
	0.30000000000E+01	0.42942526611E+01	0.42942527233E+01
	0.40000000000E+01	0.62942527112E+01	0.62942527233E+01
	0.50000000000E+01	0.82942527112E+01	0.82942527233E+01
	0.60000000000E+01	0.10294252711E+02	0.10294252723E+02
Four $P = 10$	0.10000000000E+01	0.26831273086E+00	0.29425272332E+00
	0.20000000000E+01	0.22942054407E+01	0.22942527233E+01
	0.30000000000E+01	0.42942526614E+01	0.42942527233E+01
	0.40000000000E+01	0.62942527112E+01	0.62942527233E+01
	0.50000000000E+01	0.82942527112E+01	0.82942527233E+01
	0.60000000000E+01	0.10294252711E+02	0.10294252723E+02
Six $P = 10$	0.10000000000E+01	0.26830213193E+00	0.29425272332E+00
	0.20000000000E+01	0.22942054264E+01	0.22942527233E+01
	0.30000000000E+01	0.42942526614E+01	0.42942527233E+01
	0.40000000000E+01	0.62942527112E+01	0.62942527233E+01
	0.50000000000E+01	0.82942527112E+01	0.82942527233E+01
	0.60000000000E+01	0.10294252711E+02	0.10294252723E+02
Two $P = 20$	0.10000000000E+01	0.26827942995E+00	0.29425272332E+00
	0.20000000000E+01	0.22942053307E+01	0.22942527233E+01
	0.30000000000E+01	0.42942526613E+01	0.42942527233E+01
	0.40000000000E+01	0.62942527112E+01	0.62942527233E+01
	0.50000000000E+01	0.82942527112E+01	0.82942527233E+01
	0.60000000000E+01	0.10294252711E+02	0.10294252723E+02
Four $P = 20$	0.10000000000E+01	0.26832789978E+00	0.29425272332E+00
	0.20000000000E+01	0.22942054942E+01	0.22942527233E+01
	0.30000000000E+01	0.42942526615E+01	0.42942527233E+01
	0.40000000000E+01	0.62942527112E+01	0.62942527233E+01
	0.50000000000E+01	0.82942527112E+01	0.82942527233E+01
	0.60000000000E+01	0.10294252711E+02	0.10294252723E+02
Six $P = 20$	0.10000000000E+01	0.26830961626E+00	0.29425272332E+00
	0.20000000000E+01	0.22942054332E+01	0.22942527233E+01
	0.30000000000E+01	0.42942526614E+01	0.42942527233E+01
	0.40000000000E+01	0.62942527112E+01	0.62942527233E+01
	0.50000000000E+01	0.82942527112E+01	0.82942527233E+01
	0.60000000000E+01	0.10294252711E+02	0.10294252723E+02

CHAPTER 3

THEORY OF

BOUNDARY INTEGRAL EQUATION METHODS

3.1 Theory Of Conventional Boundary Integral Equation Method

The three essential aspects of the Boundary Integral Equation Method (BIE) are: 1) the use of the ellipticity property of the partial-differential equations, such as the equilibrium equations in the theory of elasticity; 2) the use of a solution to the above partial-differential equations as the fundamental solution. Several "fundamental" solutions are available, such as the Kelvin solution and the solution for the infinite plate problem in the theory of elasticity; 3) the use of the reciprocal work theorem of Betti [37].

The current discussion will treat homogeneous, isotropic, linear elastic continua. The first two aspects of the boundary integral equations have been discussed in the previous chapter. This chapter will be devoted to the discussion of the Betti's reciprocal theorem, and the generation of the boundary integral equations. The indicial notation is used through most of the chapter. The Latin subscripts vary from 1, 2, and 3; the Greek subscripts vary from 1 to 2.

3.1.1 Somigliana Identities [38]

The reciprocal theorem of Betti forms the basis of the BIE formulation. The following discusses the generalization of the reciprocal theorem in elastostatics.

Theorem 3.1.1 (Betti's Reciprocal Theorem).
Let $\mathcal{R}$ be a regular region, and $\boldsymbol{\xi} \in \overset{\circ}{\mathcal{R}}$. Furthermore, let $\mathcal{S}^1$ and $\mathcal{S}^2$ be two elastostatic states with the following properties:

Re: state $\mathcal{S}^1$

$$\mathcal{S}^1 = \left[\boldsymbol{u}^1(\boldsymbol{x}), \boldsymbol{\sigma}^1(\boldsymbol{x})\right] \in \mathcal{E}_s(E, \nu, \boldsymbol{f}^1; \mathcal{R}), \qquad \boldsymbol{f}^1 \in \mathcal{C}(\mathcal{R}), \tag{3.1.1}$$

with $\boldsymbol{t}^1(\boldsymbol{x}; \boldsymbol{n})$ being the traction vector, which is defined as

$$t_i^1(\boldsymbol{x}; \boldsymbol{n}) = \sigma_{ij}^1(\boldsymbol{x}) n_j(\boldsymbol{x}), \qquad \forall \boldsymbol{x} \in \overset{*}{\Sigma}, \tag{3.1.2}$$

where Σ is the regular surface of $\mathcal{R}$, and $\overset{*}{\Sigma}$ is the subset of all points of Σ at which normals are defined.

Re: state $\mathcal{S}^2$

$$\mathcal{S}^2 = \left[\boldsymbol{u}^2(\boldsymbol{x}), \boldsymbol{\sigma}^2(\boldsymbol{x})\right] \in \mathcal{E}_s(E, \nu, \boldsymbol{f}^2; \mathcal{R}), \qquad \boldsymbol{f}^2 \in \mathcal{C}(\mathcal{R}), \tag{3.1.3}$$

and

$$t_i^2(\boldsymbol{x}; \boldsymbol{n}) = \sigma_{ij}^2(\boldsymbol{x}) n_j(\boldsymbol{x}), \qquad \forall \boldsymbol{x} \in \overset{*}{\Sigma}. \tag{3.1.4}$$

Then Betti's reciprocal theorem gives

$$\int_{\mathcal{R}} \sigma_{ij}^1(\boldsymbol{x}) \epsilon_{ij}^2(\boldsymbol{x}) \, dV_{\boldsymbol{x}} = \int_{\mathcal{R}} \sigma_{ij}^2(\boldsymbol{x}) \epsilon_{ij}^1(\boldsymbol{x}) \, dV_{\boldsymbol{x}}, \tag{3.1.5}$$

where the superscripts denote the different solution states.

Since the two regions have the same material properties, (3.1.5) can be proved easily by substituting the form of Hooke's law for both stress states. In linear elasticity, the components of the strain tensor can be written as,

$$\begin{aligned} \epsilon^1_{ij}(\boldsymbol{x}) &= \frac{1}{2}\Big(u^1_{i,j}(\boldsymbol{x}) + u^1_{j,i}(\boldsymbol{x})\Big); \\ \epsilon^2_{ij}(\boldsymbol{x}) &= \frac{1}{2}\Big(u^2_{i,j}(\boldsymbol{x}) + u^2_{j,i}(\boldsymbol{x})\Big). \end{aligned} \tag{3.1.6}$$

Substitution of the second strain component of (3.1.6) into (3.1.5), one has,

$$\int_{\mathcal{R}} \sigma^1_{ij}(\boldsymbol{x}) u^2_{i,j}(\boldsymbol{x})\, dV_{\boldsymbol{x}} = \int_{\mathcal{R}} \sigma^2_{ij}(\boldsymbol{x}) u^1_{i,j}(\boldsymbol{x})\, dV_{\boldsymbol{x}}. \tag{3.1.7}$$

Integrate by parts from the above equation,

$$\begin{aligned} \int_{\mathcal{R}} \sigma^1_{ij}(\boldsymbol{x}) u^2_{i,j}(\boldsymbol{x})\, dV_{\boldsymbol{x}} = & \int_{\mathcal{R}} \Big(\sigma^1_{ij}(\boldsymbol{x}) u^2_i(\boldsymbol{x})\Big)_{,j}\, dV_{\boldsymbol{x}} \\ & - \int_{\mathcal{R}} \sigma^1_{ij,j}(\boldsymbol{x}) u^2_i(\boldsymbol{x})\, dV_{\boldsymbol{x}}, \end{aligned} \tag{3.1.8}$$

and apply the divergence theorem to obtain

$$\begin{aligned} \int_{\mathcal{R}} \sigma^1_{ij}(\boldsymbol{x}) u^2_{i,j}(\boldsymbol{x})\, dV_{\boldsymbol{x}} = & \int_{*\,\Sigma} t^1_i(\boldsymbol{x};\boldsymbol{n}) u^2_i(\boldsymbol{x})\, dA_{\boldsymbol{x}} \\ & + \int_{\mathcal{R}} f^1_i(\boldsymbol{x}) u^2_i(\boldsymbol{x})\, dV_{\boldsymbol{x}}. \end{aligned} \tag{3.1.9}$$

After applying the same integration by parts with the divergence theorem on the right-hand side of the equation (3.1.7), one obtains,

$$\begin{aligned} \int_{\mathcal{R}} \sigma^2_{ij}(\boldsymbol{x}) u^1_{i,j}(\boldsymbol{x})\, dV_{\boldsymbol{x}} = & \int_{*\,\Sigma} t^2_i(\boldsymbol{x};\boldsymbol{n}) u^1_i(\boldsymbol{x})\, dA_{\boldsymbol{x}} \\ & + \int_{\mathcal{R}} f^2_i(\boldsymbol{x}) u^1_i(\boldsymbol{x})\, dV_{\boldsymbol{x}}. \end{aligned} \tag{3.1.10}$$

Therefore,

$$\begin{aligned} & \int_{*\,\Sigma} t^1_i(\boldsymbol{x};\boldsymbol{n}) u^2_i(\boldsymbol{x})\, dA_{\boldsymbol{x}} + \int_{\mathcal{R}} f^1_i(\boldsymbol{x}) u^2_i(\boldsymbol{x})\, dV_{\boldsymbol{x}} \\ = & \int_{*\,\Sigma} t^2_i(\boldsymbol{x};\boldsymbol{n}) u^1_i(\boldsymbol{x})\, dA_{\boldsymbol{x}} + \int_{\mathcal{R}} f^2_i(\boldsymbol{x}) u^1_i(\boldsymbol{x})\, dV_{\boldsymbol{x}}. \end{aligned} \tag{3.1.11}$$

(3.1.11) is called the Somigliana Identity.

3.1.2 Conventional Boundary Integral Equation Method

Let a plate shaped region $\mathcal{R} \subset E_3$ be defined as

$$\begin{aligned} \mathcal{R} &= \{\boldsymbol{x} \mid \boldsymbol{x} \in \pi,\ 0 \le \boldsymbol{x}\cdot\boldsymbol{e}_3 \le h\}; \\ \partial\mathcal{R} &= \partial\mathcal{R}_1 \cup \partial\mathcal{R}_2 \cup \mathcal{L}, \quad where \\ \partial\mathcal{R}_1 &= \{\boldsymbol{x} \mid \boldsymbol{x} \in \pi,\ \boldsymbol{x}\cdot\boldsymbol{e}_3 = 0\}, \quad \partial\mathcal{R}_2 = \{\boldsymbol{x} \mid \boldsymbol{x} \in \pi,\ \boldsymbol{x}\cdot\boldsymbol{e}_3 = h\}, \\ \mathcal{L} &= \{\boldsymbol{x} \mid (\boldsymbol{x}\cdot\boldsymbol{e}_1, \boldsymbol{x}\cdot\boldsymbol{e}_2) \in \partial\pi,\ \ 0 \le \boldsymbol{x}\cdot\boldsymbol{e}_3 \le h\}, \end{aligned} \tag{3.1.1}$$

where π is the mid-plane of the plate, and $\partial\pi$ is the boundary of π.

Let state–1 be a well–posed boundary value problem in the plate shaped region with the following properties,

Re: state $\mathcal{S}$ (regular state)

$$\begin{aligned} &a)\ \mathcal{S} = \Big[\boldsymbol{u}(\boldsymbol{x}), \boldsymbol{\xi}(\boldsymbol{x})\Big] \in \mathcal{E}_s(E, \nu, \boldsymbol{0}; \mathcal{R}); \\ &b)\ \boldsymbol{t}(\boldsymbol{x}; \boldsymbol{n}) = \boldsymbol{\sigma}(\boldsymbol{x})\boldsymbol{n}(\boldsymbol{x}) = \boldsymbol{0}, \quad \forall \boldsymbol{x} \in \partial\mathcal{R}_1 \cup \partial\mathcal{R}_2; \\ &c)\ \boldsymbol{t}(\boldsymbol{x}; \boldsymbol{n}) = \bar{\boldsymbol{t}}, \qquad\quad \forall \boldsymbol{x} \in \mathcal{L} \end{aligned} \tag{3.1.2}$$

where $\boldsymbol{t}(\boldsymbol{x}; \boldsymbol{n})$ is the traction vector.

Let state-2 be the "singular" state $\mathcal{S}^j$ with j being the direction of the unit concentrated load. For the conventional BIEs, the singular state is provided by the Kelvin problem with the following properties,

Re: state ${\mathcal{S}_K}^j$ (Kelvin problem)

$$\begin{aligned} &a)\ {\mathcal{S}_K}^j = \Big[{\boldsymbol{u}_K}^j(\boldsymbol{x}), {\boldsymbol{\sigma}_K}^j(\boldsymbol{x})\Big] \in \mathcal{E}_s\Big(E, \nu, \boldsymbol{0}; E_3 - \{\boldsymbol{\xi}\}\Big); \\ &b)\ {\boldsymbol{u}_K}^j(\boldsymbol{x}, \boldsymbol{\xi}) = O\Big(\Big|\boldsymbol{x} - \boldsymbol{\xi}\Big|^{-1}\Big), \quad {\boldsymbol{\sigma}_K}^j(\boldsymbol{x}, \boldsymbol{\xi}) = O\Big(\Big|\boldsymbol{x} - \boldsymbol{\xi}\Big|^{-2}\Big), \qquad as\ \boldsymbol{x} \to \boldsymbol{\xi}; \\ &c)\ \int_{\partial\mathcal{B}_\eta(\boldsymbol{\xi})} {\boldsymbol{t}_K}^j(\boldsymbol{x}, \boldsymbol{\xi}; \boldsymbol{n})\, dA_{\boldsymbol{x}} = \boldsymbol{e}_j, \ \int_{\partial\mathcal{B}_\eta(\boldsymbol{\xi})} (\boldsymbol{x} - \boldsymbol{\xi}) \wedge {\boldsymbol{t}_K}^j(\boldsymbol{x}, \boldsymbol{\xi}; \boldsymbol{n}) dA_{\boldsymbol{x}} = 0 \forall \eta > 0, \end{aligned} \tag{3.1.3}$$

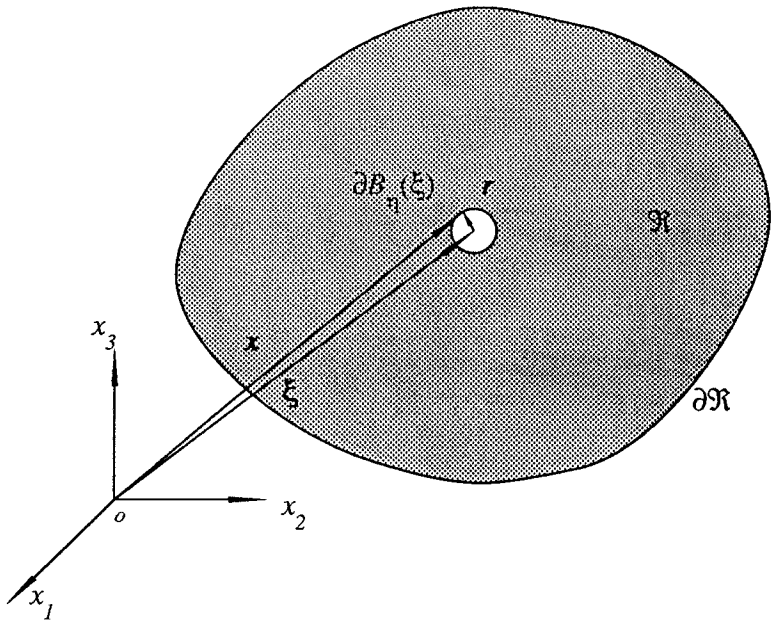

FIGURE 3.1 Interior point

where the subscript K indicates the Kelvin solution as opposed to any other fundamental solution; $\boldsymbol{t}_K{}^j(\boldsymbol{x},\boldsymbol{\xi};\boldsymbol{n})$ is the traction vector acting on the surface of $\partial\mathcal{B}_\eta(\boldsymbol{\xi})$ that faces $\boldsymbol{\xi}$.

It is important to notice that $\mathcal{R} \subset E_3$. Both elastostatic states have no body forces. For a unit concentrated load acting in the interior of the region $\mathcal{R}$, as shown in Figure 3.1, the Somigliana Identity gives

$$\int_{\overset{*}{\Sigma}} t_i(\boldsymbol{x};\boldsymbol{n}) u_K{}_i^j(\boldsymbol{x},\boldsymbol{\xi})\, dA_{\boldsymbol{x}} = \int_{\overset{*}{\Sigma}} t_K{}_i^j(\boldsymbol{x},\boldsymbol{\xi};\boldsymbol{n}) u_i(\boldsymbol{x},\boldsymbol{\xi})\, dA_{\boldsymbol{x}}, \tag{3.1.4}$$

where

$$\overset{*}{\Sigma} = \partial\mathcal{R} + \partial\mathcal{B}_\eta(\boldsymbol{\xi}), \tag{3.1.5}$$

and

$$\partial\mathcal{R} = \partial\mathcal{R}_1 \cup \partial\mathcal{R}_2 \cup \mathcal{L}, \tag{3.1.6}$$

then (3.1.4) becomes

$$\begin{aligned}&\int_{\partial\mathcal{B}_\eta(\boldsymbol{\xi})} t_i(\boldsymbol{x};\boldsymbol{n}) u_K{}_i^j(\boldsymbol{x},\boldsymbol{\xi})\, dA_{\boldsymbol{x}} + \int_{\partial\mathcal{R}} t_i(\boldsymbol{x};\boldsymbol{n}) u_K{}_i^j(\boldsymbol{x},\boldsymbol{\xi};\boldsymbol{n})\, dA_{\boldsymbol{x}} \\ &= \int_{\partial\mathcal{B}_\eta(\boldsymbol{\xi})} t_K{}_i^j(\boldsymbol{x},\boldsymbol{\xi};\boldsymbol{n}) u_i(\boldsymbol{x};\boldsymbol{n})\, dA_{\boldsymbol{x}} + \int_{\partial\mathcal{R}} t_K{}_i^j(\boldsymbol{x},\boldsymbol{\xi};\boldsymbol{n}) u_i(\boldsymbol{x},\boldsymbol{\xi})\, dA_{\boldsymbol{x}}.\end{aligned} \tag{3.1.7}$$

However, the boundary value problem under consideration (state S) does not have a spherical cavity of $\mathcal{B}_\eta(\boldsymbol{\xi})$ in its interior. The spherical region is artificially excluded to avoid the problems caused by the unit concentrated load. This problem can be remedied by taking the radius η of the small spherical ball $\mathcal{B}_\eta(\boldsymbol{\xi})$ to zero in a limiting process. Recall that the Kelvin solution has the asymptotic property $u_i^j(\boldsymbol{x},\boldsymbol{\xi}) = O\left(|\boldsymbol{x}-\boldsymbol{\xi}|^{-1}\right)$ as $\boldsymbol{x} \to \boldsymbol{\xi}$. Since the surface area of the cavity is of the order $|\boldsymbol{x}-\boldsymbol{\xi}|^2$, the integral of $u_K{}_i^j(\boldsymbol{x},\boldsymbol{\xi})$ over $\partial\mathcal{B}_\eta(\boldsymbol{\xi})$, as $|\boldsymbol{x}-\boldsymbol{\xi}| \to 0$, vanishes, i.e.,

$$\lim_{\eta\to 0} \int_{\partial\mathcal{B}_\eta(\boldsymbol{\xi})} t_i(\boldsymbol{x};\boldsymbol{n}) u_K{}_i^j(\boldsymbol{x},\boldsymbol{\xi})\, dA_{\boldsymbol{x}} = 0. \tag{3.1.8}$$

To obtain the limiting form of the other integral over the cavity surface $\partial\mathcal{B}_\eta(\boldsymbol{\xi})$ in equation (3.1.7), then this can be rewritten as follows,

$$\begin{aligned}\int_{\partial\mathcal{B}_\eta(\boldsymbol{\xi})} t_K{}_i^j(\boldsymbol{x},\boldsymbol{\xi};\boldsymbol{n}) u_i(\boldsymbol{x})\, dA_{\boldsymbol{x}}\} = &\int_{\partial\mathcal{B}_\eta(\boldsymbol{\xi})} t_K{}_i^j(\boldsymbol{x},\boldsymbol{\xi};\boldsymbol{n})(u_i(\boldsymbol{x}) - u_i(\boldsymbol{\xi}))\, dA_{\boldsymbol{x}} \\ &+ u_i(\boldsymbol{\xi}) \int_{\partial\mathcal{B}_\eta(\boldsymbol{\xi})} t_K{}_i^j(\boldsymbol{x},\boldsymbol{\xi};\boldsymbol{n})\, dA_{\boldsymbol{x}}.\end{aligned} \tag{3.1.9}$$

By doing so, the term $(u_i(\boldsymbol{x}) - u_i(\boldsymbol{\xi}))$ is of order $|\boldsymbol{x}-\boldsymbol{\xi}|$ due to the continuity of the displacements; thus, the first integral in (3.1.9) is of order $|\boldsymbol{x}-\boldsymbol{\xi}|$, and it vanishes in the limit as $\boldsymbol{x} \to \boldsymbol{\xi}$. Only the last integral in (3.1.9) is non-zero. Also, by employ property c) of the Kelvin solution, one obtains,

$$\int_{\partial\mathcal{B}_\eta(\boldsymbol{\xi})} t_K{}_i^j(\boldsymbol{x},\boldsymbol{\xi};\boldsymbol{n})\, dA_{\boldsymbol{x}} = \delta_{ij}. \tag{3.1.10}$$

where,

$$\delta_{ij} = \begin{cases} 1 & \text{if } i = j; \\ 0 & \text{otherwise.} \end{cases} \tag{3.1.11}$$

Thus,

$$\lim_{\eta \to 0} \int_{\partial \mathcal{B}_\eta(\boldsymbol{\xi})} t_{K_i^j}(\boldsymbol{x}, \boldsymbol{\xi}; \boldsymbol{n}) u_i(\boldsymbol{x}) \, dA_{\boldsymbol{x}} = u_j(\boldsymbol{\xi}), \tag{3.1.12}$$

and (3.1.7) becomes

$$u_j(\boldsymbol{\xi}) + \int_{\partial \mathcal{R}} t_{K_i^j}(\boldsymbol{x}, \boldsymbol{\xi}; \boldsymbol{n}) u_i(\boldsymbol{x}) \, dA_{\boldsymbol{x}} = \int_{\partial \mathcal{R}} t_i(\boldsymbol{x}; \boldsymbol{n}) u_{K_i^j}(\boldsymbol{x}, \boldsymbol{\xi}) \, dA_{\boldsymbol{x}}. \tag{3.1.13}$$

This boundary integral equation can not provide the solution for the displacement u_j at any interior point $\boldsymbol{\xi}$ unless the boundary data are totally specified, which means that tractions and displacements at all the surface points have to be specified. Since among the displacement and traction at a particular point, only one is specified, a method of obtaining the rest of the required information in equation (3.1.13) is essential. A significant contribution in this aspect has been made by Jaswon and Ponter[39] and Rizzo[40], and their effort made it possible to evaluate the rest of the unspecified values on the surface. The bottom line of their approach is to take the interior point in the boundary integral equation onto the surface in a limiting process, see schematics shown in Figure 3.2. By doing so, the boundary integral equation yields,

$$\int_{\partial \mathcal{R}_* + \partial \mathcal{B}_\eta(\boldsymbol{\xi}) \cap \mathcal{R}} t_i(\boldsymbol{x}; \boldsymbol{n}) u_{K_i^j}(\boldsymbol{x}, \boldsymbol{\xi}) \, dA_{\boldsymbol{x}} = \int_{\partial \mathcal{R}_* + \partial \mathcal{B}_\eta(\boldsymbol{\xi}) \cap \mathcal{R}} t_{K_i^j}(\boldsymbol{x}, \boldsymbol{\xi}; \boldsymbol{n}) u_i(\boldsymbol{x}) \, dA_{\boldsymbol{x}}, \tag{3.1.14}$$

where

$$\partial \mathcal{R}_* = \partial \mathcal{R} - \partial \mathcal{R} \cap \mathcal{B}_\eta(\boldsymbol{\xi}). \tag{3.1.15}$$

Then (3.1.14) becomes,

$$\begin{aligned} &\int_{\partial \mathcal{B}_\eta(\boldsymbol{\xi}) \cap \mathcal{R}} t_i(\boldsymbol{x}; \boldsymbol{n}) u_{K_i^j}(\boldsymbol{x}, \boldsymbol{\xi}) \, dA_{\boldsymbol{x}} + \int_{\partial \mathcal{R}_*} t_i(\boldsymbol{x}; \boldsymbol{n}) u_{K_i^j}(\boldsymbol{x}, \boldsymbol{\xi}) \, dA_{\boldsymbol{x}} \\ &= \int_{\partial \mathcal{B}_\eta(\boldsymbol{\xi}) \cap \mathcal{R}} t_{K_i^j}(\boldsymbol{x}, \boldsymbol{\xi}; \boldsymbol{n}) u_i(\boldsymbol{x}) \, dA_{\boldsymbol{x}} + \int_{\partial \mathcal{R}_*} t_{K_i^j}(\boldsymbol{x}, \boldsymbol{\xi}; \boldsymbol{n}) u_i(\boldsymbol{x}) \, dA_{\boldsymbol{x}}. \end{aligned} \tag{3.1.16}$$

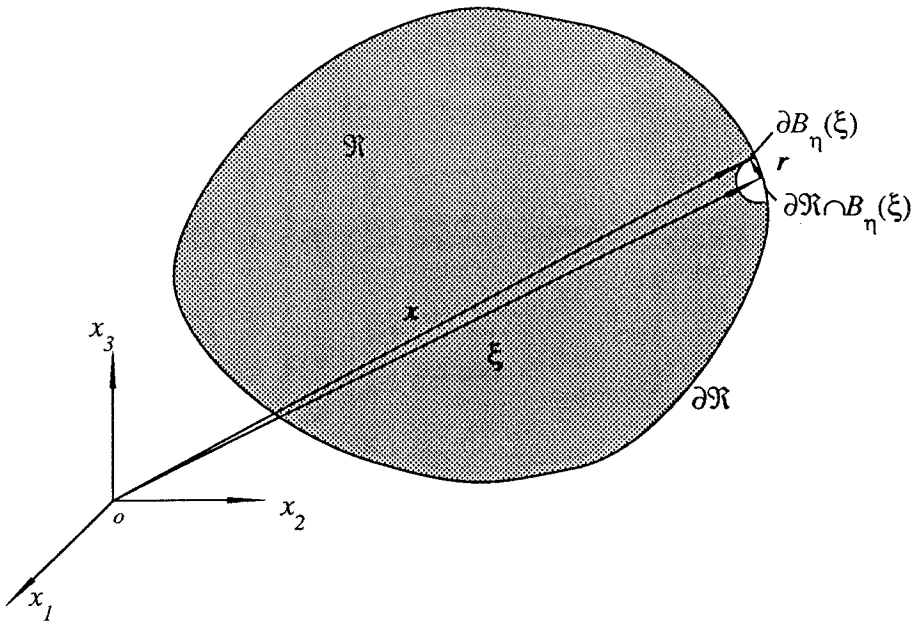

FIGURE 3.2 Surface Point

For the same reason, η is taken to be zero in a limiting process. If the surface at point $\boldsymbol{\xi}$ is smooth (no corner), then

$$\begin{aligned} \lim_{\eta\to 0}\int_{\partial\mathcal{B}_\eta(\boldsymbol{\xi})\cap\mathcal{R}} t_i(\boldsymbol{x})u_K{}^j_i(\boldsymbol{x},\boldsymbol{\xi};\boldsymbol{n})\,dA_{\boldsymbol{x}} &= 0; \\ \lim_{\eta\to 0}\int_{\partial\mathcal{B}_\eta(\boldsymbol{\xi})\cap\mathcal{R}} t_K{}^j_i(\boldsymbol{x},\boldsymbol{\xi};\boldsymbol{n})u_i(\boldsymbol{x})\,dA_{\boldsymbol{x}} &= \frac{1}{2}u_j(\boldsymbol{\xi}). \end{aligned} \tag{3.1.17}$$

The above is the well-known result for flat surfaces. Physically, only the traction on the half-sphere inside the region $\mathcal{R}$ contributes to the load applied at the point $\boldsymbol{\xi}$, the contribution of the traction from the other half-sphere outside the region $\mathcal{R}$ is not computed, this results in 1/2 in the formulation.

Mathematically, the general case of the above integral for a flat surface was calculated first by Jaswon and Ponter [39] and Rizzo [40]. The historical breakthrough of Jaswon and Rizzo cannot be overstated since this classical effort can not be applied to physical problems involving corners in the regions of interest. However,

when the surface is not flat, the value of the integral may be found analytically in two dimensions; the three-dimensional result is rather difficult to obtain in general. Cruse[8] introduced the simple way of evaluation by imposing virtual "Rigid Body Motions". Define

$$C_{ji}(\boldsymbol{\xi}) = \lim_{\eta \to 0} \int_{\partial \mathcal{B}_\eta(\boldsymbol{\xi}) \cap \mathcal{R}} t_{K_i}^j(\boldsymbol{x}, \boldsymbol{\xi}; \boldsymbol{n})\, dA_{\boldsymbol{x}} \tag{3.1.18}$$

In the case of "Rigid Body Motions",

$$t_i(\boldsymbol{x}; \boldsymbol{n}) = 0, \qquad \forall \boldsymbol{x} \in \partial \mathcal{R}, \tag{3.1.19}$$

and let 1) $u_i(\boldsymbol{x})$ be unity along direction 1, compute $C_{j1}(\boldsymbol{\xi})$; 2) $u_i(\boldsymbol{x})$ be unity along direction 2, compute $C_{j2}(\boldsymbol{\xi})$; 3) $u_i(\boldsymbol{x})$ be unity along direction 3, compute $C_{j3}(\boldsymbol{\xi})$. In all the above steps, i and j vary from 1 to 3. Then (3.1.16) gives,

$$C_{ji}(\boldsymbol{\xi}) = -\int_{\partial \mathcal{R}_*} t_{K_i}^j(\boldsymbol{x}, \boldsymbol{\xi}; \boldsymbol{n})\, dA_{\boldsymbol{x}}. \tag{3.1.20}$$

In the limiting case, the integral should be understood as in the sense of Cauchy Principal Value. In general, the principal value in Eq. (3.1.20) may be computed with good accuracy. In particular, for a point where the boundary surface is smooth,

$$C_{ji}(\boldsymbol{\xi}) = \frac{1}{2}\delta_{ji}. \tag{3.1.21}$$

Therefore, when the unit concentrated load is acting at a point on the boundary surface, (3.1.16) becomes,

$$C_{ji}(\boldsymbol{\xi}) u_i(\boldsymbol{\xi}) + \int_{\partial \mathcal{R}_*} t_{K_i}^j(\boldsymbol{x}, \boldsymbol{\xi}; \boldsymbol{n}) u_i(\boldsymbol{x})\, dA_{\boldsymbol{x}} = \int_{\partial \mathcal{R}_*} t_i(\boldsymbol{x}; \boldsymbol{n}) u_{K_i}^j(\boldsymbol{x}, \boldsymbol{\xi})\, dA_{\boldsymbol{x}}. \tag{3.1.22}$$

The integral over the surface $\partial \mathcal{R}_*$ should be considered as in the sense of Cauchy Principal Value.

Equations (3.1.13) and (3.1.22) are the two most important boundary integral equations. These two equations indicate that all the displacement components at any points either in the interior or on the surface of the region can be expressed

solely by the values on the boundary of the region.

It is important to point out that, if the Kelvin solution is used as the solution of the "singular" state, the integrations in the BIEs are over the entire surface of the region. In current research, this Kelvin solution is replaced by the fundamental solution of the infinite plate problem, and the integrations are computed only over the *lateral* surfaces of the region. The following section illustrates the difference.

3.2 Theory Of Modified Boundary Integral Equation Method

Let the regular state be the same as the state-1 defined in the previous section. Let the "singular" state be identified by the infinite plate problem as indicated in Theorem 2.3.1 in previous chapter. Since the properties of the fundamental solution are vital to the modified BIEs, they are repeated as follows,

Theorem 2.3.1 (properties of the fundamental solution for infinite plate problem).

The fundamental solution corresponding to a concentrated load $\boldsymbol{\ell}$ *at point* $\boldsymbol{\xi}$ *has the properties:*

$$
\begin{aligned}
&a)\quad \mathcal{S} = [\boldsymbol{u}, \boldsymbol{\sigma}] \in \mathcal{E}_s(E,\ \nu,\ \boldsymbol{0};\ \mathcal{P} - \{\boldsymbol{\xi}\});\\
&b)\quad \boldsymbol{t}(\boldsymbol{x}, \boldsymbol{\xi}; \boldsymbol{n}) = \boldsymbol{\sigma}(\boldsymbol{x}, \boldsymbol{\xi})\boldsymbol{n} = \boldsymbol{0};\quad
\begin{cases}
\forall \boldsymbol{x} \in \partial\mathcal{P} & for\ \boldsymbol{\xi} \in \overset{\circ}{\mathcal{P}},\\
\forall \boldsymbol{x} \in \partial\mathcal{P} - \{\boldsymbol{\xi}\} & for\ \boldsymbol{\xi} \in \partial\mathcal{P},
\end{cases}\\
&c)\quad
\left.
\begin{aligned}
&\lim_{\eta\to 0} \int\limits_{\partial\mathcal{B}_\eta(\boldsymbol{\xi})\cap\mathcal{P}} \boldsymbol{t}(\boldsymbol{x}, \boldsymbol{\xi}; \boldsymbol{n}) dA_{\boldsymbol{x}} = \boldsymbol{\ell};\\
&\lim_{\eta\to 0} \int\limits_{\partial\mathcal{B}_\eta(\boldsymbol{\xi})\cap\mathcal{P}} (\boldsymbol{x} - \boldsymbol{x}) \wedge \boldsymbol{t}(\boldsymbol{x}, \boldsymbol{\xi}; \boldsymbol{n})\ dA_{\boldsymbol{x}} = \boldsymbol{0};
\end{aligned}
\right\} \boldsymbol{\xi} \in \mathcal{P},\\
&d)\quad \boldsymbol{u}(\boldsymbol{x}, \boldsymbol{\xi}) = O\Big(|\ \boldsymbol{x} - \boldsymbol{\xi}\ |^{-1}\Big),\ \boldsymbol{\sigma}(\boldsymbol{x}, \boldsymbol{\xi}) = O\Big(|\ \boldsymbol{x} - \boldsymbol{\xi}\ |^{-2}\Big) \text{ as } \boldsymbol{x} \to \boldsymbol{\xi}.
\end{aligned}
\tag{3.2.1}
$$

where $\boldsymbol{t}(\boldsymbol{x},\boldsymbol{\xi};\boldsymbol{n})$ *in b) and c) is the traction vector on the surface of* $\partial\mathcal{B}_\eta(\boldsymbol{\xi})\cap\mathcal{P}$ *that faces* $\boldsymbol{\xi}$.

It is important to notice that $\mathcal{R}\subset\mathcal{P}$. For a unit concentrated load acting in the interior of the region $\mathcal{R}$, as shown in Figure 3.1, the Somigliana Identity gives (3.1.12), in which

$$\overset{*}{\Sigma}=\partial\mathcal{R}_1\cup\partial\mathcal{R}_2\cup\mathcal{L}+\partial\mathcal{B}_\eta(\boldsymbol{\xi}). \tag{3.2.2}$$

The left hand side of (3.1.12) can now be expressed as,

$$\begin{aligned}\int_{\overset{*}{\Sigma}} t_i(\boldsymbol{x};\boldsymbol{n})u_i^j(\boldsymbol{x},\boldsymbol{\xi})\,dA_{\boldsymbol{x}} = &\int_{\partial\mathcal{B}_\eta(\boldsymbol{\xi})} t_i(\boldsymbol{x};\boldsymbol{n})u_i^j(\boldsymbol{x},\boldsymbol{\xi})\,dA_{\boldsymbol{x}}\\ &+\int_{\partial\mathcal{R}_1} t_i(\boldsymbol{x};\boldsymbol{n})u_i^j(\boldsymbol{x},\boldsymbol{\xi})\,dA_{\boldsymbol{x}}\\ &+\int_{\partial\mathcal{R}_2} t_i(\boldsymbol{x};\boldsymbol{n})u_i^j(\boldsymbol{x},\boldsymbol{\xi})\,dA_{\boldsymbol{x}}\\ &+\int_{\mathcal{L}} t_i(\boldsymbol{x};\boldsymbol{n})u_i^j(\boldsymbol{x},\boldsymbol{\xi})\,dA_{\boldsymbol{x}}.\end{aligned} \tag{3.2.3}$$

Since the boundary value problem satisfies the traction-free boundary condition on the upper and the lower surfaces of the plate,

$$t_i(\boldsymbol{x};\boldsymbol{n})=0,\qquad \forall\boldsymbol{x}\in\partial\mathcal{R}_1\cup\partial\mathcal{R}_2, \tag{3.2.4}$$

the second and the third integrals in (3.2.3) are therefore zeros.

From the right hand side of (3.1.12) one obtains,

$$\begin{aligned}\int_{\overset{*}{\Sigma}} t_i^j(\boldsymbol{x},\boldsymbol{\xi};\boldsymbol{n})u_i(\boldsymbol{x})\,dA_{\boldsymbol{x}} = &\int_{\partial\mathcal{B}_\eta(\boldsymbol{\xi})} t_i^j(\boldsymbol{x},\boldsymbol{\xi};\boldsymbol{n})u_i(\boldsymbol{x})\,dA_{\boldsymbol{x}}\\ &+\int_{\partial\mathcal{R}_1} t_i^j(\boldsymbol{x},\boldsymbol{\xi};\boldsymbol{n})u_i(\boldsymbol{x})\,dA_{\boldsymbol{x}}\\ &+\int_{\partial\mathcal{R}_2} t_i^j(\boldsymbol{x},\boldsymbol{\xi};\boldsymbol{n})u_i(\boldsymbol{x})\,dA_{\boldsymbol{x}}\\ &+\int_{\mathcal{L}} t_i^j(\boldsymbol{x},\boldsymbol{\xi};\boldsymbol{n})u_i(\boldsymbol{x})\,dA_{\boldsymbol{x}}.\end{aligned} \tag{3.2.5}$$

Since the fundamental solution satisfies the traction-free boundary conditions on the upper and lower surfaces of the plate,

$$t_i^j(\boldsymbol{x},\boldsymbol{\xi};\boldsymbol{n}) = \sigma_{ik}^j(\boldsymbol{x},\boldsymbol{\xi})n_k(\boldsymbol{x}) = 0, \quad \begin{cases} \forall \boldsymbol{x} \in \partial\mathcal{R}_1 \cup \partial\mathcal{R}_2 & \forall \boldsymbol{\xi} \in \overset{\circ}{\mathcal{P}}, \\ \forall \boldsymbol{x} \in \partial\mathcal{R}_1 \cup \partial\mathcal{R}_2 - \{\boldsymbol{\xi}\} & \forall \boldsymbol{\xi} \in \partial\mathcal{R}, \end{cases} \tag{3.2.6}$$

then, the second and the third integrals in (3.2.5) are zeros. Thus,

$$\begin{aligned} &\int_{\partial\mathcal{B}_\eta(\boldsymbol{\xi})} \boldsymbol{t_i^j}(\boldsymbol{x},\boldsymbol{\xi};\boldsymbol{n})u_i(\boldsymbol{x})\, dA_{\boldsymbol{x}} + \int_{\mathcal{L}} \boldsymbol{t_i^j}(\boldsymbol{x},\boldsymbol{\xi};\boldsymbol{n})u_i(\boldsymbol{x})\, dA_{\boldsymbol{x}} \\ &= \int_{\partial\mathcal{B}_\eta(\boldsymbol{\xi})} \boldsymbol{u_i^j}(\boldsymbol{x},\boldsymbol{\xi})t_i(\boldsymbol{x};\boldsymbol{n})\, dA_{\boldsymbol{x}} + \int_{\mathcal{L}} \boldsymbol{u_i^j}(\boldsymbol{x},\boldsymbol{\xi})t_i(\boldsymbol{x};\boldsymbol{n})\, dA_{\boldsymbol{x}}. \end{aligned} \tag{3.2.7}$$

Same as in the previous section, the spherical cavity is artificially excluded from the region to avoid the singularity problem at point $\boldsymbol{\xi}$. This problem is cured by taking the radius of the spherical ball to zero in a limiting process. When the unit concentrated load is acting in the interior of the region, by the use of the properties of the fundamental solution and following the same procedure as illustrated in the previous section, one has,

$$\begin{aligned} &\lim_{\eta\to 0} \int_{\partial\mathcal{B}_\eta(\boldsymbol{\xi})\cap\mathcal{R}} t_i(\boldsymbol{x};\boldsymbol{n})u_i^j(\boldsymbol{x},\boldsymbol{\xi})\, dA_{\boldsymbol{x}} = 0; \\ &\lim_{\eta\to 0} \int_{\partial\mathcal{B}_\eta(\boldsymbol{\xi})\cap\mathcal{R}} t_i^j(\boldsymbol{x},\boldsymbol{\xi};\boldsymbol{n})u_i(\boldsymbol{x})\, dA_{\boldsymbol{x}} = u_j(\boldsymbol{\xi}). \end{aligned} \tag{3.2.8}$$

Then, equation (3.2.7) yields,

$$u_j(\boldsymbol{\xi}) + \int_{\mathcal{L}} t_i^j(\boldsymbol{x},\boldsymbol{\xi};\boldsymbol{n})u_i(\boldsymbol{x})\, dA_{\boldsymbol{x}} = \int_{\mathcal{L}} t_i(\boldsymbol{x};\boldsymbol{n})u_i^j(\boldsymbol{x},\boldsymbol{\xi})\, dA_{\boldsymbol{x}}. \tag{3.2.9}$$

Similarly, when the unit concentrated load is acting on the lateral surface of the plate, as shown in Figure 3.2, one has,

$$C_{ji}(\boldsymbol{\xi})u_i(\boldsymbol{\xi}) + \int_{\mathcal{L}_*} t_i^j(\boldsymbol{x},\boldsymbol{\xi};\boldsymbol{n})u_i(\boldsymbol{x})\, dA_{\boldsymbol{x}} = \int_{\mathcal{L}_*} t_i(\boldsymbol{x},\boldsymbol{\xi};\boldsymbol{n})u_i^j(\boldsymbol{x},\boldsymbol{\xi})\, dA_{\boldsymbol{x}}, \tag{3.2.10}$$

where

$$C_{ji}(\boldsymbol{\xi}) = \begin{cases} \dfrac{1}{2}, & \text{for smooth surface at } \boldsymbol{\xi}, \\ -\displaystyle\int_{\mathcal{L}_*} t_i^j(\boldsymbol{x}, \boldsymbol{\xi}; \boldsymbol{n})\, dA_{\boldsymbol{x}} & \text{otherwise,} \end{cases} \tag{3.2.11}$$

and

$$\mathcal{L}_* = \mathcal{L} - \{\boldsymbol{\xi}\}. \tag{3.2.12}$$

The integrations over the lateral surface $\mathcal{L}_*$ should be understood as in the sense of Cauchy Principal Values.

It can be easily seen from (3.2.9) and (3.2.10) that the integrations over the upper and lower surfaces of the plate are not necessary since the integrands are zero. Therefore, the displacements either in the interior or on the boundary of the region can be expressed by the data only on the *lateral* boundary. The savings in not computing the surface integral on the two planar surfaces is a great advantage compared to the conventional boundary element method. The savings in modeling effort and the reduction in the final problem size will be tremendous especially in the analysis of problems involving multi-crack interactions.

3.3 Boundary Element Formulation With Fundamental Solution Of Infinite Plate Problem

The boundary and boundary data will be approximated in order to solve the boundary integral equations numerically. The approximations involve replacing the lateral boundary by a complete set of surface patches called boundary elements, and this process is the so called discretization. The boundary data is then interpolated over each boundary element. Writing the discretized boundary integral equation

(3.2.10) for every nodal point yields a system of linear algebraic equations. Once the boundary conditions are imposed, the system can be solved to obtain all the unknown values. Consequently, an approximate solution to the boundary value problem is obtained.

Because of the complexity of the fundamental solution, the boundary elements are taken to be flat in the process of discretization, and the boundary data is taken from the element centroid. In other words, "constant elements" are used.

It is now more convenient to work with matrix notation rather than carry on with the the indicial notation. To this effect, define the displacement and the traction vectors that apply over the element l by the values at its centroid, i.e.,

$$\begin{aligned} \boldsymbol{u}\Big(\boldsymbol{x}^l, \boldsymbol{\xi}\Big) &= \Big\{\boldsymbol{u}^l\Big\}, \\ \boldsymbol{t}\Big(\boldsymbol{x}^l, \boldsymbol{\xi}; \boldsymbol{n}\Big) &= \Big\{\boldsymbol{t}^l\Big\}, \end{aligned} \tag{3.3.1}$$

where the superscript l denotes the element, and $\Big\{\boldsymbol{u}^l\Big\}$ and $\Big\{\boldsymbol{t}^l\Big\}$ indicate the displacement and traction vectors at the element centroid $\boldsymbol{x}^l$. They are usually called the element nodal values.

Denote the coefficients of the fundamental solution as,

$$\Big[\boldsymbol{t}^*\Big] = \begin{pmatrix} t_1^1(\boldsymbol{x}, \boldsymbol{\xi}; \boldsymbol{n}) & t_2^1(\boldsymbol{x}, \boldsymbol{\xi}; \boldsymbol{n}) & t_3^1(\boldsymbol{x}, \boldsymbol{\xi}; \boldsymbol{n}) \\ t_1^2(\boldsymbol{x}, \boldsymbol{\xi}; \boldsymbol{n}) & t_2^2(\boldsymbol{x}, \boldsymbol{\xi}; \boldsymbol{n}) & t_3^2(\boldsymbol{x}, \boldsymbol{\xi}; \boldsymbol{n}) \\ t_1^3(\boldsymbol{x}, \boldsymbol{\xi}; \boldsymbol{n}) & t_2^3(\boldsymbol{x}, \boldsymbol{\xi}; \boldsymbol{n}) & t_3^3(\boldsymbol{x}, \boldsymbol{\xi}; \boldsymbol{n}) \end{pmatrix}, \tag{3.3.2}$$

and

$$\Big[\boldsymbol{u}^*\Big] = \begin{pmatrix} u_1^1(\boldsymbol{x}, \boldsymbol{\xi}) & t_2^1(\boldsymbol{x}, \boldsymbol{\xi}) & u_3^1(\boldsymbol{x}, \boldsymbol{\xi}) \\ u_1^2(\boldsymbol{x}, \boldsymbol{\xi}) & u_2^2(\boldsymbol{x}, \boldsymbol{\xi}) & u_3^2(\boldsymbol{x}, \boldsymbol{\xi}) \\ u_1^3(\boldsymbol{x}, \boldsymbol{\xi}) & u_2^3(\boldsymbol{x}, \boldsymbol{\xi}) & u_3^3(\boldsymbol{x}, \boldsymbol{\xi}) \end{pmatrix}. \tag{3.3.3}$$

Suppose that the unit concentrated load is acting at the centroid of the lth element. Substitute the above functions into equation (3.2.10), and discretize the boundary to obtain the equation corresponding to the displacement vector at the nodal point l,

$$[C_l]\left\{\boldsymbol{u}^l\right\} + \sum_{m=1}^{NE} \int_{\mathcal{L}_{*m}} \left[\boldsymbol{t}^*\right]\left\{\boldsymbol{u}^m\right\} dA_{\boldsymbol{x}} = \sum_{m=1}^{NE} \int_{\mathcal{L}_{*m}} \left[\boldsymbol{u}^*\right]\left\{\boldsymbol{t}^m\right\} dA_{\boldsymbol{x}}, \tag{3.3.4}$$

where $\mathcal{L}_{*m}$ is the surface of the mth element, and the point $\boldsymbol{\xi}$ is excluded from this surface element if it is on the element. NE stands for the number of elements used. $[C_l]$ $(l = 1, ..., NE)$ are a series of 3×3 submatrices,

$$[C_l] = \begin{pmatrix} \frac{1}{2} & 0 & 0 \\ 0 & \frac{1}{2} & 0 \\ 0 & 0 & \frac{1}{2} \end{pmatrix}. \tag{3.3.5}$$

Since $\left\{\boldsymbol{u}^m\right\}$ and $\left\{\boldsymbol{t}^m\right\}$ are constants vectors over the mth element, they can be taken out of the integrals. Thus,

$$[C_l]\left\{\boldsymbol{u}^l\right\} + \sum_{m=1}^{NE} \int_{\mathcal{L}_{*m}} \left[\boldsymbol{t}^*\right] dA_{\boldsymbol{x}} \left\{\boldsymbol{u}^m\right\} = \sum_{m=1}^{NE} \int_{\mathcal{L}_{*m}} \left[\boldsymbol{u}^*\right] dA_{\boldsymbol{x}} \left\{\boldsymbol{t}^m\right\}. \tag{3.3.6}$$

where the superscript i denotes the position of the unit concentrated load, and j indicates the element at which the response is computed. Both i and j vary from 1 through NE. Once the terms are integrated, (3.3.6) can be written as,

$$[C_l]\left\{\boldsymbol{u}^l\right\} + \sum_{m=1}^{NE} \left[\hat{\boldsymbol{H}}^{lm}\right]\left\{\boldsymbol{u}^m\right\} = \sum_{m=1}^{NE} \left[\boldsymbol{G}^{lm}\right]\left\{\boldsymbol{t}^m\right\}, \tag{3.3.7}$$

The influence matrices $\left[\hat{\boldsymbol{H}}^{lm}\right]$ and $\left[\boldsymbol{G}^{lm}\right]$ are 3×3 matrices, and they are defined as.

$$\begin{aligned} \left[\hat{\boldsymbol{H}}^{lm}\right] &= \int_{\mathcal{L}_{*m}} \left[\boldsymbol{t}^*\right] dA_{\boldsymbol{x}}, \\ \left[\boldsymbol{G}^{lm}\right] &= \int_{\mathcal{L}_{*m}} \left[\boldsymbol{u}^*\right] dA_{\boldsymbol{x}}, \end{aligned} \tag{3.3.8}$$

and

$$[\hat{\boldsymbol{H}}^{lm}] = \begin{pmatrix} \int_{\mathcal{L}_{*m}} t_1^1(\boldsymbol{x},\boldsymbol{\xi};\boldsymbol{n})\, dA_{\boldsymbol{x}} & \int_{\mathcal{L}_{*m}} t_2^1(\boldsymbol{x},\boldsymbol{\xi};\boldsymbol{n})\, dA_{\boldsymbol{x}} & \int_{\mathcal{L}_{*m}} t_3^1(\boldsymbol{x},\boldsymbol{\xi};\boldsymbol{n})\, dA_{\boldsymbol{x}} \\ \int_{\mathcal{L}_{*m}} t_1^2(\boldsymbol{x},\boldsymbol{\xi};\boldsymbol{n})\, dA_{\boldsymbol{x}} & \int_{\mathcal{L}_{*m}} t_2^2(\boldsymbol{x},\boldsymbol{\xi};\boldsymbol{n})\, dA_{\boldsymbol{x}} & \int_{\mathcal{L}_{*m}} t_3^2(\boldsymbol{x},\boldsymbol{\xi};\boldsymbol{n})\, dA_{\boldsymbol{x}} \\ \int_{\mathcal{L}_{*m}} t_1^3(\boldsymbol{x},\boldsymbol{\xi};\boldsymbol{n})\, dA_{\boldsymbol{x}} & \int_{\mathcal{L}_{*m}} t_2^3(\boldsymbol{x},\boldsymbol{\xi};\boldsymbol{n})\, dA_{\boldsymbol{x}} & \int_{\mathcal{L}_{*m}} t_3^3(\boldsymbol{x},\boldsymbol{\xi};\boldsymbol{n})\, dA_{\boldsymbol{x}} \end{pmatrix};$$

$$[\boldsymbol{G}^{lm}] = \begin{pmatrix} \int_{\mathcal{L}_{*m}} u_1^1(\boldsymbol{x},\boldsymbol{\xi})\, dA_{\boldsymbol{x}} & \int_{\mathcal{L}_{*m}} u_2^1(\boldsymbol{x},\boldsymbol{\xi})\, dA_{\boldsymbol{x}} & \int_{\mathcal{L}_{*m}} u_3^1(\boldsymbol{x},\boldsymbol{\xi})\, dA_{\boldsymbol{x}} \\ \int_{\mathcal{L}_{*m}} u_1^2(\boldsymbol{x},\boldsymbol{\xi})\, dA_{\boldsymbol{x}} & \int_{\mathcal{L}_{*m}} u_2^2(\boldsymbol{x},\boldsymbol{\xi})\, dA_{\boldsymbol{x}} & \int_{\mathcal{L}_{*m}} u_3^2(\boldsymbol{x},\boldsymbol{\xi})\, dA_{\boldsymbol{x}} \\ \int_{\mathcal{L}_{*m}} u_1^3(\boldsymbol{x},\boldsymbol{\xi})\, dA_{\boldsymbol{x}} & \int_{\mathcal{L}_{*m}} u_2^3(\boldsymbol{x},\boldsymbol{\xi})\, dA_{\boldsymbol{x}} & \int_{\mathcal{L}_{*m}} u_3^3(\boldsymbol{x},\boldsymbol{\xi})\, dA_{\boldsymbol{x}} \end{pmatrix}. \tag{3.3.9}$$

From (3.3.7), the following holds,

$$\begin{aligned} \left[\boldsymbol{H}^{lm}\right] &= \left[\hat{\boldsymbol{H}}^{lm}\right], && \text{if } l \neq m; \\ \left[\boldsymbol{H}^{lm}\right] &= \left[\hat{\boldsymbol{H}}^{lm}\right] + \left[C_l\right], && \text{if } l = m. \end{aligned} \tag{3.3.10}$$

Equation (3.3.7) for node l then becomes

$$\sum_{m=1}^{NE} \left[\boldsymbol{H}^{lm}\right]\left\{\boldsymbol{u}^m\right\} = \sum_{m=1}^{NE} \left[\boldsymbol{G}^{lm}\right]\left\{\boldsymbol{t}^m\right\}. \tag{3.3.11}$$

Similarly, the contribution for all the nodes can be written. The equations can then be assemble into the global system of equations according to the nodes, i.e.,

$$[\boldsymbol{H}]\{\boldsymbol{u}\} = [\boldsymbol{G}]\{\boldsymbol{t}\}. \tag{3.3.12}$$

Matrices $[\boldsymbol{H}]$ and $[\boldsymbol{G}]$ are both $3NE \times 3NE$ matrices, $\{\boldsymbol{u}\}$ and $\{\boldsymbol{t}\}$ are $3NE \times 1$ vectors.

In the actual situations, the full $[\boldsymbol{H}]$ and $[\boldsymbol{G}]$ matrices are never stored according to these sizes. As the system of equations is generated, the known boundary conditions are multiplied to generate the right-hand side vector; the coefficients of the unknown terms – either the displacement components or the traction components – populate the coefficient matrix $[\boldsymbol{A}]$,

$$[\boldsymbol{A}]\,\{\boldsymbol{y}\} = \{\boldsymbol{b}\}, \tag{3.3.13}$$

where $[\boldsymbol{A}]$ is a $3NE \times 3NE$ matrix, $\{\boldsymbol{y}\}$ is the vector of unknowns, $\{\boldsymbol{b}\}$ is the known right-hand side. $\{\boldsymbol{y}\}$ and $\{\boldsymbol{b}\}$ are both $3NE \times 1$ vectors. Equation (3.3.13) is the actual form of equations that is to be solved. The Gauss matrix reduction method will be used to solve the equations.

3.4 Element Matrices Construction

The evaluation of the element matrices $\left[\hat{\boldsymbol{H}}^{lm}\right]$ and $\left[\boldsymbol{G}^{lm}\right]$ is crucial to the modified boundary element formulation. Since the components of the matrices involve the integration of the fundamental solution, and the expressions of the fundamental solution are very complicated, the integrals can not be computed analytically.

One way to evaluate the matrix components is to use the Gaussian Quadrature scheme. But when an element is very close to the unit concentrated load or when the load is on the element, the variation of the fundamental solution is great. In such cases, the Gaussian Quadrature scheme is effective only if many Gaussian points are used. Because of the consideration of the computational time, it is not practically feasible to employ too many Gaussian points because of the complexity of the fundamental solution.

One alternative way is to evaluate the matrix components partially analytically and partially numerically. This procedure is called the *proposed procedure* to evaluate the matrix components. The idea of the *proposed procedure* can be expressed as follows,

$$\begin{aligned}\left[\hat{\boldsymbol{H}}^{lm}\right] &= \int_{\mathcal{L}_{*m}} \left[\boldsymbol{t}^* - \boldsymbol{t}_K\right] dA_{\boldsymbol{x}} + \int_{\mathcal{L}_{*m}} \left[\boldsymbol{t}_K\right] dA_{\boldsymbol{x}};\\ \left[\boldsymbol{G}^{lm}\right] &= \int_{\mathcal{L}_{*m}} \left[\boldsymbol{u}^* - \boldsymbol{u}_K\right] dA_{\boldsymbol{x}} + \int_{\mathcal{L}_{*m}} \left[\boldsymbol{u}_K\right] dA_{\boldsymbol{x}},\end{aligned} \tag{3.4.1}$$

where

$$\left[\boldsymbol{t}^* - \boldsymbol{t}_K\right] =$$

$$\begin{pmatrix} t_1^1(\boldsymbol{x},\boldsymbol{\xi};\boldsymbol{n}) - t_K{}_1^1(\boldsymbol{x},\boldsymbol{\xi};\boldsymbol{n}) & t_2^1(\boldsymbol{x},\boldsymbol{\xi};\boldsymbol{n}) - t_K{}_1^1(\boldsymbol{x},\boldsymbol{\xi};\boldsymbol{n}) & t_3^1(\boldsymbol{x},\boldsymbol{\xi};\boldsymbol{n}) - t_K{}_1^1(\boldsymbol{x},\boldsymbol{\xi};\boldsymbol{n}) \\ t_1^2(\boldsymbol{x},\boldsymbol{\xi};\boldsymbol{n}) - t_K{}_1^1(\boldsymbol{x},\boldsymbol{\xi};\boldsymbol{n}) & t_2^2(\boldsymbol{x},\boldsymbol{\xi};\boldsymbol{n}) - t_K{}_1^1(\boldsymbol{x},\boldsymbol{\xi};\boldsymbol{n}) & t_3^2(\boldsymbol{x},\boldsymbol{\xi};\boldsymbol{n}) - t_K{}_1^1(\boldsymbol{x},\boldsymbol{\xi};\boldsymbol{n}) \\ t_1^3(\boldsymbol{x},\boldsymbol{\xi};\boldsymbol{n}) - t_K{}_1^1(\boldsymbol{x},\boldsymbol{\xi};\boldsymbol{n}) & t_2^3(\boldsymbol{x},\boldsymbol{\xi};\boldsymbol{n}) - t_K{}_1^1(\boldsymbol{x},\boldsymbol{\xi};\boldsymbol{n}) & t_3^3(\boldsymbol{x},\boldsymbol{\xi};\boldsymbol{n}) - t_K{}_1^1(\boldsymbol{x},\boldsymbol{\xi};\boldsymbol{n}) \end{pmatrix}, \tag{3.4.2}$$

and

$$\left[\boldsymbol{u}^* - \boldsymbol{u}_K\right] =$$

$$\begin{pmatrix} u_1^1(\boldsymbol{x},\boldsymbol{\xi}) - u_K{}_1^1(\boldsymbol{x},\boldsymbol{\xi}) & u_2^1(\boldsymbol{x},\boldsymbol{\xi}) - u_K{}_1^1(\boldsymbol{x},\boldsymbol{\xi}) & u_3^1(\boldsymbol{x},\boldsymbol{\xi}) - u_K{}_1^1(\boldsymbol{x},\boldsymbol{\xi}) \\ u_1^2(\boldsymbol{x},\boldsymbol{\xi}) - u_K{}_1^1(\boldsymbol{x},\boldsymbol{\xi}) & u_2^2(\boldsymbol{x},\boldsymbol{\xi}) - u_K{}_1^1(\boldsymbol{x},\boldsymbol{\xi}) & u_3^2(\boldsymbol{x},\boldsymbol{\xi}) - u_K{}_1^1(\boldsymbol{x},\boldsymbol{\xi}) \\ u_1^3(\boldsymbol{x},\boldsymbol{\xi}) - u_K{}_1^1(\boldsymbol{x},\boldsymbol{\xi}) & u_2^3(\boldsymbol{x},\boldsymbol{\xi}) - u_K{}_1^1(\boldsymbol{x},\boldsymbol{\xi}) & u_3^3(\boldsymbol{x},\boldsymbol{\xi}) - u_K{}_1^1(\boldsymbol{x},\boldsymbol{\xi}) \end{pmatrix}. \tag{3.4.3}$$

The subscript K denotes the Kelvin solution, while $\boldsymbol{t}^*$ and $\boldsymbol{u}^*$ are the fundamental solution of the infinite plate problem. The first integral of each equation in (3.4.1) is to be integrated numerically, and the second integral of each equation is to be integrated analytically.

As illustrated in the previous chapter, although the fundamental solution and the Kelvin solution deal with totally different problems, they exhibit the same singular behavior. When the unit concentrated load is acting in the interior of the infinite plate, the fundamental solution tends to the Kelvin solution as the observation point approaches the loading point. Therefore, when the two points approach each other, the result of the subtraction of the fundamental solution by the Kelvin solution tends to zero. When the points of observation and loading are far apart, both the fundamental solution and the Kelvin solution are expected to be small in the in-plane directions since they vary as $O(1/r^2)$. In general, the fundamental solution may not be comparable to the Kelvin solution in the out-of plane direction as the two points are far away from each other since they are different solutions.

3.4.1 Numerical Integration Over An Arbitrary Element

The first integral in each equation in (3.4.1) is to be computed numerically. The numerical integration of all the above components over an arbitrary element can be abstracted to the following simple expression,

$$v = \int_{\mathcal{L}_{*_m}} f(\boldsymbol{x}, \boldsymbol{\xi}) dA_{\boldsymbol{x}}, \tag{3.4.4}$$

where v stands for any matrix component, and $f(\boldsymbol{x}, \boldsymbol{\xi})$ stands for the corresponding traction or displacement component of the fundamental solution of the infinite plate problem. Take a four noded flat element as an example, see Figure 3.3.

Any four-noded flat element can be obtained from a four-noded square element,

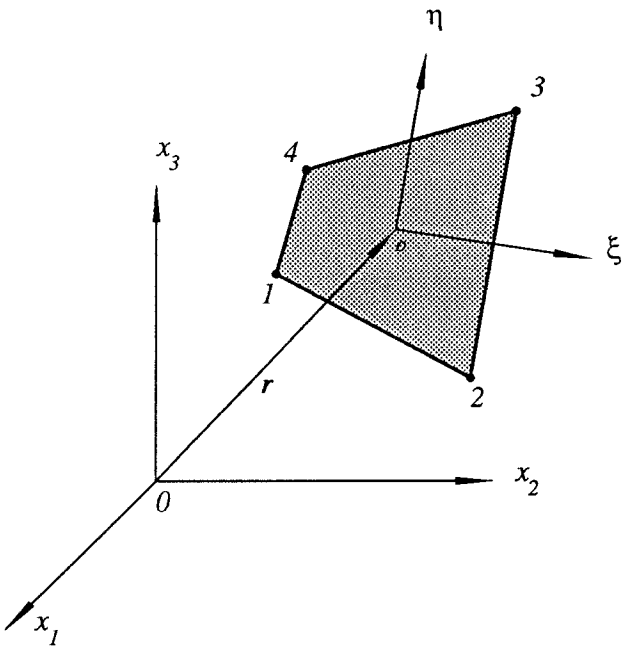

FIGURE 3.3 Arbitrary Element In Space

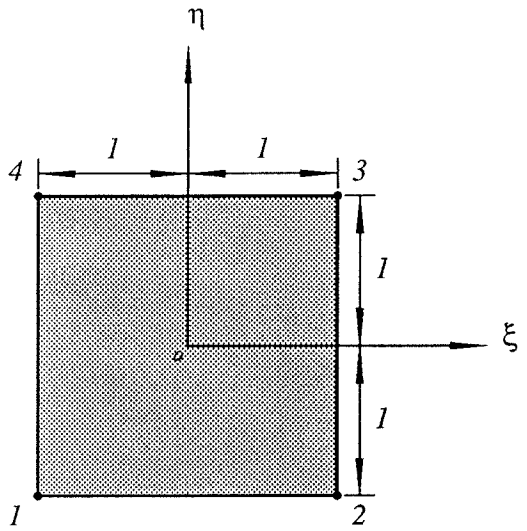

FIGURE 3.4 Parent Element

see Figure 3.4, by using the following mapping,

$$\begin{aligned} x_1 &= P_1(\xi,\eta)x_1^1 + P_2(\xi,\eta)x_1^2 + P_3(\xi,\eta)x_1^3 + P_4(\xi,\eta)x_1^4; \\ x_2 &= P_1(\xi,\eta)x_2^1 + P_2(\xi,\eta)x_2^2 + P_3(\xi,\eta)x_2^3 + P_4(\xi,\eta)x_2^4; \\ x_3 &= P_1(\xi,\eta)x_3^1 + P_2(\xi,\eta)x_3^2 + P_3(\xi,\eta)x_3^3 + P_4(\xi,\eta)x_3^4, \end{aligned} \tag{3.4.5}$$

where (x_1, x_2, x_3) is the global coordinate of a point inside the element; (ξ, η) is the local coordinate of the same point; (x_1^1, x_2^1, x_3^1), (x_1^2, x_2^2, x_3^2), (x_1^3, x_2^3, x_3^3) and (x_1^4, x_2^4, x_3^4) are the global coordinates of the four corners of the element; finally, $P_1(\xi,\eta)$, $P_2(\xi,\eta)$, $P_3(\xi,\eta)$ and $P_4(\xi,\eta)$ are the so called shape functions, and they are given by,

$$\begin{aligned} P_1(\xi,\eta) &= \frac{1}{4}(1-\xi)(1-\eta); \\ P_2(\xi,\eta) &= \frac{1}{4}(1+\xi)(1-\eta); \\ P_3(\xi,\eta) &= \frac{1}{4}(1+\xi)(1+\eta); \\ P_4(\xi,\eta) &= \frac{1}{4}(1-\xi)(1+\eta), \end{aligned} \tag{3.4.6}$$

For surface transformation,

$$dA_{\boldsymbol{x}} = |J(\xi,\eta)|\, d\xi d\eta, \tag{3.4.7}$$

where $|J(\xi,\eta)|$ is called the Jacobian of area transformation.

$$|J(\xi,\eta)| = \left| \frac{\frac{\partial \boldsymbol{r}}{\partial \xi} \times \frac{\partial \boldsymbol{r}}{\partial \eta}}{\left|\frac{\partial \boldsymbol{r}}{\partial \xi}\right| \left|\frac{\partial \boldsymbol{r}}{\partial \eta}\right|} \right|, \tag{3.4.8}$$

where

$$\begin{aligned} \frac{\partial \boldsymbol{r}}{\partial \xi} &= \left(\frac{\partial x_1}{\partial \xi}, \frac{\partial x_2}{\partial \xi}, \frac{\partial x_3}{\partial \xi} \right); \\ \frac{\partial \boldsymbol{r}}{\partial \eta} &= \left(\frac{\partial x_1}{\partial \eta}, \frac{\partial x_2}{\partial \eta}, \frac{\partial x_3}{\partial \eta} \right), \end{aligned} \tag{3.4.9}$$

Since

$$\frac{\partial x_i}{\partial \xi} = \frac{\partial P_1(\xi,\eta)}{\partial \xi} x_i^1 + \frac{\partial P_2(\xi,\eta)}{\partial \xi} x_i^2 + \frac{\partial P_3(\xi,\eta)}{\partial \xi} x_i^3 + \frac{\partial P_4(\xi,\eta)}{\partial \xi} x_i^4;$$

$$\frac{\partial x_i}{\partial \eta} = \frac{\partial P_1(\xi,\eta)}{\partial \eta} x_i^1 + \frac{\partial P_2(\xi,\eta)}{\partial \eta} x_i^2 + \frac{\partial P_3(\xi,\eta)}{\partial \eta} x_i^3 + \frac{\partial P_4(\xi,\eta)}{\partial \eta} x_i^4, \qquad (i = 1,2,3), \tag{3.4.10}$$

where

$$\begin{aligned}
\frac{\partial P_1(\xi,\eta)}{\partial \xi} &= -\frac{1}{4}(1-\eta);\\
\frac{\partial P_2(\xi,\eta)}{\partial \xi} &= \frac{1}{4}(1-\eta);\\
\frac{\partial P_3(\xi,\eta)}{\partial \xi} &= \frac{1}{4}(1+\eta);\\
\frac{\partial P_4(\xi,\eta)}{\partial \xi} &= -\frac{1}{4}(1+\eta);\\
\frac{\partial P_1(\xi,\eta)}{\partial \eta} &= -\frac{1}{4}(1-\xi);\\
\frac{\partial P_2(\xi,\eta)}{\partial \eta} &= -\frac{1}{4}(1+\xi);\\
\frac{\partial P_3(\xi,\eta)}{\partial \eta} &= \frac{1}{4}(1+\xi);\\
\frac{\partial P_4(\xi,\eta)}{\partial \eta} &= \frac{1}{4}(1-\xi).
\end{aligned} \tag{3.4.11}$$

It can be easily seen from Eq. (3.4.5) that $x_i = f_i(\xi,\eta)$, $(i = 1,2,3)$, are single valued continuous functions; Eq. (3.4.8) shows that $|J|$ is finite at any point (ξ,η), where $-1 \le \xi \le 1$, and $-1 \le \eta \le 1$. These two facts gives the sufficient conditions for the mapping in (3.4.5) to be one–to–one mapping. Then (3.4.4) becomes,

$$v = \int_{-1}^{1}\int_{-1}^{1} \hat{f}(\xi,\eta)|J(\xi,\eta)|\, d\xi d\eta, \tag{3.4.12}$$

where

$$\hat{f}(\xi,\eta) = f(\boldsymbol{x}(\xi,\eta), \boldsymbol{\xi}(\xi,\eta)). \tag{3.4.13}$$

From the Gauss Quadrature Scheme,

$$v = \sum_{i=1}^{N}\sum_{j=1}^{N} \hat{f}(\xi_i, \eta_i)|J(\xi_i, \eta_j)|\, \omega_i \omega_j, \tag{3.4.14}$$

where N^2 is the number of Gaussian Quadrature points; (ξ_i, η_j), and ω_i, ω_j, $(i, j = 1, \ldots, N)$, are the positions of the Gauss Quadrature points, and the weights. All the values used in the Gauss Quadrature Scheme can be obtained from [41].

Equation (3.4.14) is the result of the numerical integration of function $f(\boldsymbol{x}, \boldsymbol{\xi})$ over an arbitrary element $\mathcal{L}_{*_m}$. Therefore, the evaluation of all the components in $\left[\boldsymbol{H}^{lm}\right]$ and $\left[\boldsymbol{G}^{lm}\right]$ may follow suit.

3.5 Analytical Integration Of Kelvin Solution

This section gives the detailed formulation for the analytical integration of the Kelvin solution over an arbitrary flat-element in the Eulerian space. The formulation was originally outlined by Thomas A. Cruse in 1969. In the following sections, the indicial notation is used, i, j and k vary over 1, 2, and 3, and they will be specified otherwise. The displacement and the traction components of the Kelvin solution are as defined in (2.2.10),

$$\begin{aligned} u_j^i(\boldsymbol{x}, \boldsymbol{\xi}) &= \frac{1}{4\pi\mu r}\left[\frac{3-4\nu}{4(1-\nu)}\delta_{ij} + \frac{1}{4(1-\nu)} r_{,i} r_{,j}\right]; \\ t_j^i(\boldsymbol{x}; \boldsymbol{\xi}; \boldsymbol{n}) &= -\frac{1-2\nu}{8\pi(1-\nu)r^2}\left[\frac{\partial r}{\partial n}\left(\delta_{ij} + \frac{3}{1-2\nu} r_{,i} r_{,j}\right)\right] \\ &\quad + \frac{1-2\nu}{8\pi(1-\nu)r^2}(n_j r_{,i} - n_i r_{,j}). \end{aligned} \tag{3.5.15}$$

where

$$r = |\boldsymbol{x}| = \sqrt{{x_1}^2 + {x_2}^2 + {x_3}^2}, \tag{3.5.16}$$

the superscript i denotes the direction of the unit concentrated load; the subscript j indicates the component. For the convenience of the illustration, let the tractions be decomposed as follows,

$$t_j^i(\boldsymbol{x}, \boldsymbol{0}; \boldsymbol{n}) = t_j^{oi}(\boldsymbol{x}, \boldsymbol{0}; \boldsymbol{n}) + t_j^{*i}(\boldsymbol{x}, \boldsymbol{0}; \boldsymbol{n}), \tag{3.5.17}$$

where

$$\begin{aligned} t_j^{oi}(\boldsymbol{x}, \boldsymbol{0}; \boldsymbol{n}) &= -\frac{1-2\nu}{8\pi(1-\nu)r^2}\left[\frac{\partial r}{\partial n}\left(\delta_{ij} + \frac{3}{1-2\nu} r_{,i} r_{,j}\right)\right]; \\ t_j^{*i}(\boldsymbol{x}, \boldsymbol{0}; \boldsymbol{n}) &= \frac{1-2\nu}{8\pi(1-\nu)r^2}(n_j r_{,i} - n_i r_{,j}). \end{aligned} \tag{3.5.18}$$

The integrations of the displacement and the traction components of the Kelvin solution over an arbitrary flat-element $\triangle S$ are given as,

$$\begin{aligned} G_{ij} &= \iint_{\triangle S} u_j^i(\boldsymbol{x}; \boldsymbol{0})\, dA_{\boldsymbol{x}}; \\ \hat{H}_{ij}^o &= \iint_{\triangle S} t_j^{oi}(\boldsymbol{x}, \boldsymbol{0}; \boldsymbol{n})\, dA_{\boldsymbol{x}}; \\ \hat{H}_{ij}^* &= \iint_{\triangle S} t_j^{*i}(\boldsymbol{x}, \boldsymbol{0}; \boldsymbol{n})\, dA_{\boldsymbol{x}}, \end{aligned} \tag{3.5.19}$$

and

$$\hat{H}_{ij} = \hat{H}_{ij}^o + \hat{H}_{ij}^*. \tag{3.5.20}$$

For the sake of simplicity, a three noded element is chosen to demonstrate the process (Figure 3.5). The corners 1, 2 and 3 are located in the right-hand sense with respect to the normal at the element. The global Cartesian coordinate system is indicated by $X = \{0; \boldsymbol{e}_1, \boldsymbol{e}_2, \boldsymbol{e}_3\}$ with the axes x_1, x_2 and x_3 as shown in Figure 3.5.

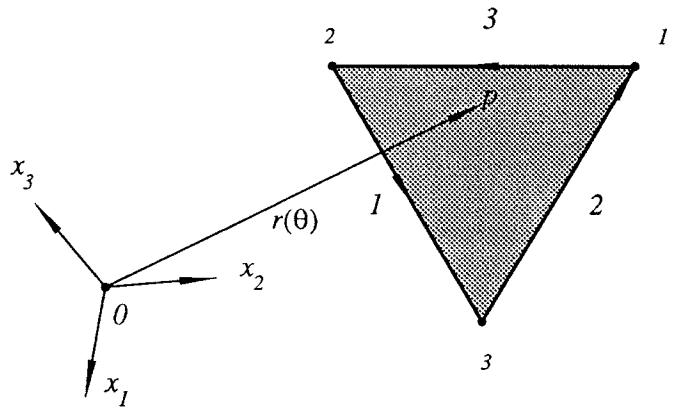

FIGURE 3.5 Orientation Of Element In Global Coordinate System

3.5.1 Local Coordinate System

Because of the complexity of the integrands, the direct analytical integration of the above integrals may not be obvious. However, as will be shown later, by using coordinate transformations, the above integrals can be reduced into the combinations of the standard elliptical or pseudo elliptical types of integrals, which are tabulated in [42].

Introduce a local coordinate system as shown in Figure 3.6, and denote this coordinate system as $Z = \{o; \iota_1, \iota_2, \iota_3\}$ with the axes ζ_1, ζ_2 and ζ_3. The local coordinate system is defined such that

1) the element $\triangle S$ is located in the $\zeta_1 - \zeta_2$ plane;

2) ζ_3-axis is chosen to be in the direction of the element normal, and the loading point $\boldsymbol{\xi} = \boldsymbol{0}$ is located on the ζ_3-axis. The intersection of the ζ_3-axis and the

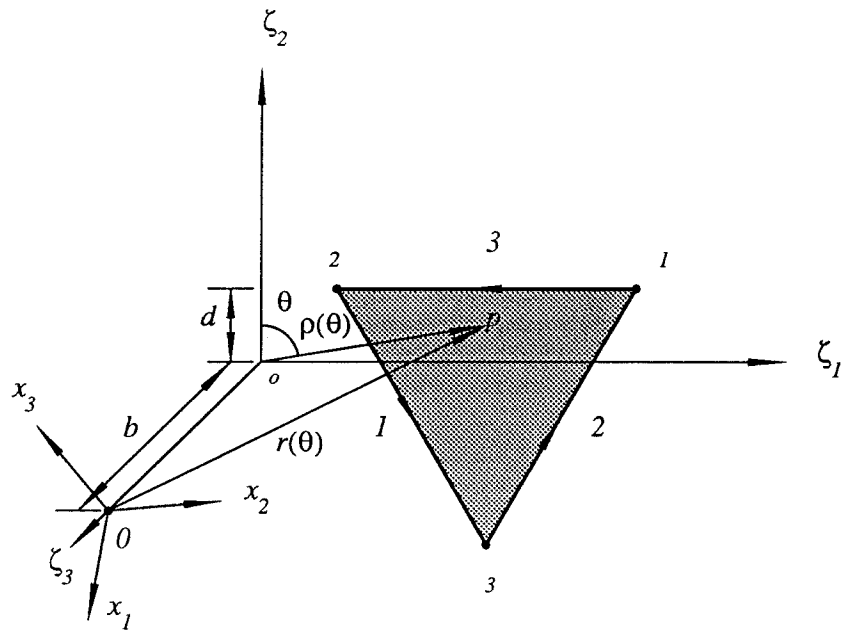

FIGURE 3.6 Orientation Of Element And Coordinate Systems

element plane determines the origin of the local coordinate system;

3) the edge 1–2 of the element is parallel to the ζ_1-axis and it goes in the direction of $-\boldsymbol{\iota}$ (unit vector along ζ_1).

The above conditions uniquely determine the local coordinate system. The shaded part is the element over which the Kelvin solution is to be integrated. Call the edge opposite vertex 3 $edge_3$; the edge opposite vertex 1 $edge_1$; and the edge opposite vertex 2 $edge_2$. Call the distance between the loading point and the element $\triangle S$ b: the distance between the projection o and the edge that determines the ζ_1-axis d: the angle between the line op and the axis ζ_2 θ, where p is an arbitrary point on the element $\triangle S$. It is important to notice that b is positive if the loading point is located in the side that the element normal is pointing, and negative otherwise. From Figure 3.6, it can be easily seen that

$$dA_{\boldsymbol{x}} = \rho d\rho d\theta,$$

and

$$r = \sqrt{\rho^2 + b^2}. \tag{3.5.21}$$

Then

$$r dr = \rho d\rho. \tag{3.5.22}$$

Define

$$k = \frac{|b|}{d^2 + b^2}, \qquad k' = \frac{|d|}{d^2 + b^2}, \tag{3.5.23}$$

Then

$$\frac{k}{k'} = \frac{|b|}{|d|}. \tag{3.5.24}$$

Define also,

$$\triangle = \sqrt{1 - k^2 \sin^2 \theta}. \tag{3.5.25}$$

By using the chain rule of partial differentiation,

$$r_{,i} = \frac{\partial r}{\partial \rho}\left(\frac{\partial \rho}{\partial \zeta_1}\varepsilon_{1i} + \frac{\partial \rho}{\partial \zeta_2}\varepsilon_{2i}\right) + \frac{\partial r}{\partial \zeta_3}\varepsilon_{3i}, \tag{3.5.26}$$

where ε_{1i}, ε_{2i} and ε_{3i} are the direction cosines of the ζ_1, ζ_2 and ζ_3 axes with respect to the global system. From simple geometry,

$$\frac{\partial \rho}{\partial \zeta_1} = \sin\theta; \qquad \frac{\partial \rho}{\partial \zeta_2} = \cos\theta; \qquad \frac{\partial \rho}{\partial \zeta_3} = -\frac{b}{r}, \tag{3.5.27}$$

and from (3.5.22)

$$\frac{\partial r}{\partial \rho} = \frac{\rho}{r}. \tag{3.5.28}$$

Then

$$r_{,i} = \frac{\rho}{r}(\sin\theta\ \varepsilon_{1i} + \cos\theta\ \varepsilon_{2i}) - \frac{b}{r}\varepsilon_{3i}. \tag{3.5.29}$$

Hence,

$$\begin{aligned} r_{,i}r_{,j} = \frac{\rho^2}{r^2}\Big[& \sin^2\theta\ \varepsilon_{1i}\varepsilon_{1j} + \cos^2\theta\ \varepsilon_{2i}\varepsilon_{2j} + \sin\theta\cos\theta(\varepsilon_{1i}\varepsilon_{2j} + \varepsilon_{2i}\varepsilon_{1j})\Big] \\ & + \frac{b^2}{r^2}\varepsilon_{3i}\varepsilon_{3j} - \frac{b\rho}{r^2}\Big[\sin\theta(\varepsilon_{1i}\varepsilon_{3j} + \varepsilon_{3i}\varepsilon_{1j}) + \cos\theta(\varepsilon_{2i}\varepsilon_{3j} + \varepsilon_{3i}\varepsilon_{2j})\Big]. \end{aligned} \tag{3.5.30}$$

Along the edge

$$\rho(\theta) = \frac{d}{\cos\theta}, \tag{3.5.31}$$

and

$$r(\theta) = \sqrt{b^2 + \frac{d^2}{\cos^2\theta}} = \frac{\rho(\theta)\triangle}{k'} = \frac{d}{\cos\theta}\frac{\triangle}{k'}. \tag{3.5.32}$$

3.5.2 Coordinate Transformations

Since the variable transformation will not alter the result of an integral, the first two integrals in (3.5.19) can be obtained by the following three steps. Because of the special property of $t_j^{*i}(\boldsymbol{x}, \boldsymbol{0}; \boldsymbol{n})$, the evaluation of $\hat{H}_{ij}^*$ will be discussed separately.

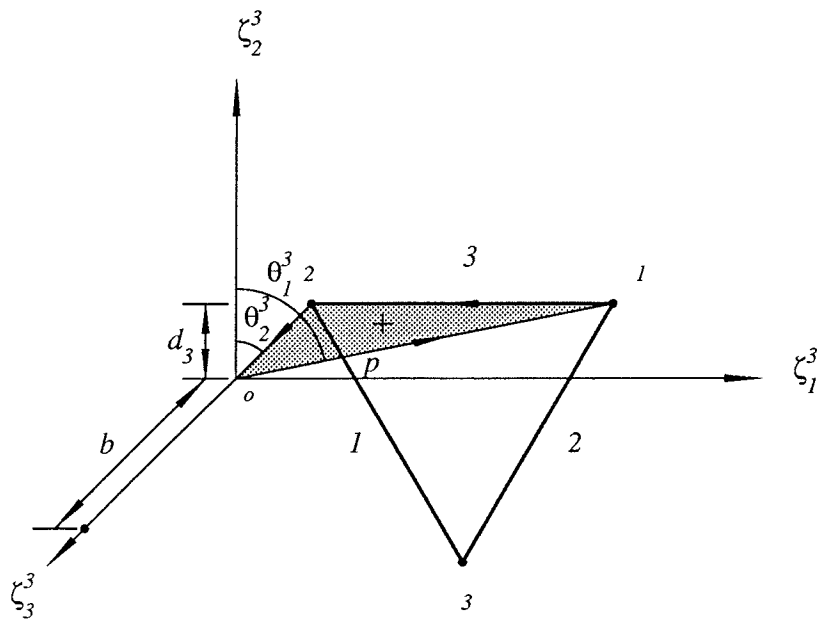

FIGURE 3.7a Integration Over $\triangle S_{12o}$

a) integrate the displacement and the traction components over the shaded triangular sub-area $\triangle S_{12o}$ as shown in Figure 3.7a. In this case, the local coordinate system is called

$$Z^3 = \{o; \boldsymbol{\iota}_1^3, \boldsymbol{\iota}_2^3, \boldsymbol{\iota}_3^3\}, \tag{3.5.33}$$

with the axes ζ_1^3, ζ_2^3 and ζ_3^3. Call the angle between line $o1$ and axis ζ_2^3 as θ_1^3, the angle between line $o2$ and axis ζ_2^3 as θ_2^3; the distance between the projection point o and the $edge_3$ as d_3. The integrals can then be expressed as,

$$\begin{aligned} G_{ij}^3 &= \iint_{\triangle S_{12o}} u_j^i(\boldsymbol{x}, \boldsymbol{0})\, dA_{\boldsymbol{x}} \\ &= \int_{\theta_1^3}^{\theta_2^3} \int_{|b|}^{r_3(\theta)} u_j^i(\boldsymbol{x}, \boldsymbol{0})\, r dr d\theta, \\ \hat{H}_{ij}^{o3} &= \iint_{\triangle S_{12o}} t_j^{oi}(\boldsymbol{x}, \boldsymbol{0}; \boldsymbol{n})\, dA_{\boldsymbol{x}} \\ &= \int_{\theta_1^3}^{\theta_2^3} \int_{|b|}^{r_3(\theta)} t_j^{oi}(\boldsymbol{x}, \boldsymbol{0}; \boldsymbol{n})\, r dr d\theta. \end{aligned} \tag{3.5.34}$$

The subscripts of $\triangle S$ are written in such a order that the direction marked by the subscripts coincides with that by the integration argument θ.

b) re-orient the ζ_1- and ζ_2- axes with respect to $edge_2$ according to 3), and then integrate the corresponding components over the shaded triangular sub-area $\triangle S_{23o}$ as shown in Figure 3.7b. Call the local coordinate system here

$$Z^2 = \{o; \boldsymbol{\iota}_1^2, \boldsymbol{\iota}_2^2, \boldsymbol{\iota}_3^2\}, \tag{3.5.35}$$

with the axes ζ_1^2, ζ_2^2 and ζ_3^2. Call the angle between line $o3$ and axis ζ_2^2 as θ_3^2, the angle between line $o1$ and axis ζ_2^2 as θ_1^2; the distance between the point o

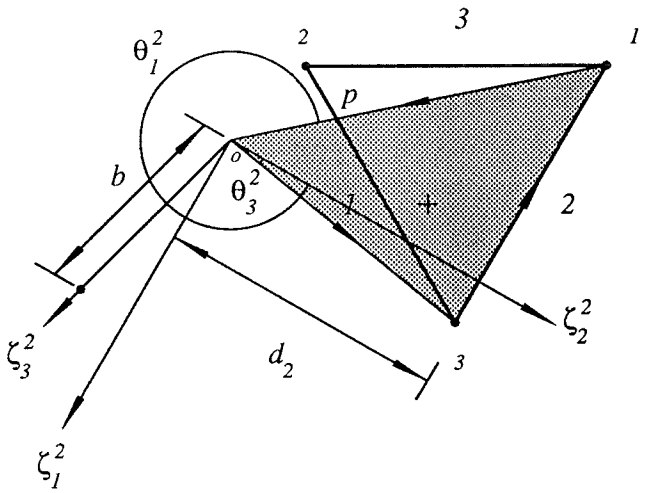

FIGURE 3.7b Integration Over $\triangle S_{31o}$

and the $edge_2$ as d_2. The integrals are then given by,

$$\begin{aligned} G_{ij}^2 &= \iint_{\triangle S_{31o}} u_j^i(\boldsymbol{x}, \boldsymbol{0})\, dA_{\boldsymbol{x}} \\ &= \int_{\theta_3^2}^{\theta_1^2} \int_{|b|}^{r_2(\theta)} u_j^i(\boldsymbol{x}, \boldsymbol{0})\, r dr d\theta, \end{aligned} \tag{3.5.36}$$

$$\begin{aligned} \hat{H}_{ij}^{o2} &= \iint_{\triangle S_{31o}} t_j^{oi}(\boldsymbol{x}, \boldsymbol{0}; \boldsymbol{n})\, dA_{\boldsymbol{x}} \\ &= \int_{\theta_3^2}^{\theta_1^2} \int_{|b|}^{r_2(\theta)} t_j^{oi}(\boldsymbol{x}, \boldsymbol{0}; \boldsymbol{n})\, r dr d\theta. \end{aligned}$$

c) re-orient the ζ_1- and ζ_2- axes with respect to $edge_1$ according to 3), and then integrate corresponding components over the shaded triangular sub-area $\triangle S_{31o}$ as shown in Figure 3.7c. The local coordinate system is expressed by

$$Z^1 = \{o; \boldsymbol{\iota}_1^1, \boldsymbol{\iota}_2^1, \boldsymbol{\iota}_3^1\}, \tag{3.5.37}$$

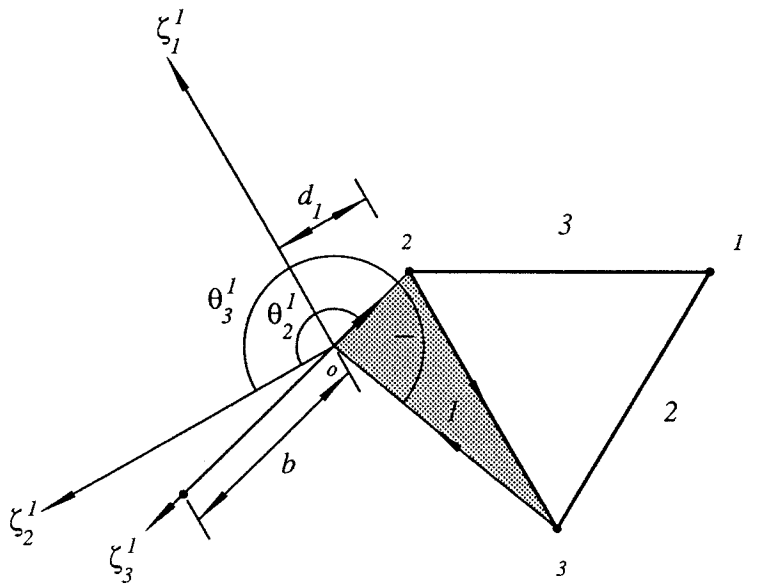

FIGURE 3.7c Integration Over $\triangle S_{23o}$

with the axes ζ_1^1, ζ_2^1 and ζ_3^1. Call the angle between line $o2$ and axis ζ_2^1 as θ_2^1, the angle between line $o3$ and axis ζ_2^1 as θ_3^1; the distance between the projection point o and the $edge_1$ as d_1. The integrations over the shaded area can now be written as,

$$\begin{aligned} G_{ij}^1 &= \iint_{\triangle S_{23o}} u_j^i(\boldsymbol{x}, \boldsymbol{0})\, dA_{\boldsymbol{x}} \\ &= \int_{\theta_3^1}^{\theta_2^1} \int_{|b|}^{r_1(\theta)} u_j^i(\boldsymbol{x}, \boldsymbol{0})\, r dr d\theta; \end{aligned} \tag{3.5.38}$$

$$\begin{aligned} \hat{H}_{ij}^{o1} &= \iint_{\triangle S_{23o}} t_j^{oi}(\boldsymbol{x}, \boldsymbol{0}; \boldsymbol{n})\, dA_{\boldsymbol{x}} \\ &= \int_{\theta_3^1}^{\theta_2^1} \int_{|b|}^{r_1(\theta)} t_j^{oi}(\boldsymbol{x}, \boldsymbol{0}; \boldsymbol{n})\, r dr d\theta. \end{aligned}$$

As shown by the shaded areas, the components of the Kelvin solution has been integrated once over the triangular sub–area $\triangle S_{32o}$, and the second time over the triangular sub-area $\triangle S_{23o}$. The sum of the two integral over $\triangle S_{320}$ and the integral

over $\triangle S_{230}$ vanishes. This can be illustrated as follows,

let p denote the intersection of lines $o1$ and 23. Case 1, the components of the Kelvin solution is integrated over the sub-area $\triangle S_{32o}$ through

$$\begin{aligned}\iint_{\triangle S_{32o}} u_j^i(\boldsymbol{x},\boldsymbol{0})\,dA_{\boldsymbol{x}} = &\iint_{\triangle S_{p2o}} u_j^i(\boldsymbol{x},\boldsymbol{0})\,dA_{\boldsymbol{x}} \\ &+ \iint_{\triangle S_{3po}} u_j^i(\boldsymbol{x},\boldsymbol{0})\,dA_{\boldsymbol{x}},\end{aligned} \tag{3.5.39}$$

$$\begin{aligned}\iint_{\triangle S_{32o}} t_j^{oi}(\boldsymbol{x},\boldsymbol{0};\boldsymbol{n})\,dA_{\boldsymbol{x}} = &\iint_{\triangle S_{p2o}} t_j^{oi}(\boldsymbol{x},\boldsymbol{0};\boldsymbol{n})\,dA_{\boldsymbol{x}} \\ &+ \iint_{\triangle S_{3po}} t_j^{oi}(\boldsymbol{x},\boldsymbol{0};\boldsymbol{n})\,dA_{\boldsymbol{x}},\end{aligned}$$

where, $\triangle S_{p2o}$ is a part of the area of $\triangle S_{12o}$ as shown in Figure 3.7a; while $\triangle S_{3po}$ is a part of the area of $\triangle S_{31o}$ as shown in Figure 3.7b.

Case 2, the components of the Kelvin Solution is integrated over the sub-area $\triangle S_{23o}$ as shown in Figure 3.7c and (3.5.38).

In both cases, the components of the Kelvin solution are the same, and the integration argument θ sweeps through the same angular range. However, in both cases, θ is opposite in signs. Therefore,

$$\begin{aligned}\iint_{\triangle S_{p2o}} u_j^i(\boldsymbol{x},\boldsymbol{0})\,dA_{\boldsymbol{x}} + &\iint_{\triangle S_{3po}} u_j^i(\boldsymbol{x},\boldsymbol{0})\,dA_{\boldsymbol{x}} \\ &+ \iint_{\triangle S_{23o}} u_j^i(\boldsymbol{x},\boldsymbol{0})\,dA_{\boldsymbol{x}} = 0;\end{aligned} \tag{3.5.40}$$

$$\begin{aligned}\iint_{\triangle S_{p2o}} t_j^{oi}(\boldsymbol{x},\boldsymbol{0};\boldsymbol{n})\,dA_{\boldsymbol{x}} + &\iint_{\triangle S_{3po}} t_j^{oi}(\boldsymbol{x},\boldsymbol{0};\boldsymbol{n})\,dA_{\boldsymbol{x}} \\ &+ \iint_{\triangle S_{23o}} t_j^{oi}(\boldsymbol{x},\boldsymbol{0};\boldsymbol{n})\,dA_{\boldsymbol{x}} = 0.\end{aligned}$$

So, the result of (3.5.19) can be written as,

$$\begin{aligned} G_{ij} &= G^1_{ij} + G^2_{ij} + G^3_{ij}; \\ \hat{H}^o_{ij} &= \hat{H}^{o1}_{ij} + \hat{H}^{o2}_{ij} + \hat{H}^{o3}_{ij}. \end{aligned} \tag{3.5.41}$$

3.5.3 Evaluation Of Integrals In G_{ij} And $\hat{H}^o_{ij}$

The advantage of placing the local coordinate system in the way shown is that all the components of the Kelvin solution can be expressed by the known arguments b, d, θ, etc. All the integrations can be computed by the use of the tables of integrals of elliptical type or pseudo elliptical type. Examining the G^1_{ij}, G^2_{ij} and G^3_{ij} closely, it can be easily seen that all the integrals have the same structures. This observation is also true for $\hat{H}^{o1}_{ij}$, $\hat{H}^{o2}_{ij}$ and $\hat{H}^{o3}_{ij}$. Thus, if the expressions for G^3_{ij} and $\hat{H}^{o3}_{ij}$ are obtained, the others can follow suit by changing the variables d, b, and θ to the appropriate ones. This section is devoted to the derivation of the expressions for G^3_{ij} and $\hat{H}^{o3}_{ij}$. By substituting $u^i_j(\boldsymbol{x}, \boldsymbol{0})$ in equation (3.5.15) and $t^{oi}_j(\boldsymbol{x}, \boldsymbol{0}; \boldsymbol{n})$ in equation (3.5.18), G^3_{ij} and $\hat{H}^{o3}_{ij}$ can be written as,

$$\begin{aligned} G^3_{ij} = -\frac{1}{4\pi\mu} \int_{\theta^3_1}^{\theta^3_2} d\theta \int_{\bar{e}}^{r_3(\theta)} \Bigg(& \frac{(3-4\nu)}{4(1-\nu)}\delta_{ij} \\ & + \frac{1}{4(1-\nu)} \Bigg\{ \frac{\rho^2}{r^2}\sin^2\theta e_{1i}e_{1j} + \frac{\rho^2}{r^2}\cos^2\theta e_{2i}e_{2j} \\ & + \frac{\rho^2}{r^2}\sin\theta\cos\theta(e_{1i}e_{2j} + e_{2i}e_{1j}) + \frac{e^2}{r^2}e_{3i}e_{3j} \\ & - \frac{e\rho}{r^2}\sin\theta(e_{1i}e_{3j} + e_{3i}e_{1j}) - \frac{e\rho}{r^2}\cos\theta(e_{2i}e_{3j} + e_{3i}e_{2j}) \Bigg\} \Bigg) dr; \end{aligned}$$

$$\begin{aligned} \hat{H}^{o3}_{ij} = -\frac{1-2\nu}{8\pi(1-\nu)} \int_{\theta^3_1}^{\theta^3_2} d\theta \int_{\bar{e}}^{r_3(\theta)} \Bigg(& \frac{e}{r^2}\delta_{ij} \\ & + \frac{3}{1-2\nu} \Bigg\{ \frac{e\rho^2}{r^4}\sin^2\theta e_{1i}e_{1j} + \frac{e\rho^2}{r^4}\cos^2\theta e_{2i}e_{2j} \end{aligned}$$

$$+\frac{e\rho^2}{r^4}\sin\theta\cos\theta(e_{1i}e_{2j}+e_{2i}e_{1j})+\frac{e^3}{r^4}e_{3i}e_{3j}$$
$$-\frac{e^2\rho}{r^4}\sin\theta(e_{1i}e_{3j}+e_{3i}e_{1j})-\frac{e^2\rho}{r^4}\cos\theta(e_{2i}e_{3j}+e_{3i}e_{2j})\Bigg\}\Bigg)\,dr. \tag{3.5.42}$$

For the sake of simplicity of later discussion, define each term in the above two expressions as follows,

$$\begin{aligned}
I^3_{G_1}(\theta) &= \int d\theta\int_{\bar{e}}^{r_3(\theta)} dr \\
I^3_{G_2}(\theta) &= \int \sin^2\theta\, d\theta \int_{\bar{e}}^{r_3(\theta)} \frac{\rho^2}{r^2}\, dr; \\
I^3_{G_3}(\theta) &= \int \cos^2\theta\, d\theta \int_{\bar{e}}^{r_3(\theta)} \left(1-\frac{e^2}{r^2}\right) dr; \\
I^3_{G_4}(\theta) &= \int \sin\theta\cos\theta\, d\theta \int_{\bar{e}}^{r_3(\theta)} \left(1-\frac{e^2}{r^2}\right) dr; \\
I^3_{G_5}(\theta) &= \int d\theta \int_{\bar{e}}^{r_3(\theta)} \frac{e^2}{r^2}\, dr; \\
I^3_{G_6}(\theta) &= \int \sin\theta\, d\theta \int_{\bar{e}}^{r_3(\theta)} \frac{e\rho}{r^2}\, dr; \\
I^3_{G_7}(\theta) &= \int \cos\theta\, d\theta \int_{\bar{e}}^{r_3(\theta)} \frac{e\rho}{r^2}\, dr,
\end{aligned} \tag{3.5.43}$$

and

$$\begin{aligned}
I^3_{H_1}(\theta) &= \int d\theta \int_{\bar{e}}^{r_3(\theta)} \frac{e}{r^2}\, dr; \\
I^3_{H_2}(\theta) &= \int \sin^2\theta d\theta \int_{\bar{e}}^{r_3(\theta)} \frac{e\rho^2}{r^4}\, dr; \\
I^3_{H_3}(\theta) &= \int \cos^2\theta d\theta \int_{\bar{e}}^{r_3(\theta)} \frac{e(r^2-e^2)}{r^4}\, dr; \\
I^3_{H_4}(\theta) &= \int \sin\theta\cos\theta\, d\theta \int_{\bar{e}}^{r_3(\theta)} \frac{e(r^2-e^2)}{r^4}\, dr; \\
I^3_{H_5}(\theta) &= \int d\theta \int_{\bar{e}}^{r_3(\theta)} \frac{e^3}{r^4}\, dr; \\
I^3_{H_6}(\theta) &= \int \sin\theta\, d\theta \int_{\bar{e}}^{r_3(\theta)} \frac{e^2\rho}{r^4}\, dr; \\
I^3_{H_7}(\theta) &= \int \cos\theta\, d\theta \int_{\bar{e}}^{r_3(\theta)} \frac{e^2\rho}{r^4}\, dr.
\end{aligned} \tag{3.5.44}$$

Then the integrations of the Kelvin solution over the triangular sub-area $\triangle S_{12o}$ as shown in Figure 3.7a can be written as,

$$
\begin{aligned}
G^3_{ij} = &-\frac{1}{4\pi\mu}\Bigg\{\frac{3-4\nu}{4(1-\nu)} I^3_{G_1}(\theta)\delta_{ij} \\
&+ \frac{1}{4(1-\nu)}\Big[I^3_{G_2}(\theta)\,\varepsilon_{1i}\varepsilon_{1j} + I^3_{G_3}(\theta)\varepsilon_{2i}\varepsilon_{2j} + I^3_{G_4}(\theta)(\varepsilon_{1i}\varepsilon_{2j} + \varepsilon_{2i}\varepsilon_{1j}) \\
&+ I^3_{G_5}(\theta)\,\varepsilon_{3i}\varepsilon_{3j} - I^3_{G_6}(\theta)(\varepsilon_{1i}\varepsilon_{3j} + \varepsilon_{3i}\varepsilon_{1j}) - I^3_{G_7}(\theta)(\varepsilon_{2i}\varepsilon_{3j} + \varepsilon_{3i}\varepsilon_{2j})\Big]\Bigg\}\Bigg|_{\theta^3_1}^{\theta^3_2};
\end{aligned}
$$

$$
\begin{aligned}
\hat{H}^{o3}_{ij} = &-\frac{1-2\nu}{8\pi(1-\nu)}\Bigg\{I^3_{H_1}(\theta)\delta_{ij} \\
&+ \frac{3}{1-2\nu}\Big[I^3_{H_2}(\theta)\,\varepsilon_{1i}\varepsilon_{1j} + I^3_{H_3}(\theta)\,\varepsilon_{2i}\varepsilon_{2j} + I^3_{H_4}(\theta)(\varepsilon_{1i}\varepsilon_{2j} + \varepsilon_{2i}\varepsilon_{1j}) \\
&+ I^3_{H_5}(\theta)\varepsilon_{3i}\varepsilon_{3j} - I^3_{H_6}(\theta)(\varepsilon_{1i}\varepsilon_{3j} + \varepsilon_{3i}\varepsilon_{1j}) - I^3_{G_7}(\theta)(\varepsilon_{2i}\varepsilon_{3j} + \varepsilon_{3i}\varepsilon_{2j})\Big]\Bigg\}\Bigg|_{\theta^3_1}^{\theta^3_2}.
\end{aligned}
\tag{3.5.45}
$$

In the results shown below, the superscript 3 of θ^3_1 and θ^3_2 and the subscript 3 d_3, $\triangle_3$, k_3 and k'_3 are left out for simplicity. We write

$$
\begin{aligned}
d \to d_3, \qquad & \triangle \to \triangle_3; \\
k \to k_3, \qquad & k' \to k'_3; \\
\theta_1 \to \theta^3_1, \qquad & \theta_2 \to \theta^3_2.
\end{aligned}
\tag{3.5.46}
$$

Using equations (3.5.31) and (3.5.32) and evaluating equations (3.5.43) and (3.5.44), one has,

$$
\begin{aligned}
I^3_{G_1}(\theta) &= \frac{d}{2}\ln\Big(\frac{\triangle + k'\sin\theta}{\triangle - k'\sin\theta}\Big) + \mathrm{sgn}(d)\;|b|\sin^{-1}(k\sin\theta) - |b|\theta; \\
I^3_{G_2}(\theta) &= -d\Big(\frac{\triangle}{k'}\Big)\sin\theta + \mathrm{sgn}(d)|b|\sin^{-1}(k\sin\theta) \\
&\quad + \frac{d}{2}\ln\Big(\frac{\triangle + k'\sin\theta}{\triangle - k'\sin\theta}\Big) - |b|\Big(\theta - \frac{1}{2}\sin 2\theta\Big);
\end{aligned}
$$

$$
\begin{aligned}
I^3_{G_3}(\theta) &= |b|\frac{\mathrm{sgn}(d)}{k}\triangle\sin\theta + \mathrm{sgn}(d)|b|\sin^{-1}(k\sin\theta) \\
&\quad - |b|(\theta + \frac{1}{2}\sin 2\theta); \\
I^3_{G_4}(\theta) &= -\frac{d}{k'}\triangle\cos\theta - |b|\sin^2\theta; \\
I^3_{G_5}(\theta) &= |b|\Big\{\theta - \mathrm{sgn}(d)\sin^{-1}(k\sin\theta)\Big\}; \\
I^3_{G_6}(\theta) &= \frac{bk'}{k}\ln(k\cos\theta+\triangle) - \mathrm{sgn}(b)d\ln\Big(\frac{|b|\cos\theta}{d} + \frac{\triangle}{k'}\Big) \\
&\quad + b\cos\theta\Big(\ln\frac{|b|k'\cos\theta}{d(k'+\triangle)}\Big); \\
I^3_{G_7}(\theta) &= -\frac{b}{2}\ln\Big(\frac{1+\sin\theta}{1-\sin\theta}\Big) + b\sin\theta\ln\Big(\frac{1+\triangle/k'}{|b|\cos\theta/d}\Big) \\
&\quad + \mathrm{sgn}(\theta)b\ln\Big(\frac{1+k'\triangle+k^2|\sin\theta|}{k'+\triangle}\Big),
\end{aligned}
\tag{3.5.47}
$$

and

$$
\begin{aligned}
I^3_{H_1}(\theta) &= \mathrm{sgn}(b)\Big\{\theta - \mathrm{sgn}(d)\sin^{-1}(k\sin\theta)\Big\}; \\
I^3_{H_2}(\theta) &= \frac{bk'}{d}\cos^2\theta\frac{\sin\theta}{3\triangle} - \frac{bk'}{3dk}\sin^{-1}(k\sin\theta) \\
&\quad + \frac{1}{3}\mathrm{sgn}(b)(\theta - \frac{1}{2}\sin 2\theta); \\
I^3_{H_3}(\theta) &= \frac{bk'}{3d}(k^2 - 1 - \cos^2\theta)\frac{\sin\theta}{\triangle} - \frac{bk'}{3dk}\sin^{-1}(k\sin\theta) \\
&\quad + \frac{1}{3}\mathrm{sgn}(b)(\theta + \frac{1}{2}\sin 2\theta); \\
I^3_{H_4}(\theta) &= \frac{bk'}{d}\frac{\cos^3\theta}{3\triangle} + \frac{1}{3}\mathrm{sgn}(b)\sin^2\theta; \\
I^3_{H_5}(\theta) &= \frac{1}{3}\Big\{\mathrm{sgn}(b)\theta + \frac{k'^3 b\sin\theta}{d\triangle} \\
&\quad - \mathrm{sgn}(b)\mathrm{sgn}(d)\sin^{-1}(k\sin\theta)\Big\}; \\
I^3_{H_6}(\theta) &= -\frac{k'\cos\theta}{3\triangle}; \\
I^3_{H_7}(\theta) &= \frac{k'^3\sin\theta}{3\triangle},
\end{aligned}
\tag{3.5.48}
$$

where

$$
\mathrm{sgn}(e) = \frac{b}{|b|}, \quad \mathrm{sgn}(d) = \frac{d}{|d|}, \quad \mathrm{sgn}(\theta) = \frac{\sin\theta}{|\sin\theta|}. \tag{3.5.49}
$$

The physical meaning of $b \neq 0$ is that the unit concentrated load is applied at a point away from the element. Theoretically, the displacement and the traction components are not singular with respect to the points on the element. Thus, the above integrals can be computed without any problem.

However, when the unit concentrated load is applied on the element, $b = 0$, the displacement and the traction components are both singular at the point of application of the load. Therefore, special care has to be taken in order to evaluate the above integrals correctly. In stead of taking b as 0, a limiting process is employed such that the integrals are evaluated as the limit case as $b \to 0$. In this case, $\bar{k} \to 0$, $k' \to 1$, and $\triangle \to 1$ as $b \to 0$. By taking limits of the integrals in (3.5.47) and (3.5.48), the following is obtained,

$$\begin{aligned}
I^3_{G_1}(\theta) &= \frac{d}{2}\ln\Big(\frac{1+\sin\theta}{1-\sin\theta}\Big);\\
I^3_{G_2}(\theta) &= \frac{d}{2}\ln\Big(\frac{1+\sin\theta}{1-\sin\theta}\Big) - d\sin\theta;\\
I^3_{G_3}(\theta) &= d\sin\theta;\\
I^3_{G_4}(\theta) &= -d\cos\theta;\\
I^3_{G_5}(\theta) &= I^3_{G_6}(\theta) = I^3_{G_7}(\theta) = 0.
\end{aligned} \tag{3.5.50}$$

Since $\partial r/\partial n = 0$ when the loading point is on the element, $t^{oi}_j(\boldsymbol{x}, \boldsymbol{0}; \boldsymbol{n}) = 0$ from (3.5.18). Thus,

$$I^3_{H_1}(\theta) = I^3_{H2}(\theta) = I^3_{H3}(\theta) = I^3_{H4}(\theta) = I^3_{H5}(\theta) = I^3_{H6}(\theta) = I^3_{H7}(\theta) = 0. \tag{3.5.51}$$

Therefore, the full expressions of G^3_{ij} and $\hat{H}^{o3}_{ij}$ can be obtained by substituting (3.5.50) and (3.5.51) or (3.5.47) and (3.5.48) into (3.5.45) depending on whether the loading point is on or off the element.

G^2_{ij}, $\hat{H}^{o2}_{ij}$ and G^1_{ij}, $\hat{H}^{o1}_{ij}$ can be obtained in the similar manner by following step b) and step c), respectively.

3.5.4 Evaluation of $\hat{H}^*_{ij}$

In general,

$$\hat{H}^*_{ij} = \iint_{\triangle S} \frac{1-2\nu}{8\pi(1-\nu)r^2}(n_j r_{,i} - n_i r_{,j})\, dA_{\boldsymbol{x}}. \tag{3.5.52}$$

Since

$$\frac{1}{r^2}(n_i r_{,j} - n_j r_{,i}) = \epsilon_{ijk}\epsilon_{rsk} n_r \Big(\frac{1}{r}\Big)_{,s}, \tag{3.5.53}$$

By using direct application of the divergence theorem, $\hat{H}^*_{ij}$ can be written as

$$\begin{aligned} \hat{H}^*_{ij} &= \frac{1-2\nu}{8\pi(1-\nu)}\epsilon_{ijk} \oint \epsilon_{rsk} n_r \Big(\frac{1}{r}\Big)_{,s}\, ds \\ &= \frac{1-2\nu}{8\pi(1-\nu)}\epsilon_{ijk} \oint \frac{1}{r}\, dx_k, \end{aligned} \tag{3.5.54}$$

where

$$dx_k = \varepsilon_{1k} d\zeta_1 + \varepsilon_{2k} d\zeta_2 + \varepsilon_{3k} d\zeta_3, \tag{3.5.55}$$

and $\oint$ stands for the line integration along the outside edges of the element $\triangle S$. Thus,

$$\hat{H}^*_{ij} = \frac{1-2\nu}{8\pi(1-\nu)}\epsilon_{ijk}\left(\int_1^2 \frac{1}{r}dx_k + \int_2^3 \frac{1}{r}dx_k + \int_3^1 \frac{1}{r}dx_k\right). \tag{3.5.56}$$

The above integrations can be evaluated easily by using the local coordinate systems introduced before, see Figures 7a, 7b and 7c. In particular, on the $edge_3$, see Figure 3.7a, $d\zeta^3_2 = d\zeta^3_3 = 0$, then $dx_k = \varepsilon^3_{1k} d\zeta^3_1$, where ε^3_{1k} are the direction cosines of the ζ^3_1−axis with respect to the global coordinate system.

$$\begin{aligned} \int_1^2 \frac{1}{r}dx_k &= \frac{1-2\nu}{8\pi(1-\nu)}\epsilon_{ijk}\int_1^2 \frac{\varepsilon^3_{1k} d\zeta_1}{\sqrt{b^2 + (\zeta^3_1)^2 + (\zeta^3_2)^2}} \\ &= \frac{1-2\nu}{8\pi(1-\nu)}\epsilon_{ijk}\varepsilon^3_{1k} \ln(\zeta^3_1 + r_3)\Big|_1^2. \end{aligned} \tag{3.5.57}$$

On the $edge_2$, see Figure 3.7b, $d\zeta_2^2 = d\zeta_3^2 = 0$, then $dx_k = \varepsilon_{1k}^2 d\zeta_1^2$, where ε_{1k}^2 has a similar meaning as ε_{1k}^3. Then

$$\begin{aligned}\int_3^1 \frac{1}{r} dx_k =& \frac{1-2\nu}{8\pi(1-\nu)} \epsilon_{ijk} \int_3^1 \frac{\varepsilon_{1k}^2 d\zeta_1}{\sqrt{b^2 + (\zeta_1^2)^2 + (\zeta_2^2)^2}} \\ =& \frac{1-2\nu}{8\pi(1-\nu)} \epsilon_{ijk} \varepsilon_{1k}^2 \ln(\zeta_1^2 + r_2)\Big|_3^1.\end{aligned} \tag{3.5.58}$$

On the $edge_1$, see Figure 3.7c, $d\zeta_2^1 = d\zeta_3^1 = 0$, then $dx_k = \varepsilon_{1k}^1 d\zeta_1^1$. Thus,

$$\begin{aligned}\int_2^3 \frac{1}{r} dx_k =& \frac{1-2\nu}{8\pi(1-\nu)} \epsilon_{ijk} \int_2^3 \frac{\varepsilon_{1k}^1 d\zeta_1}{\sqrt{b^2 + (\zeta_1^1)^2 + (\zeta_2^1)^2}} \\ =& \frac{1-2\nu}{8\pi(1-\nu)} \epsilon_{ijk} \varepsilon_{1k}^1 \ln(\zeta_1^1 + r_1)\Big|_2^3.\end{aligned} \tag{3.5.59}$$

Thus,

$$\hat{H}_{ij}^* = \frac{1-2\nu}{8\pi(1-\nu)} \epsilon_{ijk} \Big(\varepsilon_{1k}^1 \ln(\zeta_1^1 + r_1)\Big|_2^3 + \varepsilon_{1k}^2 \ln(\zeta_1^2 + r_2)\Big|_3^1 + \varepsilon_{1k}^3 \ln(\zeta_1^3 + r_3)\Big|_1^2 \Big). \tag{3.5.60}$$

Having obtained the expressions for G_{ij}^3, G_{ij}^2, G_{ij}^1 and $\hat{H}_{ij}^{o3}$, $\hat{H}_{ij}^{o2}$, $\hat{H}_{ij}^{o1}$, the integration of the Kelvin solution over an arbitrary element $\triangle S$, as show in Figure 3.6, can be given as,

$$\begin{aligned} G_{ij} =& \quad G_{ij}^3 + G_{ij}^2 + G_{ij}^1; \\ \hat{H}_{ij} =& \quad \hat{H}_{ij}^{o3} + \hat{H}_{ij}^{o2} + \hat{H}_{ij}^{o1} + \hat{H}_{ij}^*. \end{aligned} \tag{3.5.61}$$

Thus, the evaluation of the integrations of the Kelvin solution over an arbitrary element is now completed.

3.5.5 Compare Matrix Results Of Proposed Procedure With Pure Numerical Integration With Subdivisions

Because the integrands of the numerical integral in (3.4.1) do not vary very much with distance due to the subtraction of "singularities", a few Gaussian points are expected to capture the variation well. The analytical part of the solution can be obtained accurately. Therefore, by using the proposed procedure, the components of the matrices $[H_{ij}]$ and $[G_{ij}]$, $(i, j = 1, 2, 3)$, can be evaluated with good accuracy using only a few Gaussian Quadrature Points.

The above argument can be verified by direct calculation using many Gaussian Quadrature points in an element. One way to do this is to subdivide the element if the fundamental solution is expected to vary highly in it. The rules for subdividing the most commonly used three-noded and four-noded elements are set as follows,

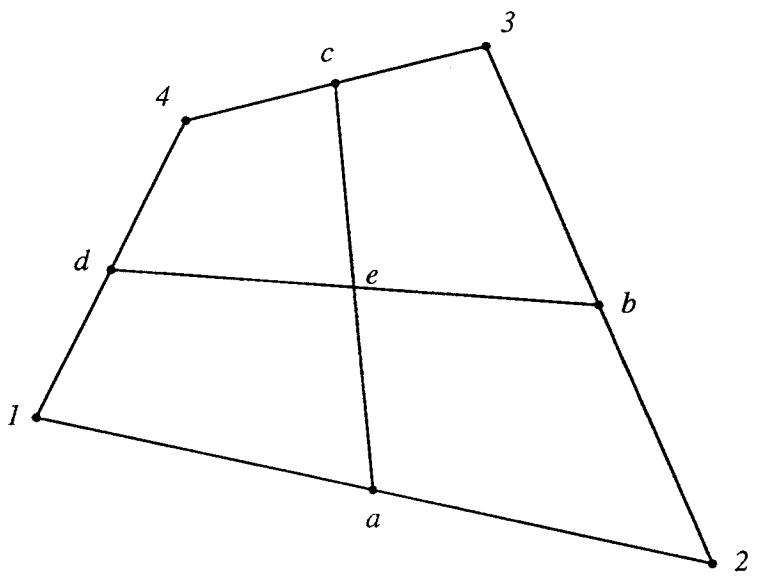

FIGURE 3.8 Subdivision Of An Element With Four Nodes

1) find the mid-points on the edges of an element, i.e., a, b, c, and d for an element with four nodes, or a, b and c for an element with three nodes;

2) connect the mid-points on the opposite edges as shown in Figures 8 and 9.

Several criteria have to be used in order to control the subdivision process.

1) the *length* criterion:

The subdivision stops if the distance between the loading point and the element is larger than or equal to C_{length} (a prechosen number) times the length of the smallest edge of the subdivided element.

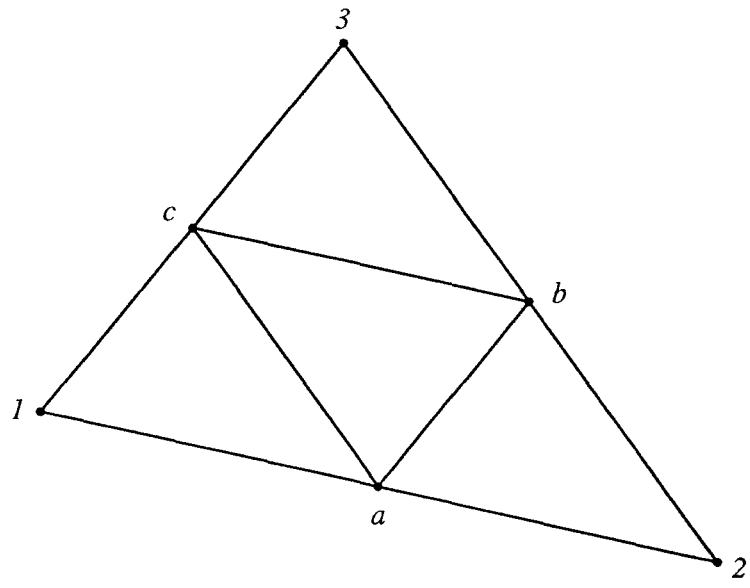

FIGURE 3.9 Subdivision Of An Element With Three Nodes

2) the *area* criterion:

The subdivision stops if the area of the smallest subdivided element is less than or equal to C_{area} (a prechosen number) times the area of the original element.

3) the above two criteria may both be in effect at the same time, such as in the case when the loading point is on an element or close to it.

An element is then subdivided into sub-elements. It is important to point out that both criteria must be compatible, otherwise, the singularity property of the fundamental solution can not be captured. The compatability of the two criteria means also that the above two criteria are not independent, i.e., if one criterion is specified, the other criterion can be derived. This can be done by the following

simple calculation. Let

d : be the distance between the loading point and the element;

L : be the typical length of the undivided element;

l : be the typical length of the smallest subdivided element;

C_{length} : be the designated number for length criterion, and

C_{area} : be the designated number for area criterion.

then the area of the undivided element is of the order of L^2, and the area of the smallest subdivided element is of the order of l^2. From the length criterion,

$$l = \frac{d}{C_{length}}. \tag{3.5.62}$$

while from the area criterion,

$$l^2 = C_{area} \times L^2. \tag{3.5.63}$$

In order for the two criteria to be imposed properly, the following equations has to be satisfied,

$$\left(\frac{d}{C_{length}}\right)^2 = C_{area} \times L^2, \tag{3.5.64}$$

thus

$$C_{area} = \left(\frac{d}{L \times C_{length}}\right)^2. \tag{3.5.65}$$

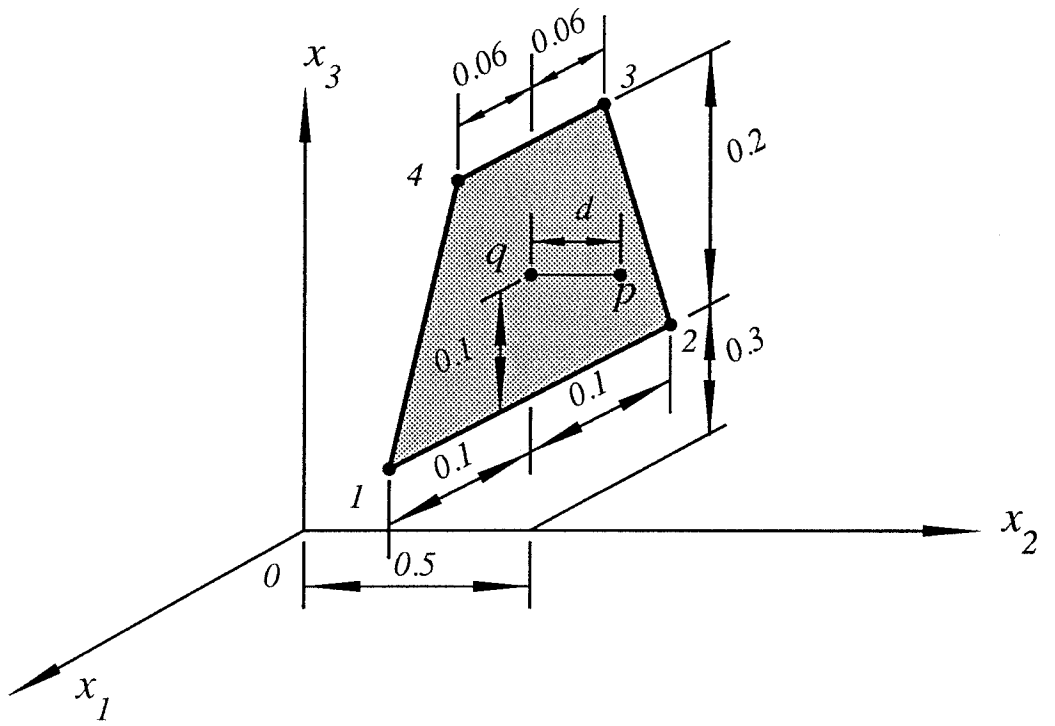

FIGURE 3.10 Dimensions of Test Element

3.5.6 Test Problem

In the example, a four-noded element, as shown in Figure 3.10, is chosen to demonstrate the accuracy of the proposed procedure. This process consists of two steps,

a) the matrices $[G_{ij}]$ and $[H_{ij}]$, using only the Kelvin solution, are evaluated over the element show in Figure 3.10 with both the analytical calculation and numerical calculation with subdivisions. The correctness of the subdivision scheme is established by comparing the analytical and the numerical results;

b) the matrices $[G_{ij}]$ and $[H_{ij}]$, using the fundamental solution of the infinite plate problem, are evaluated over the same element with the proposed procedure and the numerical calculation with the same subdivision scheme. The

correctness of the proposed procedure is shown by comparing the results of the two calculations.

In Figure 3.10, point p is the point at which the unit concentrated load is acting; while point q is the projection of p along the direction of the element-normal onto the element. Eight subdivision cases are shown for different distances d between the loading point and the element. The length criterion is set as $C_{length} = 2$ for all the cases. Figures 3.11, 3.12, 3.13, 3.14, 3.15, 3.16, show the subdivisions with $d = 0.00001$, $d = 0.0001$, $d = 0.001$, $d = 0.01$, $d = 0.1$, respectively. Figure 3.16 shows also the subdivision with $d = -0.1$.

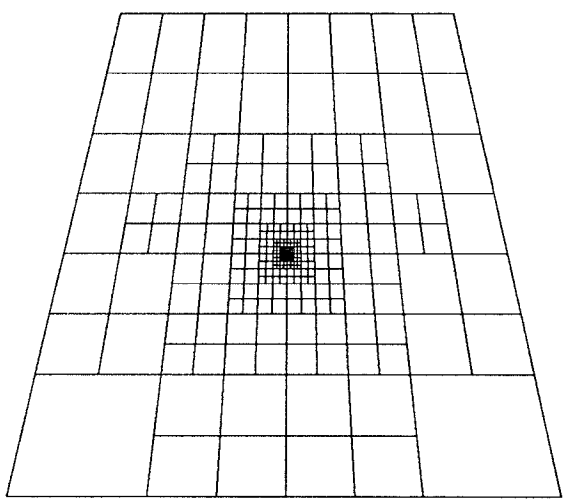

FIGURE 3.11 Subdivision with 796 Elements

The materials are idealized in this example, $E = 1$, $\nu = 0.3$, and the thickness of the plate is taken to be $h = 1.0$. The result of this calculation can be trivially generated to a realistic value of Young's modulus. However, if a different value of Poisson's ratio is desired, the calculation should be repeated. In the part of

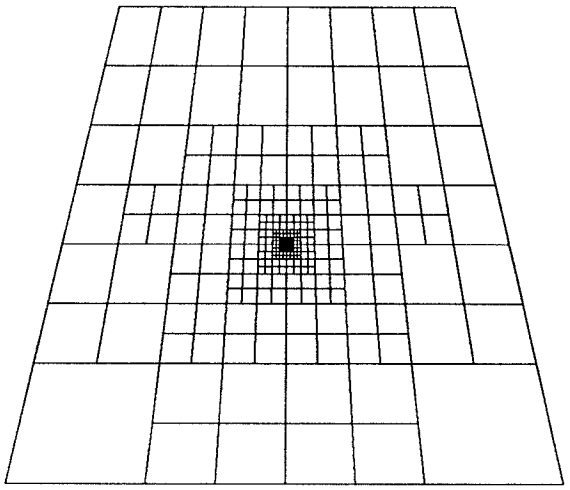

FIGURE 3.12 Subdivision with 640 Elements

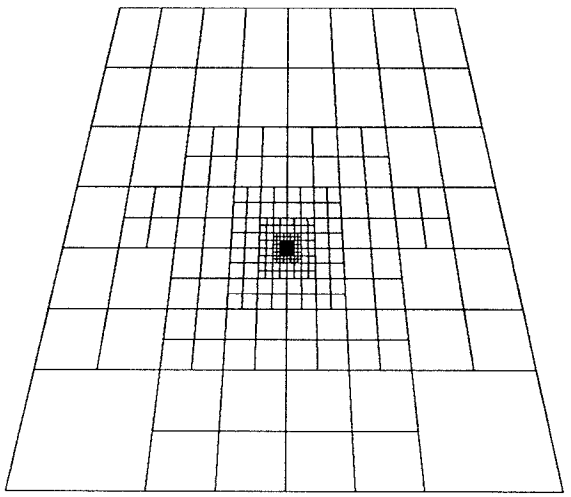

FIGURE 3.13 Subdivision with 484 Elements

numerical integration with subdivisions, 4, 16, and 36 Gaussian points are used. The results of the matrix components involving only Kelvin's solution computed by

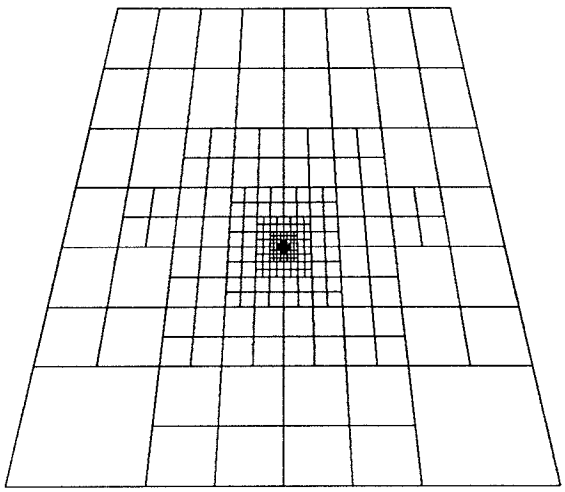

FIGURE 3.14 Subdivision with 316 Elements

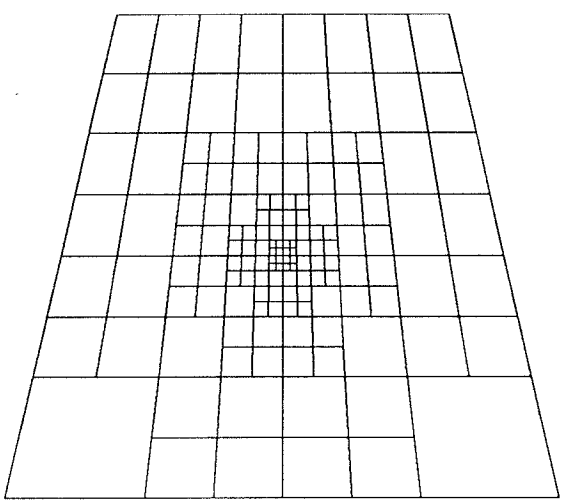

FIGURE 3.15 Subdivision with 148 Elements

numerical integration with subdivisions are shown in Tables 1a, 1b, and 1c, and the results of the same integrals computed by the analytical integration are shown in

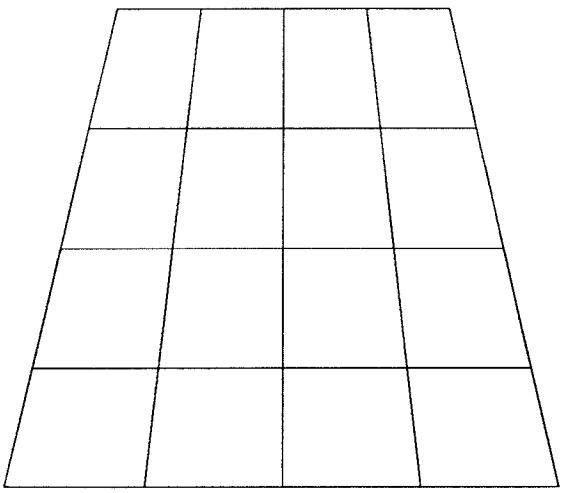

FIGURE 3.16 Subdivision with 16 Elements

Table 2.

Comparing Table 1a, 1b, and 1c with Table 2, it can be easily seen that the results of the numerical integration with subdivisions are very close to the results of the analytical integration. The errors are negligible. This supports the correctness of both the analytical integration and the numerical integration with subdivisions.

The matrices $[G_{ij}]$ and $[H_{ij}]$ involving the fundamental solution of the infinite plate problem are computed over the same element. The results of the matrices $[G_{ij}]$ and $[H_{ij}]$ from the proposed procedure are shown in Tables 3a, 3b and 3c, while the results from the numerical calculation with subdivisions are shown in Tables 4a, 4b and 4c.

Comparing Tables 3a, 3b, 3c with Tables 4a, 4b, 4c, the errors are also negligible. This fact proves the feasibility of the proposed procedure. The tremendous savings of the computational effort introduced by the proposed procedure is vital

to the later application to the boundary element method.

Table 1a. Numerical Integration of Kelvin Solution with subdivisions

G.P. Distance # Elements	$[G^{ij}]$			$[\hat{H}^{ij}]$		
2	0.10502027835E+00	-0.19027057381E-17	-0.21278394077E-18	0.50000000000E+00	0.11164165295E-14	-0.46213678537E-14
0	-0.19027057381E-17	0.83338436083E-01	-0.25765114352E-17	-0.11164165295E-14	0.50000000000E+00	0.49171572668E-02
496	-0.15857383215E-18	-0.25765114352E-17	0.10795572497E+00	0.46213678537E-14	-0.49171572668E-02	0.50000000000E+00
2	0.10502242022E+00	-0.74433025410E-18	0.15268756321E-18	0.49989083319E+00	-0.20266937000E-13	-0.40248295148E-14
10^{-6}	-0.74435842994E-18	0.83340285079E-01	0.15986176598E-07	0.10489113918E-14	0.49986999290E+00	0.49188235500E-02
796	0.91728591367E-19	0.15986176598E-07	0.10795665778E+00	-0.42645737202E-14	-0.49188235884E-02	0.50000062890E+00
2	0.10501072355E+00	-0.53349758069E-18	0.22739236398E-18	0.49982383269E+00	0.23815042820E-14	0.72636124546E-15
10^{-5}	-0.53360759571E-18	0.83336943640E-01	0.15986172486E-06	0.64834205712E-14	0.49995875753E+00	0.49188235836E-02
640	0.11692652908E-18	0.15986172486E-06	0.10794496157E+00	0.73873470275E-15	-0.49188210232E-02	0.49987642308E+00
2	0.10489382781E+00	-0.35330042015E-18	0.96019125505E-19	0.49917403450E+00	-0.84317047701E-16	-0.12376167799E-15
10^{-4}	-0.35314821892E-18	0.83303520085E-01	0.15986117429E-05	0.23227676293E-15	0.49977644862E+00	0.49188520731E-02
484	0.12664466050E-18	0.15986117429E-05	0.10782806432E+00	-0.12405983359E-15	-0.49187586523E-02	0.49925091132E+00
2	0.10373215345E+00	-0.15283650742E-18	0.89944311087E-19	0.49254498636E+00	-0.21087732255E-16	-0.53668007538E-17
10^{-3}	-0.14648376032E-18	0.82968933873E-01	0.15983342987E-04	0.83483567281E-17	0.49839506761E+00	0.49213441239E-02
316	0.58312924463E-19	0.15983342987E-04	0.10666595689E+00	-0.89446679230E-17	-0.49145592528E-02	0.49344555345E+00
2	0.92834080007E-01	0.68609668728E-19	-0.17258296300E-19	0.42705709357E+00	0.67220534694E-17	0.19515639105E-17
10^{-2}	0.67339119307E-19	0.79581864482E-01	0.15809687725E-03	0.12630955309E-16	0.48498914522E+00	0.52082909511E-02
148	-0.45316262678E-19	0.15809687725E-03	0.95720124908E-01	-0.27647155398E-17	-0.45207476489E-02	0.43473059576E+00
2	0.37269824431E-01	0.10164395367E-19	-0.13552527156E-19	0.77420406760E-01	-0.43368086899E-18	-0.10842021725E-18
10^{-1}	0.10164395367E-19	0.48259158210E-01	0.60531768097E-03	-0.54210108624E-18	0.26846893762E+00	0.83744649308E-02
16	-0.16940658945E-19	0.60531768097E-03	0.38214492416E-01	-0.32526065175E-18	0.46494330479E-02	0.88852844621E-01
2	0.37269824431E-01	0.33881317890E-20	0.67762635780E-20	-0.77420406760E-01	0.48789097762E-18	0.37947076037E-18
-10^{-1}	-0.10164395367E-19	0.48259158210E-01	-0.60531768097E-03	0.65052130349E-18	-0.26846893762E+00	0.83744649308E-02
16	0.67762635780E-20	-0.60531768097E-03	0.38214492416E-01	0.00000000000E+00	0.46494330479E-02	-0.88852844621E-01

Table 1b. Numerical Integration of Kelvin Solution with subdivisions

G.P. Distance # Elements	$[G^{ij}]$			$[\hat{H}^{ij}]$		
4	0.10502444634E+00	0.20666820910E-18	0.57811983884E-18	0.500000000000E+00	-0.16499243649E-12	-0.82798918439E-14
0	0.20666820910E-18	0.83341226490E-01	-0.55941535646E-17	0.16499243649E-12	0.500000000000E+00	0.49169324186E-02
496	0.57663753118E-18	-0.55941535646E-17	0.10795868803E+00	0.82798918439E-14	-0.49169324186E-02	0.500000000000E+00
4	0.10502413735E+00	0.25840129719E-18	-0.12346117837E-18	0.49999270446E+00	0.84280455878E-15	0.14991263439E-14
10^{-6}	0.25839778168E-18	0.83341450114E-01	0.15981965119E-07	-0.68214748086E-14	0.49999857306E+00	0.49175277345E-02
796	-0.14892179762E-18	0.15981965119E-07	0.10795791772E+00	0.13410496671E-14	-0.49175277243E-02	0.49999330613E+00
4	0.10501243815E+00	0.19546422631E-18	-0.40709360225E-18	0.49992650523E+00	-0.11659510163E-14	-0.49260725707E-15
10^{-5}	0.19546443311E-18	0.83338107210E-01	0.15981964882E-06	-0.19476065725E-14	0.49998534524E+00	0.49175280215E-02
640	-0.32127684652E-18	0.15981964882E-06	0.10794621848E+00	-0.49146884479E-15	-0.49175272907E-02	0.49993412556E+00
4	0.10489551852E+00	0.14841770859E-18	-0.29339434583E-18	0.49926435965E+00	0.81582825348E-16	0.54481159167E-17
10^{-4}	0.14755909511E-18	0.83304673919E-01	0.15981942200E-05	0.88755500345E-16	0.49985335185E+00	0.49175558490E-02
484	0.23938606927E-18	0.15981942200E-05	0.10782929384E+00	-0.28189256485E-17	-0.49174855047E-02	0.49934221228E+00
4	0.10373355575E+00	0.64745080906E-19	-0.23753980215E-18	0.49264388712E+00	0.13552527156E-17	-0.29815559743E-18
10^{-3}	0.70939009333E-19	0.82969916426E-01	0.15979685658E-04	-0.14311468677E-16	0.49853299190E+00	0.49203323545E-02
316	-0.23748686259E-18	0.15979685658E-04	0.10666682939E+00	-0.92699285748E-17	-0.49133203583E-02	0.49342332866E+00
4	0.92834077100E-01	-0.39175273811E-19	-0.82903349713E-19	0.42713678512E+00	-0.13823577699E-17	-0.36591823321E-17
10^{-2}	-0.55692416282E-19	0.79581328275E-01	0.15756968887E-03	0.54210108624E-19	0.48500865616E+00	0.51900914264E-02
148	-0.87985547396E-19	0.15756968887E-03	0.95717908961E-01	-0.46620693417E-17	-0.45065048120E-02	0.43470849691E+00
4	0.37270132732E-01	-0.30493186101E-19	-0.10164395367E-19	0.77423588272E-01	0.00000000000E+00	-0.54210108624E-19
10^{-1}	-0.44045713257E-19	0.48259342222E-01	0.60531287997E-03	0.10842021725E-18	0.26844516634E+00	0.83743297902E-02
16	-0.13552527156E-19	0.60531287997E-03	0.38215167739E-01	-0.32526065175E-18	0.46493274519E-02	0.88868769619E-01
4	0.37270132732E-01	-0.16940658945E-19	-0.10164395367E-19	-0.77423588272E-01	-0.43368086899E-18	0.10842021725E-18
10^{-1}	0.00000000000E+00	0.48259342222E-01	-0.60531287997E-03	-0.86736173799E-18	-0.26844516634E+00	0.83743297902E-02
16	-0.16940658945E-19	-0.60531287997E-03	0.38215167739E-01	-0.16263032587E-18	0.46493274519E-02	-0.88868769619E-01

Table 1c. Numerical Integration of Kelvin Solution with subdivisions

G.P. Distance # Elements	$[G^{ij}]$			$[\hat{H}^{ij}]$		
6	0.10502496827E+00	-0.462307058476-18	0.67166403995E-18	0.50000000000E+00	-0.34253674929E-12	-0.40413378183E-14
0	-0.46230705847E-18	0.83341547205E-01	-0.37574224716E-18	0.34253674929E-12	0.50000000000E+00	0.49172269902E-02
496	0.65856149905E-18	-0.37574224716E-18	0.10795898570E+00	0.40413378183E-14	-0.49172269902E-02	0.50000000000E+00
6	0.10502413629E+00	-0.15163874989E-19	-0.20062190423E-18	0.49999264312E+00	-0.17285435236E-14	0.26583553067E-14
10^{-6}	-0.15151570678E-19	0.83341450068E-01	0.15981956298E-07	-0.49927510043E-15	0.49999853325E+00	0.49175250177E-02
796	-0.22758434743E-18	0.15981956298E-07	0.10795791866E+00	0.24912797519E-14	-0.49175250109E-02	0.49999342297E+00
6	0.10501243710E+00	-0.77186290909E-20	-0.84851566850E-19	0.49992643115E+00	0.45528359728E-15	0.35751566638E-16
10^{-5}	-0.76971223950E-20	0.83338107164E-01	0.15981956072E-06	0.73834167946E-15	0.49998533273E+00	0.49175252958E-02
640	-0.37476865218E-19	0.15981956072E-06	0.10794621941E+00	0.40996394647E-16	-0.49175245947E-02	0.49993422962E+00
6	0.10480551747E+00	-0.13698110944E-19	-0.23229547706E-18	0.49926431196E+00	-0.48873801057E-16	-0.40657581468E-16
10^{-4}	-0.12998316146E-19	0.83304673873E-01	0.15981933514E-05	-0.80596878997E-16	0.49985332681E+00	0.49175530598E-02
484	-0.23282156393E-18	0.15981933514E-05	0.10782929477E+00	-0.44763997196E-16	-0.49174829488E-02	0.49934229695E+00
6	0.10373355475E+00	-0.13234889801E-20	-0.51616070223E-20	0.49264382739E+00	-0.41199682554E-17	0.60986372202E-17
10^{-3}	0.582335151246-21	0.82969916387E-01	0.15979677980E-04	0.55294310797E-17	0.49853294054E+00	0.49203286534E-02
316	0.466662214386-19	0.15979677980E-04	0.10666683028E+00	0.62341624918E-18	-0.49133193346E-02	0.49342344872E+00
6	0.92834076186E-01	0.87667910041E-19	-0.14346620544E-18	0.42713671049E+00	0.27918205942E-17	0.14636729329E-17
10^{-2}	0.74115382885E-19	0.79581328272E-01	0.15756965915E-03	0.61799523832E-17	0.48500863252E+00	0.51900754371E-02
148	-0.96032360395E-19	0.15756965915E-03	0.95717909946E-01	0.40657581468E-18	-0.45065189724E-02	0.43470858804E+00
6	0.37270132675E-01	-0.44045713257E-19	-0.10164395367E-19	0.77423586979E-01	0.21684043450E-18	-0.32526065175E-18
10^{-1}	-0.44045713257E-19	0.48259341797E-01	0.60531287823E-03	0.65052130349E-18	0.26844512714E+00	0.83743294379E-02
16	-0.16940658945E-19	0.60531287823E-03	0.38215168015E-01	-0.43368086899E-18	0.46493271103E-02	0.88868798264E-01
6	0.37270132675E-01	-0.23716922523E-19	-0.10164395367E-19	-0.77423586979E-01	0.32526065175E-18	0.27105054312E-18
-10^{-1}	0.10164395367E-19	0.48259341797E-01	-0.60531287823E-03	-0.10842021725E-17	-0.26844512714E+00	0.83743294379E-02
16	-0.33881317890E-20	-0.60531287823E-03	0.38215168015E-01	0.54210108624E-19	0.46493271103E-02	-0.88868798264E-01

Table 2. Analytical Integration of Kelvin Solution

G.P. Distance # Elements	$[G^{ij}]$			$[\hat{H}^{ij}]$		
0	0.10502543629E+00	0.00000000000E+00	0.33881317890E-19	0.50000000000E+00	-0.26020852140E-17	0.00000000000E+00
	0.00000000000E+00	0.83341821497E-01	0.00000000000E+00	0.26020852140E-17	0.50000000000E+00	0.49175250142E-02
1	0.00000000000E+00	0.00000000000E+00	0.10795921865E+00	0.00000000000E+00	-0.49175250142E-02	0.50000000000E+00
10^{-6}	0.10502413629E+00	0.00000000000E+00	0.54210108624E-19	0.49999264311E+00	-0.34694469520E-17	0.00000000000E+00
	0.00000000000E+00	0.83341450068E-01	0.15981935263E-07	0.34694469520E-17	0.49999853327E+00	0.49175250170E-02
1	0.47433845046E-19	0.15981935263E-07	0.10795791866E+00	0.00000000000E+00	-0.49175250100E-02	0.49999342296E+00
10^{-5}	0.10501243710E+00	0.23589867581E-18	0.13552527156E-19	0.49992643112E+00	0.00000000000E+00	0.00000000000E+00
	0.23589867581E-18	0.83338107164E-01	0.15981956283E-06	0.17347234760E-17	0.49998533271E+00	0.49175252946E-02
1	-0.20328790734E-19	0.15981956283E-06	0.10794621941E+00	0.00000000000E+00	-0.49175245935E-02	0.49993422965E+00
10^{-4}	0.10489551747E+00	0.00000000000E+00	0.81315162936E-19	0.49926431193E+00	0.00000000000E+00	0.00000000000E+00
	0.00000000000E+00	0.83304673873E-01	0.15981933527E-05	0.26020852140E-17	0.49985332680E+00	0.49175530585E-02
1	0.81315162936E-19	0.15981933527E-05	0.10782929477E+00	0.00000000000E+00	-0.49174829477E-02	0.49934229698E+00
10^{-3}	0.10373355475E+00	-0.88091426514E-19	0.13552527156E-19	0.49264382738E+00	-0.34694469520E-17	0.00000000000E+00
	-0.88091426514E-19	0.82969916387E-01	0.15979677977E-04	0.34694469520E-17	0.49853294056E+00	0.49203286519E-02
1	0.00000000000E+00	0.15979677977E-04	0.10666683028E+00	0.00000000000E+00	-0.49133193340E-02	0.49342344871E+00
10^{-2}	0.92834076186E-01	-0.10842021725E-18	0.13552527156E-19	0.42713671048E+00	0.00000000000E+00	0.00000000000E+00
	-0.10842021725E-18	0.79581328272E-01	0.15756965915E-03	0.17347234760E-17	0.48500863250E+00	0.51900754372E-02
1	0.13552527156E-19	0.15756965915E-03	0.95717909946E-01	0.00000000000E+00	-0.45065189718E-02	0.43470858807E+00
10^{-1}	0.37270132675E-01	0.29815559743E-18	0.59292306308E-19	0.77423586978E-01	-0.86736173799E-18	0.37057691442E-19
	0.29815559743E-18	0.48259341797E-01	0.60531287822E-03	0.21684043450E-17	0.26844512712E+00	0.83743294377E-02
1	0.59292306308E-19	0.60531287822E-03	0.38215168015E-01	0.37057691442E-19	0.46493271101E-02	0.88868798280E-01
-10^{-1}	0.37270132675E-01	-0.29815559743E-18	0.59292306308E-19	-0.77423586978E-01	-0.86736173799E-18	-0.37057691442E-19
	-0.29815559743E-18	0.48259341797E-01	-0.60531287822E-03	0.21684043450E-17	-0.26844512712E+00	0.83743294377E-02
1	0.59292306308E-19	-0.60531287822E-03	0.38215168015E-01	-0.37057691442E-19	0.46493271101E-02	-0.88868798280E-01

Table 3a. Partially Numerical and Partially Analytical Integration of Fundamental Solution

G.P. Distance # Elements	$[G^{ij}]$			$[\hat{H}^{ij}]$		
2	0.10947232874E+00	0.00000000000E+00	-0.19081958236E-16	0.50000000000E+00	0.88817841970E-15	0.00000000000E+00
0	0.00000000000E+00	0.87786613283E-01	0.00000000000E+00	0.44408920985E-15	0.50000000000E+00	0.27443316258E-02
1	-0.32959746044E-16	0.00000000000E+00	0.12687511722E+00	0.00000000000E+00	-0.12576092402E-01	0.50000000000E+00
2	0.10947102875E+00	0.82198194784E-17	-0.13877787808E-15	0.49999265019E+00	-0.18873791419E-14	-0.40657581468E-19
10^{-6}	0.82198194784E-17	0.87786241853E-01	0.15224868612E-07	-0.22204460493E-15	0.49999854392E+00	0.27443316286E-02
1	-0.13877787808E-15	0.17345995823E-07	0.12687381723E+00	-0.54210108624E-19	-0.12576092398E-01	0.49999346476E+00
2	0.10945932955E+00	-0.52211110869E-16	0.11102230246E-15	0.49992650188E+00	0.16653345369E-14	0.21684043450E-18
10^{-5}	-0.52211110869E-16	0.87782898948E-01	0.15229715012E-06	0.12212453271E-14	0.49998543924E+00	0.27443319089E-02
1	0.36429192996E-16	0.17350842224E-06	0.12686211798E+00	0.10842021725E-18	-0.12576091982E-01	0.49993464757E+00
2	0.10934240983E+00	-0.10842021725E-16	-0.18214596498E-15	0.49926501953E+00	-0.14432899320E-14	0.00000000000E+00
10^{-4}	-0.10842021725E-16	0.87749465571E-01	0.15229688687E-05	-0.99920072216E-15	0.49985439206E+00	0.27443599427E-02
1	-0.17347234760E-17	0.17350816216E-05	0.12674519266E+00	0.86736173799E-18	-0.12576050464E-01	0.49934647619E+00
2	0.10818043751E+00	-0.49439619065E-16	-0.11796119637E-15	0.49265090333E+00	-0.99920072216E-15	-0.13877787808E-16
10^{-3}	-0.49005938196E-16	0.87414699383E-01	0.15227415872E-04	-0.99920072216E-15	0.49854359318E+00	0.27471625165E-02
1	-0.67654215563E-16	0.17348575059E-04	0.12558266053E+00	-0.20816681712E-16	-0.12571899556E-01	0.49346524065E+00
2	0.97279999630E-01	0.45102810375E-16	0.18388068845E-15	0.42720744703E+00	0.17763568394E-14	0.00000000000E+00
10^{-2}	0.45102810375E-16	0.84025241361E-01	0.15003062067E-03	0.17763568394E-14	0.48511510585E+00	0.30196057135E-02
1	0.34694469520E-17	0.17127385913E-03	0.11462697725E+00	-0.55511151231E-16	-0.12166368302E-01	0.43512633509E+00
2	0.41621330947E-01	0.55511151231E-16	-0.97578195524E-17	0.78108559013E-01	0.00000000000E+00	0.11232334507E-15
10^{-1}	0.62450045135E-16	0.52618563032E-01	0.51408977780E-03	0.55511151231E-15	0.26945943520E+00	0.64578481125E-02
1	-0.12359904766E-16	0.75702794672E-03	0.56457054828E-01	0.56812193838E-16	-0.31228299143E-02	0.92879821480E-01
2	0.41621330947E-01	0.69388939039E-17	-0.14961989980E-16	-0.78108559013E-01	0.44408920985E-15	-0.56812193838E-16
-10^{-1}	0.00000000000E+00	0.52618563032E-01	-0.51408977780E-03	0.99920072216E-15	-0.26945943520E+00	0.64578481125E-02
1	-0.18431436932E-16	-0.75702794672E-03	0.56457054828E-01	-0.13010426070E-17	-0.31228299143E-02	-0.92879821480E-01

Table 3b. Partially Numerical and Partially Analytical Integration of Fundamental Solution

G.P. Distance # Elements	$[G^{ij}]$			$[\hat{H}^{ij}]$		
4	0.10947283730E+00	0.51275958839E-29	0.31225022568E-16	0.50000000000E+00	-0.34694469520E-17	-0.77623913074E-27
0	0.51275958839E-29	0.87787043395E-01	-0.23166730945E-18	-0.87777007884E-15	0.50000000000E+00	0.27437641305E-02
1	0.45102810375E-16	0.54604288484E-17	0.12687535973E+00	-0.80779356695E-27	-0.12587545551E-01	0.50000000000E+00
4	0.10947153731E+00	0.82217782421E-17	-0.45102810375E-16	0.49999265019E+00	-0.30045410604E-14	0.13023131564E-18
10^{-6}	0.82217782421E-17	0.87786671966E-01	0.15226999495E-07	0.31225022568E-16	0.49999854392E+00	0.27437641333E-02
1	-0.34694469520E-17	0.17351358566E-07	0.12687405974E+00	0.66915602833E-19	-0.12587545546E-01	0.49999346476E+00
4	0.10945983811E+00	-0.52193111419E-16	0.58980598183E-16	0.49992650189E+00	0.27061686225E-14	0.34897757427E-18
10^{-5}	-0.52186335155E-16	0.87783329060E-01	0.15231845896E-06	0.10512424264E-14	0.49998543924E+00	0.27437644136E-02
1	0.17347234760E-16	0.17356204962E-06	0.12686236049E+00	-0.26427427954E-18	-0.12587545131E-01	0.49993464760E+00
4	0.10934291839E+00	-0.10965688535E-16	-0.17347234760E-17	0.49926501965E+00	0.11102230246E-15	0.21684043450E-17
10^{-4}	-0.10965688535E-16	0.87749895683E-01	0.15231819571E-05	-0.24286128664E-15	0.49985439212E+00	0.27437924476E-02
1	-0.50306980803E-16	0.17356178953E-05	0.12674543517E+00	0.30899761916E-17	-0.12587503612E-01	0.49934647644E+00
4	0.10818094606E+00	-0.51567365829E-16	-0.62450045135E-16	0.49265090449E+00	-0.39898639947E-15	-0.95409791179E-17
10^{-3}	-0.51242105177E-16	0.87415129496E-01	0.15229546718E-04	-0.12836953722E-15	0.49854359371E+00	0.27465950460E-02
1	-0.10234868508E-15	0.17353937788E-04	0.12558290302E+00	-0.28622937354E-16	-0.12583352635E-01	0.49346524317E+00
4	0.97280507877E-01	0.78170976636E-16	0.60715321659E-16	0.42720745877E+00	0.20122792321E-15	0.71123662515E-15
10^{-2}	0.76436253160E-16	0.84025671596E-01	0.15005189177E-03	-0.13877787808E-16	0.48511511099E+00	0.30190406958E-02
1	0.29490299092E-16	0.17132747774E-03	0.11462721823E+00	0.71123662515E-15	-0.12177814403E-01	0.43512636018E+00
4	0.41621810356E-01	0.69822619908E-16	-0.80230960764E-17	0.78108644960E-01	0.65919492087E-16	0.14007892069E-15
10^{-1}	0.75894152074E-16	0.52619007736E-01	0.51426808861E-03	0.63143934526E-15	0.26945951600E+00	0.64574745184E-02
1	-0.11492543028E-16	0.75755438898E-03	0.56457159801E-01	0.56812193838E-16	-0.31335830511E-02	0.92879932709E-01
4	0.41621810356E-01	0.30357660830E-17	-0.22768245622E-16	-0.78108644960E-01	0.23245294578E-15	-0.56812193838E-16
-10^{-1}	-0.99746599869E-17	0.52619007736E-01	-0.51426808861E-03	0.72164496601E-15	-0.26945951600E+00	0.64574745184E-02
1	-0.25370330836E-16	-0.75755438898E-03	0.56457159802E-01	-0.70689981646E-16	-0.31335830511E-02	-0.92879932709E-01

Table 3c. Partially Numerical and Partially Analytical Integration of Fundamental Solution

G.P. Distance # Elements	$[G^{ij}]$			$[\hat{H}^{ij}]$		
6	0.10947291300E+00	0.88746851837E-30	-0.10842021725E-16	0.50000000000E+00	-0.11622647289E-15	-0.29932094453E-26
0	0.88746851837E-30	0.87787119079E-01	-0.20972349865E-17	0.42240516640E-15	0.50000000000E+00	0.27436913690E-02
1	0.80230960764E-17	0.50777147777E-17	0.12687538130E+00	-0.29914838121E-26	-0.12588251960E-01	0.50000000000E+00
6	0.10947161301E+00	0.82187805395E-17	-0.14528309111E-16	0.49999265019E+00	-0.14146669947E-14	0.70991948892E-19
10^{-6}	0.82191114118E-17	0.87786747650E-01	0.15226999412E-07	0.82399365109E-16	0.49999854393E+00	0.27436913718E-02
1	-0.57245874707E-16	0.17351359137E-07	0.12687408131E+00	-0.11117307433E-19	-0.12588251955E-01	0.49999346476E+00
6	0.10945991381E+00	-0.52220931157E-16	0.53559587321E-16	0.49992650189E+00	0.20669230216E-14	0.11130012927E-17
10^{-5}	-0.52219237091E-16	0.87783404744E-01	0.15231845814E-06	0.14042586538E-14	0.49998543926E+00	0.27436916522E-02
1	0.75460471205E-16	0.17356205534E-06	0.12686238206E+00	0.46925625278E-18	-0.12588251540E-01	0.49993464762E+00
6	0.10934299409E+00	-0.10992793589E-16	0.73725747729E-17	0.49926501964E+00	-0.11874182193E-14	0.11146953586E-16
10^{-4}	-0.10992370073E-16	0.87749971367E-01	0.15231819489E-05	-0.17659484985E-14	0.49985439232E+00	0.27437196861E-02
1	-0.36429192996E-16	0.17356179525E-05	0.12674545674E+00	0.17028750372E-16	-0.12588210021E-01	0.49934647664E+00
6	0.10818102176E+00	-0.48582421723E-16	-0.54643789493E-16	0.49265090441E+00	-0.17546727960E-14	-0.36862873865E-17
10^{-3}	-0.48460488978E-16	0.87415205180E-01	0.15229546637E-04	-0.92894442139E-15	0.49854359572E+00	0.27465222845E-02
1	-0.39248118644E-16	0.17353938359E-04	0.12558292460E+00	-0.28189256485E-16	-0.12584059046E-01	0.49346524517E+00
6	0.97280583579E-01	0.49141463468E-16	0.46837533851E-16	0.42720745843E+00	0.74246164772E-15	0.10386656812E-14
10^{-2}	0.55212995634E-16	0.84025747280E-01	0.15005189095E-03	0.82919782152E-15	0.48511513062E+00	0.30189679314E-02
1	0.60498481225E-16	0.17132748344E-03	0.11462723980E+00	0.87516799363E-15	-0.12178521059E-01	0.43512638011E+00
6	0.41621886269E-01	0.60173220573E-16	-0.29598719309E-16	0.78108643337E-01	-0.17433970934E-15	0.70689981646E-16
10^{-1}	0.53234326669E-16	0.52619083645E-01	0.51426808144E-03	0.30531133177E-15	0.26945971056E+00	0.64574014707E-02
1	-0.30357660830E-17	0.75755443768E-03	0.56457181447E-01	0.18648277367E-16	-0.31343138984E-02	0.92880131494E-01
6	0.41621886269E-01	-0.57462715142E-17	-0.10191500421E-16	-0.78108643337E-01	0.53169274539E-15	-0.75894152074E-16
-10^{-1}	-0.66136332522E-17	0.52619083645E-01	-0.51426808143E-03	0.10338951917E-14	-0.26945971056E+00	0.64574014707E-02
1	-0.17238814543E-16	-0.75755443768E-03	0.56457181447E-01	-0.10191500421E-15	-0.31343138984E-02	-0.92880131494E-01

Table 4a. Numerical Integration of Fundamental Solution with subdivisions

G.P. Distance # Elements	$[G^{ij}]$			$[\hat{H}^{ij}]$		
2	0.10946782154E+00	0.00000000000E+00	0.62072437847E-15	0.50000000000E+00	-0.11173898612E-10	0.00000000000E+00
0	0.00000000000E+00	0.87783800270E-01	0.00000000000E+00	0.11174977610E-10	0.50000000000E+00	0.27432589162E-02
496	0.56338702421E-15	0.00000000000E+00	0.12687190679E+00	0.00000000000E+00	-0.12588497925E-01	0.50000000000E+00
2	0.10946996341E+00	-0.52320563407E-17	0.82608377768E-15	0.49989084035E+00	-0.57399918152E-12	-0.56877419441E-12
10^{-6}	-0.52320563407E-17	0.87785649266E-01	0.15236060455E-07	-0.37792963203E-11	0.49987000377E+00	0.27449250877E-02
796	0.846491719 67E-15	0.17360415032E-07	0.12687283960E+00	-0.56928767256E-12	-0.12590164335E-01	0.50000067083E+00
2	0.10945826674E+00	-0.33287865432E-17	0.64708287912E-15	0.49982390344E+00	-0.46924963915E-12	-0.31159796965E-12
10^{-5}	-0.33287865432E-17	0.87782307826E-01	0.15236056472E-06	-0.66900651685E-12	0.49995886418E+00	0.27449252642E-02
640	0.55338806496E-15	0.17360411049E-06	0.12686114338E+00	-0.31276023438E-12	-0.12590161723E-01	0.49987684109E+00
2	0.10934137090E+00	-0.73450462021E-17	0.43944662227E-15	0.49917474196E+00	-0.21275516071E-13	-0.20816681712E-13
10^{-4}	-0.73450462021E-17	0.87748884184E-01	0.15236001256E-05	-0.62803928724E-13	0.49977751457E+00	0.27449540317E-02
484	0.41245591740E-15	0.17360356150E-05	0.12674424545E+00	-0.20920765120E-13	-0.12590099473E-01	0.49925509116E+00
2	0.10817968695E+00	-0.30493186101E-17	0.17930671054E-15	0.49255206252E+00	-0.66613381478E-15	-0.34208746946E-14
10^{-3}	-0.30493186101E-17	0.87414289272E-01	0.15233210353E-04	-0.23592239273E-14	0.49840572536E+00	0.27474730870E-02
316	0.18307431309E-15	0.17357596935E-04	0.12558207037E+00	-0.29976021665E-14	-0.12585912717E-01	0.49348735168E+00
2	0.97280653883E-01	-0.76436253160E-17	0.26481638063E-16	0.42712784185E+00	-0.10547118734E-14	0.52041704279E-15
10^{-2}	-0.76436253160E-17	0.84026350093E-01	0.15057009577E-03	-0.81878948066E-15	0.48509566017E+00	0.30371187756E-02
148	0.19786689648E-17	0.17185463627E-03	0.11462947302E+00	-0.24286128664E-15	-0.12193363593E-01	0.43514840555E+00
2	0.41621644483E-01	0.17347234760E-16	0.69388939039E-17	0.78105461588E-01	0.41633363423E-16	0.97144514655E-16
10^{-1}	0.17347234760E-16	0.52618966618E-01	0.51427223189E-03	0.27755575616E-16	0.26948369689E+00	0.64574719768E-02
16	0.86736173799E-17	0.75755685385E-03	0.56456525338E-01	0.69388939039E-16	-0.31348210230E-02	0.92864358138E-01
2	0.41621644483E-01	-0.17347234760E-16	0.69388939039E-17	-0.78105461588E-01	0.41633363423E-16	-0.97144514655E-16
-10^{-1}	-0.17347234760E-16	0.52618966618E-01	-0.51427223189E-03	0.27755575616E-16	-0.26948369689E+00	0.64574719768E-02
16	0.86736173799E-17	-0.75755685385E-03	0.56456525338E-01	-0.69388939039E-16	-0.31348210230E-02	-0.92864358138E-01

Table 4b. Numerical Integration of Fundamental Solution with subdivisions

G.P. Distance # Elements	$[G^{ij}]$			$[\hat{H}^{ij}]$		
4	0.10947198956E+00	-0.31566022603E-26	0.46946462288E-15	0.50000000913E+00	0.532161120 73E-12	0.22778970794E-21
0	-0.31566022603E-26	0.87786590579E-01	-0.15943614928E-14	-0.52343199219E-12	0.50000000145E+00	0.27430346741E-02
496	0.37230655570E-15	-0.15895888690E-14	0.12687486968E+00	0.22861729245E-21	-0.12588281562E-01	0.50000000789E+00
4	0.10947168057E+00	-0.45407583418E-18	0.85070553653E-15	0.49999271172E+00	-0.34433567109E-12	0.23910040614E-12
10^{-6}	-0.45407583418E-18	0.87786814203E-01	0.15231850288E-07	-0.61667337903E-12	0.49999858409E+00	0.27436300267E-02
796	0.77951203350E-15	0.17356210011E-07	0.12687409937E+00	0.23876733923E-12	-0.12588876979E-01	0.49999334806E+00
4	0.10945998137E+00	0.84470360665E-18	0.57998532302E-15	0.49992657592E+00	-0.13852113900E-12	0.88616614047E-13
10^{-5}	0.84470360665E-18	0.87783471298E-01	0.15231850169E-06	-0.77021722333E-13	0.49998545198E+00	0.27436303334E-02
640	0.62239943907E-15	0.17356209888E-06	0.12686240012E+00	0.88432733358E-13	-0.12588876480E-01	0.49993454356E+00
4	0.10934306165E+00	-0.22615779692E-17	0.45301100788E-15	0.49926506677E+00	-0.21354445989E-14	-0.76119666126E-14
10^{-4}	-0.22615779692E-17	0.87750037921E-01	0.15231827340E-05	-0.78444195584E-14	0.49985441813E+00	0.27436584254E-02
484	0.35076989599E-15	0.17356187375E-05	0.12674547481E+00	-0.95444485648E-14	-0.12588834827E-01	0.49934639212E+00
4	0.10818108927E+00	-0.40928632011E-17	0.16591681371E-15	0.49265096325E+00	-0.54123372450E-15	-0.36221026178E-14
10^{-3}	-0.40928632011E-17	0.87415271726E-01	0.15229554340E-04	0.13877787808E-15	0.49854364966E+00	0.27464619377E-02
3166	0.20174969551E-15	0.17353946062E-04	0.12558294270E+00	-0.26784130469E-14	-0.12584682322E-01	0.49346512687E+00
4	0.97280651007E-01	-0.15233040523E-16	0.31604493328E-16	0.42720753338E+00	-0.54123372450E-15	0.49960036108E-15
10^{-2}	-0.15233040523E-16	0.84025813790E-01	0.15005192083E-03	-0.97144514655E-15	0.48511517097E+00	0.30189198697E-02
148	0.39763114676E-16	0.17132751332E-03	0.11462725781E+00	0.78409501114E-15	-0.12179129372E-01	0.43512630651E+00
4	0.41621953023E-01	0.00000000000E+00	-0.260208521 40E-17	0.78108643220E-01	0.13877787808E-15	0.00000000000E+00
10^{-1}	0.00000000000E+00	0.52619150766E-01	0.51426808461E-03	-0.22204460493E-15	0.26945992104E+00	0.64573375999E-02
16	-0.86736173799E-18	0.75755444086E-03	0.56457200223E-01	-0.55511151231E-16	-0.31349576557E-02	0.92880278066E-01
4	0.41621953023E-01	-0.34694469520E-17	0.00000000000E+00	-0.78108643220E-01	0.97144514655E-16	-0.27755575616E-16
-10^{-1}	-0.34694469520E-17	0.52619150766E-01	-0.51426808461E-03	-0.55511151231E-16	-0.26945992104E+00	0.64573375999E-02
16	-0.43368086899E-17	-0.75755444086E-03	0.56457200223E-01	-0.27755575616E-16	-0.31349576557E-02	-0.92880278066E-01

Table 4c. Numerical Integration of Fundamental Solution with subdivisions

G.P. Distance # Elements	$[G^{ij}]$			$[\hat{H}^{ij}]$		
6	0.10947251149E+00	0.54106490375E-26	0.34045303469E-15	0.50000002374E+00	-0.47581730223E-12	-0.17859863906E-20
0	0.54106490375E-26	0.87786911294E-01	-0.58782378312E-16	0.47602893849E-12	0.50000000764E+00	0.27433289769E-02
496	0.38410572466E-15	-0.51836124765E-16	0.12687516735E+00	-0.16396852316E-20	-0.12588575865E-01	0.50000003102E+00
6	0.10947167951E+00	0.10009944203E-17	0.84754071042E-15	0.49999265015E+00	-0.19313717292E-12	-0.82488182951E-12
10^{-6}	0.10009944203E-17	0.87786814158E-01	0.15231841662E-07	0.43733072719E-12	0.49999854389E+00	0.27436275892E-02
796	0.81417342241E-15	0.17356201386E-07	0.12687410031E+00	-0.82645001953E-12	-0.12588873381E-01	0.49999346478E+00
6	0.10945998032E+00	-0.19984683599E-18	0.60265748335E-15	0.49992650171E+00	0.31925850852E-13	-0.18374191058E-13
10^{-5}	-0.19984683599E-18	0.87783471252E-01	0.15231841389E-06	0.31002977963E-13	0.49998543948E+00	0.27436276454E-02
640	0.57900054134E-15	0.17356201109E-06	0.12686240106E+00	-0.16705387074E-13	-0.12588873695E-01	0.49993464760E+00
6	0.10934306060E+00	-0.11015663479E-17	0.42517835227E-15	0.49926501878E+00	0.68512903684E-14	-0.13031242752E-13
10^{-4}	-0.11015663479E-17	0.87750037875E-01	0.15231818657E-05	0.61894933623E-14	0.49985439339E+00	0.27436556411E-02
484	0.35903693755E-15	0.17356178693E-05	0.12674547574E+00	-0.13933298959E-13	-0.12588832262E-01	0.49934647679E+00
6	0.10818108827E+00	-0.67627110509E-17	0.19979813160E-15	0.49265090379E+00	-0.45796699766E-15	0.31918911958E-15
10^{-3}	-0.67627110509E-17	0.87415271687E-01	0.15229546662E-04	0.19428902931E-15	0.49854359803E+00	0.27464582369E-02
316	0.22300683435E-15	0.17353938385E-04	0.12558294359E+00	-0.84654505628E-15	-0.12584681298E-01	0.49346524694E+00
6	0.97280650092E-01	-0.11763593571E-16	0.51526708247E-16	0.42720745874E+00	-0.24286128664E-15	-0.13877787808E-15
10^{-2}	-0.11763593571E-16	0.84025813787E-01	0.15005189111E-03	-0.80491169285E-15	0.48511514734E+00	0.30189038805E-02
148	0.38055496254E-16	0.17132748360E-03	0.11462725880E+00	0.38163916471E-15	-0.12179143533E-01	0.43512639765E+00
6	0.41621952966E-01	0.17347234760E-17	-0.26020852140E-17	0.78108641927E-01	0.41633363423E-16	-0.13877787808E-16
10^{-1}	0.17347234760E-17	0.52619150341E-01	0.51426808286E-03	-0.11102230246E-15	0.26945988184E+00	0.64573372475E-02
16	0.69388939039E-17	0.75755443911E-03	0.56457200499E-01	-0.41633363423E-16	-0.31349579973E-02	0.92880306711E-01
6	0.41621952966E-01	-0.13010426070E-16	0.86736173799E-17	-0.78108641927E-01	-0.83266726847E-16	0.55511151231E-16
-10^{-1}	-0.13010426070E-16	0.52619150341E-01	-0.51426808286E-03	0.30531133177E-15	-0.26945988184E+00	0.64573372475E-02
16	-0.17347234760E-17	-0.75755443911E-03	0.56457200499E-01	-0.55511151231E-16	-0.31349579973E-02	-0.92880306711E-01

CHAPTER 4

CIRCULAR HOLE SUBJECTED TO PRESSURE

In this chapter, a simple problem is used to test the idea of the modified boundary element method. The problem involves a circular hole in an infinite plate of finite thickness. The hole is subjected to uniform pressure applied on the surface of the hole. Furthermore, the upper and the lower surfaces of the plate are traction-free. Although this testing problem is strictly to be a three-dimensional one, its solution happens to coincide with both the plane-stress and the plane-strain solutions for the corresponding two-dimensional problems with the same in-plane geometry and loading. By taking advantage of this fact, the known solution of the corresponding plane-stress problem is used as the bench-mark case for comparison with our numerical results.

Besides the modified boundary element scheme, a finite element analysis scheme is also employed for further comparison. The results of both the numerical schemes are presented.

4.1 Analytical Solution For Pressurized Circular Hole Problem

Consider a problem involving a pressurized circular hole in an infinite plate of finite uniform thickness h. The pressure is uniformly applied on the surface of the the circular hole. The plate also has the traction-free boundary conditions on its upper and the lower surfaces. The radius of the hole is denoted as a, and the magnitude of the applied pressure is p. Figure 4.1 shows the problem schematically. The Cartesian coordinate system is placed at the bottom surface of the plate. The origin of the coordinates is located at the center of the circular hole.

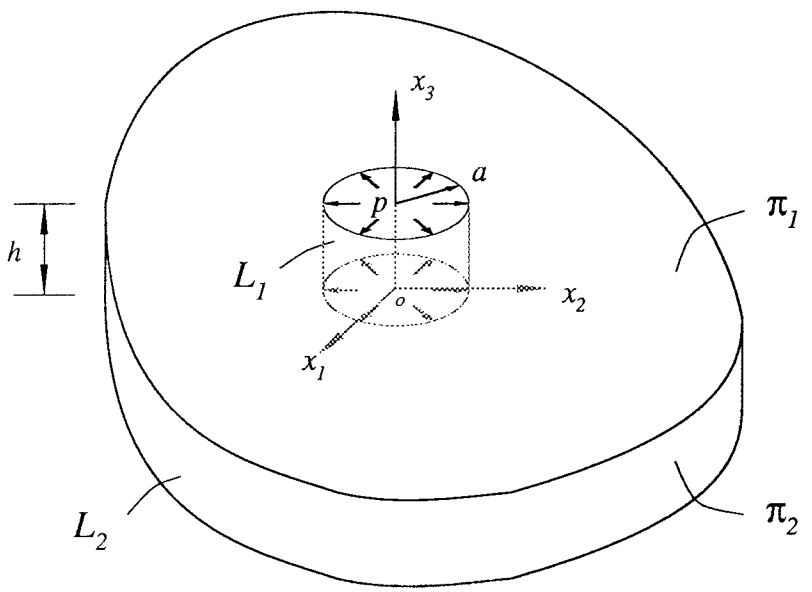

FIGURE 4.1 Pressurized Circular Hole In Infinite Plate

The traction is denoted as $\boldsymbol{t}(\boldsymbol{x};\boldsymbol{n})$, where $\boldsymbol{x} = r\boldsymbol{e}_r + \theta\boldsymbol{e}_\theta + x_3\boldsymbol{e}_3$ and $\boldsymbol{n} = n_r\boldsymbol{e}_r + n_\theta\boldsymbol{e}_\theta + n_3\boldsymbol{e}_3$. The vectors $\boldsymbol{e}_r$, $\boldsymbol{e}_\theta$, and $\boldsymbol{e}_3$ are the unit vectors of the cylindrical

coordinate system. The boundary conditions then become:

$$\begin{aligned} \boldsymbol{t}(\boldsymbol{x}; \boldsymbol{e}_3) &= \boldsymbol{0} \qquad && \forall \boldsymbol{x} \in \Pi_1, \\ \boldsymbol{t}(\boldsymbol{x}; -\boldsymbol{e}_3) &= \boldsymbol{0} \qquad && \forall \boldsymbol{x} \in \Pi_2, \\ \boldsymbol{t}(\boldsymbol{x}; -\boldsymbol{e}_r) &= -p\boldsymbol{e}_r \qquad && \forall \boldsymbol{x} \in \mathcal{L}. \end{aligned} \tag{4.1.1}$$

The in-plane stress components corresponding to the two-dimensional plane-stress and plane-strain approximations of the three-dimensional problem is given in [43], and the components of the stress fields expressed in the polar coordinates are,

$$\begin{aligned} &\sigma_{rr}(r,\theta) = -\sigma_{\theta\theta}(r,\theta) = -\frac{a^2}{r^2}p, \quad \forall r \geq a; \\ &\sigma_{r\theta}(r,\theta) = 0, \qquad\qquad 0 \leq \theta \leq 2\pi. \end{aligned} \tag{4.1.2}$$

In this particular problem, $\epsilon_{3r}(r,\theta)$, $\epsilon_{3\theta}(r,\theta)$, $\epsilon_{33}(r,\theta)$ and $\sigma_{3r}(r,\theta)$, $\sigma_{3\theta}(r,\theta)$, $\sigma_{33}(r,\theta)$ are zero simultaneously.

$$\sigma_{33}(r,\theta) = \sigma_{3r}(r,\theta) = \sigma_{3\theta}(r,\theta) = 0. \tag{4.1.3}$$

In addition, the displacement fields for both cases are identical and they can be expressed as,

$$\begin{aligned} u_r(r,\theta) &= \frac{1}{2\mu}\frac{a^2}{r}p, \\ u_\theta(r,\theta) &= 0, \\ u_3(r,\theta) &= 0. \end{aligned} \tag{4.1.4}$$

Therefore, the solutions of the plane-stress and the plane-strain approximation of this three-dimensional problem coincide. This fact suggests the possibility that the two-dimensional solutions may also be the solution of the fully three-dimensional problem. Indeed, if the above solutions in Eqs. (4.1.2), (4.1.3), and (4.1.4) are substituted into the three-dimensional governing equations for linear elastostatics,

all the governing equations are satisfied identically. In addition, the boundary conditions on the upper and the lower surfaces of the plate are trivially satisfied. For convenience, call the solution in (4.1.2), (4.1.3), and (4.1.4) the *analytical solution* to the pressurized circular hole problem, and choose the diameter of the hole the same as the thickness of the plate.

4.2 Modeling Of Circular Hole Surface

Recall the modified Boundary Integral Equations, the displacement field in the interior of the three-dimensional plate can be related to the traction and the displacement fields of only the lateral surfaces of the plate. This relationship is shown in Eq. (3.2.9) in Chapter Three. Because of the difficulty in solving the integral equations analytically for the tractions or the displacements on the lateral surfaces, the discretization scheme has to be introduced. However, in the modified boundary integral equations, the discretization is limited *only* to the lateral surfaces. This fact is also the key difference between the modified boundary element scheme and the conventional one, which employs the Kelvin solution as the fundamental solution.

In this test problem, the lateral surfaces coincide with the surface of the circular hole $\mathcal{L}_1$.

Seven mesh schemes are employed for the modified boundary element scheme. One mesh is designed to suit the finite element scheme, in which 700 eight noded brick elements with 1008 nodes and 3024 degrees of freedom are used. In the boundary element mesh schemes, 72, 120, 196, 224 and 420 elements are used. Three different mesh arrangements are made involving 120 elements.

Call the dimension of an element in the x_3 direction the element-thickness, and the corresponding dimension in the circular direction the element width. All the elements used have the same width unless the mesh is locally refined. The elements in a layer have the same thickness.

For the modified boundary element scheme, the circular hole is modeled by flat rectangular elements of the same width. The thickness direction of the hole is modeled by an odd number of layers that are symmetric about the mid-plane of the plate. In all the calculations, constant elements are used. The displacement and the traction are computed only at the element centroids, which are called the element nodes.

The fundamental solution for the three-dimensional infinite plate problem is evaluated partially analytically and partially numerically over an infinite integral interval $[0, \infty)$. To avoid the numerical difficulties, a pre-set designated number P is introduced so that the numerical part of the integrals are evaluated over a truncated interval $[0, P]$. By increasing the number P, the accuracy of the numerical integrals can be improved. This scheme is justified by the results shown in Table 1a through 4c in Chapter Three. In the following mesh arrangements, P is chosen to be 10 or 20.

Two groups (Group A and Group B) of internal points are placed in the interior of the plate. The 48 internal points in the Group A are selected to examine the displacement variation along the radius direction; the other 44 internal points in Group B are assigned to observe the displacement variation through the thickness.

The points in Group A are placed in three radial arrays at different depths. All the arrays contain the same number of points (16 points each), and the points in the

three arrays have the same radial positions respectively. The first array of points is usually placed in the element nodal plane of the top layer; the second array of points is placed in the plane three quarters of the thickness from the bottom surface of the plate; the third array of points is placed in the mid-plane of the plate. Since the displacement field is expected to exhibit higher gradient with respect to r near the surface of the hole, the points in each array are placed closer to each other when they are near the circular hole surface, and further apart when they are away from the hole surface. The position of the points in the r direction are,

$$r = a + 0.01h,\ a + 0.03h,\ a + 0.05h,\ a + 0.07h,\ a + 0.09h,$$
$$a + 0.11h,\ a + 0.13h,\ a + 0.23h,\ a + 0.33h,\ a + 0.43h,$$
$$a + 0.50h,\ a + 0.70h,\ a + 0.90h,\ a + 1.1h,\ a + 1.30h,\ a + 1.50h.$$

where h stands for the thickness of the plate.

The points in Group B are positioned along four different lines through the thickness of the plate. On each line, the displacement is evaluated at eleven points. The positions of the lines are $r = 0.53h$, $0.73h$, $1.00h$, and $1.60h$. The positions of the points on the line at $r = 0.53h$ are $x_3 = 0.030h$, $0.124h$, $0.218h$, $0.312h$, $0.406h$, $0.500h$, $0.594h$, $0.688h$, $0.782h$, $0.876h$, and $0.970h$. The positions of the points on the other three lines are $r = 0$, $0.1h$, $0.2h$, $0.3h$, $0.4h$, $0.5h$, $0.6h$, $0.7h$, $0.8h$, $0.9h$, and $1.0h$.

4.2.1 Mesh With Seventy Two Elements

The cross section of the circular hole is modeled by 24 elements of equal width, and the hole is modeled by three layers of elements in the thickness direction. The thicknesses of the layers are $0.2h$, $0.6h$, and $0.2h$. P is taken to be 10 for this mesh arrangement. Furthermore, the Group A points are placed in the radius direction at the depths of $x_3 = 0.9h$, $0.75h$ and $0.5h$. The Group B points used are the same as discussed before. The element and the internal-point arrangements are displayed in Figure 4.2.

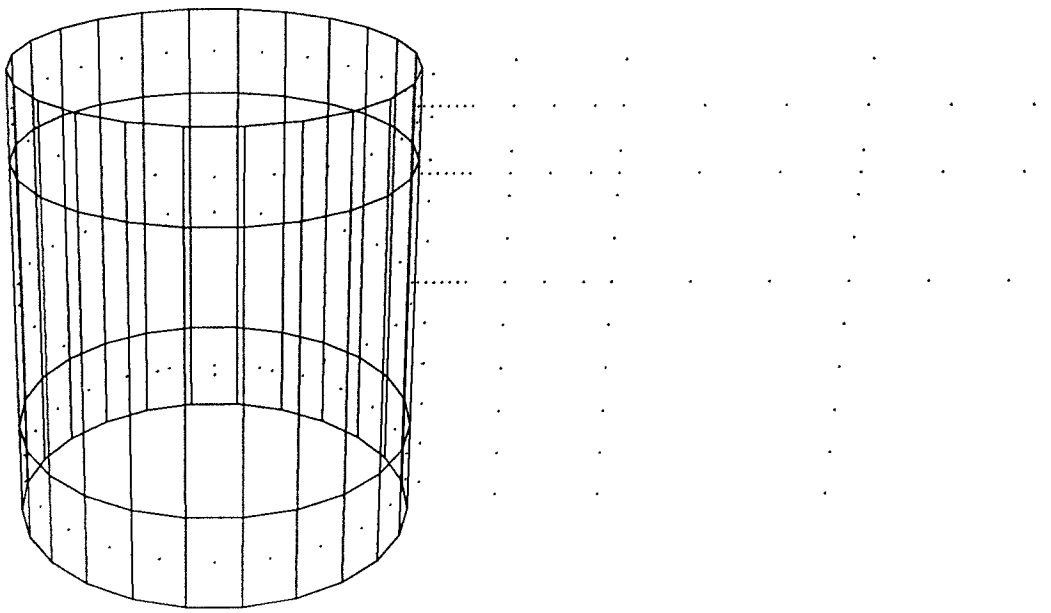

FIGURE 4.2 Mesh With Seventy Two Elements

4.2.2 Meshs With One Hundred and Twenty Elements

Three mesh schemes are made involving 120 elements.

a) The cross section of the circular hole is modeled by 24 elements of equal width, and the circular hole is modeled by five layers of elements in the thickness direction. The thicknesses of the layers are $0.1h$, $0.2h$, $0.4h$, $0.2h$, and $0.1h$. $P = 10$.

b) The cross section of the circular hole is modeled by the same 24 equally sized elements. However, the hole is modeled by five layers with the same thickness in the thickness direction, which is $0.2h$. $P = 10$.

c) The modeling of the surface of the hole is the same as in case a). However $P = 20$ for this case.

The positions of the Group A points in the x_3 direction for cases a) and c) are $x_3 = 0.95h$, $0.75h$, and $0.5h$; for case b), they are at $x_3 = 0.9h$, $0.75h$, and $0.5h$. The positions of the Group B points are the same as discussed before.

The arrangements of the elements and the internal points are displayed in Figures 4.3 and 4.4.

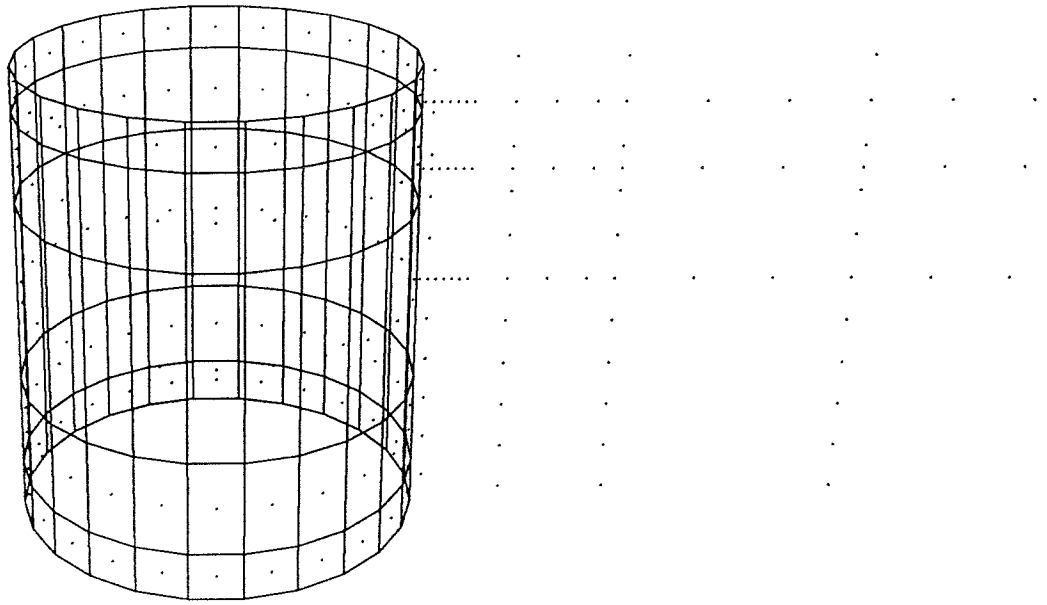

FIGURE 4.3 One Hundred and Twenty Elements, Different Thicknesses

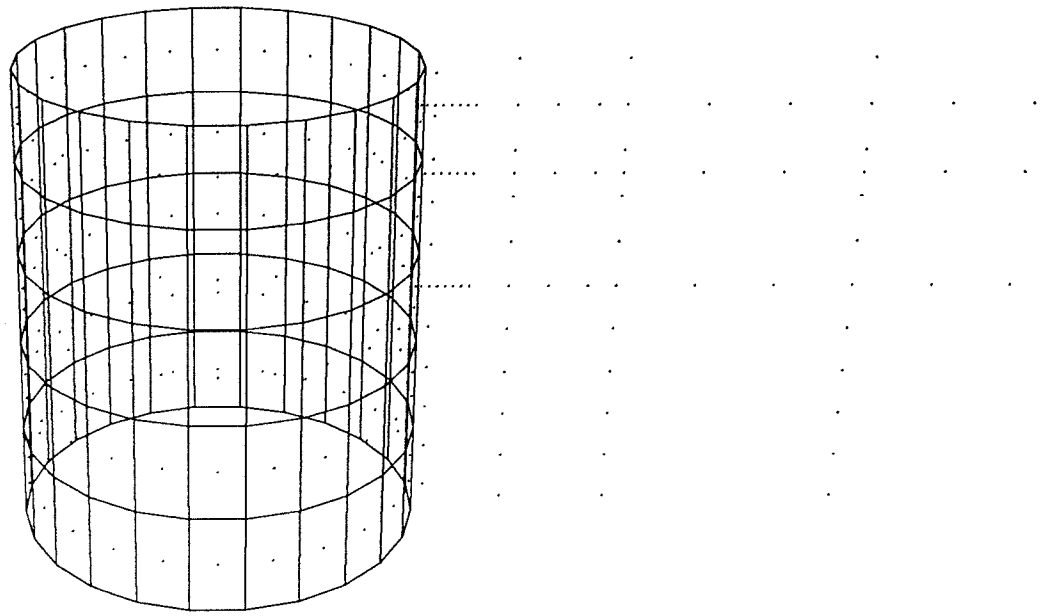

FIGURE 4.4 One Hundred and Twenty Elements, Same Thickness

4.2.3 Mesh With One Hundred And Ninety Six Elements

The cross section of the circular hole is modeled by 28 elements. This mesh arrangement is similar to the ones in which the cross section of the hole is modeled by 24 equally sized elements, but this mesh is locally refined. The difference is that one of the elements in the 24 element case is subdivided with five fine elements. The thickness direction is modeled by seven layers. The thicknesses of the layers are $0.1h$, $0.1h$, $0.2h$, $0.2h$, $0.2h$, $0.1h$, $0.1h$.

The internal points in this case are still arranged in two groups: Group A and Group B. The arrays formed by the Group A points are located in the extension of the center of the hole and the center of the five fine elements. The depths of the arrays are at $x_3 = 0.95h$, $0.75h$, and $0.5h$. The Group B points are the same as discussed before. The arrangement of the elements and the internal points are shown in Figure 4.5.

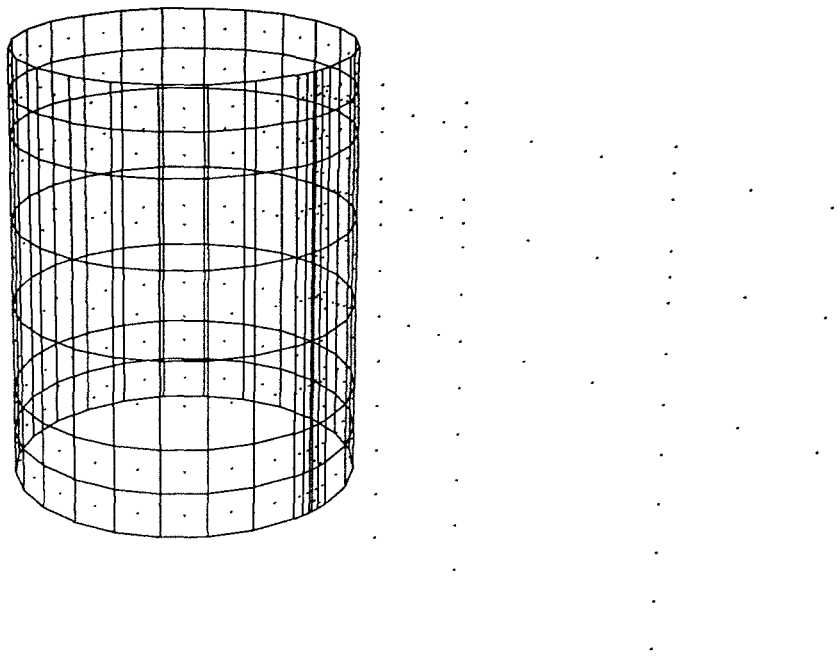

FIGURE 4.5 Mesh With One Hundred and Ninety Six Elements

4.2.4 Mesh With Two Hundred And Twenty-Four Elements

In this mesh arrangement, the cross section of the circular hole is modeled by 32 equally sized elements, and the thickness of the plate is modeled by seven layers of elements. The thicknesses of the layers from the top to the bottom are $0.1h$, $0.1h$, $0.2h$, $0.2h$, $0.2h$, $0.1h$, $0.1h$. P is chosen to be 10.

The positions of the Group A points in the x_3 direction are $x_3 = 0.95h$, $0.75h$, and $0.5h$. The positions of the Group B points in the thickness direction are the same as discussed before.

The arrangement of the elements and the internal points is shown in Figures 4.6.

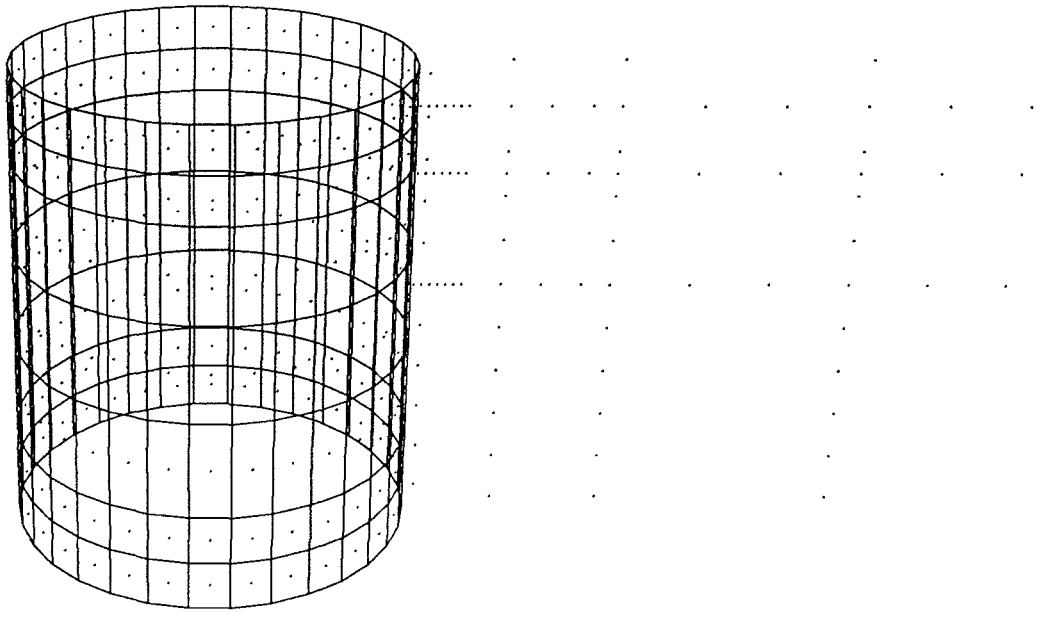

FIGURE 4.6 Two Hundred and Twenty-Four Elements

4.2.5 Mesh With Four Hundred and Twenty Elements

This mesh arrangement is very similar to the case with 196 elements. The only difference is that the thickness of the circular hole is modeled by 15 layers instead of 7 layers. Both the Group A points and the Group B points are the same as in the case with 196 elements, respectively. The arrangement of the elements and the internal points is shown in Figure 4.7.

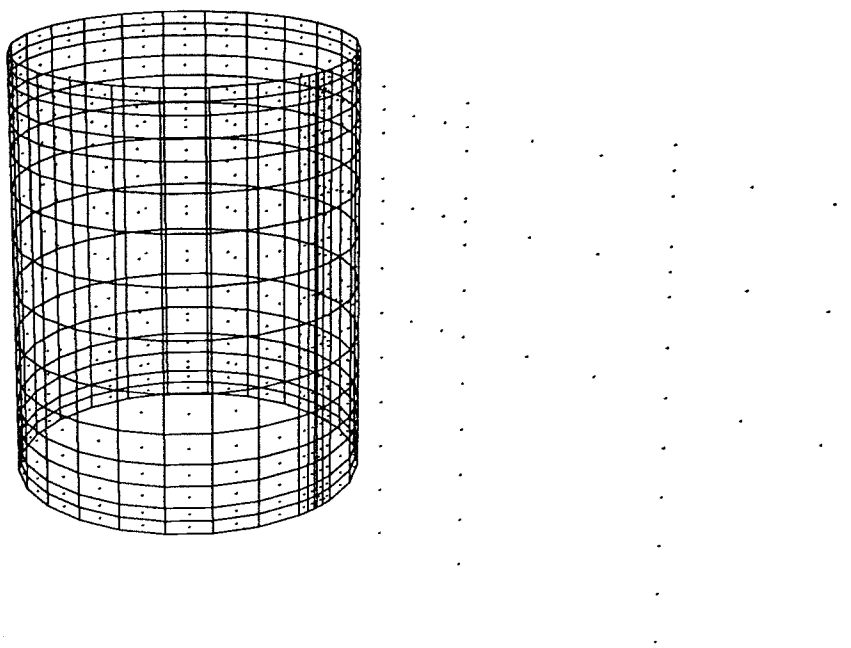

FIGURE 4.7 Mesh With Four Hundred And Twenty Elements

4.3 Mesh For Finite Element Analysis

The three-dimensional Finite Element Analysis Program, FEAP, has been adapted in the present study. The FEAP was originally developed by R. J. Taylor [4] of U. C. Berkeley and later revised at Brown University. The code was made available through the courtesy of Dr. Ravichandran.

The eight noded tri-linear brick elements are used in FEAP. FEAP computes the displacement components at the nodes of the brick elements. The nodes for an element are located at its eight corners. The displacements in the interior of an element are evaluated through linearly interpolating the values at the nodes. The stress and the strain components are evaluated at the elements centroids.

The three-dimensional problem involving pressurized circular hole in an infinite plate is axially symmetric regarding the geometry and the loading. The modeling effort can be greatly reduced by taking advantage of the symmetry. In the implementation of the FEAP, one eighth of the plate is modeled. The same FEAP will be used in the analysis of the pressurized elliptical hole problems in the next chapter. The finite element model is depicted in Figure 4.8. The model is bounded by six surfaces, which are: the two orthogonal surfaces through the thickness, the top free surface and the midplane of the plate, a quarter of the circular hole surface enclosed between the two orthogonal surfaces, and a remote surface.

The remote surface is chosen to be concentric to the circular hole surface. The radius of the remote surface is denoted by b. Because of the characteristics of the pressurized hole problem, the stress and the displacement vary inversely proportional to r^2 and r, respectively. When the radius of the surface is large compared to the radius of the circular hole, it can be assumed that the stress and the displacement on the remote surface are negligible. It is justifiable that when the radius of the remote surface is 20 times the thickness, the ratio between the stresses on the remote surface and on the circular hole is of the order of $O(10^{-4})$, and the ratio of the displacements is of the order of $O(10^{-2})$. Therefore, in the model for finite element analysis, the three-dimensional infinite plate is truncated by a remote concentric surface at the radius about 20 times the thickness of the

plate, and the traction-free boundary conditions are applied on this remote surface. The geometry of the finite element model is shown in Figure 4.8, and the mesh geometry of the simulation is shown in Figures 4.9 and 4.10. Portions of meshes shown in Figures 4.9a and 4.10a are embedded in the meshes shown in Figures 4.9b and 4.10b, respectively.

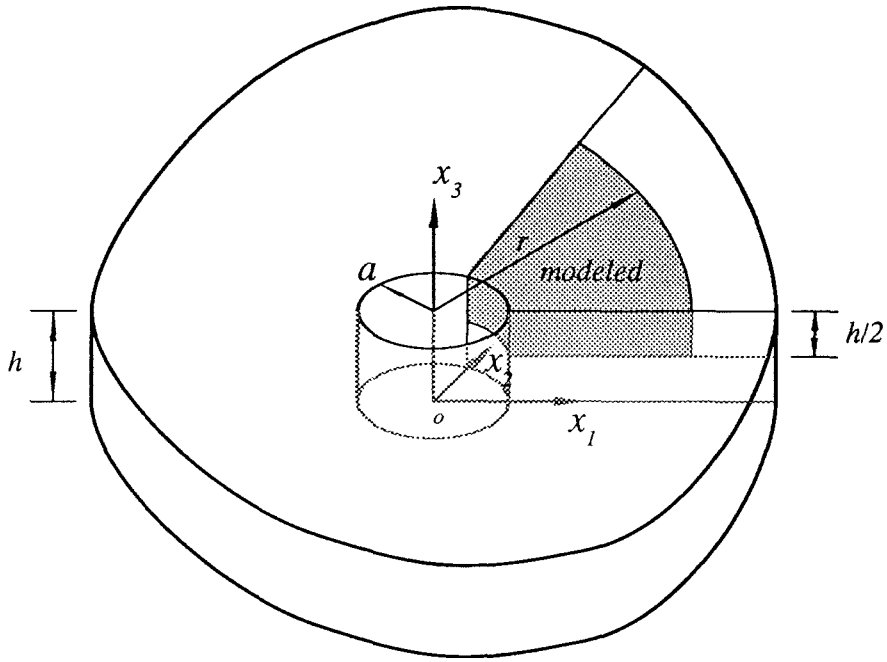

FIGURE 4.8 Geometry of Finite Element Modeling

The finite element mesh models the cross section of the circular hole surface using 7 brick elements. The surfaces of the brick elements along the circular hole surface have the same geometries as the elements used for the modified boundary element scheme. The entire model consists of 700 eight noded brick elements arranged in 5 layers. 1008 nodes are involved and 3024 degrees of freedom are generated. These 5 layers of elements are arranged through one half the thickness of the plate. Starting from the midplane, the thicknesses of the layers are $0.1h$, $0.15h$, $0.15h$, $0.05h$, and $0.05h$.

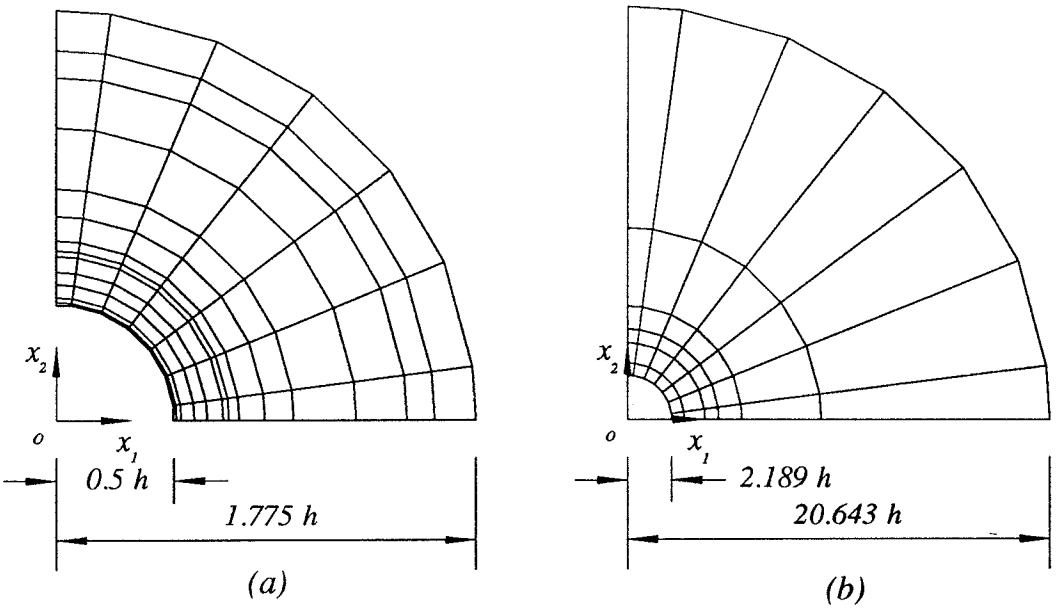

FIGURE 4.9 Detail Of In-Plane Mesh For Finite Element Analysis

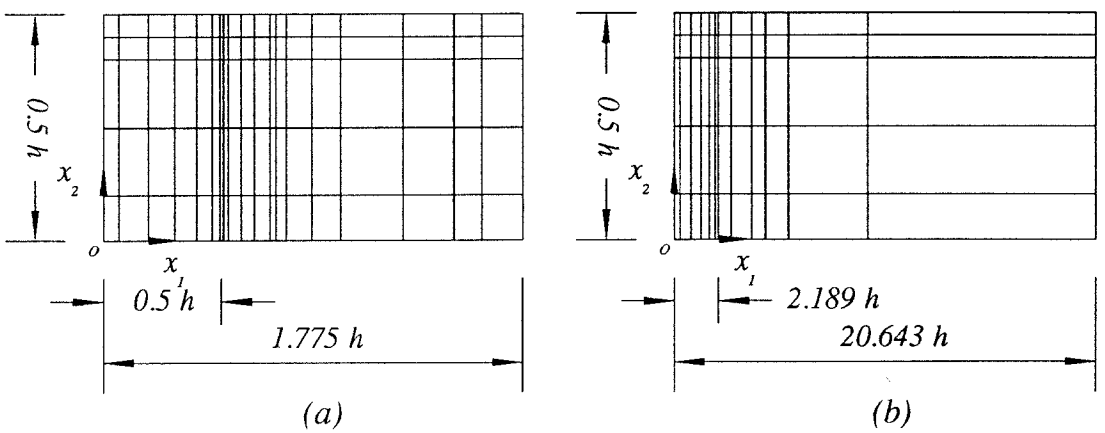

FIGURE 4.10 Detail Of Mesh Variation Through Thickness

4.4 Results And Discussions

In this section, the results from all the mesh arrangements are analyzed with the hope of establishing some insights to use the modified boundary element scheme. The sources of discrepancy are also discussed.

In this particular problem, the full three-dimensional solution is identical to those of the plane-stress and the plane-strain approximation. All the numerical results obtained from both the modified boundary element method and the finite element method are plotted against the analytical solution. In all the calculations, the Young's modulus E and the Poisson's ration ν were chosen to be 1 and 0.3, respectively. The cases involving different Young's modulus and Poisson's ratio can be computed from the above results through simple mathematical operations.

4.4.1 Results Of In-Plane Displacements

The result from the finite element analysis agrees well with the analytical solution.

Recall the solution of the stress field of the pressurized hole problem, for a finite radius of the circular hole, the stress field does not appear to have a strong stress concentration even near the surface of the hole. Furthermore, because of the axially symmetric property of the problem, it is expected that any local refinement of the numerical mesh in the circular direction would not affect the final result very much.

Figures 4.11 and 4.12, 4.13 and 4.14, 4.15 and 4.16 show the normalized displacement component u_r vs. the normalized radius r. In these cases, u_r is evaluated at the Group A points. It can be seen from Figures 4.12, 4.14, and 4.16 (finite element results are included) that, although the mesh is locally refined for the cases involving 196 and 420 elements, the result of in-plane displacements obtained from the modified boundary element method does not seem to change much compared with the case using 120 elements. Unless the mesh is uniformly refined greatly, the results of the modified boundary element method would not be changed significantly.

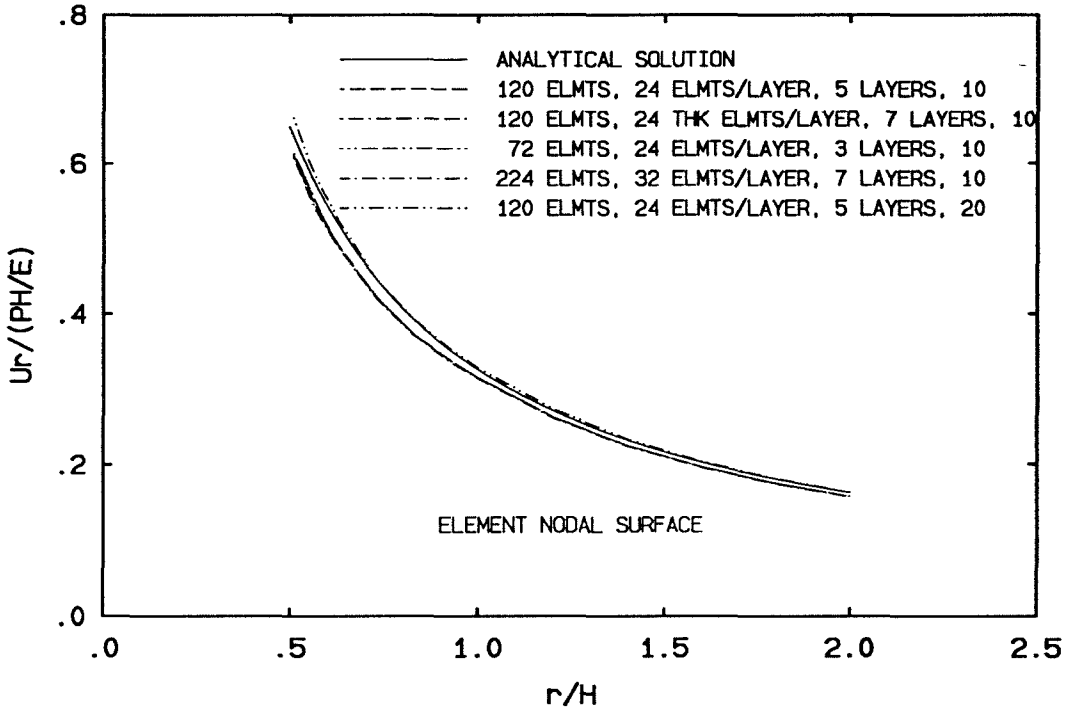

FIGURE 4.11 Normalized Displacement u_r vs. Normalized Distance r; Results Obtained At Element Nodal Plane Of First Layer

Figures 4.11, 4.12, 4.13, 4.14, 4.15, and 4.16 show that the in-plane displacement u_r, calculated from the modified boundary element method, differ from the analytical and the finite element results by less than 5%.

Two aspects contribute to the above error accumulation. One source of error

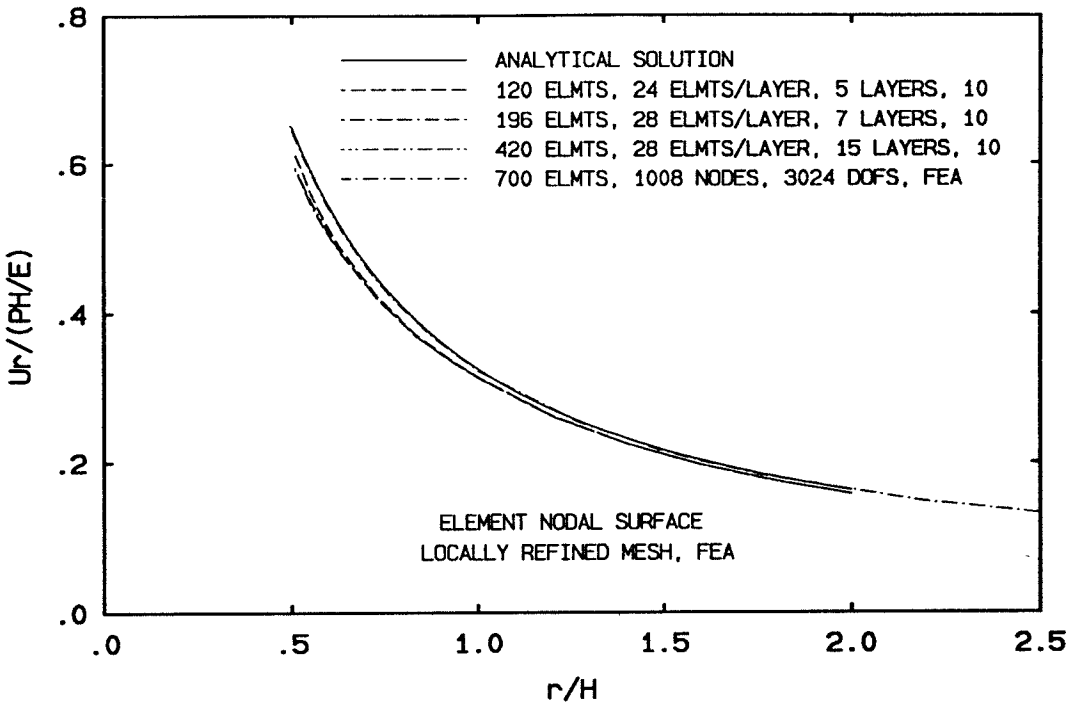

FIGURE 4.12 Normalized Displacement u_r vs. Normalized Distance r; Locally Refined Mesh; Results Obtained At Element Nodal Plane Of First Layer

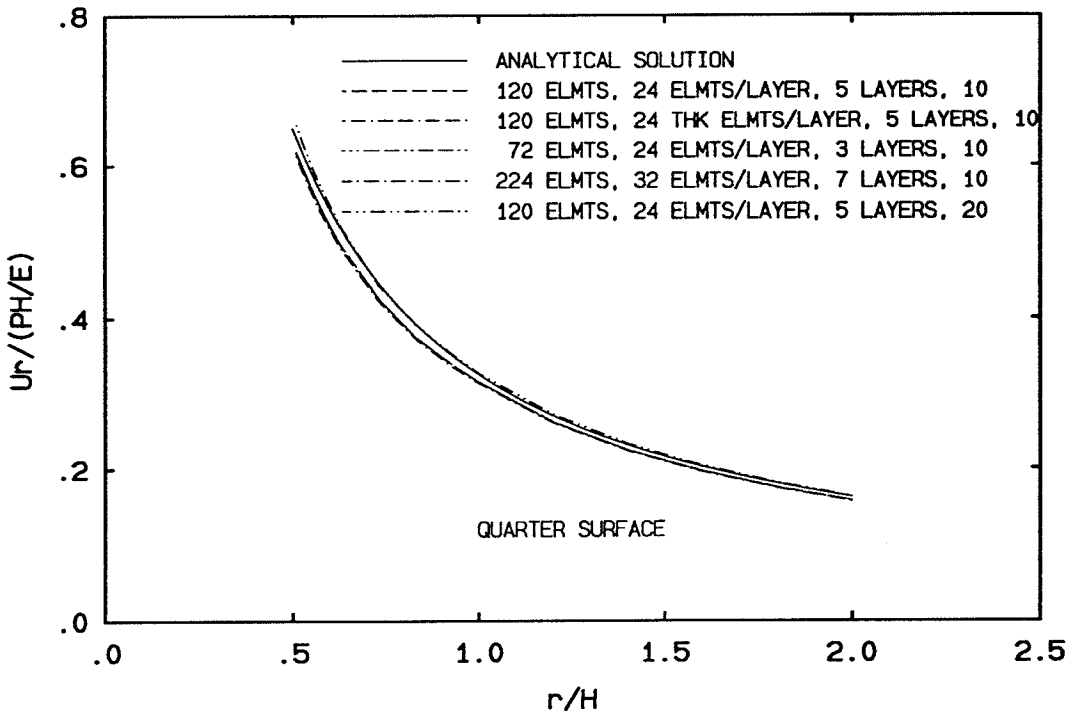

FIGURE 4.13 Normalized Displacement u_r vs. Normalized Distance r; Results Obtained At Depth Three Quarters From Bottom Surface

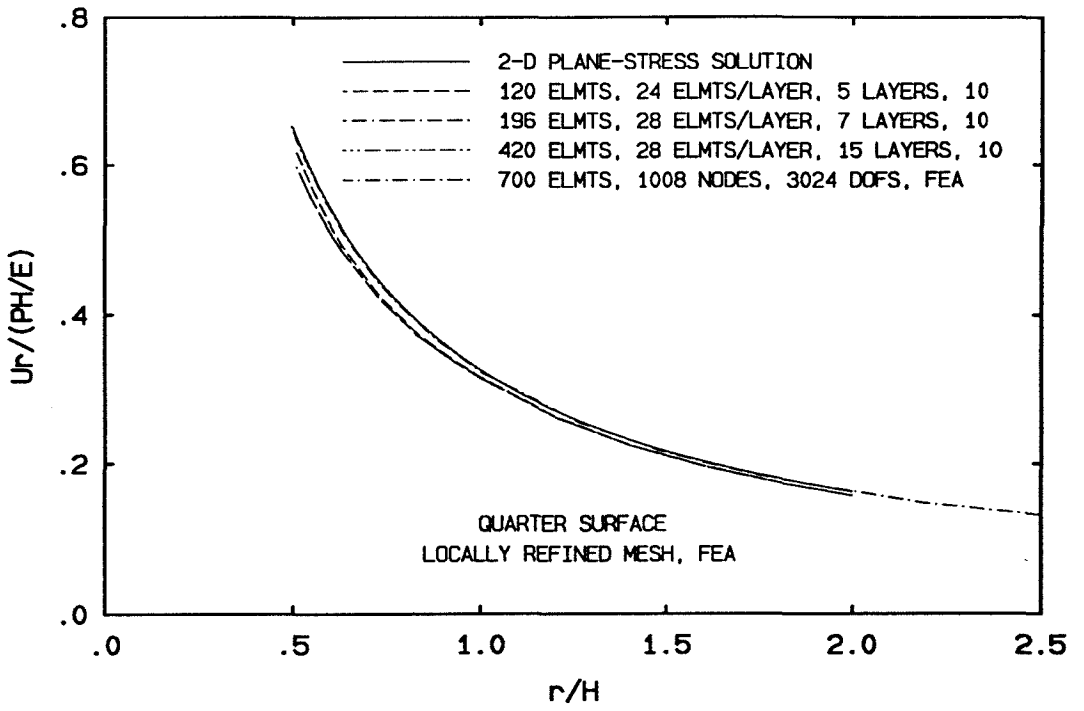

FIGURE 4.14 Normalized Displacement u_r vs. Normalized Distance r; Locally Refined Mesh; Results Obtained At Depth Three Quarters From Bottom Surface

comes from modeling. Since the polygon is used to model the circular hole surface, and the nodes of the elements are located at the centroids, the radius of the modeled "circular hole" is smaller than the actual one. This fact would result in approximately 1% of error in all the stress and the displacement components, and it may also be the reason that the results in Figures 4.11 and 4.13, obtained from various mesh arrangements, have little difference. Since the cross section of the hole is modeled by 24, 28, and 32 elements, respectively, the change of radius caused by these models are very small compared with the actual radius of the hole. The second source of the error comes from $P = 10$. As was demonstrated in Chapter Two, when P is chosen to be 10, the order of the error in the stress and the displacement components of the fundamental solution for infinite plate problem is at the order of $O(10^{-2})$. Thus, the error of the numerical integrations of the fundamental solution over the mesh elements can not be smaller than that presented in the fundamental

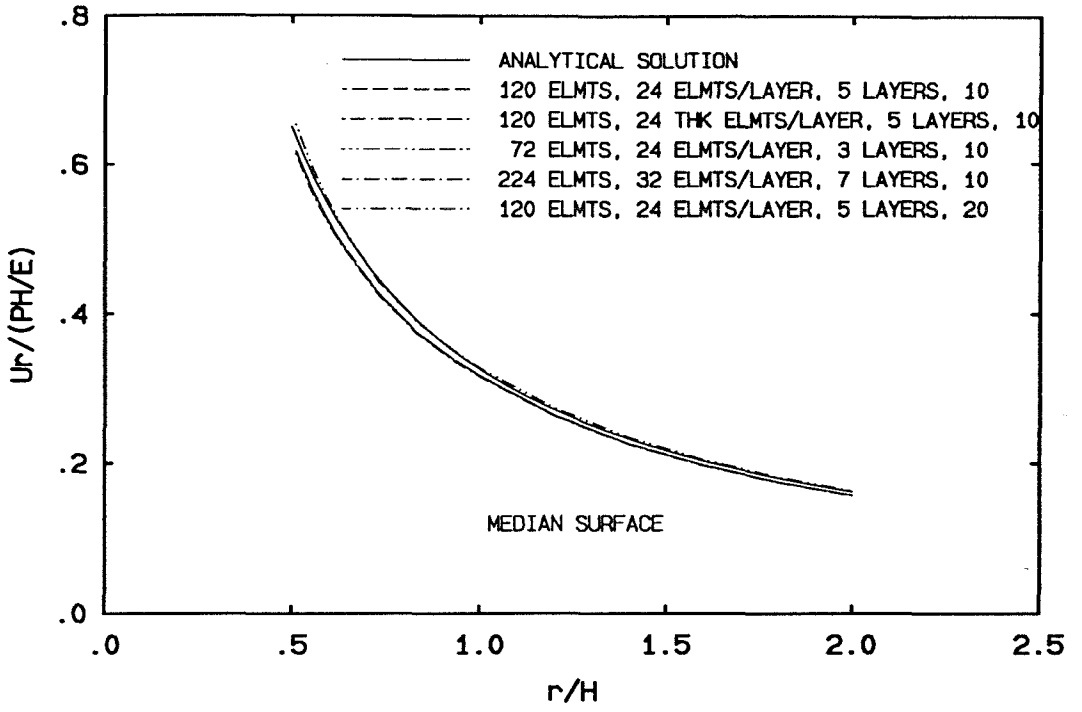

FIGURE 4.15 Normalized Displacement u_r vs. Normalized Distance r; Results Obtained At Median Plane Of Plate

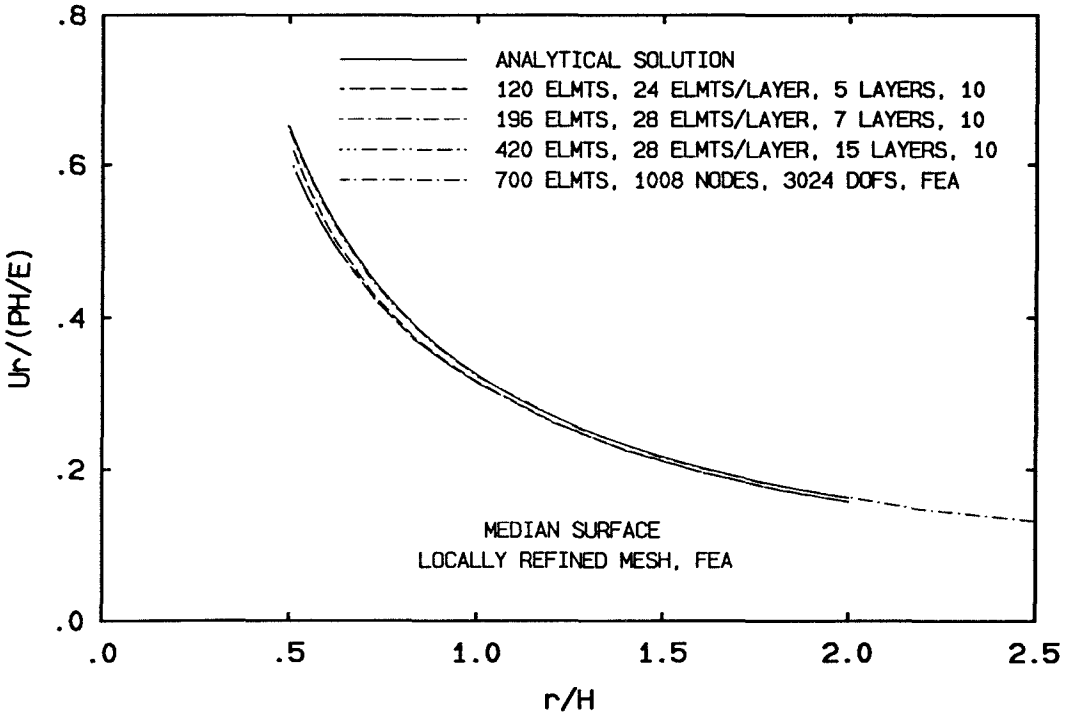

FIGURE 4.16 Normalized Displacement u_r vs. Normalized Distance r; Locally Refined Mesh; Results Obtained At Median Plane Of Plate

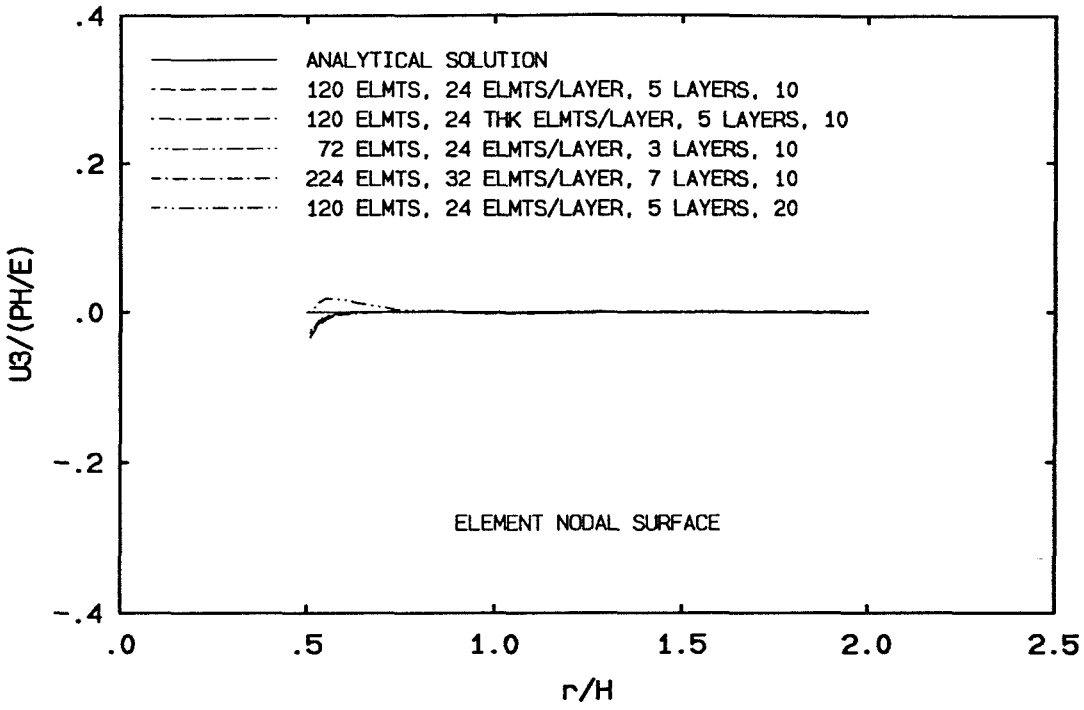

FIGURE 4.17 Normalized Displacement u_3 vs. Normalized Distance r; Results Obtained At Element Nodal Plane Of First Layer

solution. This error can be a major source.

In order to verify the assertion, a mesh with 120 elements is used with the choice of $P = 20$. The result from the modified BEM is excellent. The result agrees with both the analytical and the finite element solutions up to the point very close to the surface of the hole.

4.4.2 Results Of Out-Of-Plane Displacement

The accuracy of result of the modified BEM in the vicinity of the surface of the hole depends on the combination of the discretization sizes and the choice of P.

Figures 4.17 and 4.18, 4.19 and 4.20 show the results of the normalized out-of-plane displacement for the pressurized circular hole problem. The displacement is evaluated at the Group A points.

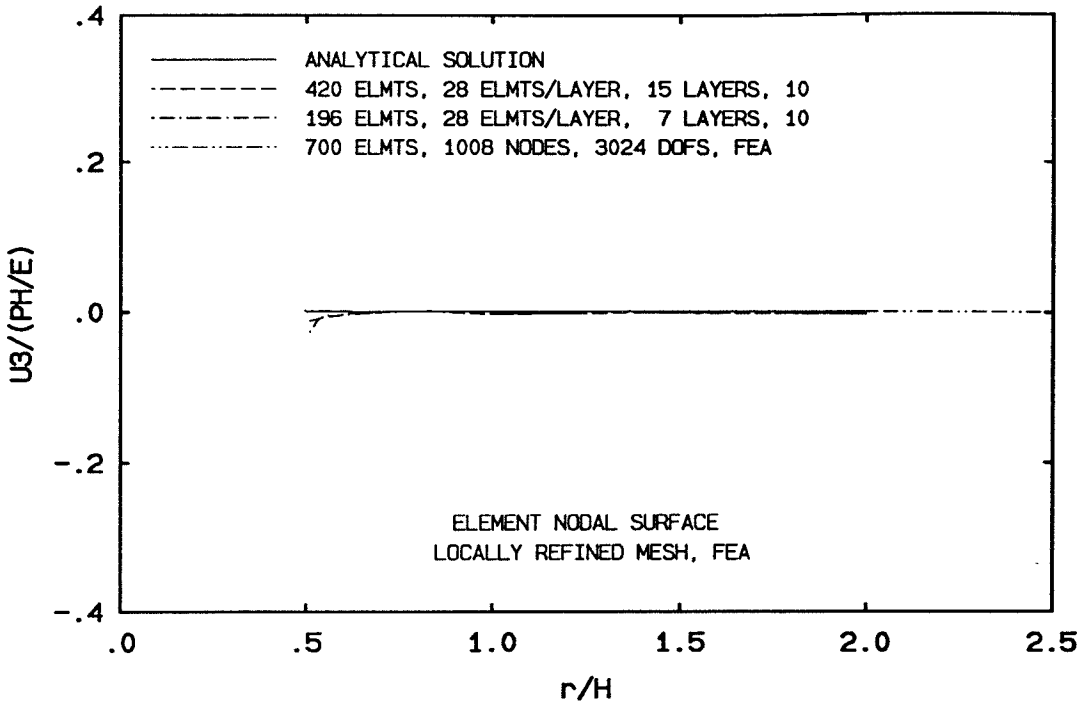

FIGURE 4.18 Normalized Displacement u_3 vs. Normalized Distance r; Locally Refined Mesh; Results Obtained At Element Nodal Plane Of First Layer

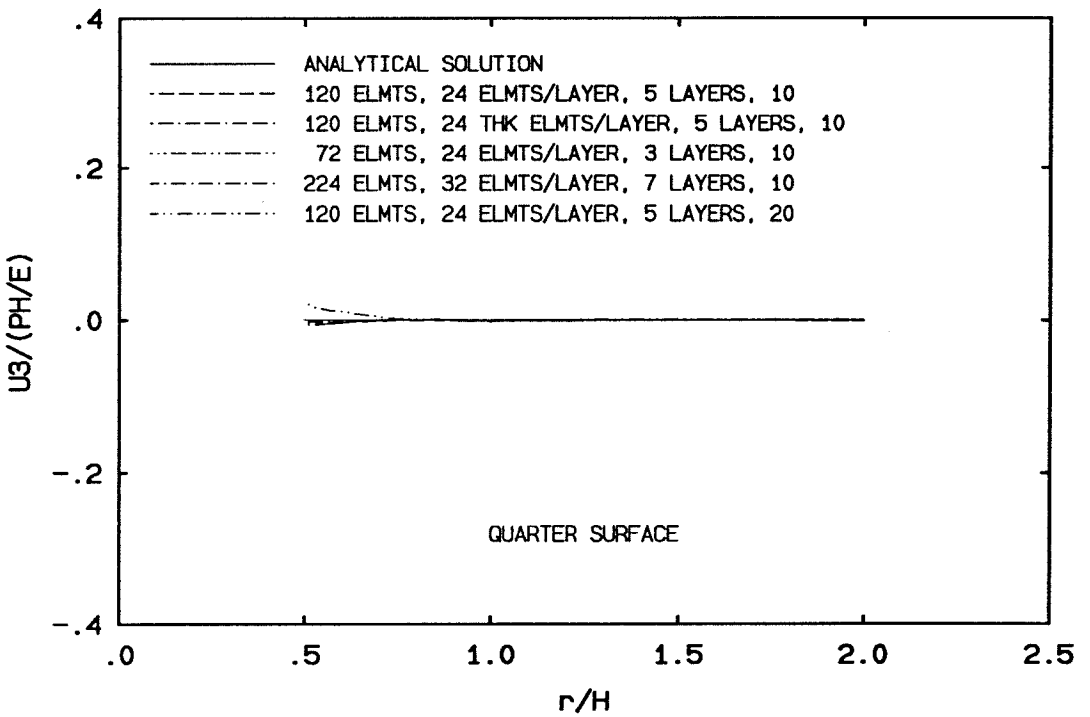

FIGURE 4.19 Normalized Displacement u_3 vs. Normalized Distance r; Results Obtained At Depth Three Quarters From Bottom Surface

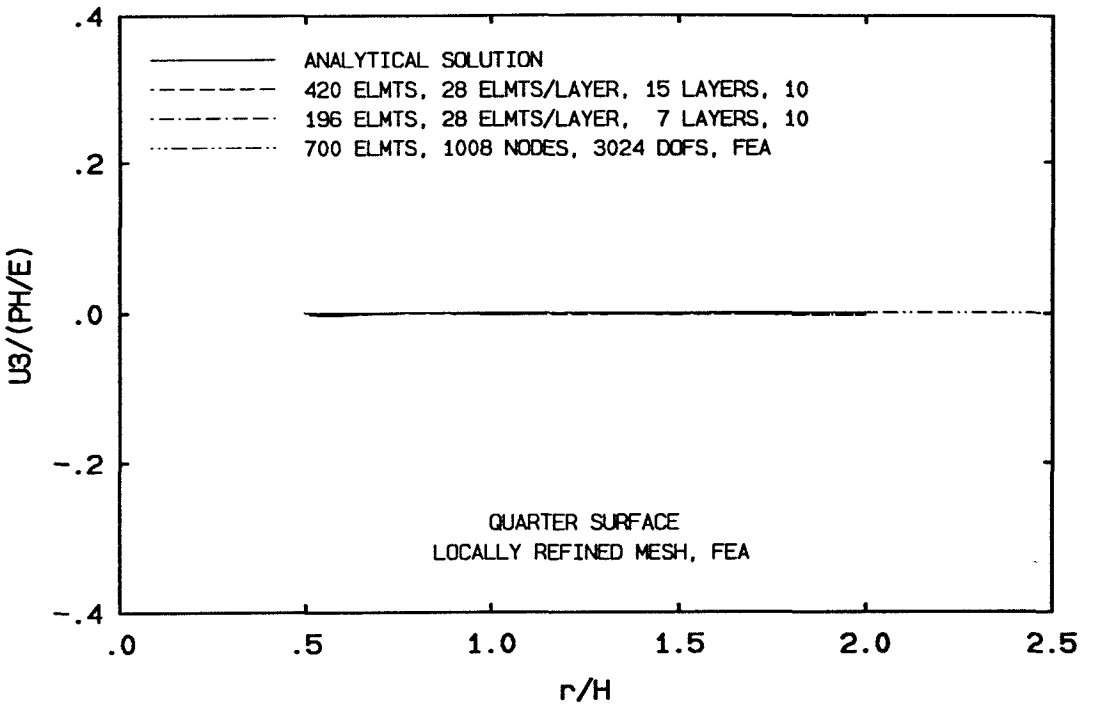

FIGURE 4.20 Normalized Displacement u_3 vs. Normalized Distance r; Locally Refined Mesh; Results Obtained At Depth Three Quarters From Bottom Surface

The displacement u_3 has good agreement with the analytical and the finite element results away from the circular hole surface. But the results deviates from the analytical and the finite element solutions when the displacement is calculated near the surface of the hole. The displacement computed in the element nodal plane of the first layer exhibits a drop near the surface of the hole.

A case involving 420 elements and $P = 10$ was run to establish the sense of how the discretization may affect the results. In this case, the cross section of the circular hole is modeled by 28 elements, and the thickness of the hole is modeled by 15 layers. Denote the overall size of an element as the largest dimension of the element. The overall sizes of the elements are reduced in the case with 420 elements compared with those in any other mesh. It can be seen from Figures 4.18 and 4.20 that the magnitude of the drop near the surface of the hole is reduced.

This fact shows the effect of the discretization error. It shows as the overall sizes of the elements decrease, the error caused by discretization decrease. Although the region in which the drop occurs is still not significantly reduced, the result of this displacement component is quiet acceptable. Further tests using $P = 20$ are in progress. It is expected that with the choice of larger P mated with fine mesh, such as the case with 420 elements, the solution can be improved.

4.4.3 Results Of Displacement Variations Through Thickness

It can be seen from the Figures 4.21, through 4.27 that the displacement variation u_r through thickness are horizontal straight lines except the ones computed very close to the hole surface at $r = 0.53h$, where both the discretization and the effect of P have strong influence. The uniform variation of the displacements through the thickness indicates the two-dimensional nature of the problem. The error between the results obtained from the modified boundary element scheme and the analytical solution is about 5%. As the distance from the center of the hole increases, the thickness variation of u_r approaches the analytical solution.

The deviation in the displacement u_3 from the plane-stress solution near the surface of the hole at $r = 0.53h$ are presented in Figure 4.24, 4.25. This deviation from the analytical solution is caused by the combining effect of the element size and the choice of P. By reducing the element size and increasing P to 20, this deviation will be reduced.

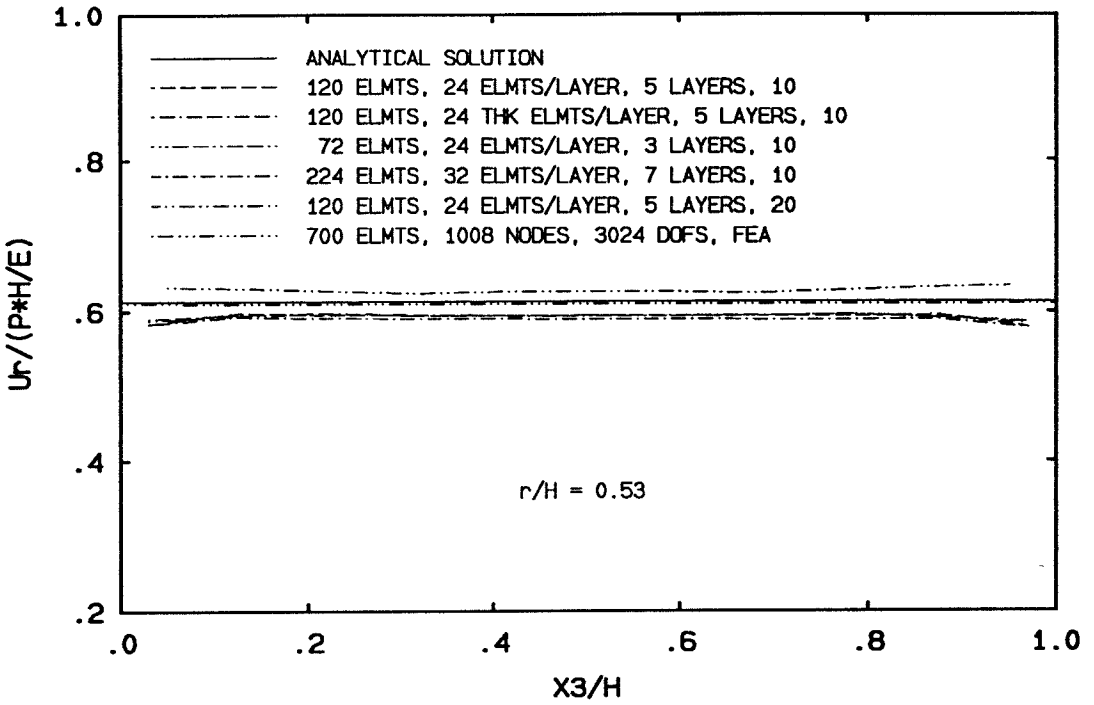

FIGURE 4.21 Normalized Displacement u_r vs. Normalized Depth x_3

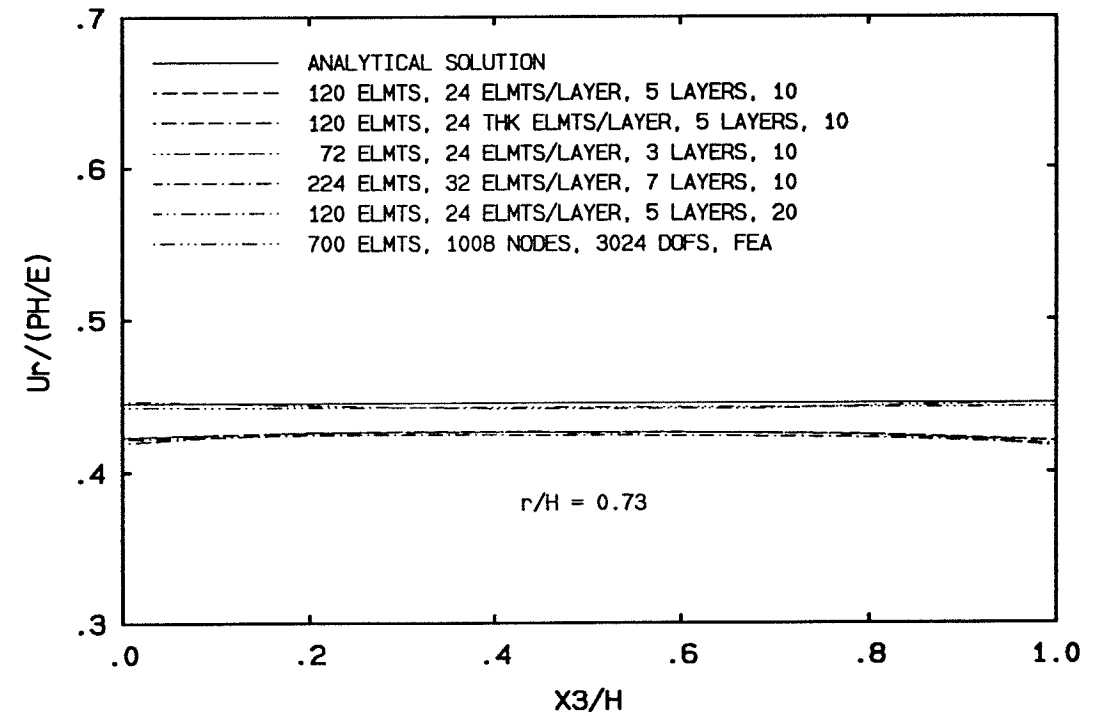

FIGURE 4.22 Normalized Displacement u_r vs. Normalized Depth x_3

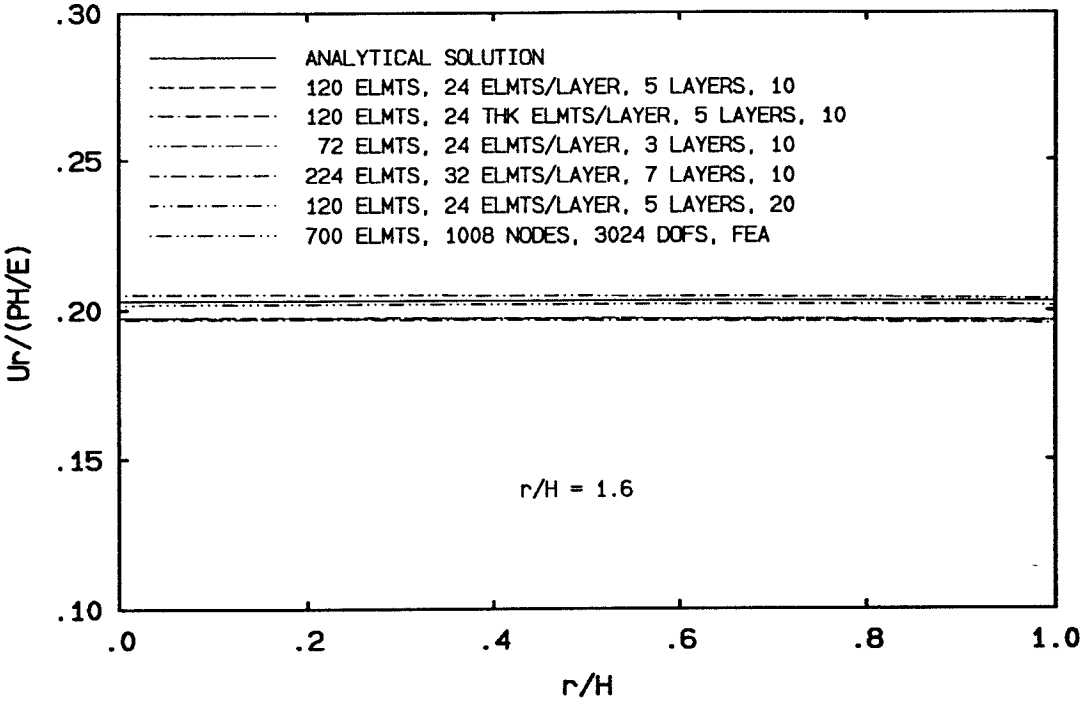

FIGURE 4.23 Normalized Displacement u_r vs. Normalized Depth x_3

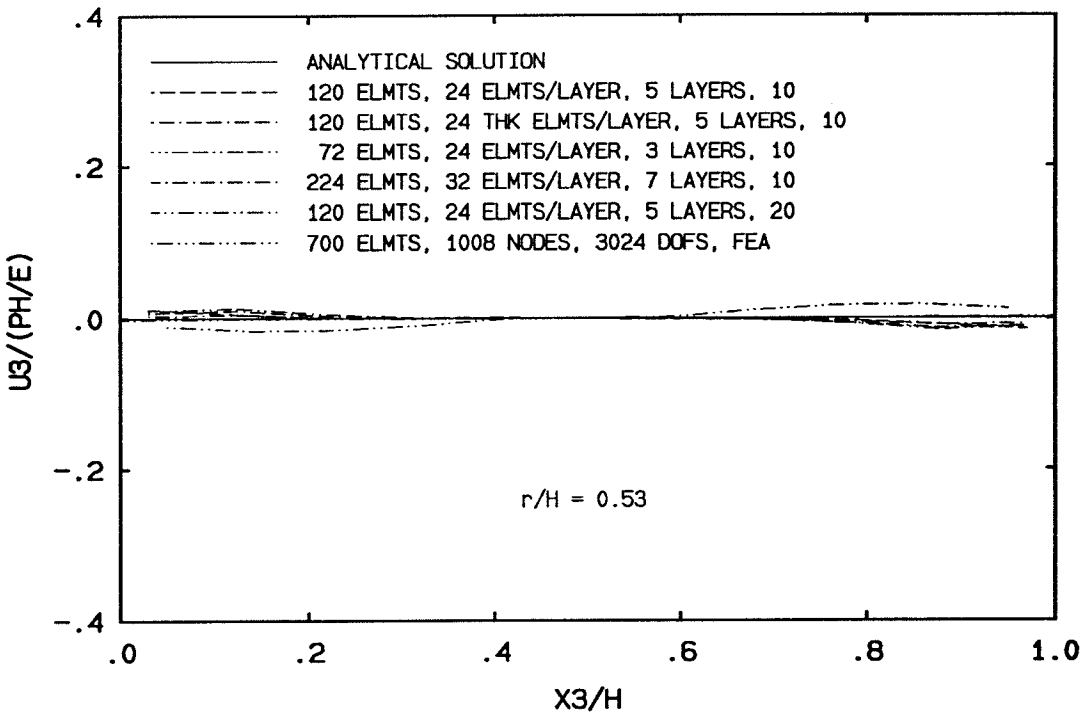

FIGURE 4.24 Normalized Displacement u_3 vs. Normalized Depth x_3

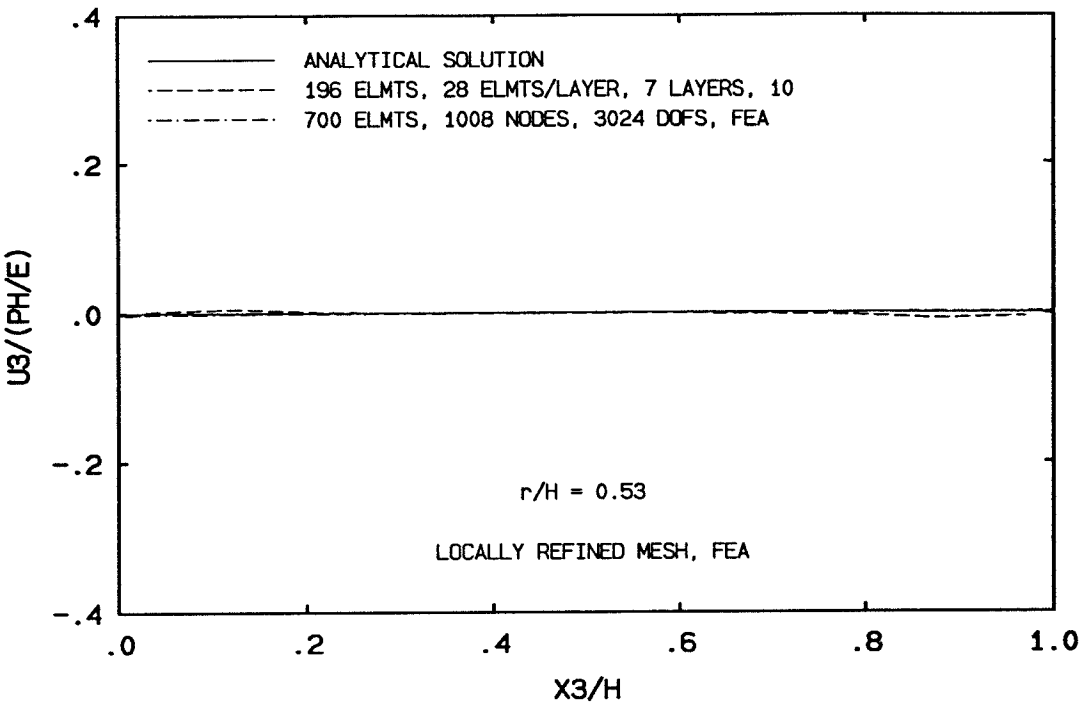

FIGURE 4.25 Normalized Displacement u_3 vs. Normalized Depth x_3; Locally Refined Mesh

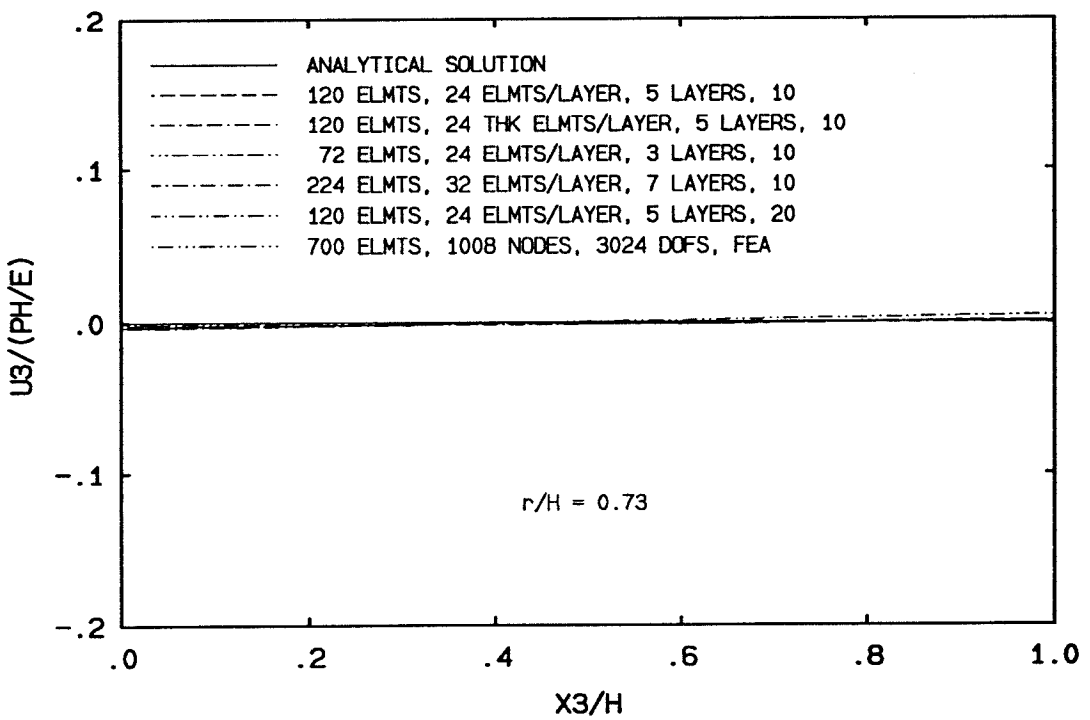

FIGURE 4.26 Normalized Displacement u_3 vs. Normalized Depth x_3

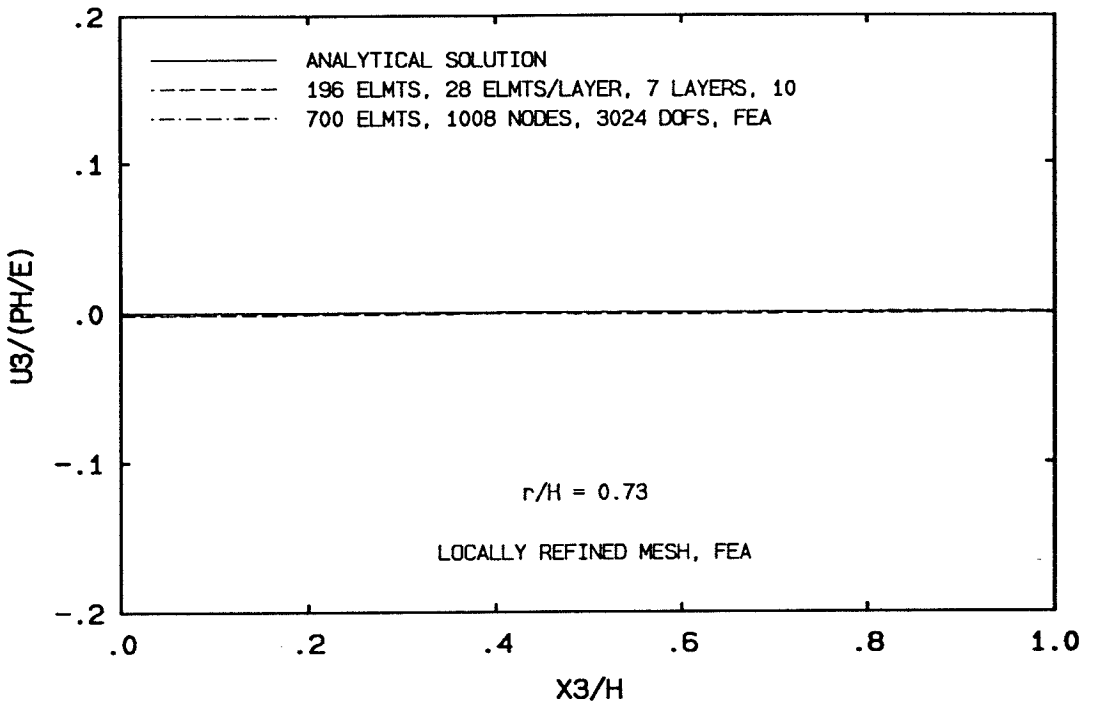

FIGURE 4.27 Normalized Displacement u_3 vs. Normalized Depth x_3; Locally Refined Mesh

4.5 Conclusions

All the above examples are designed with the sole purpose of obtaining insights in the use of the modified boundary element method. It can be concluded from the above results that, by properly modeling the circular hole surface and adequately choosing P, the modified boundary element scheme gives good results to the pressurized circular hole problem. However, these examples may not be the best ones to show the time advantage of the modified BEM. In these examples, the modified BEM runs much slower than the FEM, and this aspect will be discussed in in detail in the conclusions of the next chapter.

Two sources contribute to the error in using the modified boundary element scheme. One source is the discretization error. The overall element size affects the results. By reducing the overall size of the elements, the displacements obtained by

the modified BEM approach the analytical solution. The other source of error is the choice of P. By choosing P to be 10, the fundamental solution for the infinite plate problem can not be calculated with good accuracy, which results in about 5% of the error in the final results for displacements u_r and u_3. By choosing P to be 20, an excellent solution has been obtained, and the error is less than 0.5%.

The accuracy of the results depends on the combination of the element sizes and the choice of the value of P. Since the pressurized circular hole problem is axially symmetric, unless the mesh is uniformly refined, the results would not be changed significantly. Compromises have to be made between the desire of getting accurate results and the expense of obtaining them. Indeed, it is expensive to use both small elements and $P = 20$.

CHAPTER 5

ELLIPTICAL HOLE SUBJECTED TO PRESSURE

This Chapter considers two problems involving an elliptical hole in an infinite three-dimensional plate of uniform thickness, h, subjected to uniform internal pressure p. The upper and the lower surfaces of the plate are traction free. The geometry and loading of the problem is similar to the one shown in Figure 4.1 in Chapter Four. The displacement and the stress fields near the elliptical holes are three-dimensional in nature. Unlike the pressurized circular hole problem, the three-dimensional analytical solutions are not available for these two problems.

These pressurized elliptical hole problems are studied by both the modified boundary element method and the finite element method. One of the problems involves an elliptical hole whose major axis is four times its minor axis, and the other consists of an elliptical hole whose major axis is ten times its minor axis. The boundary element results are compared with the finite element results and with the plane-stress and plane-strain approximations to these problems. The purpose of such comparisons is to identify the region near the elliptical hole surface where the three-dimensional effects are dominant.

5.1 Plane-Stress and Plane-Strain Solutions of Elliptical Hole Subjected to Pressure

Consider the two-dimensional plane-stress and plane-strain approximations of the three-dimensional pressurized elliptical hole problem. The two-dimensional approximations have the same in-plane geometry and loading. Denote the major axis of the elliptical hole as a_0 and the minor axis as b_0. The magnitude of the applied pressure is p. The shear modulus and the Young's modulus are E and ν, respectively.

At this point, only the plane-stress approximation of the pressurized elliptical hole problem is analyzed. The plane-strain approximation of the same problem can be easily formulated by changing the Young's modulus E and the Poisson's ratio ν in the plane-stress problem to $E/(1-\nu^2)$ and $\nu/(1-\nu)$, respectively.

In the plane-stress problem, the thin plate is loaded by pressure applied on the boundary, parallel to the midplane of the plate and distributed uniformly over the thickness, the stress components σ_{33}, σ_{13}, σ_{23} are zero on both surfaces of the plate. It may be assumed that they are zero also within the plate. The state of stress is then specified by σ_{11}, σ_{22}, and σ_{12}. The corresponding displacement components are u_1 and u_2. The stress and displacement components are independent of x_3. Furthermore, this problem can be decomposed as shown in Figure 5.1.

From Figure 5.1, the displacement field of the pressurized elliptical hole problem can be expressed as the superposition of the displacement fields of problems a) and b).

$$\begin{aligned} u_1(x_1,x_2) &= u_{1_a}(x_1,x_2) + u_{1_b}(x_1,x_2), \\ u_2(x_1,x_2) &= u_{2_a}(x_1,x_2) + u_{2_b}(x_1,x_2). \end{aligned} \tag{5.1.1}$$

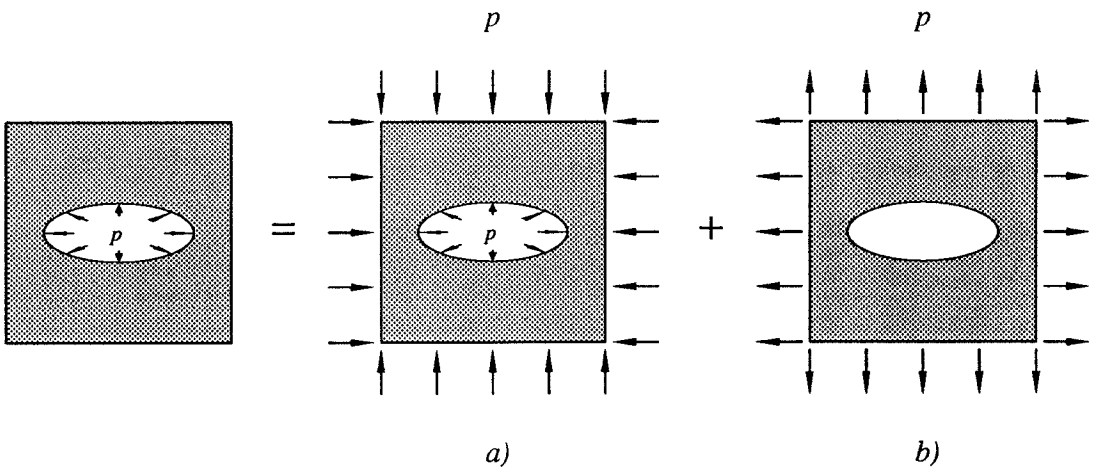

FIGURE 5.1 Problem Decomposition

It is trivial to evaluate the displacement components for problem a).

$$\begin{aligned} u_{1_a}(x_1, x_2) &= \frac{\nu - 1}{E} p x_1; \\ u_{2_a}(x_1, x_2) &= \frac{\nu - 1}{E} p x_2. \end{aligned} \tag{5.1.2}$$

The solutions for the stress and displacement fields of problem b) can be found in [42]. The solutions are described in the elliptical coordinates, which are defined as,

$$x_1 = c_0 \cosh\xi \cos\eta, \qquad x_2 = c_0 \sinh\xi \sin\eta, \tag{5.1.3}$$

where c_0 stands for the focal length of the ellipse, and ξ, η are the elliptical coordinates. The inverse transformation of the above equation for any x_1 and x_2 is given by,

$$\xi = \ln \frac{a+b}{c_0};$$

$$\eta = \begin{cases} \sin^{-1}\left(\dfrac{x_2}{c_0 \sinh\xi}\right), & \text{if } x_2 \geq 0; \\ \pi - \sin^{-1}\left(\dfrac{x_2}{c_0 \sinh\xi}\right), & \text{if } x_2 < 0, \end{cases} \tag{5.1.4}$$

where

$$a = \sqrt{\frac{{x_1}^2 + {x_2}^2 + {c_0}^2 + \sqrt{\left({x_1}^2 + {x_2}^2 - {c_0}^2\right)^2 + 4{x_2}^2{c_0}^2}}{2}};$$

$$b = \sqrt{\frac{{x_1}^2 + {x_2}^2 - {c_0}^2 + \sqrt{\left({x_1}^2 + {x_2}^2 - {c_0}^2\right)^2 + 4{x_2}^2{c_0}^2}}{2}}. \tag{5.1.5}$$

The in-plane displacement fields for the plane-stress problem are given by,

$$\begin{aligned} u_{1_b}(\xi,\eta) = \Big\{ & -Ac\Big[\sin\eta\sinh\xi\left(\cos\eta\sin\eta\sinh^2\xi + \cos\eta\sin\eta\cosh^2\xi\right) \\ & + \cos\eta\cosh\xi\left(\cos^2\eta\cosh\xi\sinh\xi - \sin^2\eta\cosh\xi\sinh\xi\right)\Big] \\ & \Big/\left(\cos^2\eta\sinh^2\xi + \sin^2\eta\cosh^2\xi\right) \\ & - Bc\cos\eta\sinh\xi\Big/\left(\cos^2\eta\sinh^2\xi + \sin^2\eta\cosh^2\xi\right) \\ & + Ac\cos\eta(3-\nu)\sinh\xi\Big/(1-\nu)\Big\}\Big/(2\mu); \end{aligned}$$

$$\begin{aligned} u_{2_b}(\xi,\eta) = \Big\{ & -Ac\Big[\cos\eta\cosh\xi\left(\cos\eta\sin\eta\sinh^2\xi + \cos\eta\sin\eta\cosh^2\xi\right) \\ & - \sin\eta\sinh\xi\left(\cos^2\eta\cosh\xi\sinh\xi - \sin^2\eta\cosh\xi\sinh\xi\right)\Big] \\ & \Big/\left(\cos^2\eta\sinh^2\xi + \sin^2\eta\cosh^2\xi\right) \\ & - Bc\sin\eta\cosh\xi\Big/\left(\cos^2\eta\sinh^2\xi + \sin^2\eta\cosh^2\xi\right) \\ & + Ac\sin\eta(3-\nu)\cosh\xi\Big/(1-\nu)\Big\}\Big/(2\mu), \end{aligned} \tag{5.1.6}$$

where μ is the shear modulus, and A, B and ξ_0 are defined as follows,

$$\begin{aligned} A &= \frac{p}{2}, \\ B &= -A\cosh 2\xi_0 = -\frac{1}{2}p\cosh 2\xi_0, \\ \xi_0 &= tanh^{-1}\Big(\frac{b_0}{a_0}\Big). \end{aligned} \tag{5.1.7}$$

The above is the plane-stress solution of the pressurized elliptical hole problem. An estimation of the out-of-plane displacement u_3 for the pressurized elliptical hole problem can be obtained as follows. From the three-dimensional strain-displacement relationships, one has,

$$u_3(x_1, x_2, x_3) = \int_{h/2}^{x_3} \epsilon_{33}(x_1, x_2, x_3)\, dx_3, \qquad 0 \le x_3 \le h. \tag{5.1.8}$$

The coordinate system for the above expression is located at the bottom surface of the plate. The origin of the coordinate system is at the center of the ellipse. The x_1 and x_2 axes are placed along the major and minor axes of the ellipse, respectively. x_2 axis is along the minor By using the constitutive law, the above equation becomes,

$$\begin{aligned} u_3(x_1, x_2, x_3) = -\int_{\frac{h}{2}}^{x_3} & \frac{\nu(\sigma_{11}(x_1, x_2, x_3) + \sigma_{22}(x_1, x_2, x_3))}{E} \\ & \left[1 - \frac{\sigma_{33}(x_1, x_2, x_3)}{\nu(\sigma_{11}(x_1, x_2, x_3) + \sigma_{22}(x_1, x_2, x_3))}\right] dx_3. \end{aligned} \tag{5.1.9}$$

When the ratio of $\sigma_{33}(x_1, x_2, x_3)/(\nu(\sigma_{11}(x_1, x_2, x_3) + \sigma_{22}(x_1, x_2, x_3)))$ is zero, and plane-stress conditions are achieved, then the above equation reduces to,

$$\begin{aligned} u_3(x_1, x_2, x_3) &= -\frac{\nu}{E}(x_3 - \frac{h}{2})(\sigma_{11}(x_1, x_2) + \sigma_{22}(x_1, x_2)) \\ &= -\frac{\nu}{E}(x_3 - \frac{h}{2})\left[\frac{2p\sinh 2\xi}{\cosh 2\xi - \cos 2\eta} - 2p\right], \end{aligned} \tag{5.1.10}$$

where $\sigma_{11}(x_1, x_2)$ and $\sigma_{22}(x_1, x_2)$ are the plane-stress thickness averages. The first term in the square bracket comes from problem b), while the second term comes from problem a). Eqs. (5.1.1), (5.1.2), (5.1.6) and (5.1.10) provide the approximations for the displacement fields for the analytical solution.

As mentioned before, the plane-strain solution of the pressurized elliptical hole problem can be easily obtained by replacing E and ν in equations (5.1.2), (5.1.6). In addition, both ϵ_{33} and u_3 vanish identically in the plane-strain solution.

5.2 Modeling Of Elliptical Hole Surface

Similar to the circular-hole case, this pressurized elliptical hole problem is self-equilibrated. The upper and lower surfaces of the plate are traction-free. The modeling and discretization of the problem is only limited on the elliptical hole surface.

The Cartesian coordinate system for this problem is located in the lower surface of the plate; the origin of the coordinate system is located at the center of the elliptical hole. The x_1 and the x_2 axes are in the directions of the major and the minor axes of the ellipse, respectively. The x_3 axis is in the thickness direction pointing towards the upper surface of the plate.

Two problems involving different elliptical holes are analyzed. The ratios of the major and the minor axes of the elliptical holes are 4 and 10, respectively. This ratio is referred to as the *aspect ratio* in the following sections. Three boundary element meshes are used to model the two elliptical holes. Two meshes involving 280 and 336 elements are used to model the elliptical hole with the aspect ratio of 4, and the other involving 280 elements is used to model the elliptical hole with the aspect ratio of 10. Two finite element meshes are also used. One mesh consists of 1045 elements with 1440 nodes and 4320 degrees of freedom, and it models the elliptical hole with aspect ratio of 4. The other finite element mesh is composed of 1200 elements with 1638 nodes and 4914 degrees of freedom, this mesh models

the elliptical hole with the aspect ratio of 10. It is important to point out that the boundary element meshes coincide with the finite element meshes along the surface of the elliptical hole.

All the elements used are flat rectangular elements. The displacement and the traction variations over an element are assumed to be constant. The cross section of the elliptical hole is modeled by 40 elements with different widths. In the case involving 336 elements, the mesh for modeling the cross section is locally refined. Two of the biggest elements on both sides of the ellipse are subdivided with five fine elements, respectively.

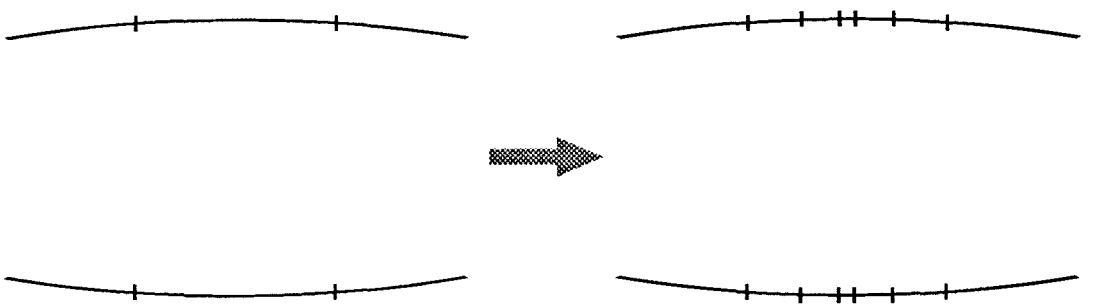

FIGURE 5.2 Local Refinement Of Elements

The thickness of the hole is modeled by 7 layers of of elements. The thicknesses of the layers are $0.1h$, $0.1h$, $0.2h$, $0.2h$, $0.2h$, $0.1h$, and $0.1h$. Because of the limitation of the computational time, only $P = 10$ is used in all these mesh schemes.

Four groups (Group A, B, C, and D) of internal points are used to examine the displacement field inside the plate. For the elliptical hole with the axial ratio of 10, only two groups (Group A and Group B) of internal points are used.

Group A contains 48 internal points, and the points are equally divided, and they are placed in three arrays at three different depths along the extension of the *major* axis of the ellipse. The first array contains 16 points and it is located in the element nodal plane of the first layer, the depth of which is: $x_3 = 0.95h$; the second array contains the same number of points and its depth is $0.75h$, and the third array of points is located in the mid-plane of the plate. The positions of the points in an array in the x_1 direction are: $x_1 = 0.51h$, $0.53h$, $0.55h$, $0.57h$, $0.59h$, $0.63h$, $0.73h$, $0.83h$, $0.93h$, $1.0h$, $1.2h$, $1.4h$, $1.6h$, $1.8h$, and $2.0h$.

Group B has 55 internal points, and these points are placed in five lines through the thickness. These lines are parallel to one another, and they are placed along the extension of the *major* axis of the ellipse. The positions of the lines are: $x_2 = 0$ and $x_1 = 0.51h$, $0.53h$, $0.73h$, $1.0h$, $1.6h$. The displacements are evaluated at 11 points in each line. The first and the last points at both ends of the lines are: $x_3 = 0.03h$ and $0.97h$ for the first and the second lines; and $x_3 = 0$ and $x_3 = 1.0h$ for the rest three lines.

Group C also contains 48 internal points. Contrast to the Group A points, these points are placed in three arrays along the extension of the *minor* axis of the elliptical hole. All the arrays contain the same number of points, and they are located at the same depths as those placed along the major axis, respectively. The positions of the points in an array in the x_2 direction are: $x_2 = 0.13h$, $0.15h$, $0.17h$, $0.19h$, $0.21h$, $0.23h$, $0.26h$, $0.45h$, $0.64h$, $0.83h$, $1.0h$, $1.2h$, $1.4h$, $1.6h$, $1.8h$, $2.0h$.

Group D has also 55 internal points. Similar to the Group B points, these points are placed in five lines through the thickness. The lines are parallel to one another, and they are placed along the extension of the *minor* axis of the ellipse. The positions of the lines are: $x_1 = 0$ and $x_2 = 0.13h$, $0.15h$, $0.45h$, $1.0h$, and $1.6h$. The positions of the points in each line are the same as those of the Group B points.

For the elliptical hole with the aspect ratio of 4, the internal points in the Group A, B, C, and D are used in the mesh with 280 elements; only the Group A, C, and D points are used in the mesh with 336 elements. For the elliptical hole with the aspect ratio of 10, the internal points in the Group A and B are used.

Figure 5.3, 5.4 show the meshes and the internal points for the elliptical hole with the aspect ratio of 4. Figure 5.5 shows the mesh and the internal points for the elliptical hole with the aspect ratio of 10.

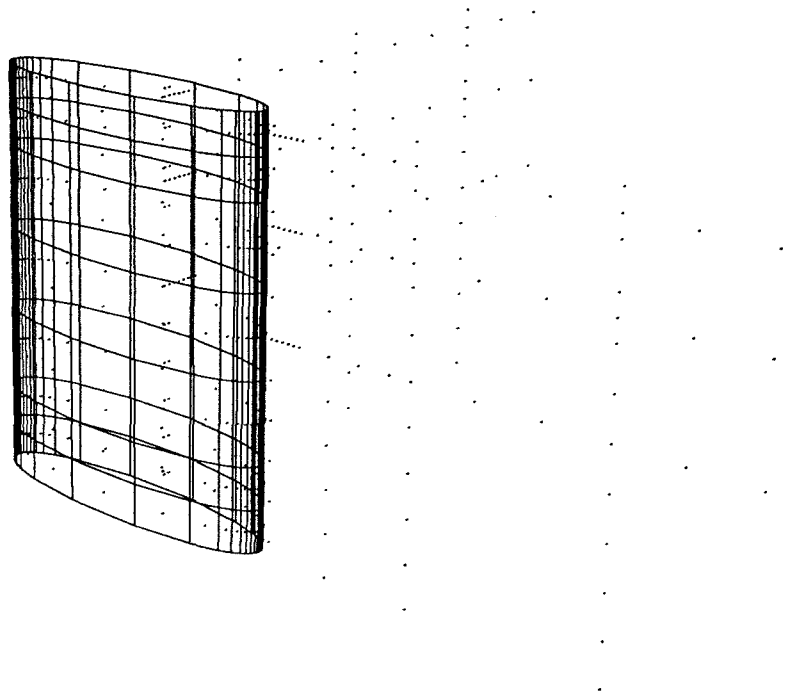

FIGURE 5.3 Mesh For Elliptical Hole With 280 Elements, Aspect Ratio is 4.

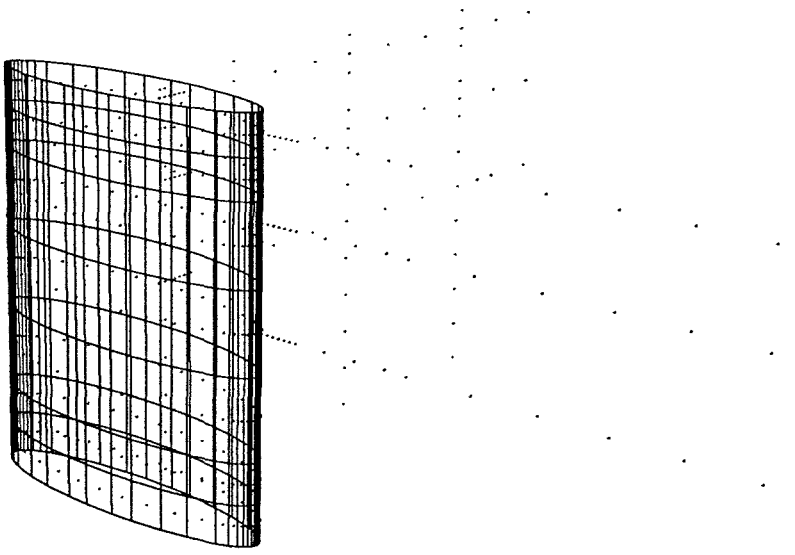

FIGURE 5.4 Locally Refined Mesh For Elliptical Hole With 336 Elements, Axial Ratio is 4.

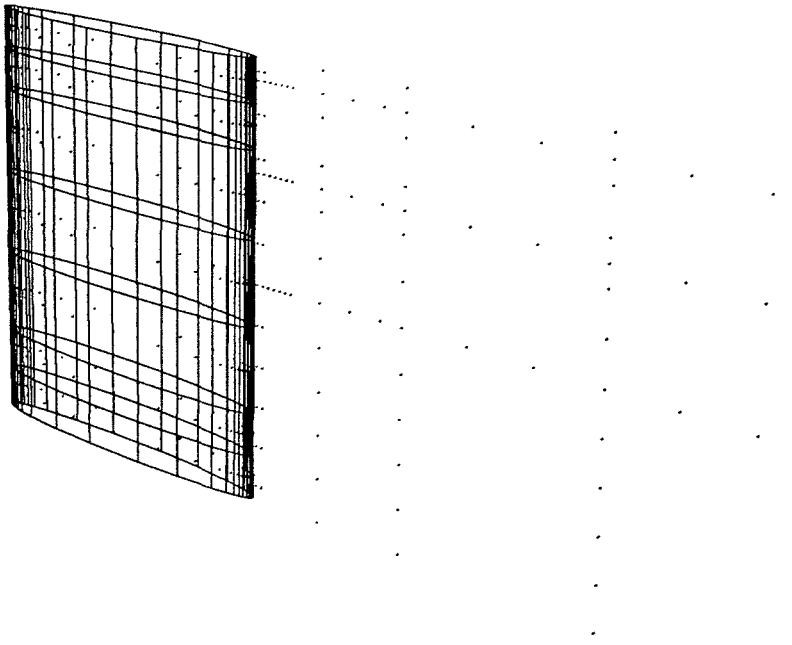

FIGURE 5.5 Mesh For Elliptical Hole With 280 Elements, Aspect Ratio is 10

5.3 Modeling Of Elliptical-Hole Problem For FEA

Similar to the circular hole problem, only one eighth of the truncated plate is modeled for the finite element analysis. By analyzing the two-dimensional plane-stress solution of the pressurized elliptical hole problem, when the remote surface is chosen to be at the radius of about 20 times the thickness, the stress and the displacement at the remote surface are of the order of $O(10^{-4})$, and $O(10^{-2})$. It is then assumed based on the above facts that the traction-free boundary conditions can be applied on the remote surface. The schematic of the finite element model is shown in Figure 5.6. The finite element meshes for both elliptical holes are shown in Figures 5.7, 5.8, 5.9, and 5.10.

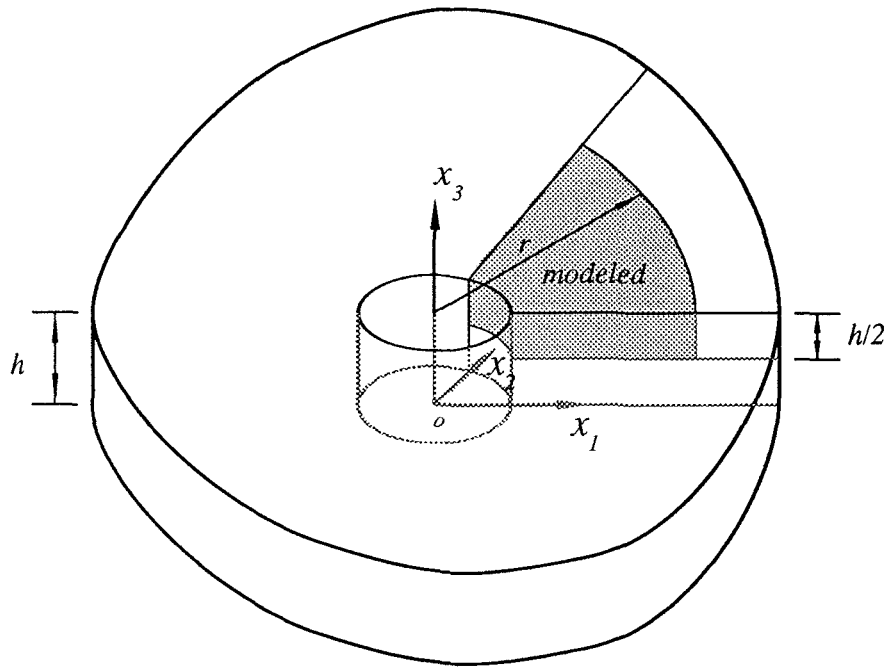

FIGURE 5.6 Model For Finite Element Analysis

The boundary conditions for the finite element model are:

1) $u_2 = 0$ at the nodal points on the x_1–x_3 plane;

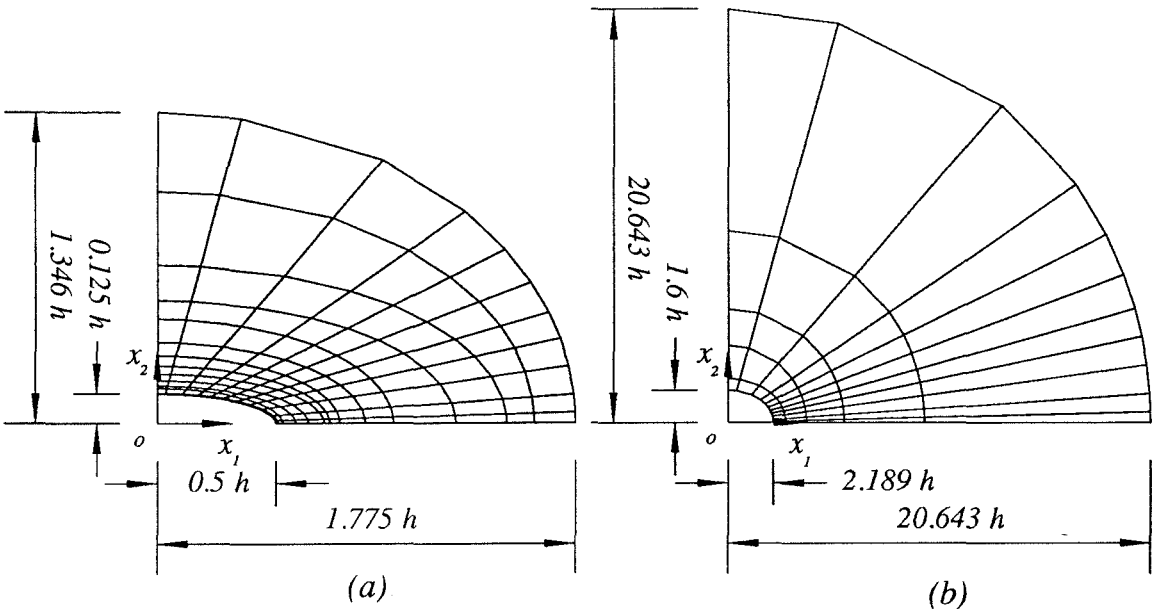

FIGURE 5.7 Detail Of In-Plane Mesh For FEA With 1045 Elements; Axial Ratio is 4.

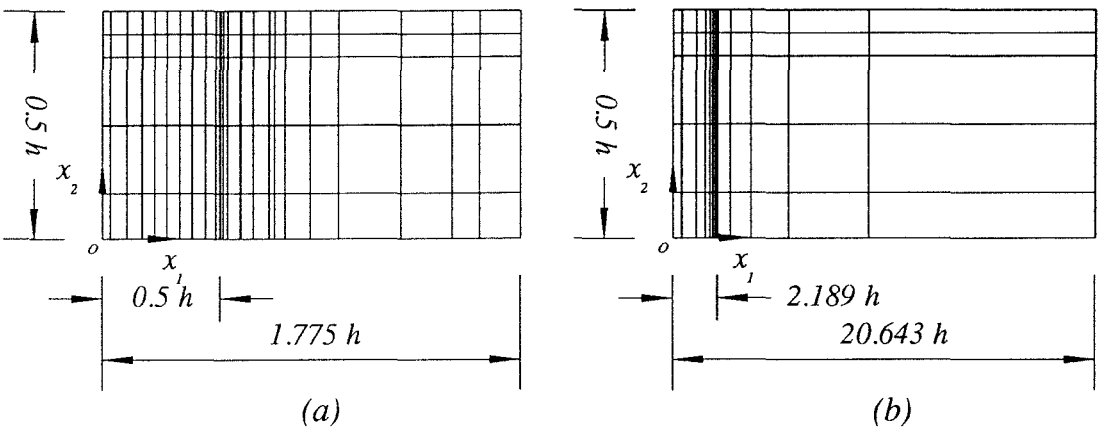

FIGURE 5.8 Detail Of Mesh Variation Through Thickness, 1045 Elements; Axial Ratio is 4.

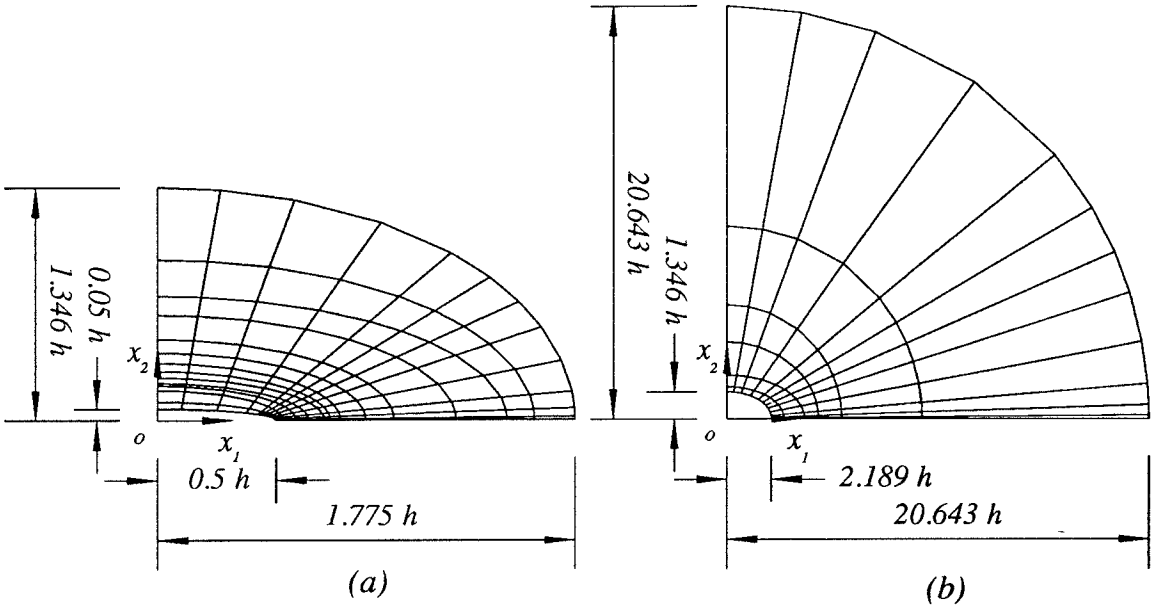

FIGURE 5.9 Detail Of In-Plane Mesh For FEA With 1200 Elements; Axial Ratio is 10.

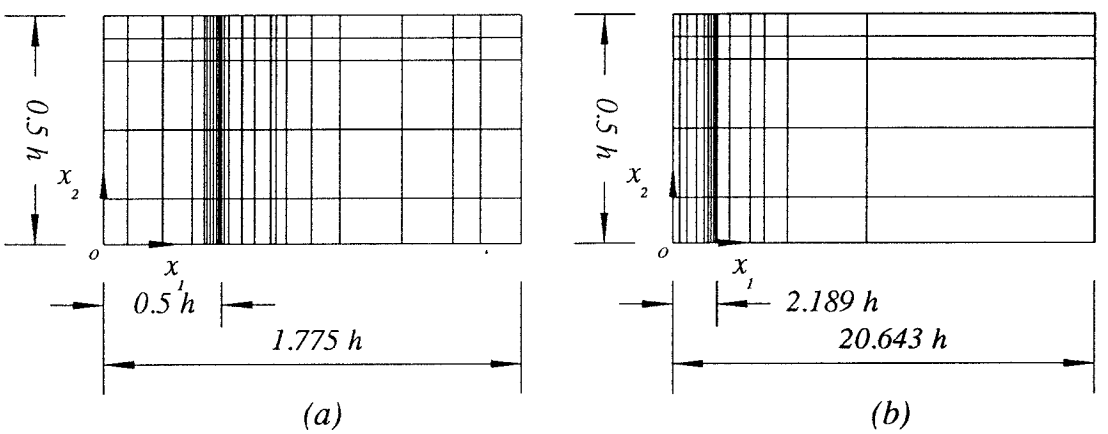

FIGURE 5.10 Detail Of Mesh Variation Through Thickness, 1200 Elements; Axial Ratio is 10.

2) $u_1 = 0$ at the nodal points on the x_2–x_3 plane;

3) $u_3 = 0$ at the nodal points on the x_1–x_2 plane;

4) $t_1 = t_2 = t_3 = 0$ at the nodal points on the top surface of the plate;

5) specified traction boundary condition on the elliptical hole surface;

6) traction-free boundary condition of the truncated cylindrical surface.

All the elements are placed evenly in five element layers. The thicknesses of the layers from the midplane to the top of the plate are $0.1h$, $0.15h$, $0.15h$, $0.05h$, and $0.05h$. The elliptical hole with the aspect ratio of 4 is modeled by 1045 elements with 1440 nodes, and the other elliptical hole is modeled by 1200 elements with 1638 nodes. Each nodes have six degrees of freedom, in which three degrees of freedom are specified.

5.4 Results And Discussions

In this section, the results of the proposed BEM are presented. These results are compared with the finite element results. In addition, all numerical results are compared with the plane-stress and plane-strain approximations of the problems. By including comparisons of the three-dimensional results with the two-dimensional approximations, the regions at the vicinity of the elliptical hole, where the three-dimensional effects dominate, can be identified. Furthermore, the two-dimensional idealizations will be proved to be inadequate in this region.

The results are summarized in Figures 5.11 through 5.48. When the displacements are computed at the Group A points, the normalized displacements u_1 and u_3 are plotted versus the normalized distance x_1; when the displacements are computed at the Group C points, the normalized displacements u_2 and u_3 are plotted against the normalized distance x_2; finally, when the displacements are computed at the points in Group C and D, the normalized displacements u_1, u_2 and u_3 are displayed with respect to the normalized depth x_3.

The tips of the ellipse are located at $x_1/h = \pm 0.5$, $x_2 = 0$ and $0 \leq x_3/h \leq 1.0$. For the same reason as in the pressurized circular hole problem, the Young's modulus E and the Poisson's ratio are taken to be 1 and 0.3.

Call the pressurized elliptical hole problem with the aspect ratio of 4 *problem one*; call the pressurized elliptical hole problem with the axial ratio of 10 *problem two*.

5.4.1 Results Of In-Plane Displacements For Problem One

The in-plane displacements do not show strong three-dimensional signs as compared to the out-of-plane displacement. The results of the displacement u_1 computed at different cross sections of the plate (nodal surface $0.95h$, three quarter surface $0.75h$, and midplane $0.5h$) along the x_1 direction are shown in Figures 5.11, 5.12 and 5.13; the results of the displacement u_2 evaluated at the same cross sections along the x_2 direction are show in figures 5.19, 5.20, 5.21. The numerical results obtained from both the modified BEM and the FEM are in fairly good agreement, and they are situated between the plane-stress and the plane-strain solutions with the plane-stress solution acting as the lower limit of the three-dimensional solutions.

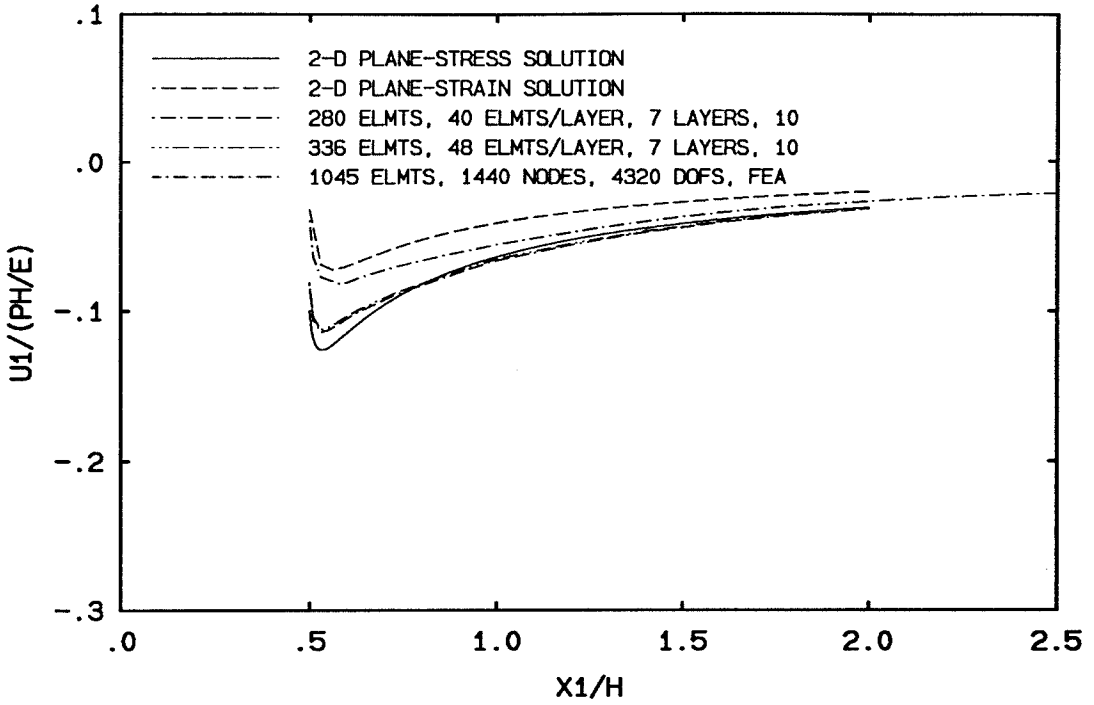

FIGURE 5.11 Normalized Displacement u_1 vs. Normalized Distance x_1; Results Obtained In Element Nodal Plane Of First Layer.

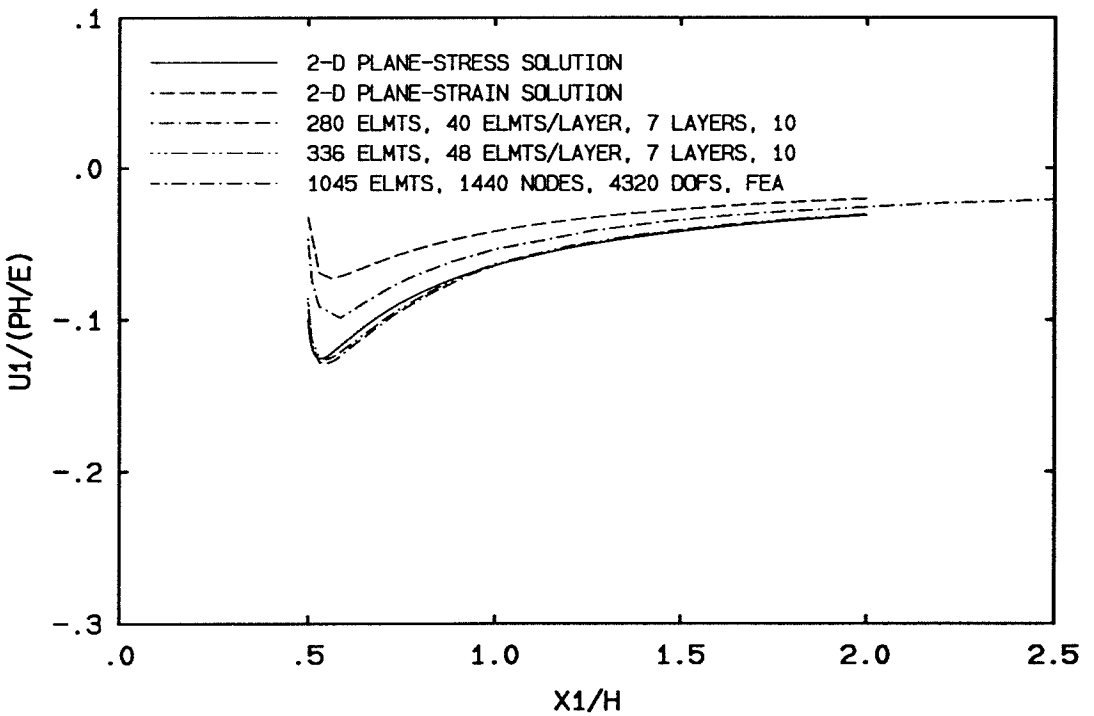

FIGURE 5.12 Normalized Displacement u_1 vs. Normalized Distance x_1; Results Obtained At Depth Three Quarters From Lower Surface Of Plate.

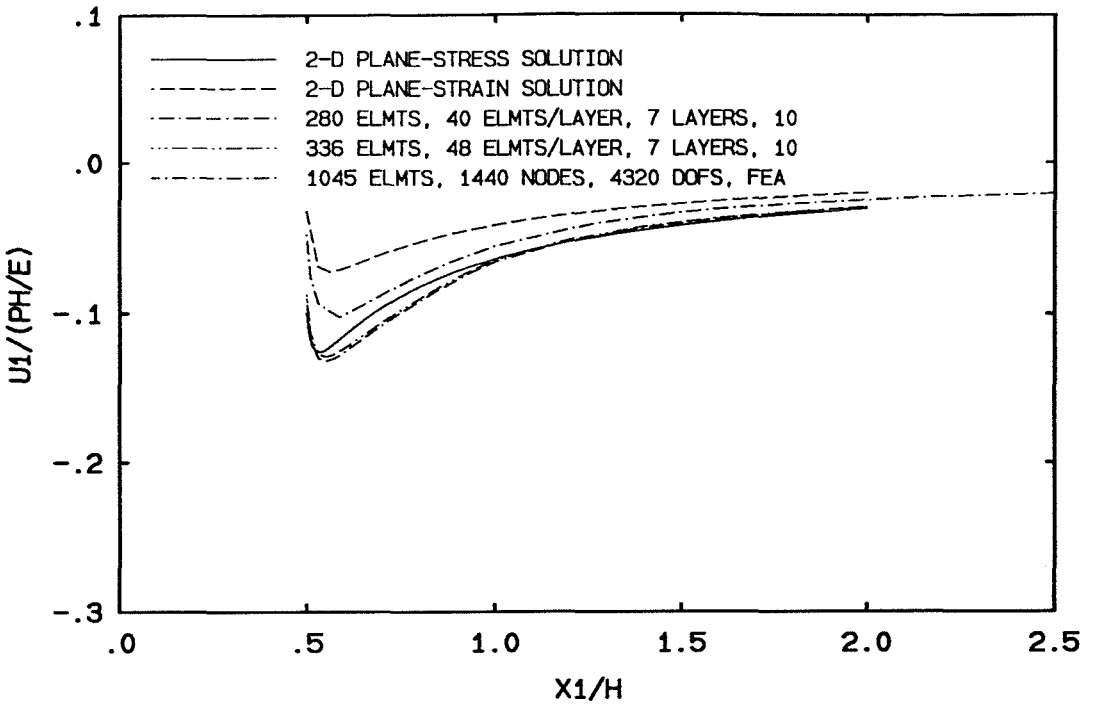

FIGURE 5.13 Normalized Displacement u_1 vs. Normalized Distance x_1; Results Obtained In Median Plane Of Plate.

The BEM results of the displacement u_1 along the x_1 direction shows better agreement with the plane-stress solution. Because of the finite thickness of the plate, and the fact that the dimensions of the elliptical hole are comparable to the thickness of the plate, the displacements will not be close to the plane-strain solution unless it is observed very close to the surface of the elliptical hole and near the midplane of the plate. Figure 5.14 and 5.15 show the strain ϵ_{33} and stress ratio $\sigma_{33}/(\nu(\sigma_{11}+\sigma_{22}))$ along the x_1 direction obtained by the FEM, respectively. Both figures show that the plane-strain conditions can not be satisfied anywhere along the x_1 direction.

However, Figure 5.16 shows that σ_{33} approaches zero very quickly. σ_{33} approaches zero at about half the plate thickness away from the surface of the hole, and it remains zero afterwards. Figure 5.17 and 5.18 show that the stress components σ_{11} and σ_{22} are independent of x_3 when the distance to the surface of the

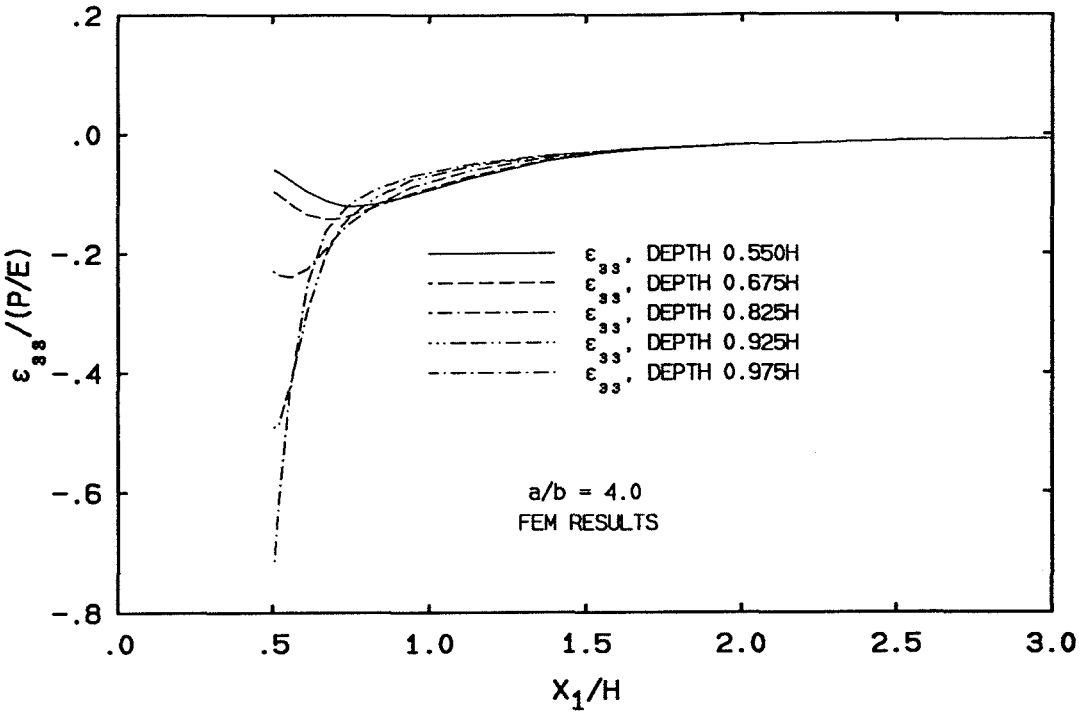

FIGURE 5.14 Normalized Strain ϵ_{33} vs. Normalized Distance x_1; Results Obtained From FEM

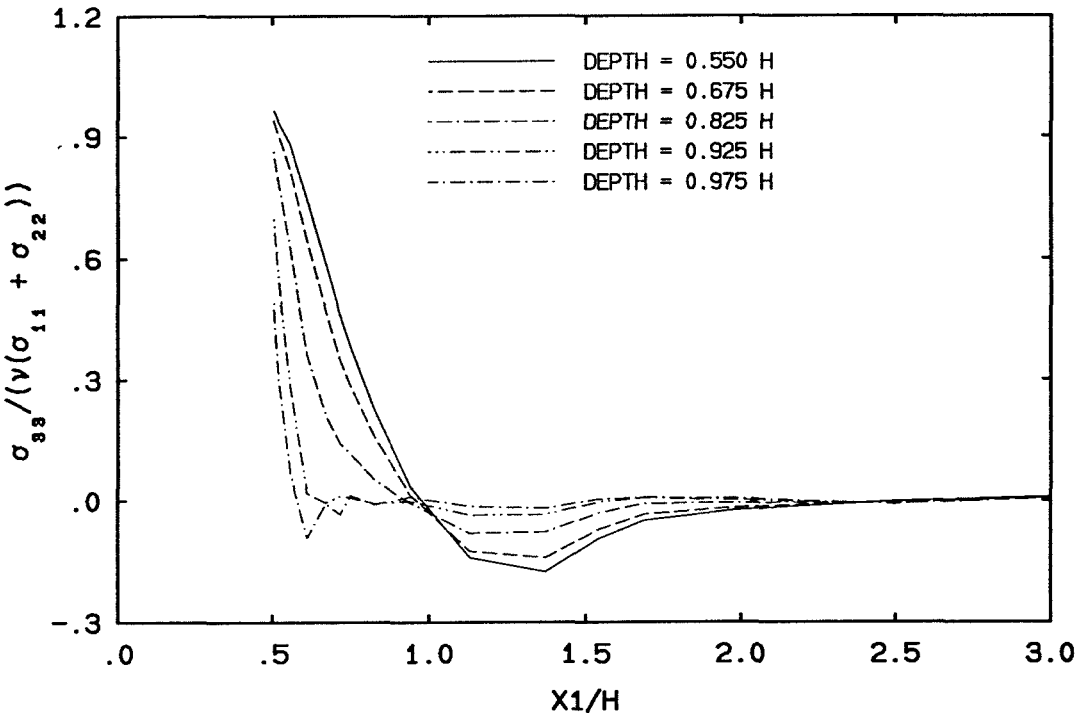

FIGURE 5.15 Stress Ratio $\sigma_{33}(x_1, x_2, x_3)/(\nu(\sigma_{11}(x_1, x_2, x_3))$ vs. Normalized Distance x_1; Results Obtained From FEM

hole is larger than about 3/4 of the plate thickness. Therefore, the plane-stress conditions are better satisfied, and the three-dimensional solution is expected to be closer to the plane-stress solution. These stress variations along the x_1 direction are obtained from the FEM.

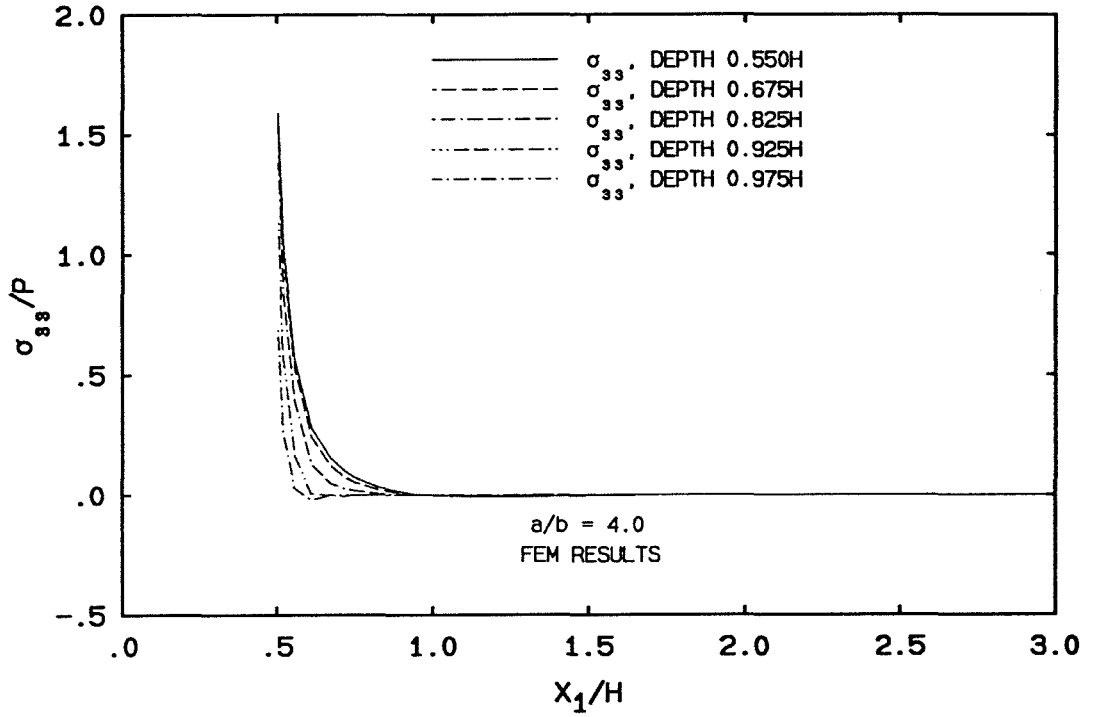

FIGURE 5.16 Normalized Stress σ_{33} vs. Normalized Distance x_1; Results Obtained From FEM.

Figures 5.11 through 5.21 show that, as the cross section on which the displacement is computed moves towards the midplane of the plate, the displacement u_1 along the x_1 direction obtained from both the BEM and the FEM approaches to the plane-stress solution. At the tips of the ellipse, by close observation, the results have a tendency to approach the plane-strain solution.

In the x_2 direction however, when the displacement u_2 is computed at the Group C points, the BE and FE results of the displacement variations of u_2 with

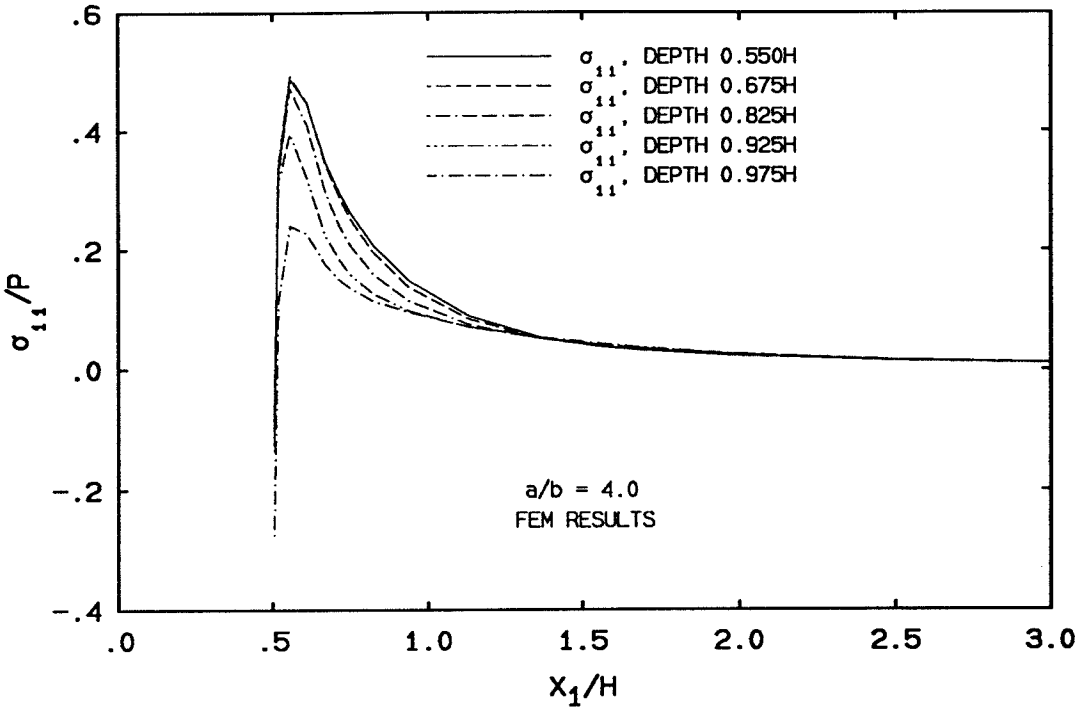

FIGURE 5.17 Normalized Stress σ_{11} vs. Normalized Distance x_1; Results Obtained From FEM.

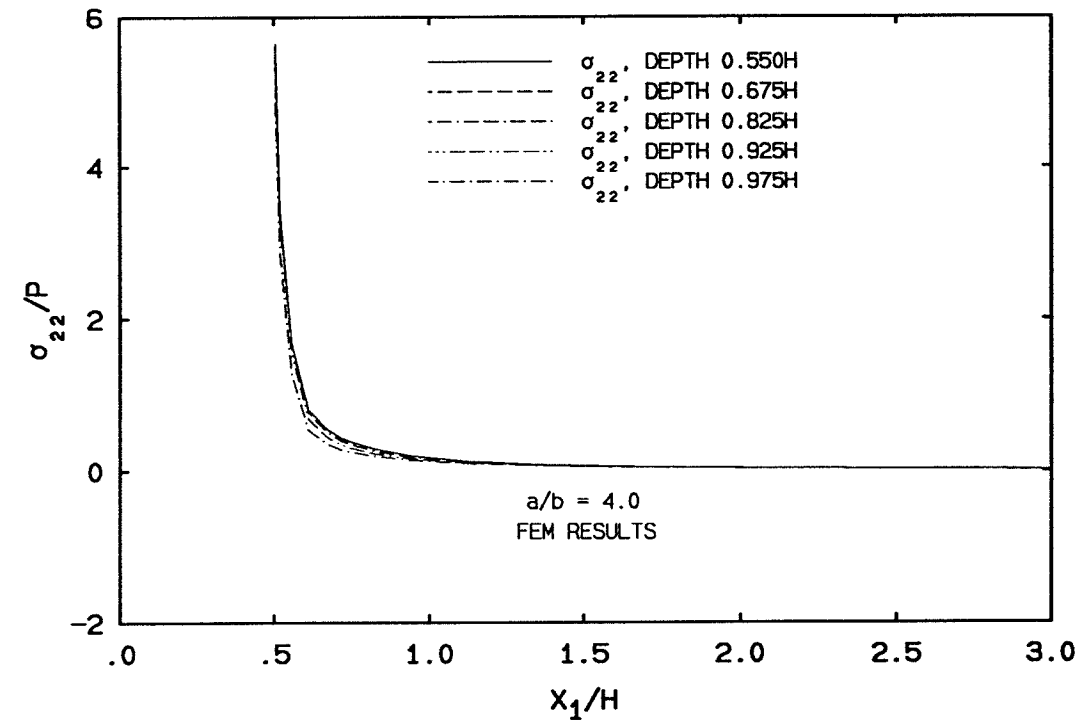

FIGURE 5.18 Normalized Stress σ_{22} vs. Normalized Distance x_1; Results Obtained From FEM.

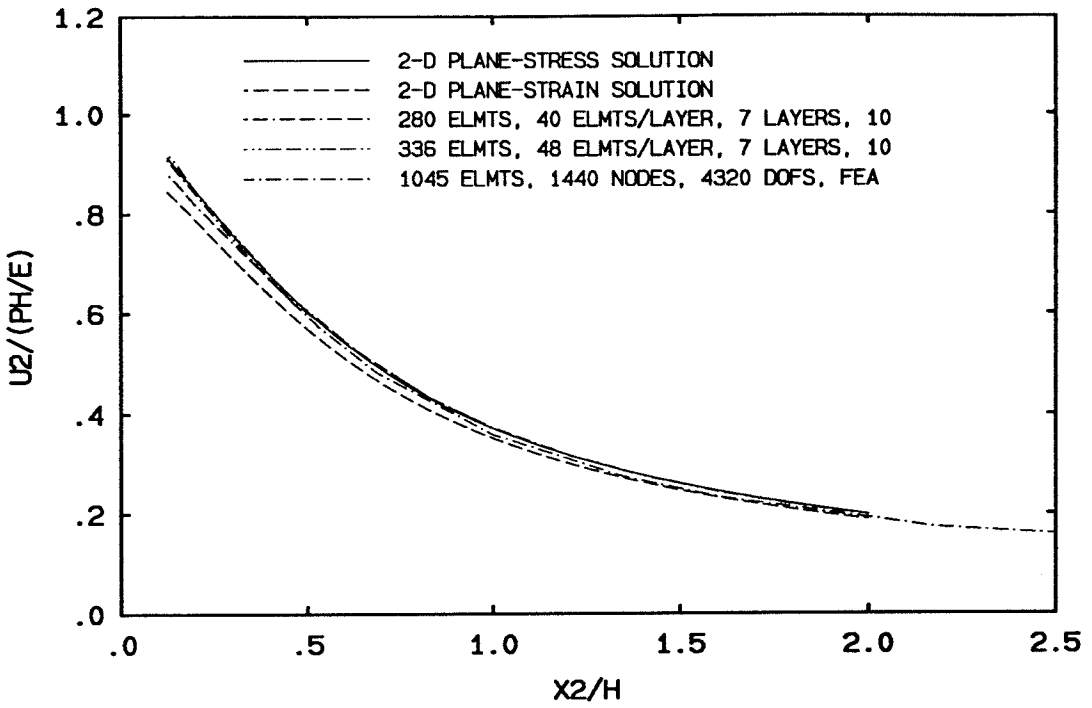

FIGURE 5.19 Normalized Displacement u_2 vs. Normalized Distance x_2; Results Obtained In Element Nodal Plane Of First Layer.

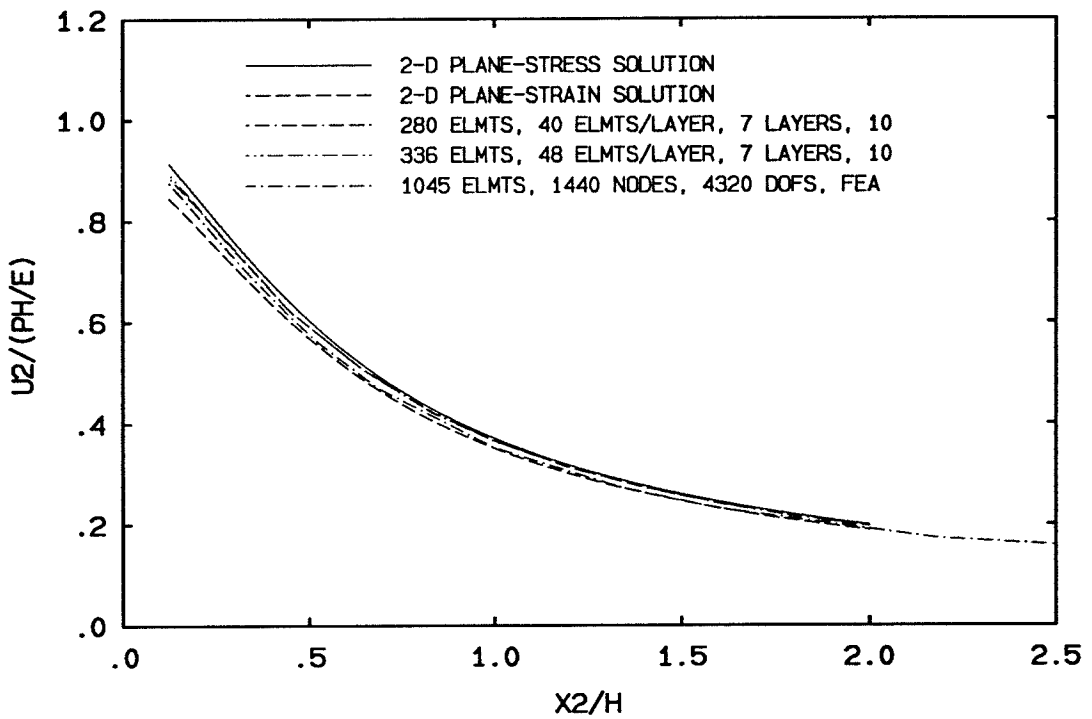

FIGURE 5.20 Normalized Displacement u_2 vs. Normalized Distance x_2; Results Obtained At Depth Three Quarters From Lower Surface Of Plate.

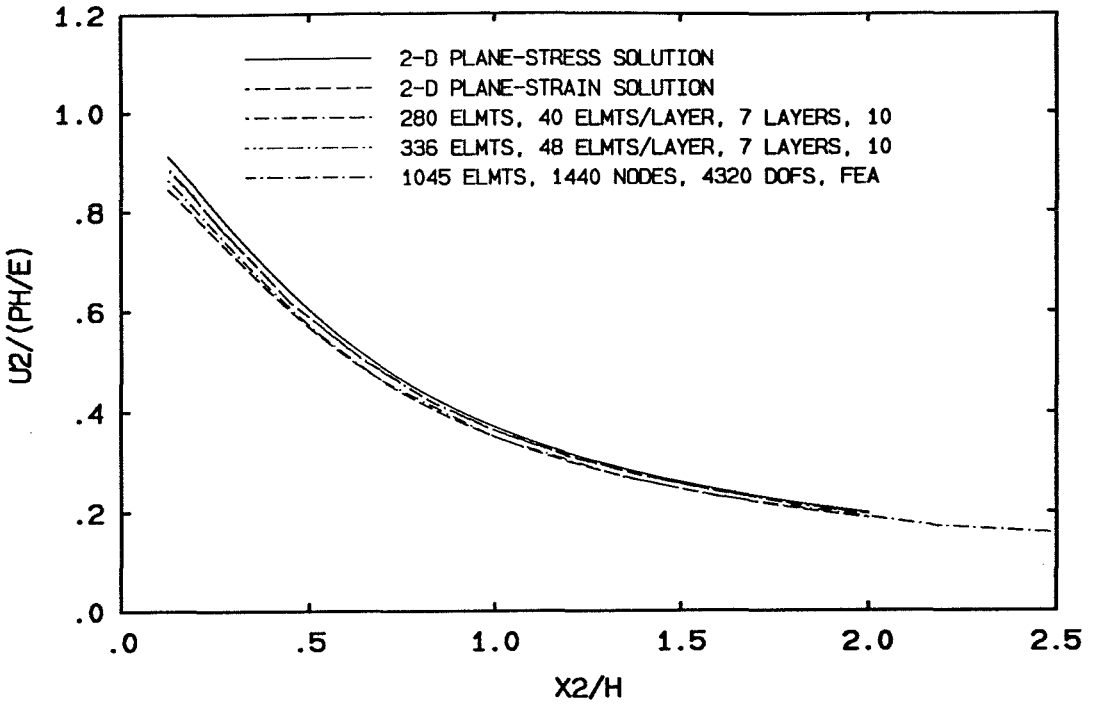

FIGURE 5.21 Normalized Displacement u_2 vs. Normalized Distance x_2; Results Obtained In Median Plane Of Plate.

respect to x_2 gets closer to the plane-strain solution as the arrays approach the midplane of the plate. This effect is shown in Figures 5.19, 5.20 and 5.21.

Away from the elliptical hole, the three-dimensional solutions of the displacements u_1 and u_2 are expected to converge to the plane-stress solution. It shows in Figures 5.11 through 5.21 that the displacement components u_1 and u_2 obtained from both the proposed BEM and the FEM approach the plane-stress solution. It also shows clearly that the BEM results of the displacements u_1 and u_2 have better agreement to the plane-stress solution away from the elliptical hole than the FEM results. The figures also show that the plane-strain solution gets closer and closer to the plane-stress solution as the distance from the surface of the elliptical hole increases. However, the two solutions can never be the same.

5.4.2 Results Of Out-Of-Plane Displacement For Problem One

Figures 5.22 through 5.25 show the variations of the normalized displacement u_3 with respect to the normalized distance x_1 and x_2, respectively. The agreement between the proposed BEM and the FEM is excellent. It can be seen from the Figures 5.22, 5.23 that the deviation of the three-dimensional numerical results from the two-dimensional plane-stress predictions is dramatic. This deviation is noticeable up to a distance of $0.5h$ from the tip of the ellipse at the nodal surface, and $0.4h$ from the tip of the ellipse at the plane 3/4 thicknesses from the lower surface of the plate. This observation is consistent with the analytical, numerical and experimental investigations of the three-dimensional effects near a crack obtained by Yang & Freund [44], Rosakis & Ravichandar [45]. As expected, u_3 is identically zero at the midplane.

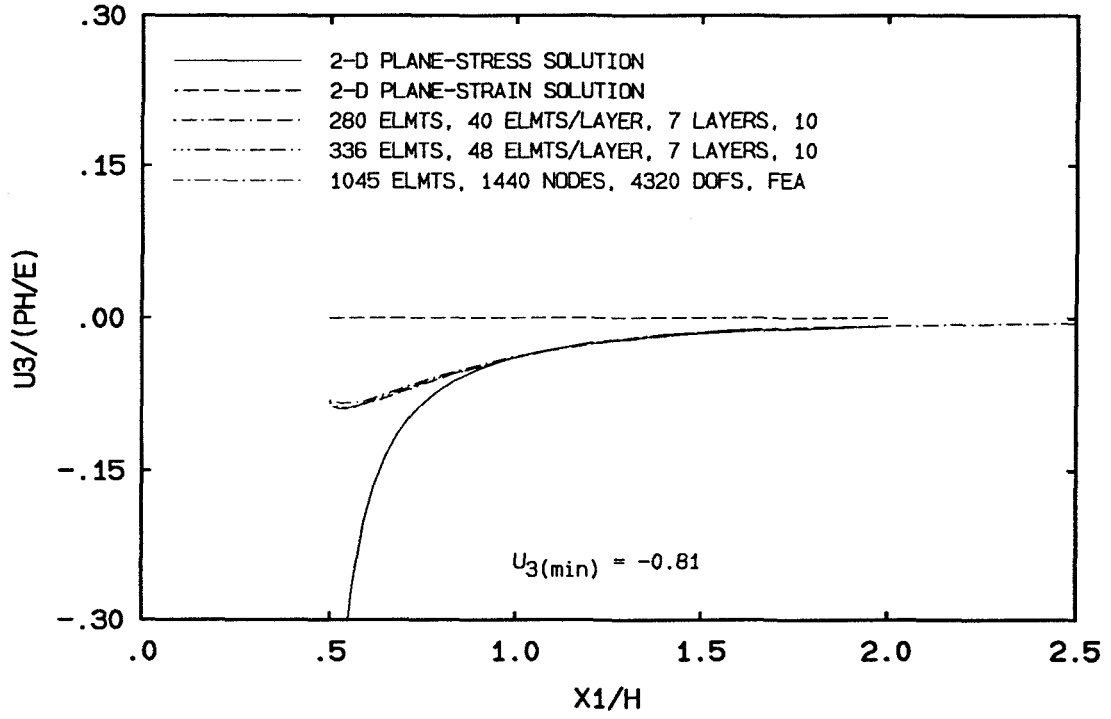

FIGURE 5.22 Normalized Displacement u_3 vs. Normalized Distance x_1; Results Obtained In Element Nodal Plane Of First Layer.

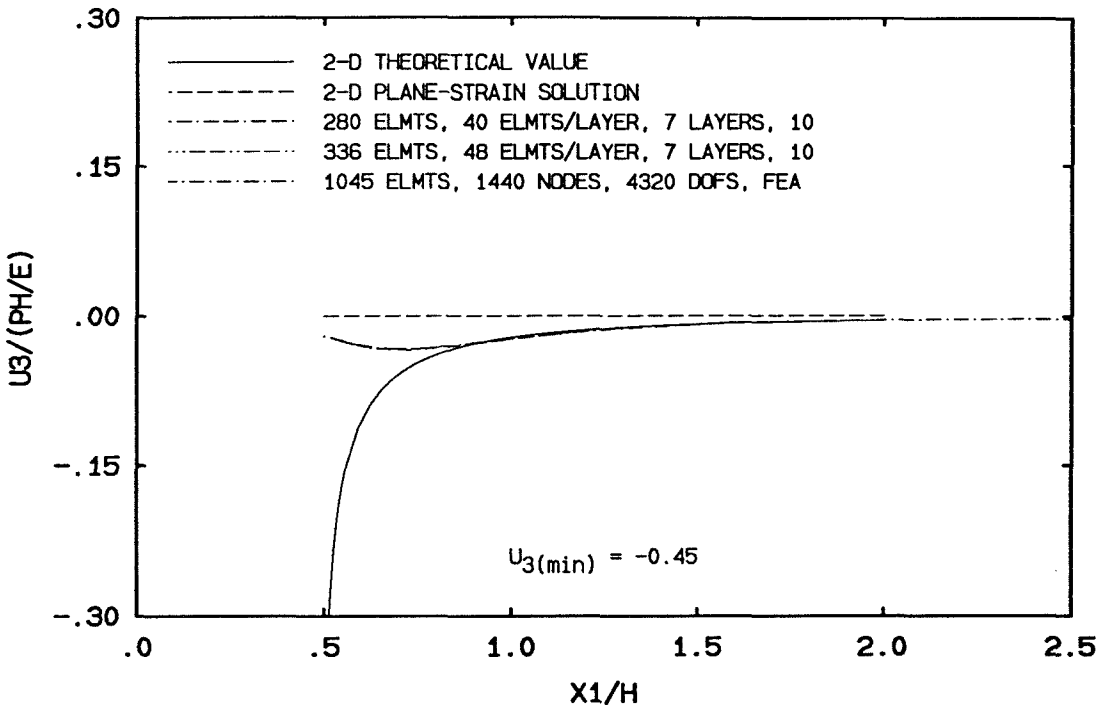

FIGURE 5.23 Normalized Displacement u_3 vs. Normalized Distance x_1; Results Obtained At Depth Three Quarters From Lower Surface Of Plate.

The plane-stress predictions of u_3 are false near the surface of the hole in the sense that it over-predicts the out-of-plane displacement u_3. This over-prediction of u_3 is caused by the plane-stress assumption $\sigma_{33} = 0$. The FEM results in Figure 5.16 show that σ_{33} does not vanish near the surface of the hole, and it presents the feature of stress concentration near the hole. σ_{33} is relatively large ($\sigma_{33}/(Ph/E) = 1.5$) near the midplane of the plate as compared to σ_{33} near the surface of the plate ($\sigma_{33}/(Ph/E) = 0.8$). σ_{33} rapidly decreases to almost zero at a distance of half the plate thickness. The physical meaning of the three-dimensional results can be explained as follows. The applied pressure has the tendency to deform the ellipse towards a circle. The tips of the ellipse are stretched by this effect, and thus, the thickness of the plate at the tips of the ellipse decreases. In the plane-stress solution, the stress σ_{33} is zero, therefore, the two-dimensional plane-stress solution will be significantly more out-of-plane displacement in u_3 than that of the three-dimensional

result. In addition, near the tips of the ellipse, σ_{33} has a fairly large positive value, which reduces the displacement u_3 more significantly near the surface of the hole than elsewhere. This is the reason that a magnitude decrease in the displacement u_3 is presented near the surface of the elliptical hole. This feature does not appear in the pressurized circular hole problem because of the two-dimensional nature of the problem, in which the actual stress σ_{33} is identically zero.

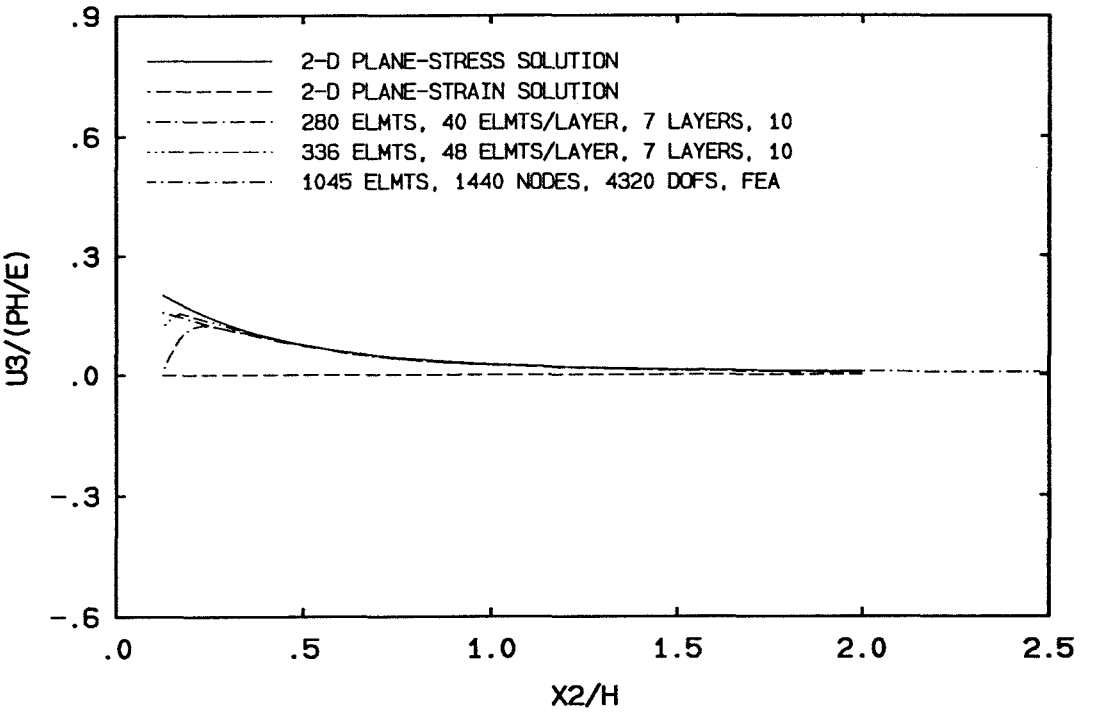

FIGURE 5.24 Normalized Displacement u_3 vs. Normalized Distance x_2; Results Obtained In Element Nodal Plane Of First Layer.

Figure 5.24 displays the normalized u_3 versus normalized x_2, and some discrepancy between the proposed BEM and the FEM is noticeable. This discrepancy is due to the use of large elements on the flatter sides of the ellipse. After local mesh refinement, Figure 5.2, the result with 336 elements in Figure 5.24 shows much improvement. It will be shown in the later discussion that, in the x_2 direction, the thickness variation of u_3 improves very significantly after local mesh refinement as

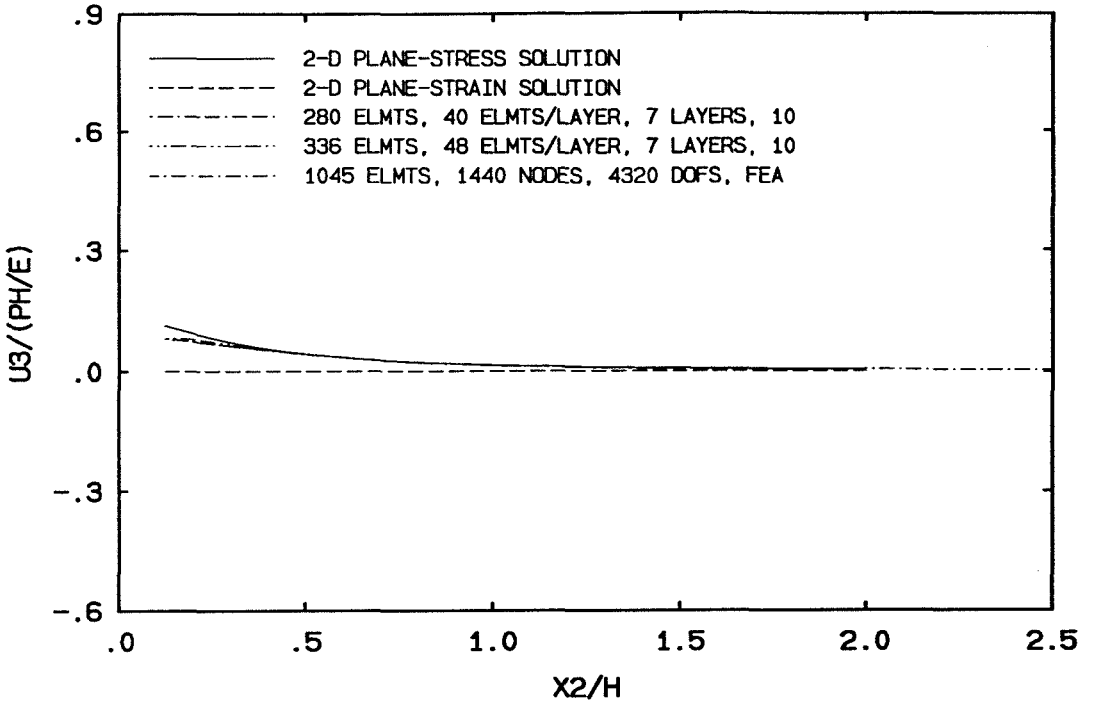

FIGURE 5.25 Normalized Displacement u_3 vs. Normalized Distance x_2; Results Obtained At Depth Three Quarters From Lower Surface Of Plate.

well. It is expected that the BEM results will converge to the FEM results after further refinement on the meshes for both methods.

The three-dimensional effect in the x_2 direction near the surface of the elliptical hole is confined to within a distance of $0.3h$ at the nodal plane, and to within a distance of $0.25h$ at the plane 3/4 thicknesses from the lower surface of the plate. u_3 is identically zero at the midplane of the plate.

5.4.3 Results Of Displacement Variations Through Thickness For Problem One

The thickness variations of the displacement u_1 along the x_1 direction are shown in Figures 5.26 through 5.28. Again, the numerical solutions are situated in between the plane-stress and the plane-strain solutions. The two features worth mentioning are: a) the thickness variation of the numerical results are not horizontal straight lines anymore. This feature indicates the three-dimensionality of the problem; b) it can be seen from Figures 5.26 through 5.28 that the numerical solutions approach the plane-stress solutions as the distance to the surface of the hole increases. It can also be seen from these figures that the BEM results converge to the plane-stress solutions faster than the FEM results as the distance to the surface of the hole increases. In Figure 5.28, the scale for the vertical axis is changed in order to explore the detailed features of the thickness variation of u_1 relatively far away from the elliptical hole surface.

Some interesting features are presented in the thickness variations of the displacement u_2 in the direction x_2. It can be seen from Figure 5.29 that the displacement u_2 obtained by the proposed BEM using 280 elements deviates from the FEM result. The deviation is most noticeable when the displacement u_2 is computed near both surface of the hole and the surface of the plate. After mesh local refinement, the result improves very significantly as compared with the FEM results. The two features discussed in the thickness variations of u_1 are also applicable here. The apparent slope discontinuity in the BEM solution are due to the use of relatively large elements along the flatter sides of the ellipse.

Figures 5.29 through 5.31 also show that the points near the two surfaces of the plate displace more in the x_2 direction than the ones near the midplane of the

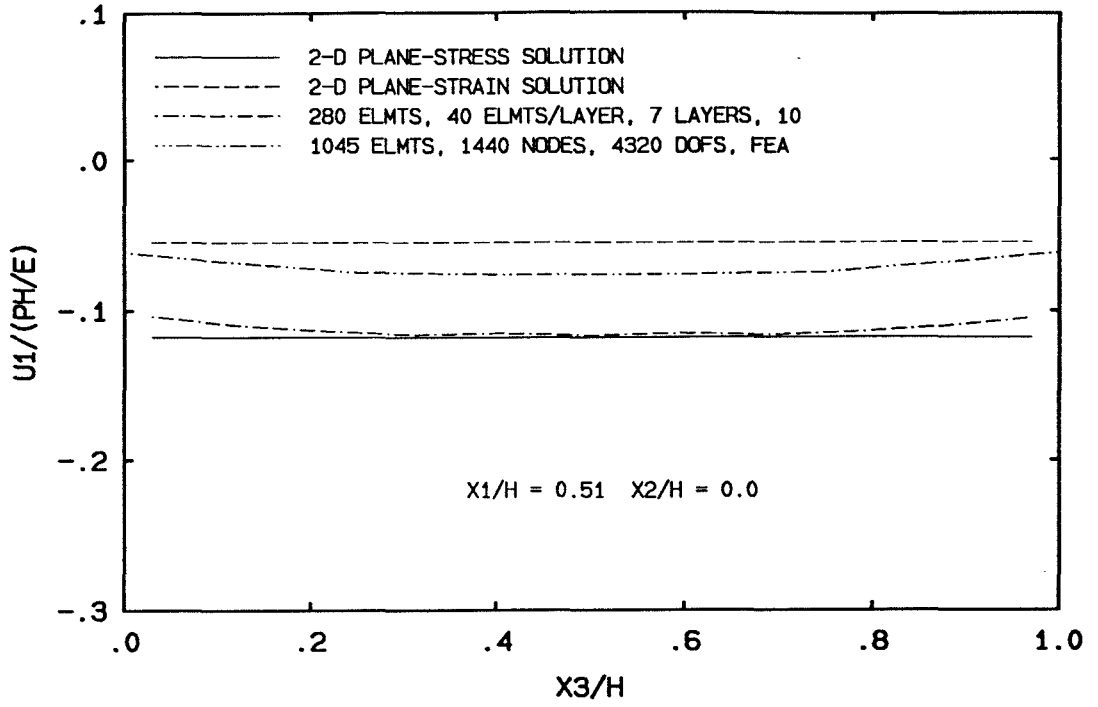

FIGURE 5.26 Normalized Displacement u_1 vs. Normalized Distance x_3; Results Obtained Along Line Positioned At $x_1 = 0.51h$, $x_2 = 0.00$.

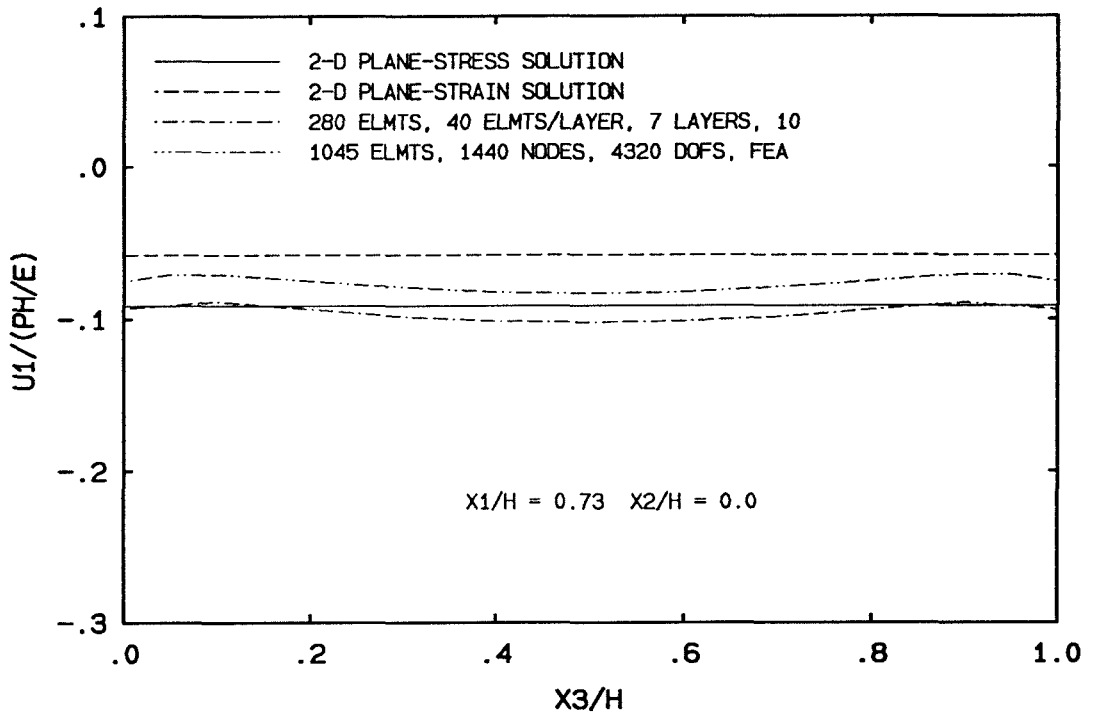

FIGURE 5.27 Normalized Displacement u_1 vs. Normalized Distance x_3; Results Obtained Along Line Positioned At $x_1 = 0.73h$, $x_2 = 0.00$.

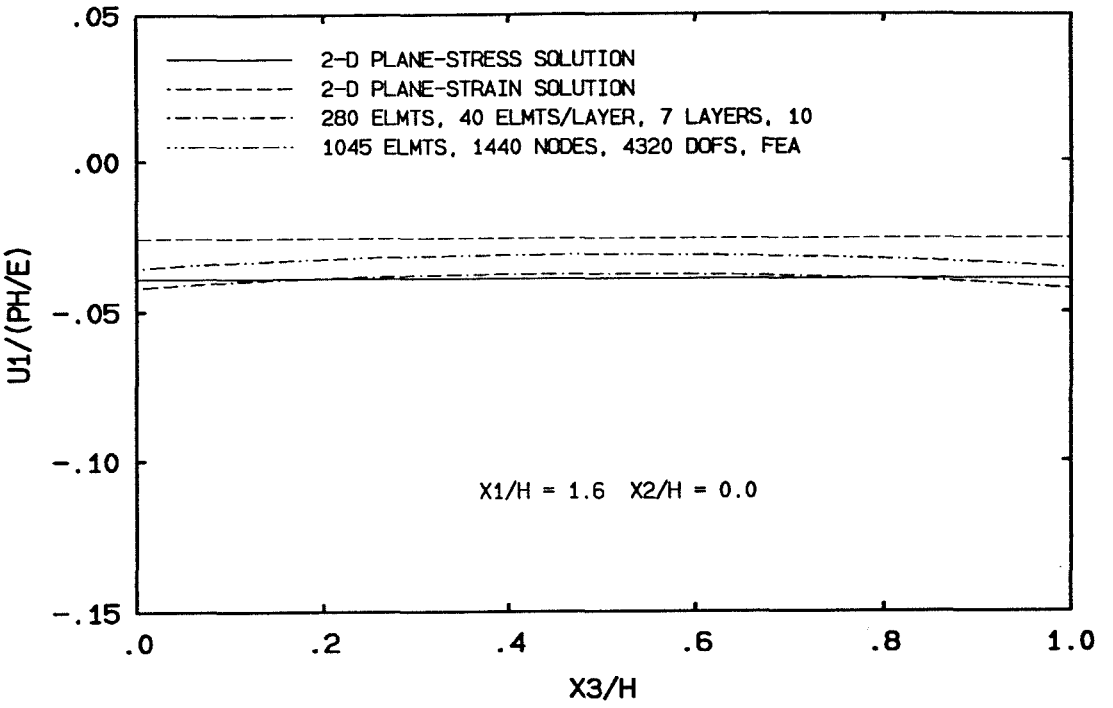

FIGURE 5.28 Normalized Displacement u_1 vs. Normalized Distance x_3; Results Obtained Along Line Positioned At $x_1 = 1.60h$, $x_2 = 0.00$.

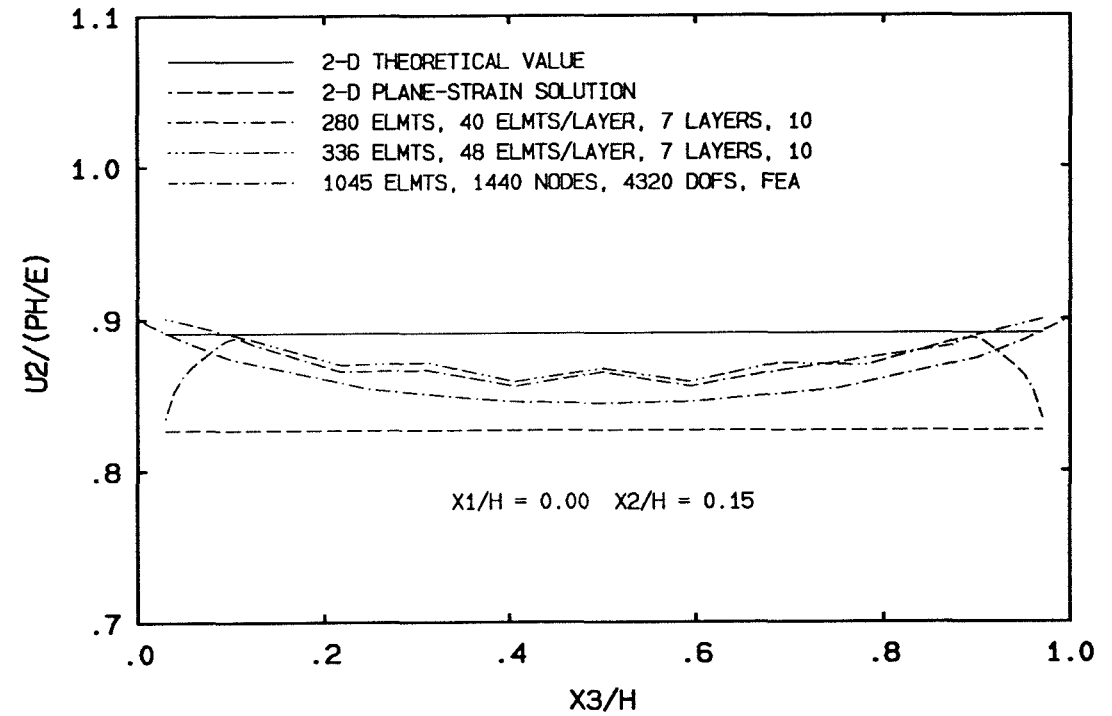

FIGURE 5.29 Normalized Displacement u_2 vs. Normalized Distance x_3; Results Obtained Along Line Positioned At $x_1 = 0.00$, $x_2 = 0.15h$.

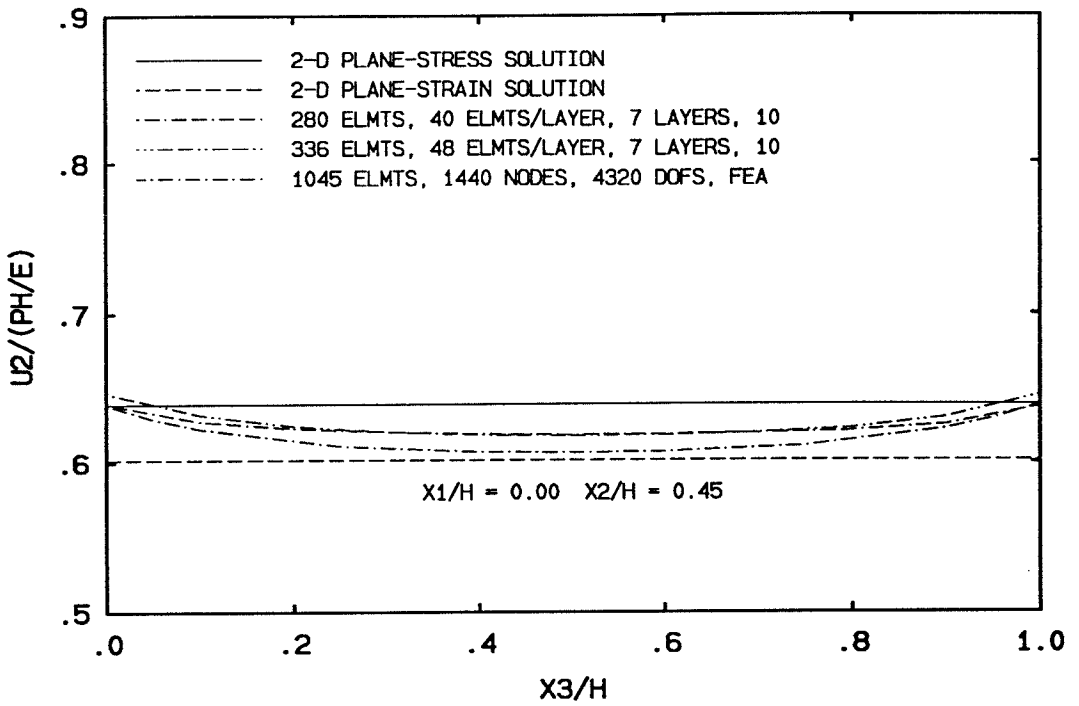

FIGURE 5.30 Normalized Displacement u_2 vs. Normalized Distance x_3; Results Obtained Along Line Positioned At $x_1 = 0.00$, $x_2 = 0.45h$.

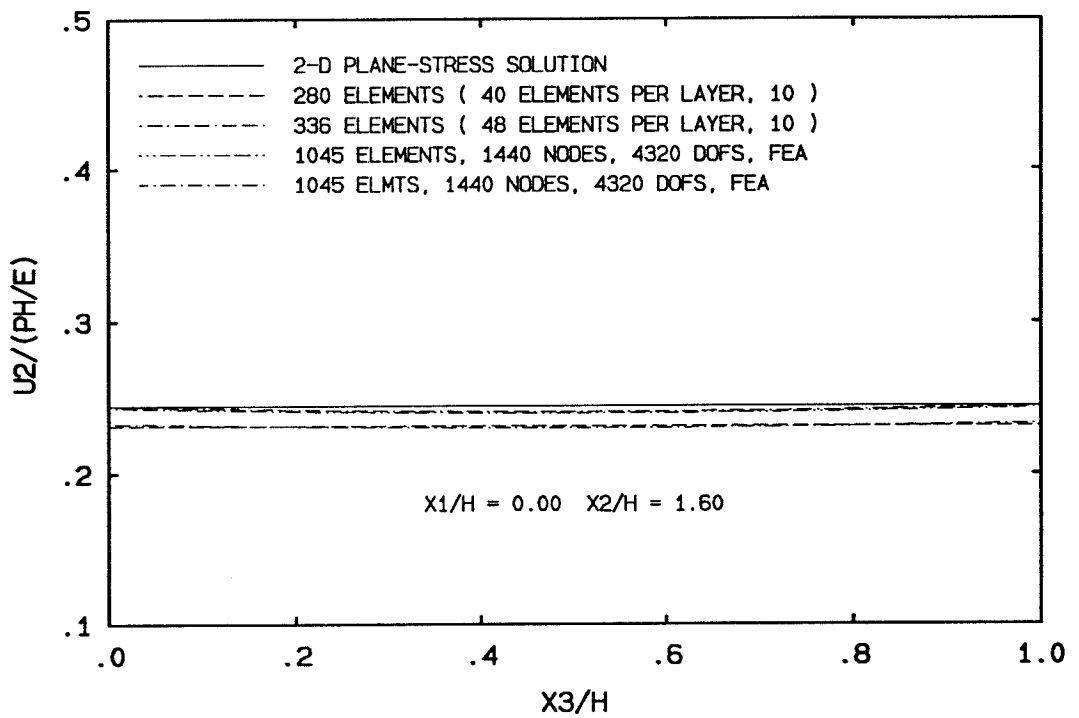

FIGURE 5.31 Normalized Displacement u_2 vs. Normalized Distance x_3; Results Obtained Along Line Positioned At $x_1 = 0.00$, $x_2 = 1.60h$.

plate. This phenomenon is due to the constraint difference for points in the plate. There is less constraint to the points near the free surface of the plate than to those near the midplane of the plate. It is easier for a point near the surfaces of the plate to deform in the x_3 direction than the one near the midplane. Because of the Poisson's effect, the points near the surfaces of the plate can displace more in the x_2 direction than those near the midplane of the plate. The above argument can be applied to explain why, at the tips of the ellipse, the displacement u_1 deforms less near the free surface than near the midplane.

The most interesting features lies in the thickness variations of u_3. As shown in the out-of-plane displacement, the three-dimensional effects are expected to be strongly demonstrated. The thickness variations of u_3 at different distances from the tip of the ellipse along the x_1 direction are shown in Figures 5.32 through 5.34. The thickness variations of u_3 along the x_2 direction are shown in Figures 5.35 through 5.37. The numerical results of the thickness variations from the proposed BEM agree very well with those from the FEM.

Figure 5.32 shows that, at points close to the tip ($0.01h$), u_3 varies rather uniformly through the thickness and deviates from zero only when the points are close to the plate surfaces. u_3 varies anti-symmetrically with respect to the midplane. The BEM results and the FEM results are in very good agreement. Figures 5.33 and 5.34 show that the three-dimensional results of the thickness variations of u_3 approach the plane-stress solution, which is linear in x_3 as the distance to the surface of the elliptical hole increases. It can also be seen that the three-dimensional results fall on top of the plane-stress solution at a distance of about half the plate thickness away from the elliptical hole surface. Further away from the elliptical hole, u_3 varies very little throughout the thickness, and the value of u_3 of all the solutions

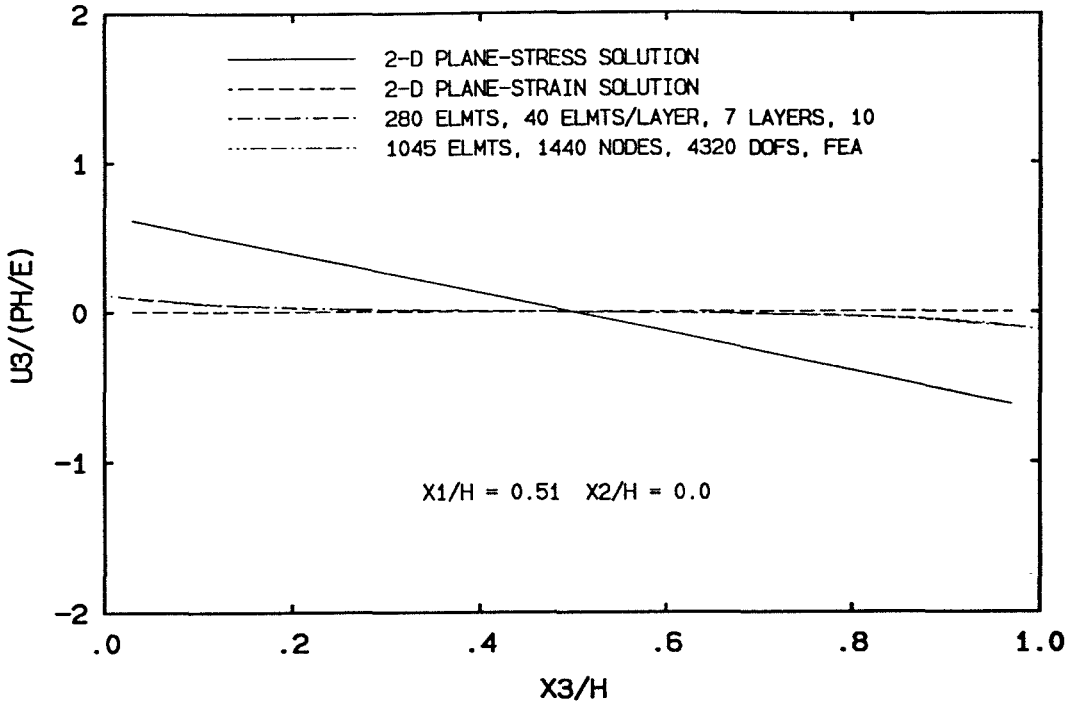

FIGURE 5.32 Normalized Displacement u_3 vs. Normalized Distance x_3; Results Obtained Along Line Positioned At $x_1 = 0.51h$, $x_2 = 0.00$.

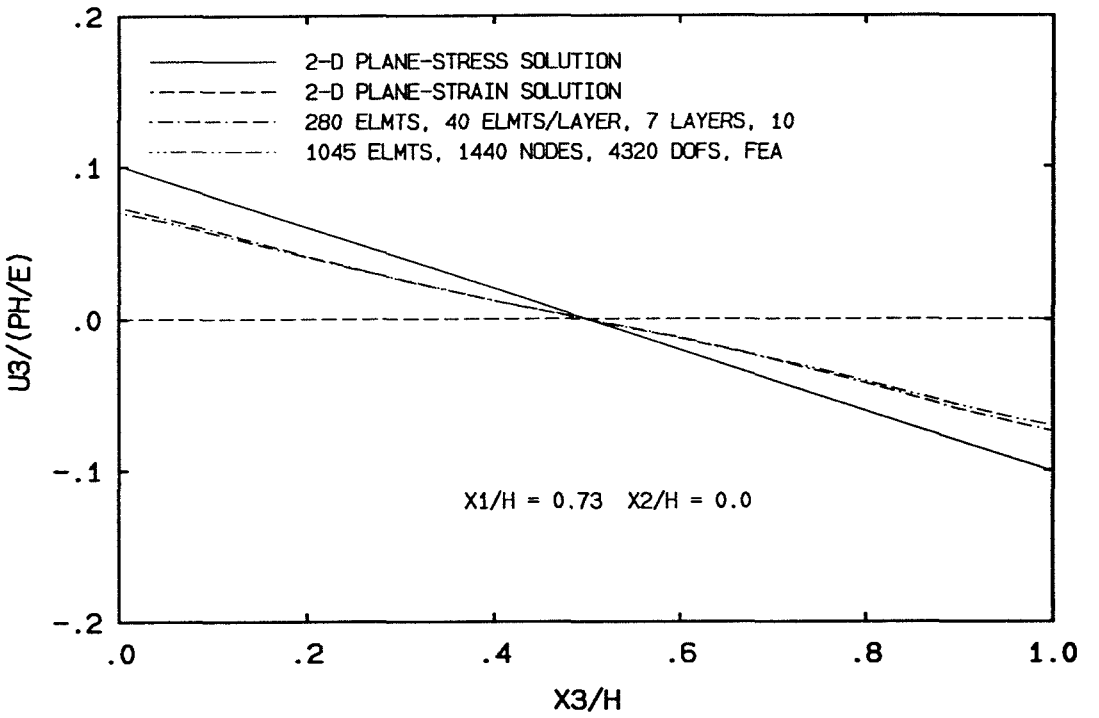

FIGURE 5.33 Normalized Displacement u_3 vs. Normalized Distance x_3; Results Obtained Along Line Positioned At $x_1 = 0.73h$, $x_2 = 0.00$.

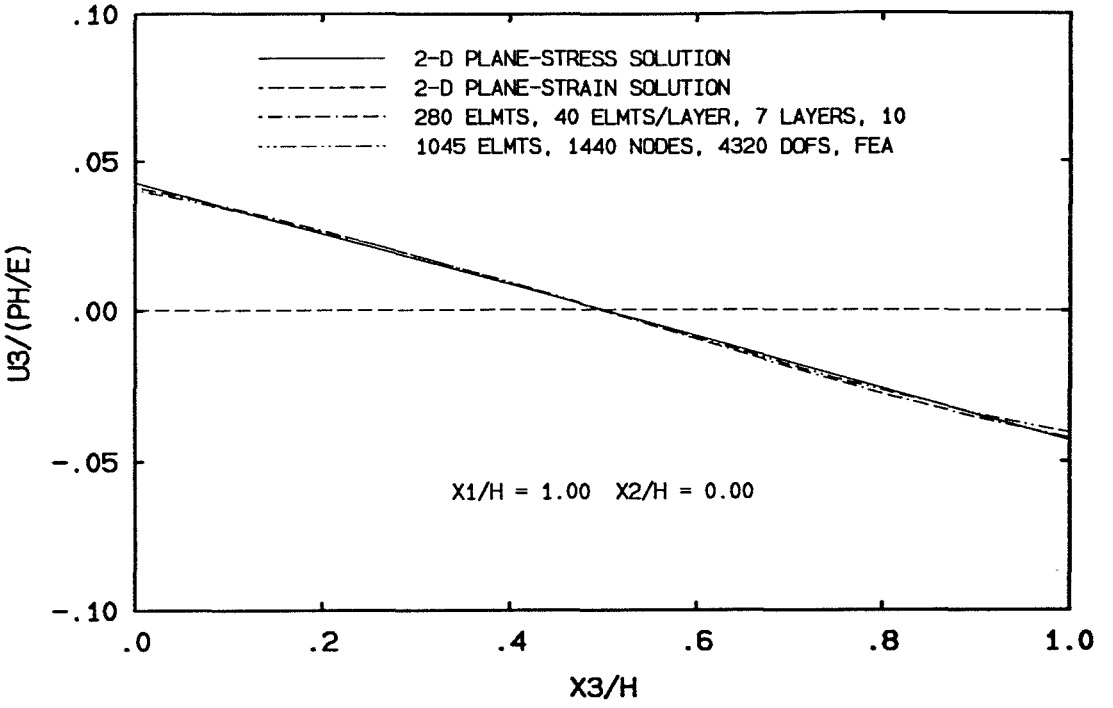

FIGURE 5.34 Normalized Displacement u_3 vs. Normalized Distance x_3; Results Obtained Along Line Positioned At $x_1 = 1.00h$, $x_2 = 0.00$.

generally reduces to zero as the distance to the surface of the hole increases.

Because of the use of the large elements on the flatter sides of the ellipse in the mesh with 280 elements, u_3 in Figure 5.35 obtained by the proposed BEM shows some deviation from the FEM result when u_3 is computed near the surfaces of the plate. By local mesh refinement and the use of 336 elements in the mesh, u_3 improves very much, and it is almost the same as the FEM result. There is very little three-dimensional effect in the x_2 direction. The numerical results quickly converge to the plane-stress solution in this case.

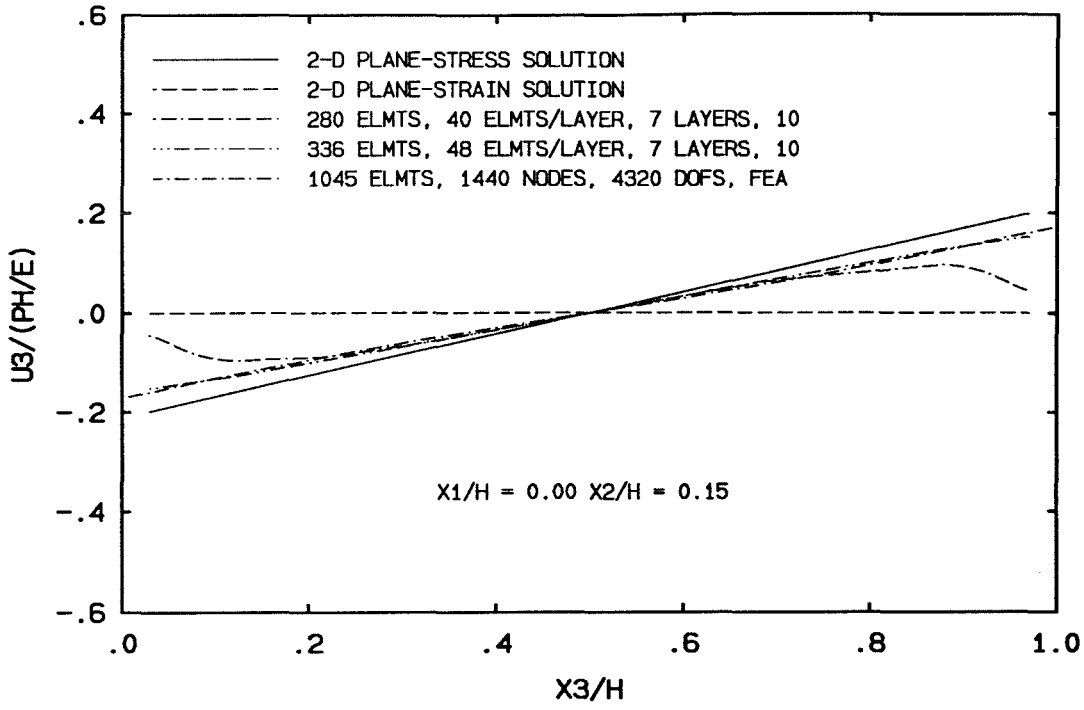

FIGURE 5.35 Normalized Displacement u_3 vs. Normalized Distance x_3; Results Obtained Along Line Positioned At $x_1 = 0.00$, $x_2 = 0.15h$.

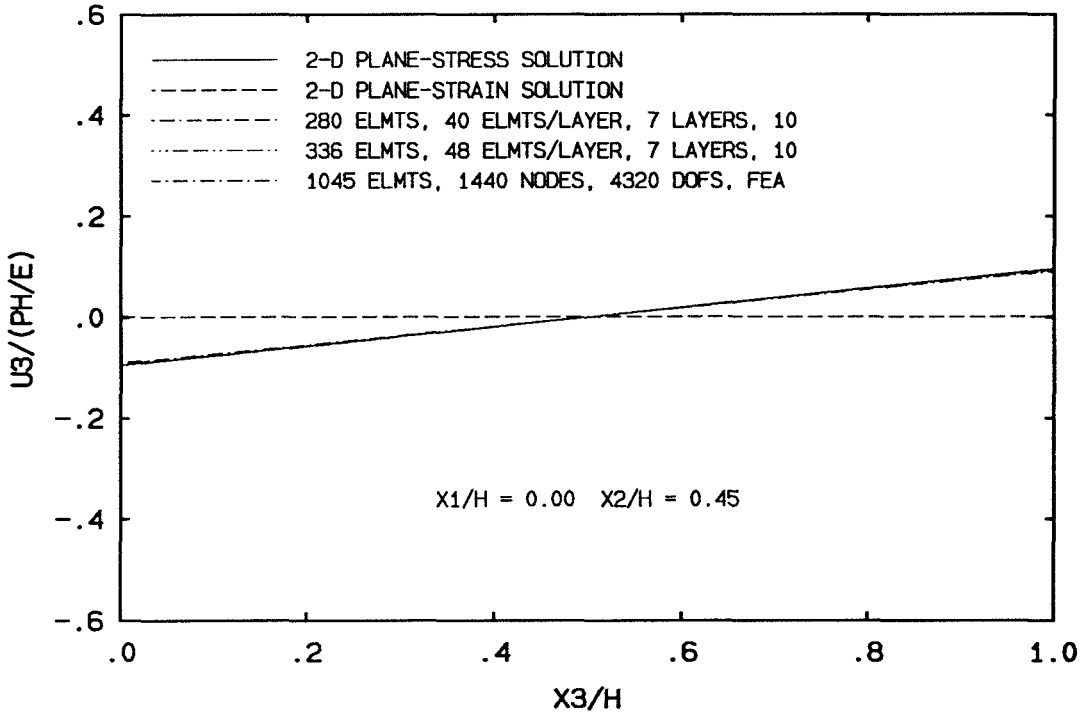

FIGURE 5.36 Normalized Displacement u_3 vs. Normalized Distance x_3; Results Obtained Along Line Positioned At $x_1 = 0.00$, $x_2 = 0.45h$.

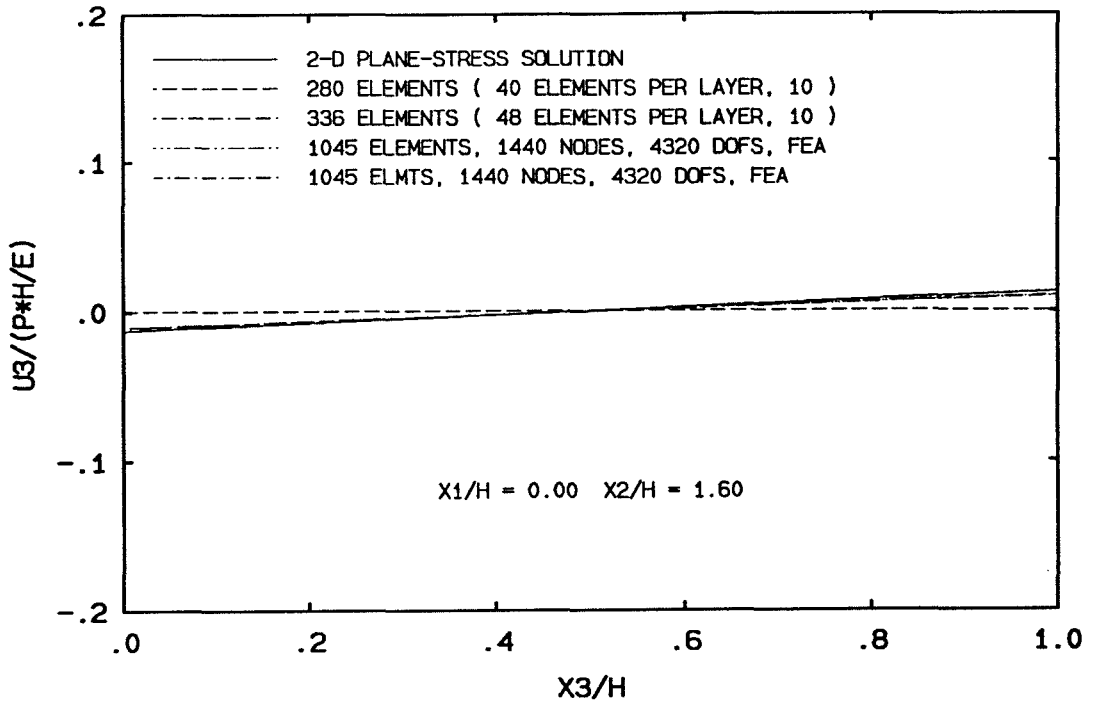

FIGURE 5.37 Normalized Displacement u_3 vs. Normalized Distance x_3; Results Obtained Along Line Positioned At $x_1 = 0.00$, $x_2 = 1.60h$.

5.4.4 Results Of In-Plane Displacements For Problem Two

The accuracy and the physical meaning of the solution for *problem one* has been established in the last section. The proposed BEM gives good results compared to those given by the FEM. The goal of this section is to examine how the different aspect ratios affect the displacement fields.

In *problem two*, only the displacements at the points in the Group A and B are investigated since large stress concentration is expected near the tips of the ellipse. As established in *problem one*, the three-dimensional effects present strongly near the tips of the elliptical hole.

Figures 5.38, 5.39, and 5.40 show that the results of the displacement component u_1 along the x_1 direction. The variation of u_1 in *problem two* is quantitatively similar to that of *problem one*. However, in *problem two*, the discrepancy between

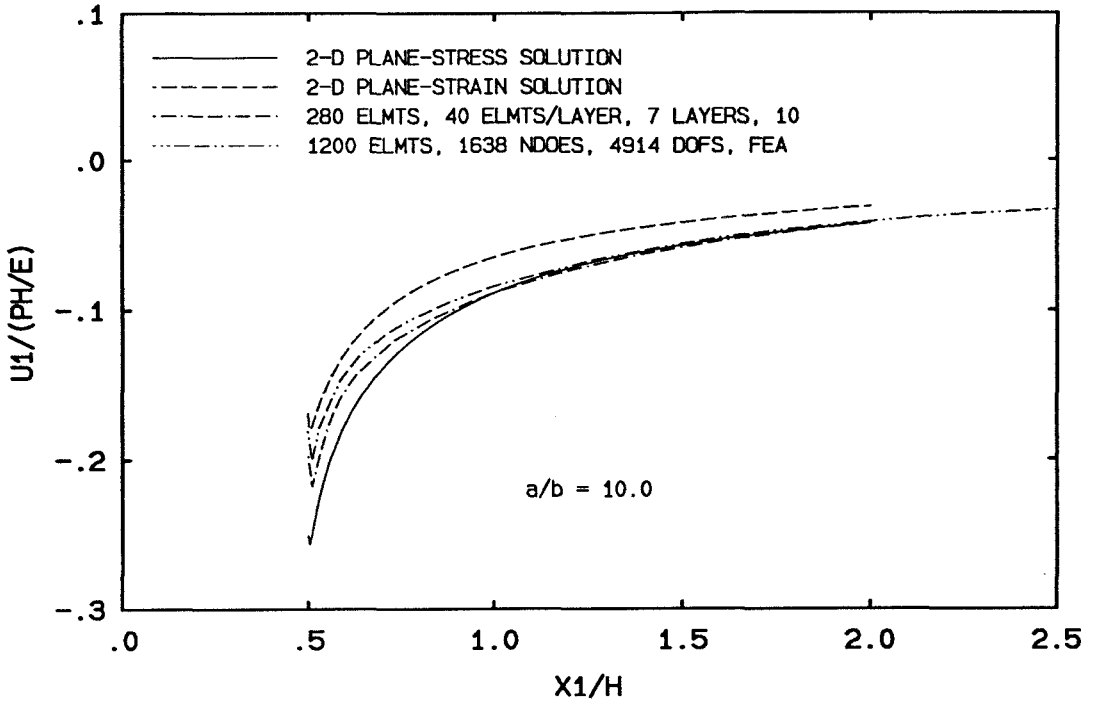

FIGURE 5.38 Normalized Displacement u_1 vs. Normalized Distance x_1; Results Obtained In Element Nodal Plane Of First Layer.

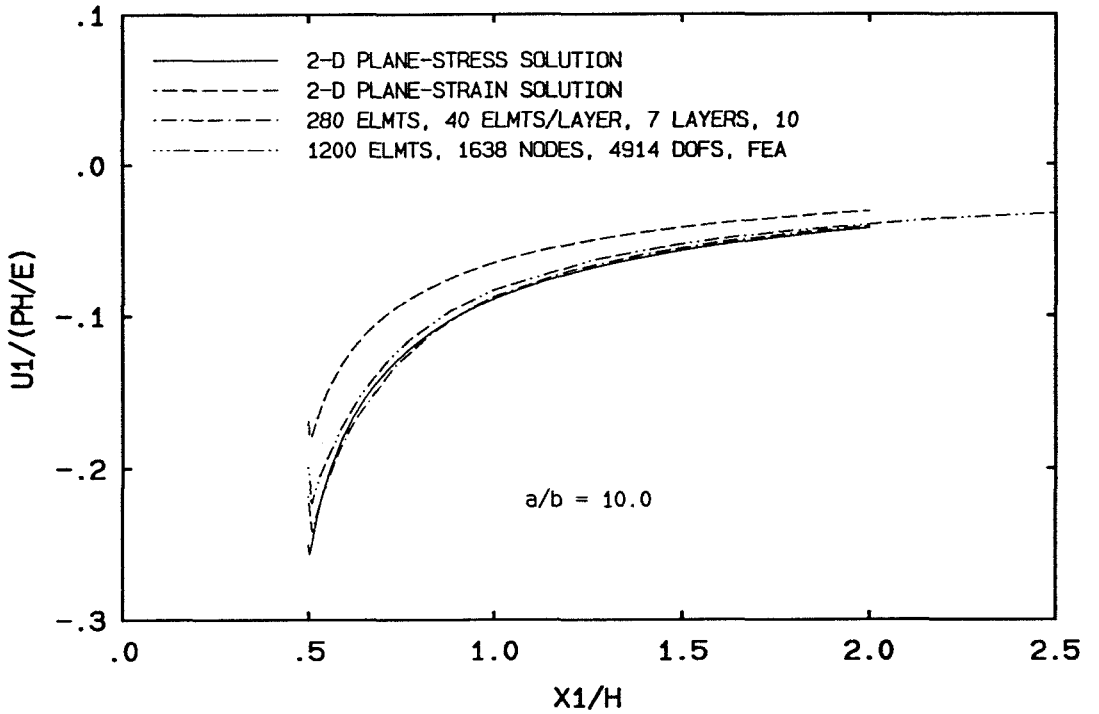

FIGURE 5.39 Normalized Displacement u_1 vs. Normalized Distance x_1; Results Obtained At Depth Three Quarters From Lower Surface Of Plate.

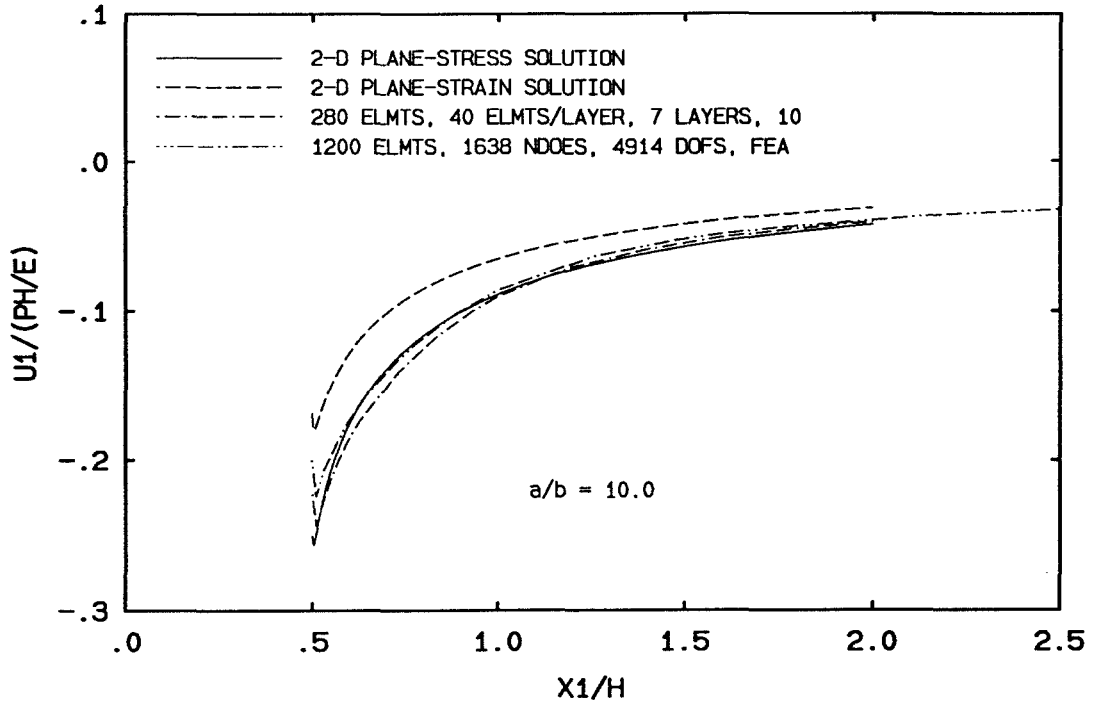

FIGURE 5.40 Normalized Displacement u_1 vs. Normalized Distance x_1; Results Obtained In Median Plane Of Plate.

the BEM results and the FEM results is much smaller than that shown in Figures 5.11, 5.12, 5.13 of *problem one*. The convergence of the BEM and FEM results is caused by the use of small elements near the tips of the elliptical hole for both methods. Since the stress concentration of the in-plane stress components is high near the tips of the ellipse, and the elements used in the proposed BEM are constant elements, the use of small elements near the tips of the ellipse seems to cut down the discretization error considerably.

Figures 5.38, 5.39, 5.40 also show that both numerical results are closer to the plane-stress solution. The agreement is very good between the proposed BEM solutions and the FEM solutions. Although the three-dimensional effect in the in-plane displacement u_1 is very weak compared with that in the out-of-plane displacement u_3, Figures 5.38, 5.39, 5.40 still show that the three-dimensional effects are mainly presented within a distance about half the plate thickness from the surface of the

hole.

5.4.5 Results Of Out-Of-Plane Displacement For Problem Two

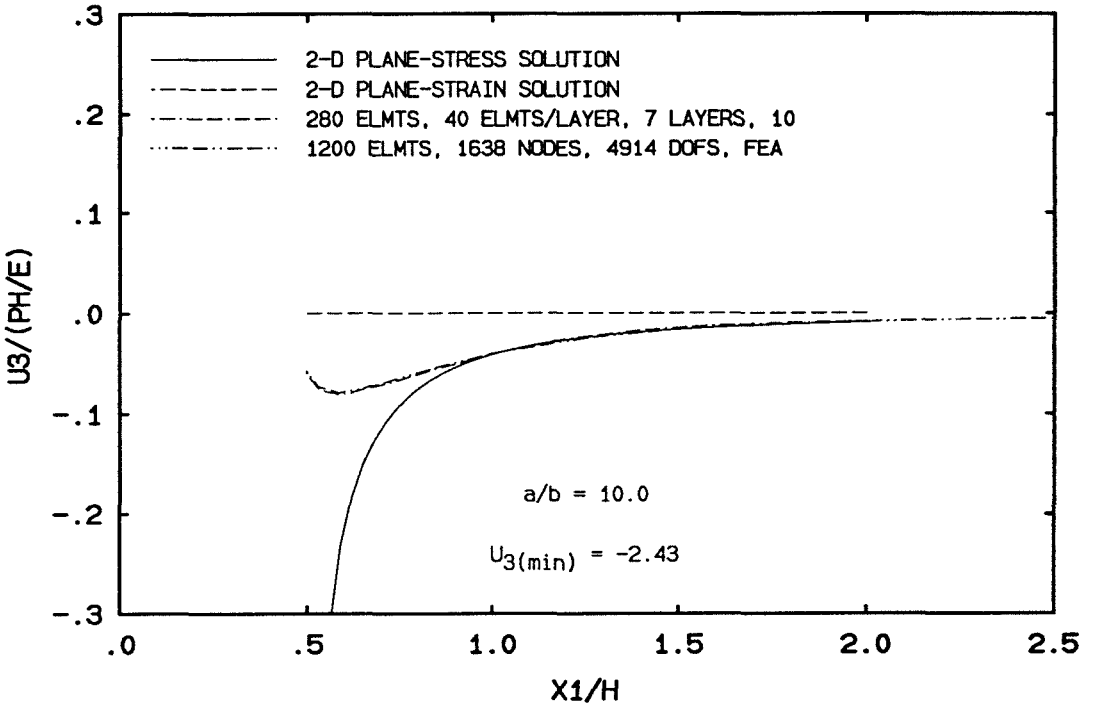

FIGURE 5.41 Normalized Displacement u_3 vs. Normalized Distance x_1; Results Obtained In Element Nodal Plane Of First Layer.

Excellent agreement has been obtained between the proposed BEM solutions and the FEM solutions in the out-of-plane displacement u_3 along the x_1 direction.

Figures 5.41 and 5.42 show the similar strong three-dimensional effect in the out-of-plane displacement u_3 along x_1 direction. Compared with the thickness variations of u_3 shown in Figures 5.22 and 5.23, u_3 in this case presents more reduction in the displacement near the surface of the hole, and the region of the displacement reduction is relatively larger than that shown in the ellipse with the aspect ratio of 4. This feature is caused by the higher stress concentration in σ_{33}.

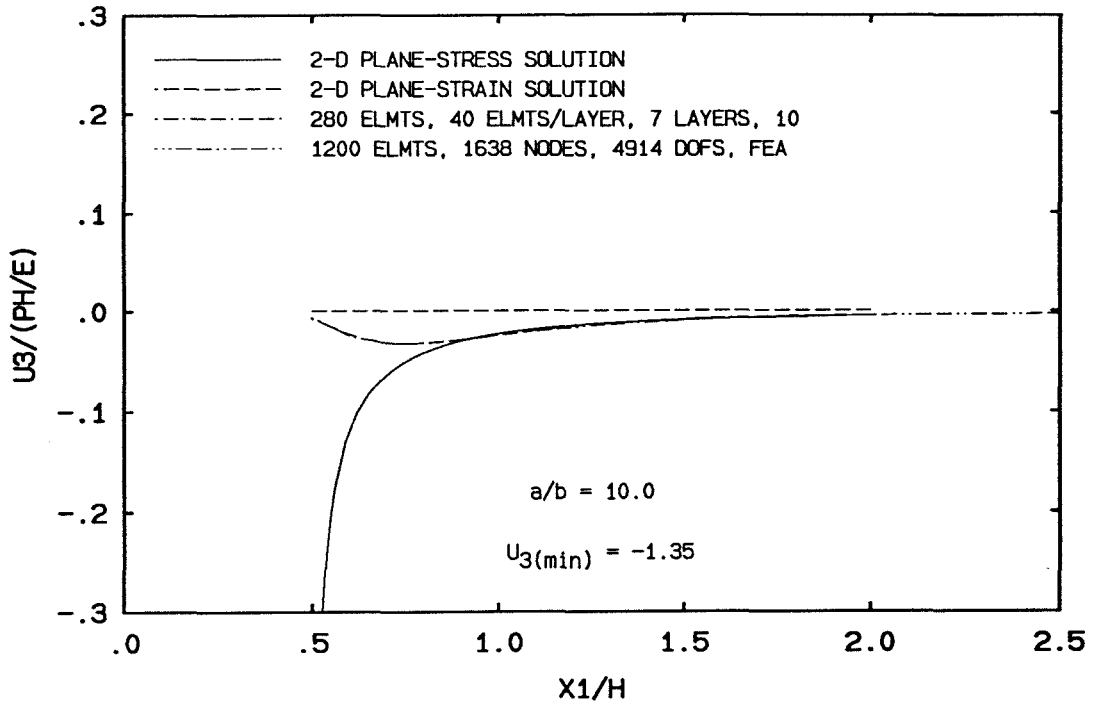

FIGURE 5.42 Normalized Displacement u_3 vs. Normalized Distance x_1; Results Obtained At Depth Three Quarters From Lower Surface Of Plate.

It is very interesting to notice that the displacement u_3 from the plane-stress solutions to both problems are almost the same. The numerical solutions of u_3 to both problems are very close except the difference near the surface of the hole. The size of the three-dimensional zone stays almost unchanged. At the nodal plane ($0.95h$), the size of the three-dimensional zone is about $0.5h$; the size of the three-dimensional zone at the plane $0.75h$ from the lower surface is about $0.4h$. At the midplane of the plate, u_3 is identically zero as assumed.

5.4.6 Results Of Displacement Variations Through Thickness For Problem Two

The thickness variations of the displacement u_1 at different distances are shown in Figures 5.43 through 5.45. The curved lines demonstrate the three-dimensional effect of the problem. The numerical solutions of both the BEM and the FEM are bounded by the plane-strain and the plane-stress solutions. u_1 presents less displacement near the free surfaces of the plate than near the midplane. As the points are placed far away from the surface, the difference between the solutions of u_1 from both the proposed BEM and the FEM becomes very small, and the numerical solutions agree with the plane-stress solution well.

Compare the results of u_1 thickness variations of *problem two*, shown in Figures 5.43, 5.44 and 5.45, with those of *problem one*, displayed in Figures 5.26, 5.27 and 5.28, it can be seen that the BEM results are closer to the FEM results in *problem two* than in *problem one*. The results from both methods converge better in *problem two* than in *problem one* because of the local mesh refinement used in *problem two*. The relatively large curvatures presented in the BEM and the results in Figure 5.43 compared with those in Figure 5.26 suggest that the three-dimensional effect is stronger in *problem two* near the surface of the hole and the surfaces of the plate than in *problem one*. In the same two figures, the plane-stress solutions and the plane-strain solutions do not change much for both problems.

Consider the thickness variations of the out-of-plane displacement u_3 in the x_1 direction. Similar to *problem one*, the solutions in u_3 of the proposed BEM displays excellent agreement with those of FEM. The strongest three-dimensional effect in this problem is still presented in the out-of-plane displacement u_3. The displacement u_3 has the same patterns of variations through the thickness of the plate. It

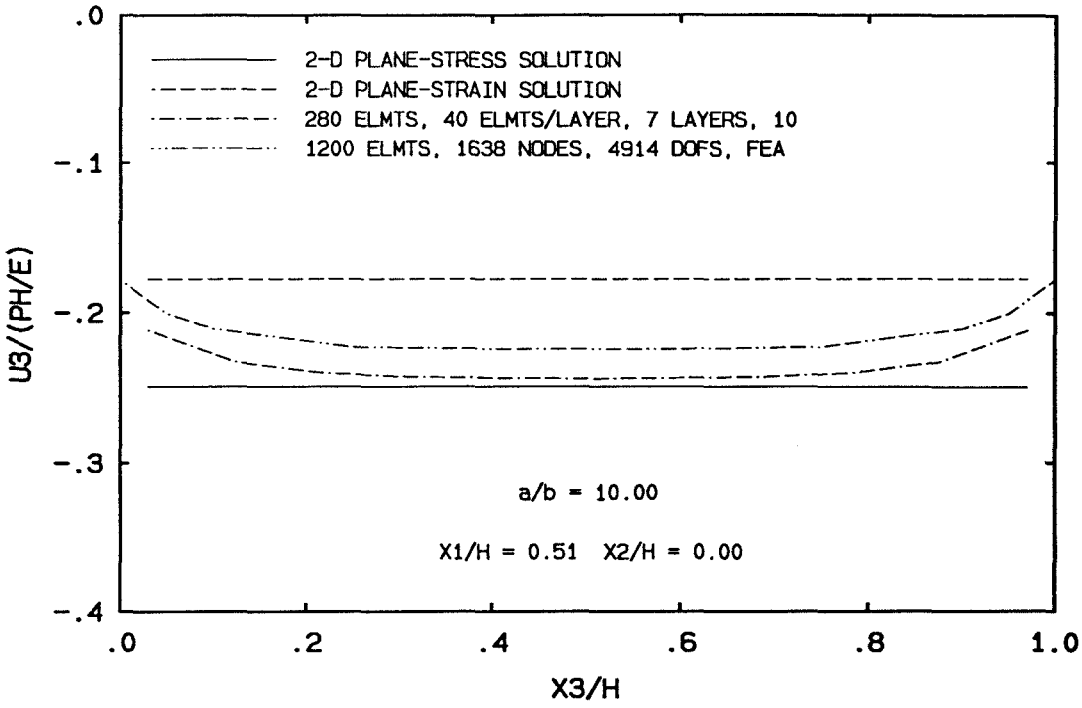

FIGURE 5.43 Normalized Displacement u_1 vs. Normalized Distance x_3; Results Obtained Along Line Positioned At $x_1 = 0.51h$, $x_2 = 0.00$.

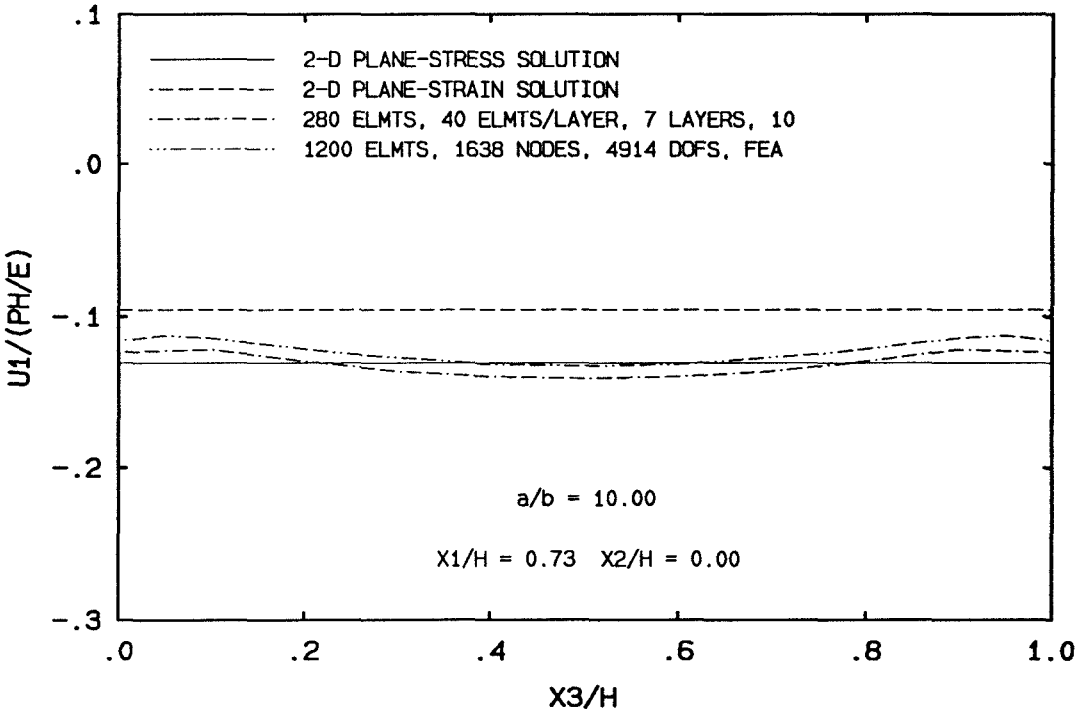

FIGURE 5.44 Normalized Displacement u_1 vs. Normalized Distance x_3; Results Obtained Along Line Positioned At $x_1 = 0.73h$, $x_2 = 0.00$.

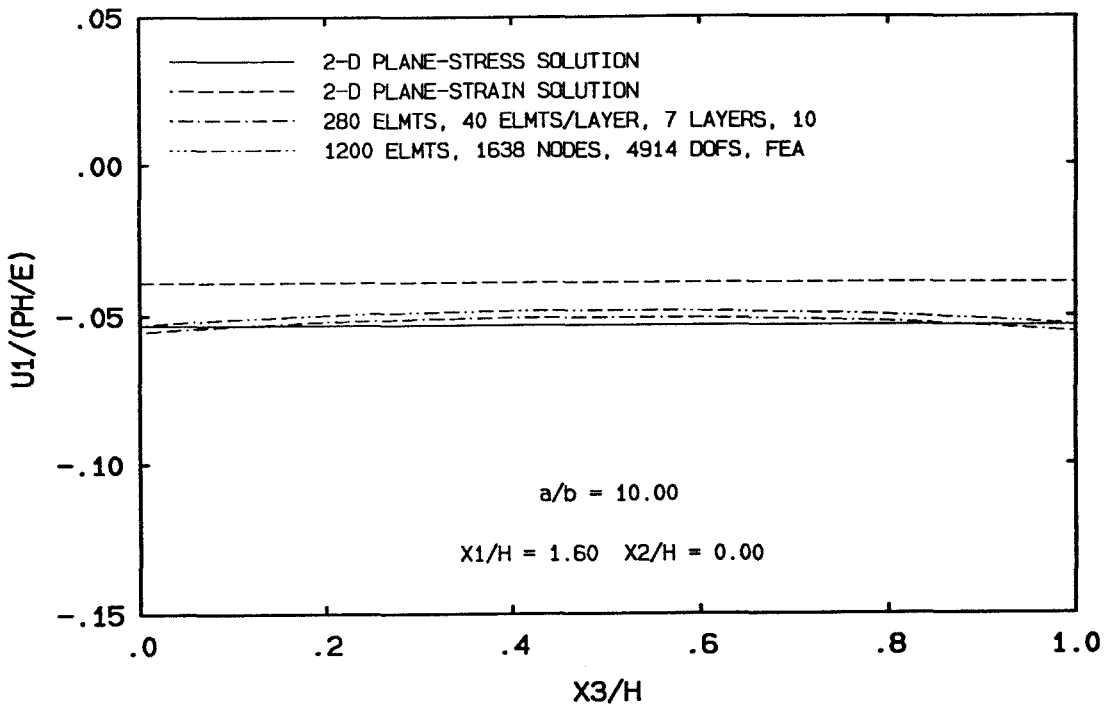

FIGURE 5.45 Normalized Displacement u_1 vs. Normalized Distance x_3; Results Obtained Along Line Positioned At $x_1 = 1.60h$, $x_2 = 0.00$.

is interesting to notice in Figures 5.32 and 5.46 that, although the plane-stress solutions of u_3 in *problem one* and *two* differ noticeably, the three-dimensional solutions for both problems have little difference. As the internal points through thickness are placed farther away from the surface of the hole, the numerical solutions approach the plane-stress solutions and become linear in x_3.

5.5 Conclusions

Two pressurized elliptical hole problems have been studied in this chapter. The results obtained from both the BEM and the FEM are in very good agreement. All the displacement components obtained from both the BEM and FEM converge to the plane-stress solutions when they are computed several plate thicknesses away from the elliptical hole surface. One very interesting aspect is that the BEM results,

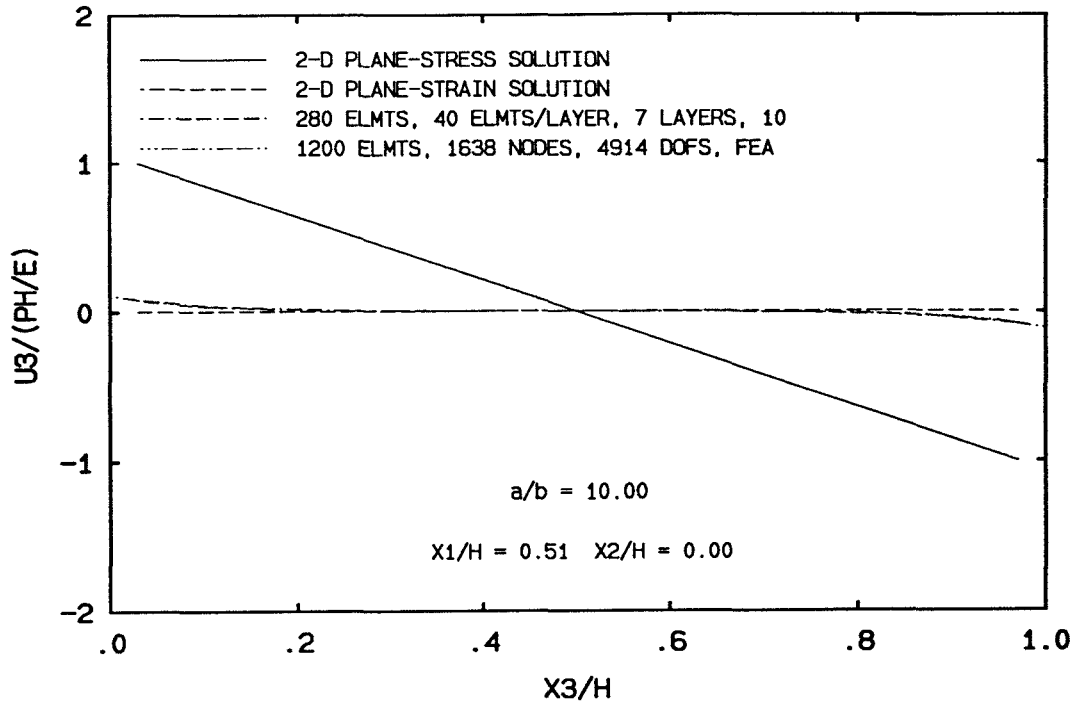

FIGURE 5.46 Normalized Displacement u_3 Vs. Normalized Distance x_3; Results Obtained Along Line Positioned At $x_1 = 0.51h$, $x_2 = 0.00$.

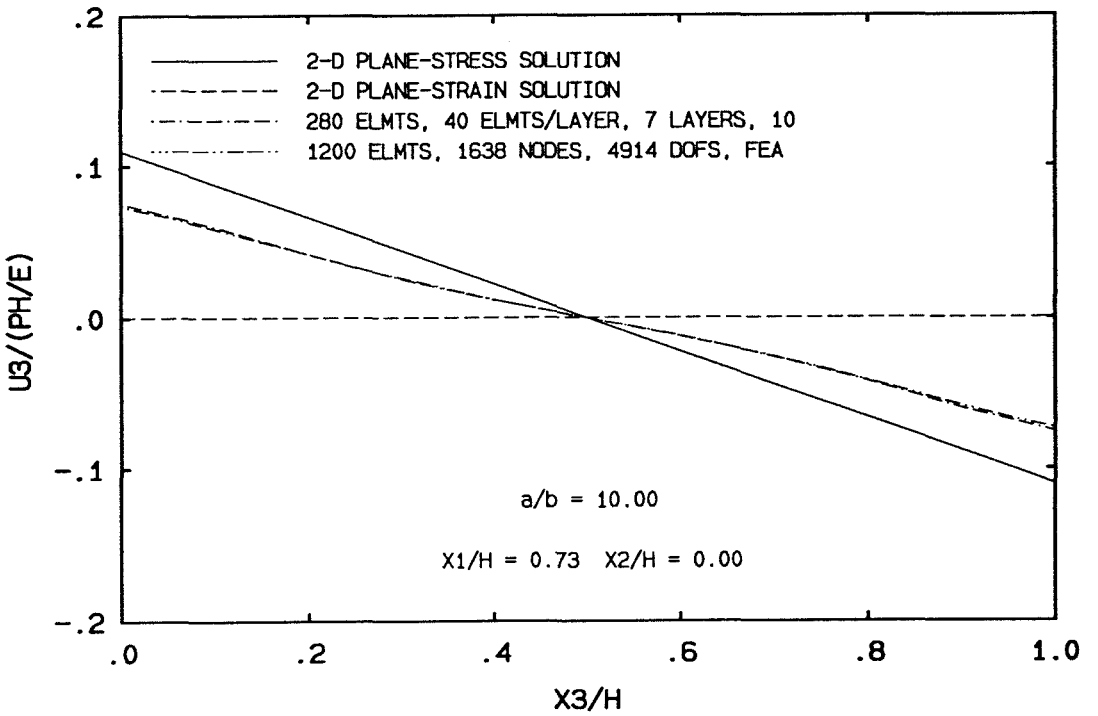

FIGURE 5.47 Normalized Displacement u_3 vs. Normalized Distance x_3; Results Obtained Along Line Positioned At $x_1 = 0.73h$, $x_2 = 0.00$.

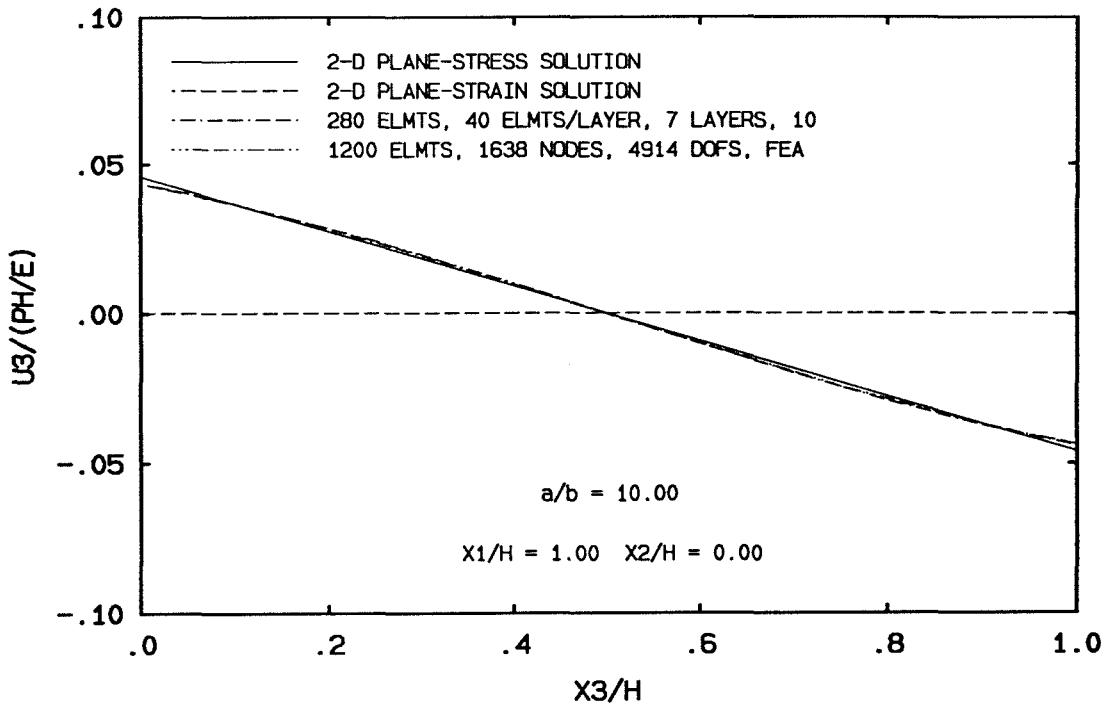

FIGURE 5.48 Normalized Displacement u_3 vs. Normalized Distance x_3; Results Obtained Along Line Positioned At $x_1 = 1.00h$, $x_2 = 0.00$.

particularly u_1 and u_2, are closer to the plane-stress solutions than their FEM counterparts when they are obtained several plate thicknesses away from the surface of the hole.

It is very important to notice that the local mesh refinement improves the results considerably. This aspect is shown thoroughly in *problem one*. The local mesh refinement on the flatter sides of the ellipse does not affect the results near the tips much. This observation makes it possible to use relatively large elements on the flatter sides of the ellipse, and refine the elements near the tips without changing the total number of elements. The results of *problem two* agree with the FEM results better than those of *problem one*. This is attributed to the local mesh refinement on both methods.

The study of these problems show that u_1 and u_2 do not differ from the plane-

stress and plane-strain solutions as much as u_3 does. The variations of u_1 with respect to x_1 agree better with the plane-stress solution than the plane-strain solution. In the region near the surface of the hole ($0.5h \leq x_1 \leq h$), the results for u_1 differ from both the plane-stress and plane-strain solutions due to the three-dimensional effects. However, on the flatter sides of the ellipse, the variations of u_2 with respect to x_2 agree better with the plane-stress solution when they are evaluated near the surfaces of the plate. On the other hand, u_2 thickness variations approach the plane-strain solution when they are computed closer to the midplane of the plate. As smaller elements are used in the meshes for both the BEM and the FEM in *problem two*, the agreement between the BEM and the FEM results in the u_1 versus x_1 variations improve very much as compared to those shown in *problem one*. When the displacements u_1 and u_2 are computed far away from the surface of the elliptical hole, in both problems, the BEM results demonstrate better agreement with the plane-stress solution than the FEM results.

The numerical results obtained by the BEM and the FEM show that the u_3 versus x_1 variations for both problems are almost the same except in the region within about $0.2h$ from the surface of the hole. In this region, the results of *problem two* show more displacement reduction in u_3 than in *problem one*, which suggests the presence of higher stress concentration in *problem two*. The sizes of the three-dimensional zones have almost no difference for the two problems. In the x_1-direction, the three-dimensional zone at the depth of $0.95h$ is about $0.5h$, and the three-dimensional zone size is about $0.4h$ at the depth $0.75h$. On the other hand, in the x_2-direction, the sizes of the three-dimensional zones are about $0.3h$ at the depth of $0.95h$ and about $0.25h$ at the depth of $0.75h$, respectively.

The thickness variations of u_1 in the x_1 direction show that a stronger three-

dimensional effect is presented in *problem two* near the tips of the ellipse than in *problem one*. However, in both problems, the thickness variations of u_3 in the x_1 direction obtained by the BEM and the FEM are almost the same despite the difference in the plane-stress solutions.

All these test problems may not be the best examples to show the time advantage of the modified BEM, since in these cases the FEM takes advantage of the symmetry while the modified BEM does not. As a matter of fact, in some case, the modified BEM is much slower (about 120 times slower) than the FEM in dealing with these test problems. The major strength of the modified BEM lies in analyzing problems with no symmetry in both loading and geometry, furthermore, the problems may involve complicated geometry. In these problems, it is a painstaking process for using the FEM. One of the reasons is that it is difficult for FEM to model the problems and to remodel them if the changes do occur. The major obstacle in using the FEM to study this type of problems is that, in stead of modeling only one eighth of a problem, the FEM has to model the entire problem. Thus, the total number of unknowns will increase eight times; the bandwidth of the final stiffness matrix may increase at least eight times. Since the computational time for the FEM is approximately proportional to nm^2, where n is the number of unknowns and m is the bandwidth. Hence, for problems with no symmetry, the total computational time consumed by the FEM would increase at least 512 times. This makes the FEM inferior compared to the modified BEM in dealing with this type of problems.

5.6 Future Work

Although much has been accomplished in this primary study, much future development is still needed. In addition, future development will concentrate on stress calculations. The major goal of these calculations is to compute the first order derivatives of the stress and displacement components of the fundamental solution of the infinite plate problem and to implement these results in the boundary element code. A lot of work in this area has already been done by the author.

Another part that needs development is the implementation of the modified boundary element method using a parallel computer. In any boundary element method, a boundary integral equation is obtained by applying a concentrated load at a node, and then computing the components of the 3×3 submatrices $[G_{ij}]$ and $[\hat{H}_{ij}]$ for each element. These submatrices can be computed independently for different loading points. The use of a parallel computer can take great advantage of this characteristic of the boundary element method. As a result, the computing speed for a problem can be improved tremendously.

Finally, future work can be directed towards the development and the use of higher order elements, such as bi-linear elements. In this area, several questions have to be addressed. The most obvious one is related to the close-form evaluation of integrals, similar to the ones presented in Chapter Three, involving both Kelvin's solution and the bi-linear function. When such bi-linear elements are used, the nodes are sometimes placed on the two planar surfaces of the plate. In such cases, when the nodes on the plate surfaces are encountered, the three-dimensional half-space solution may have to be used to replace Kelvin's solution in the proposed procedure. This is a major difference between the use of constant elements and the use of the bi-linear elements. It should be noted that, in the case of constant elements, the

nodes are never placed on the two planar surfaces. In addition, the corner problems will be introduced because of the use of bi-linear elements. It is indeed a challenging task to deal with three-dimensional corner and edge problems. Chaudonneret [46] and later Mustoe [47] proposed methods for analyzing such corner problems in two-dimensions. Banerjee and Butterfield [1] extended Chaudonneret's procedure to deal with three-dimensional corner and edge problems.

Although this study has been focused on the development of the modified boundary method, it should be pointed out that many engineering problems can be explored by this method. One class of such problems is the multiple domain problems. These are problems involving plates of different materials and thicknesses. The most attractive aspect of this method is that it can be efficiently applied to the analysis of interaction problems in plates containing holes, voids and cracks. However, this method is not restricted to problems involving plate structures. It can deal with any problem with two or more planar surfaces. A connecting rod problem is one of many engineering examples. Indeed, the potential uses of this method include a multitude of engineering applications.

CHAPTER 6

APPENDIX

In this appendix, the formulas of the analytical integration of the integrals of the following form

$$G(\nu, n, \alpha, \beta) = \int_0^\infty \lambda^n e^{-\alpha\lambda} J_\nu(\beta\lambda)\, d\lambda$$

are given, and they are listed below. Define

$$R = \sqrt{\alpha^2 + \beta^2}$$

$$G(0, 0, \alpha, \beta) = \frac{1}{R} \tag{A.1}$$

$$G(0, 1, \alpha, \beta) = \frac{\alpha}{R^3} \tag{A.2}$$

$$G(0, 2, \alpha, \beta) = -\frac{1}{R^3}\left(1 - \frac{3\alpha^2}{R^2}\right) \tag{A.3}$$

$$G(0, 3, \alpha, \beta) = -\frac{3\alpha}{R^5}\left(3 - \frac{5\alpha^2}{R^2}\right) \tag{A.4}$$

$$G(0, 4, \alpha, \beta) = \frac{3}{R^5}\left(3 - \frac{30\alpha^2}{R^2} + \frac{35\alpha^4}{R^4}\right) \tag{A.5}$$

$$G(1, 0, \alpha, \beta) = \frac{\beta}{R(R + \alpha)} \tag{A.6}$$

$$G(1,1,\alpha,\beta) = \frac{\beta}{R^3} \tag{A.7}$$

$$G(1,2,\alpha,\beta) = \frac{3\alpha\beta}{R^5} \tag{A.8}$$

$$G(1,3,\alpha,\beta) = -\frac{3\beta}{R^5}\left(1 - \frac{5\alpha^2}{R^2}\right) \tag{A.9}$$

$$G(1,4,\alpha,\beta) = -\frac{15\alpha\beta}{R^7}\left(3 - \frac{7\alpha^2}{R^2}\right) \tag{A.10}$$

$$G(2,0,\alpha,\beta) = \frac{\beta^2}{R(R+\alpha)^2} \tag{A.11}$$

$$G(2,1,\alpha,\beta) = \frac{\beta^2}{R^2(R+\alpha)^2}\left(2 + \frac{\alpha}{R}\right) \tag{A.12}$$

$$G(2,2,\alpha,\beta) = \frac{3\beta^2}{R^5} \tag{A.13}$$

$$G(2,3,\alpha,\beta) = \frac{15\alpha\beta^2}{R^7} \tag{A.14}$$

$$G(2,4,\alpha,\beta) = \frac{15\beta^2}{R^7}\left(6 - 7\frac{\beta^2}{R^2}\right) \tag{A.15}$$

$$G(3,0,\alpha,\beta) = \frac{\beta^3}{R(R+\alpha)^3} \tag{A.16}$$

$$G(3,1,\alpha,\beta) = \frac{\beta^3}{R^2(R+\alpha)^3}\left(3 + \frac{\alpha}{R}\right) \tag{A.17}$$

$$G(3,2,\alpha,\beta) = \frac{\beta^3}{R^3(R+\alpha)^3}\left(8 + 9\frac{\alpha}{R} + 3\frac{\alpha^2}{R^2}\right) \tag{A.18}$$

$$G(3,3,\alpha,\beta) = \frac{15\beta^3}{R^7} \tag{A.19}$$

$$G(3,4,\alpha,\beta) = \frac{105\alpha\beta^3}{R^9} \tag{A.20}$$

Bibliography

[1] P. K. Banerjee and R. Butterfield, "Boundary Element Methods In Engineering Science." *McGraw–Hill, London.* (1981).

[2] C. A. Brebbia and J. Dominguez, "Boundary Elements." *McGraw–Hill, Avon.* (1989).

[3] S. L. Crouch and A. M. Starfield, "Boundary Element Methods In Solid Mechanics." *George Allen & Unwin, London.* (1983).

[4] O. C. Zienkiewicz, "The Finite Element Method.", *McGraw–Hill, London.* (1977).

[5] K. J. Bathe and E. L. Wilson, "Numerical Methods In Finite Element Analysis." *Prentice–Hill, New Jersey.* (1976).

[6] W. Thomson (Lord Kelvin) and P. G. Tait, "Treatise On Natural Philosophy (reprinted as Principles Of Mechanics And Dynamics). Part II." *New York: Dover.* (1962).

[7] J. L. Swedlow and T. A. Cruse, "Formulation of Boundary Integral Equations For Three-Dimensional Elastoplastic Flow." *Int. J. Solids & Structures.* **7**. (1971), 1673–1683.

[8] T. A. Cruse, "Boundary Element Analysis In Computational Fracture Mechanics." *Kluwer Academic Publishers.* (1988).

[9] M. J. Abdel-Mihsein and R. T. Fenner, "Some Boundary Integral Equation Solutions For Three-Dimensional Stress Concentration Problems." *J. Strain Anal.* **18 (4)**. (1983), 207–215.

[10] T. A. Cruse and G. J. Meyers, "Three-Dimensional Fracture Mechanics Analysis." *ASCE J. Structural Div.* **103**. (1977), 309–320.

[11] C. L. Tan and R. T. Fenner, " Elastic Fracture Mechanics Analysis By The Boundary Integral Equation Method." *Proc. Roy. Soc. London Ser.* **A 369**. (1979), 243–260.

[12] J. O. Watson, "Hermitian Cubic Boundary Elements For Plane Problems Of Fracture Mechanics." *Res. Mech.* **4**. (1982), 23–42.

[13] T. Y. Fan and H. G. Hahn, "An Application Of The Boundary Integral Equation Method To Dynamic Fracture Mechanics." *Engrg. Fracture Mech.* **21 (2)**. (1985), 307–313.

[14] C. A. Brebbia, "The Boundary Element Method for Engineers." *Pentech Press, Plymouth.* (1978).

[15] T. A. Cruse, "Recent Advances in Boundary Element Analysis Methods." *Computer Methods in Applied Mechanics and Engineering.* **62**. (1987), 227–244.

[16] F. J. Rizzo, "A Integral Equation Approach To Boundary Value Problems Of Classical Elastostatics." *Q. Appl. Math.* **25**. (1967), 83–95.

[17] T. A. Cruse, "Numerical Solutions In Three-Dimensional Elastostatics." *Int. J. Solids Struct.* **5**. (1969), 1259–1274.

[18] T. A. Cruse, "Application Of The Boundary-Integral Equation Method Of Three-Dimensional Stress Analysis." *Comput. Struct.* **3**. (1974), 741–754.

[19] T. A. Cruse, "An Improved Boundary-Integral Equation Method For Three-Dimensional Elastic Stress Analysis." *AFOSR-TR-75-0813.* May, (1975)

[20] T. Kerminidis, "A Numerical Solution For Axially Symmetrical Elasticity Problems." *Int. J. Solids Struct.* **11**. (1975), 493–500.

[21] R. D. Mindlin, "Force At A Point In The Interior Of A Semi-Infinite Solid." *Physics, Vol.* **7**. (1936), 195–202.

[22] J. F. C. Telles and C. A. Brebbia, "Boundary Element Solution For Half-Plane Problems." *Int. J. Solids & Structures, Vol.* **17**, *No.* **12**. (1981), 1149–1158.

[23] M. D. Snyder and T. A. Cruse, "Boundary-Integral Equation Analysis Of Cracked Anisotropic Plates." *Int. J. Fracture,* **11**. (1975), 315–328.

[24] F. G. Benitez and A. J. Rosakis, "Three-Dimensional Elastics Of A Layer And A Layered Medium." *J. of Elasticity.* **18**. (1987), pp 3–50.

[25] J. Dougall, "An Analytical Theory Of The Equilibrium Of An Elastic Plate." *Trans. Roy. Soc. Edinburgh. Vol.* **41** (1904), pp. 129–228.

[26] O. Teodone, "Saggio di una teoria generale delle equazioni dell'equilibrio elastico per un corpo isotropo'." *Ann. Matematica pur. Appl., Ser. III a, Vol.* **10** (1904), pp. 13–64.

[27] L. Orlando, "Sulla deformazione di un solido isotropo limitato da due piani paralleli per tensione superficiali date." *Rend. Circ. Mat. Palermo, Vol.* **19** (1905), pp. 66–80.

[28] A. I. Lur'e, "On The Problem Of The Equilibrium Of Plates On Variable Thickness." *Trudy Leningrad. Industrial's Nago Inst., No.* **6** (1936), p. 57.

[29] A. I. Lur'e, "On The Theory Of Thick Plate." *Prikl. matem. i mekh., Vol.* **6** (1942), p. 151.

[30] G. S Shapiro, "On The Distribution Of Stresses In An Unbounded Layer." *Prikl. matem. i mekh., Vol.* **8** (1944), pp. 167–168.

[31] I. N. Sneddon, "The Elastic Stresses Produced In A Thick Plate By The Application Of Pressure To Its Free Surfaces." *Proc. Cambridge Phil. Soc. Vol.* **42** (1946), pp. 260–271.

[32] M. J. Turteltaub, and E. Sternberg, "On Concentrated Loads And Green's Functions In Elasticity." *Arch. Rational Mech. Anal. Vol.* **29** (1968), pp 193–240.

[33] V. Z. Vlasov and N. N. Leont'ev, "Beams, Plates and Shells On Elastic Foundations." *Ch.* **7**, *Jerusalem, NASA TT F–357 TT65–50135* (1966)

[34] H. Bufler, "Theory Of Elasticity Of A Multilayered Medium." *J. Elasticity, Vol.* **1**, *No.* **2**, *Dec.* (1971), pp.125–143.

[35] W. Thomson (Lord Kelvin), "On The Equations Of Equilibrium Of An Elastic Solid." *Cambridge and Dublin Mathematical Journal* **3** (1848), p. 87.

[36] E. Sternberg and R. A. Eubanks, "On The Concept Of Concentrated Loads And Extension Of The Uniqueness Theorem In The Linear Theory Of Elasticity." *J. Rational Mechanics And Analysis* **4** (1935), p. 135.

[37] E. Betti, "Teoria dell Elasticita." *Il Nuovo Ciemento*, t. 7–10, (1872).

[38] C. Somigliana, "Sopra l'equilibrio di us corpo elastico isotropo." *Il Nuovo Ciemento*, t. 17–19, (1885).

[39] M. A. Jaswon and A. R. Ponter, "An Integral Equation Solution of the Torsion Problem." *Proc. of the Roy. Soc.* **A**, pp. 237–246.

[40] F. J. Rizzo, "An Integral Equation Approach to Boundary Value Problems of Classical Elastostatics." *Quarterly of Applied Mathematics,* **25**, pp. 83–96.

[41] Milton Abramowitz and Irene A. Stegun, "Handbook of Mathematical Formulas with Formulas, Graphs, and Mathematical Tables." *National Bureau of Standards, Applied Mathematics Series.* **55**. (1964).

[42] I. S. Gradshteyn and I. M. Ryzhik, "Table of Integrals, Series, and Products." *Academic Press.* (1980)

[43] S. P. Timoshenko, J. N. Goodier, "Theory of Elasticity." Third Edition, *McGraw–Hill Book Company.* (1970)

[44] W. Yang and L. B. Freund, "Transverse Shear Effects For Through-Cracks In An Elastic Plate." *Int. J. Solids Structures. Vol.* **21**, *No.* **19**. (1985), pp. 977–994.

[45] A. J. Rosakis and K. Ravichandar, "On Crack-Tip Stress State: An Experimental Evaluation Of Three-Dimensional Effects." *Int. J. Solids Structures. Vol.* **22**. *No.* **2**. (1986), pp. 121–134.

[46] M. Chaudonneret, "Resolution of Traction Discontinuity Problem in Boundary Integral Equation Method Applied to Stress Analysis." *C.r., Acad. de Sci., Ser. A. Math.*, **284**(8) (1977), pp. 463–466.

[47] G. G. W. Mustoe, "A Combination of the Finite Element Method and Boundary Integral Procedure for Continuum Problems." *Ph.D. Thesis, Univ. of Wales, Univ. College. Swansea.* (1980).